Chapter 1

Introduction

Radio astronomy began as a result of the serendipitous discovery by Karl Jansky of noise-like 20.5 MHz radio emission from the Milky Way (Jansky, 1933). Jansky's apparatus and work commitments did not allow him to extend his investigation of this newly discovered phenomenon and no further radio measurements of the galactic radio emission were attempted during the ensuing decade. Grote Reber's hand-drawn contour map of the 160 MHz celestial radio emission was the first description of how the radio continuum emission from our parent galaxy is distributed across the sky (Reber, 1940a; Reber, 1940b; Reber, 1944). A number of radio continuum surveys spanning a wide range in frequency have been made of the northern and southern skies since 1944. One of the most recent surveys to be completed is the Rhodes/HartRAO 2326 MHz *SKYMAP* project, which is the highest resolution and highest frequency pencil-beam radio continuum survey ever made of the galactic radio continuum (Jonas et al., 1998). This thesis describes the method of observation and data reduction techniques used for this survey and presents an analysis of the galactic radio continuum emission seen in the resulting map.

1.1 Radio Continuum Surveys

Large area, medium resolution radio continuum surveys at gigahertz frequencies are long-term research projects that confront the observer with severe technical and logistic difficulties. These difficulties are balanced by strong scientific incentives to undertake this (unpopular) survey work. Radio continuum surveys provide essential basic data that is used in both galactic and extragalactic astrophysical research. For example, the radio survey data are used for the study of galactic supernova remnants, HII regions and the diffuse synchrotron and thermal emission from the Milky Way. Knowledge of the diffuse

galactic emission, in turn, allows the correction of cosmic microwave background radiation (CMBR) measurements for galactic contamination. Quantification of the structure and spectrum of the high-latitude galactic emission over a wide range of angular scales will be particularly important for the analysis of CMBR data from future experiments that probe the "doppler peak" with sub-degree resolution. Other extragalactic applications for this type of survey include the mapping of the extended radio emission from relatively nearby galaxies and the cataloguing of the point-sources associated with distant radio galaxies and quasars.

In order to set the context for discussing the attributes and characteristics of the *SKYMAP* 2326 MHz survey it is necessary to investigate the current status of existing radio continuum surveys. Table 1.1 lists all of the radio continuum surveys that cover more than 33% of the sky. The information in this table is summarised in a graphical form in figure 1.1. These surveys cover a wide range in frequency, but only a small fraction of them have FWHM resolutions that are better than 1°. Most of them are sensitive to very large angular scale structures and have been used in the past to study the structure and spectrum of the large-scale galactic emission.

Nearly all of these surveys were conducted from a single observing site, and therefore do not cover the whole sky. The first all-sky map of the large-scale celestial emission was constructed by combining the 200 MHz Dröge and Priester (1956) map of the northern sky with the 200 MHz Allen and Gum (1950) map of the southern sky. Subsequent all-sky maps were synthesized at 85 MHz (Yates, 1968), 150 MHz (Landecker and Wielebinski, 1970) and 30 MHz (Cane, 1978) by interpolating between maps at various different frequencies. The 408 MHz survey by Haslam et al. (Haslam et al., 1981; Haslam et al., 1982) remains the only all-sky radio continuum survey with an angular resolution better than 1°. Once the Argentinean 1420 MHz survey (P. Reich, private communication) has been completed it will be used to complement the existing 1420 MHz northern sky survey (Reich, 1982; Reich and Reich, 1986) to create an all-sky map with sub-degree resolution.

A number of radio continuum surveys have been undertaken which have searched large areas of sky for point-like, mostly extra-galactic, radio sources. Although these surveys were made at high resolution ($\theta_{\rm FWHM} \ll 1^\circ$) and are very sensitive to point-like sources, they were made using observation techniques that are not sensitive to large-scale radio structures. The major aim of these "point-source" surveys is the production of radio source catalogues. The more recent of these surveys/catalogues are the multi-frequency

Freq [MHz]	Resolution (FWHM)	Dec. Coverage $\delta_{\rm south}$	$\delta_{\rm north}$	Reference
8.3	$\approx 3^\circ$	-90°	0°	(Ellis, 1982)
10	2°	-5°	$+70^\circ$	(Caswell, 1976)
10	$4^\circ \times 5^\circ$	-65°	-2°	(Hamilton and Haynes, 1968)
13	$\approx 1.9^\circ$	-90°	0°	(Ellis, 1982)
16.5	$\approx 1.5^\circ$	-90°	0°	(Ellis, 1982)
30	11°	-90°	0°	(Mathewson et al., 1965)
34.5	$26' \times 42'$	-50°	$+70^\circ$	(Dwarakanath and Shankar, 1990)
38	$45'$	$+15^\circ$	$+90^\circ$	(Williams et al., 1966)
38	7.5°	-25°	$+70^\circ$	(Milogradov-Turin and Smith, 1973)
45	$4.6^\circ \times 2.4^\circ$	-90°	$+19.1^\circ$	(Alvarez et al., 1997)
85	$3.5^\circ \times 3.8^\circ$	-90°	$-20^\circ(+20^\circ)$	(Yates et al., 1967)
85	$3.8^\circ \times 3.5^\circ$	-25°	$+25^\circ$	(Landecker and Wielebinski, 1970)
100	17°	-90°	$+30^\circ$	(Bolton and Westfold, 1950)
150	2.1°	-25°	$+25^\circ$	(Landecker and Wielebinski, 1970)
153	2.2°	-90°	$+30^\circ$	(Hamilton and Haynes, 1969)
160	$\approx 12^\circ$	-35°	$+90^\circ$	(Reber, 1944)
178	$13.4' \times 4.6^\circ$	-5°	$+90^\circ$	(Turtle and Baldwin, 1962)
200	13°	-90°	$+45^\circ$	(Allen and Gum, 1950)
200	8°	-20°	$+90^\circ$	(Dröge and Priester, 1956)
250	$1.2^\circ \times 8^\circ$	-50°	$+90^\circ$	(Ko and Kraus, 1957; Ko and Kraus, 1958)
400	$2.2^\circ \times 1.7^\circ$	-35°	$+90^\circ$	(Seeger et al., 1965)
404	7.5°	-20°	$+90^\circ$	(Pauliny-Toth and Shakeshaft, 1962)
408	8°	-7.5°	$+90^\circ$	(Wielebinski and Shakeshaft, 1964)
408	$51'$	-90°	$+90^\circ$	(Haslam et al., 1982)
820	1.2°	-7°	$+85^\circ$	(Berkhuijsen, 1972)
1420	$35'$	-19°	$+90^\circ$	(Reich, 1982; Reich and Reich, 1986)
1420	$30'$	-90°	$\approx 0^\circ$	(P. Reich, private communication)
2326	$20'$	-80°	$+13^\circ(+32^\circ)$	(Jonas et al., 1998)
2700	$19'$	$\approx 0^\circ$	$+90^\circ$	(Reif, 1985) (data never published)
31500	7°	-90°	$+90^\circ$	(Bennett et al., 1996) (*COBE*)
53000	7°	-90°	$+90^\circ$	(Bennett et al., 1996) (*COBE*)
90000	7°	-90°	$+90^\circ$	(Bennett et al., 1996) (*COBE*)

Table 1.1: A frequency-ordered list of all radio continuum sky surveys that cover more than $\frac{1}{3}$ of the celestial sphere. The bracketed figures in the declination coverage columns indicate that the associated survey has steps in its declination limits. Note that the maps for some of the surveys have not yet been published. The information in this table is summarised in figure 1.1.

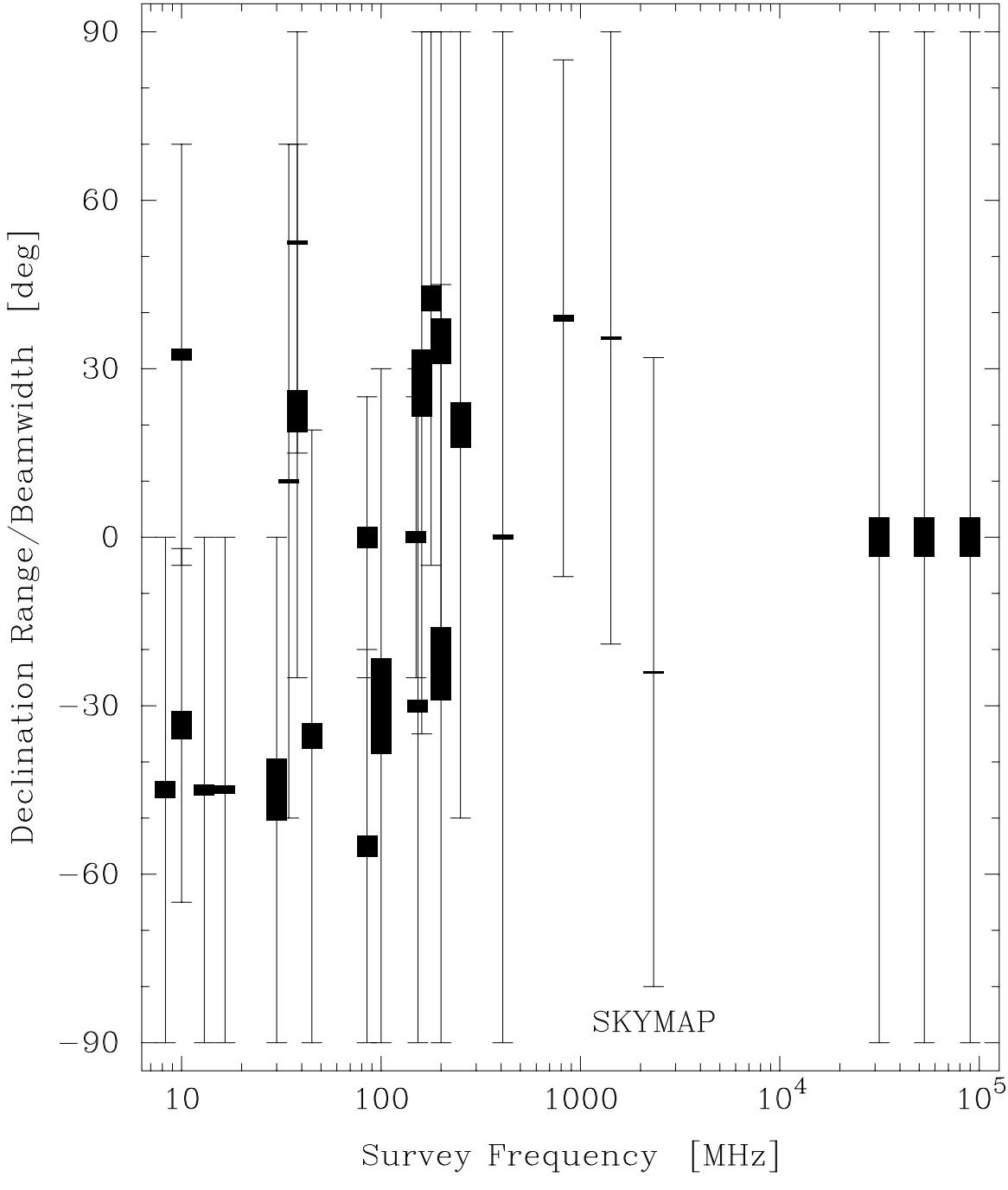

Figure 1.1: A graphical representation of the frequencies, declination spans and beamwidths of all large-area radio continuum surveys published to date. This figure summarises the surveys listed in table 1.1. The height of the filled rectangles in the centre of each marker represents the beamwidth of the relevant survey.

Parkes Catalogue (PKSCAT90, 1990), the 408 MHz Molonglo Reference Catalogue (Large et al., 1981; Large et al., 1991), the 4850 MHz PMN survey (Griffith et al., 1991; Griffith and Wright, 1993) and the 1.4 GHz NRAO VLA Sky Survey (NVSS) (Condon et al., 1993).

The "galactic plane" survey is further class of radio continuum survey that has been made over the past four decades. These surveys produce maps of the radio emission from a narrow latitude range about the galactic equator. Table 1.2 is a list of these galactic plane surveys made at frequencies above 400 MHz and figure 1.2 is a graphical summary of the frequency and sky coverage of these surveys. In addition to these systematic surveys of the galactic plane there have also been a number of surveys that consist of maps of individual sources in the galactic plane (Goss and Shaver, 1970; Shaver and Goss, 1970a; Shaver and Goss, 1970b; Reich et al., 1986; Fürst et al., 1987). All of these surveys have relatively high resolution ($43'' \leq \theta_{\rm FWHM} \leq 50'$), but do not accurately represent the large-scale galactic emission because of restricted latitude coverage and observation techniques.

The tables and figures presented here indicate that there is a need for medium resolution, large-area radio continuum surveys that tie together the disjointed sky coverage afforded by the low-resolution all-sky surveys, the medium-resolution galactic plane surveys and the high-resolution point-source surveys. Figure 1.1 also demonstrates quite clearly that there is a need for more surveys above 1 GHz, particularly in the southern hemisphere.

The Rhodes/HartRAO 2326 MHz radio continuum survey fills a number of gaps in these lists of currently available surveys:

- It is one of just two large-scale radio continuum surveys of the southern sky that have resolutions better than 1°. The 408 MHz survey (Haslam et al., 1982) is the only other existing continuum survey that covers the whole southern sky at sub-degree resolution. A 1420 MHz continuum survey with a resolution of $30'$ is currently being completed in Argentina (P. Reich, private communication) which will supplement the 408 MHz and 2362 MHz surveys.

- It is the highest frequency ground-based radio continuum survey that subtends a solid angle larger than 2π sr. The *SKYMAP* 2326 MHz survey allows the frequency dependence of the continuum spectrum of the galactic emission to be investigated more thoroughly than was possible with previous surveys.

- It is the highest resolution radio continuum survey subtending a solid angle larger than 2π sr. Unlike point-source and galactic plane surveys, the *SKYMAP* survey

Freq [MHz]	Resolution (FWHM)	ℓ Range $\ell_{\rm left}$	$\ell_{\rm right}$	$\lvert b\rvert \leq$	Reference
408	$47.5'$	355°	280°	6°	(Komesaroff, 1966)
408	$2.86'$	55°	195°	3°	(Green, 1974)
408	$1'$	145°	75°	3°	(Dougherty et al., 1996) (in progress)
610	$30'$	56°	352°	6°	(Morgan, 1965)
834	$43''$	5°	240°	10°	(Green, 1997) (in progress)
960	$50'$	267°	17°	10°	(Wilson and Bolton, 1960)
960	$50'$	320°	258°	10°	(Nicolson, 1965)
1410	$14'$	355°	280°	4°	(Hill, 1968)
1410	$9.4'$	240°	357°	4°	(Kallas and Reich, 1980; Reich et al., 1990b; Reich et al., 1997)
1414	$11'$	75°	335°	4°	(Altenhoff et al., 1970)
1420	$1'$	145°	75°	3°	(Dougherty et al., 1996) (in progress)
1440	$50'$	2°	256°	10°	(Mathewson et al., 1962a; Mathewson et al., 1962b)
2400	$10.4'$	5°	238°	5°	(Duncan et al., 1995b)
2650	$8.2'$	47°	190°	2°	(Beard, 1966; Beard and Kerr, 1969; Beard et al., 1969; Day et al., 1969; Day et al., 1970; Day et al., 1972; Goss and Day, 1970; Thomas and Day, 1969a; Thomas and Day, 1969b)
2695	$11'$	75°	335°	4°	(Altenhoff et al., 1970)
2695	$4.3'$	240°	358°	5°	(Reich et al., 1984; Junkes et al., 1987; Reich et al., 1990a; Fürst et al., 1990a; Fürst et al., 1990b)
4875	$2.6'$	60°	357.5°	1°	(Altenhoff et al., 1978)
5000	$11'$	75°	335°	4°	(Altenhoff et al., 1970)
5000	$4.1'$	40°	190°	2°	(Haynes et al., 1978)
10000	$3'$	56°	355°	1.5°	(Handa et al., 1987)

Table 1.2: Radio continuum surveys of the low-latitude radio continuum at frequencies higher than 400 MHz. The frequency and spatial distributions of these surveys are illustrated in figure 1.2.

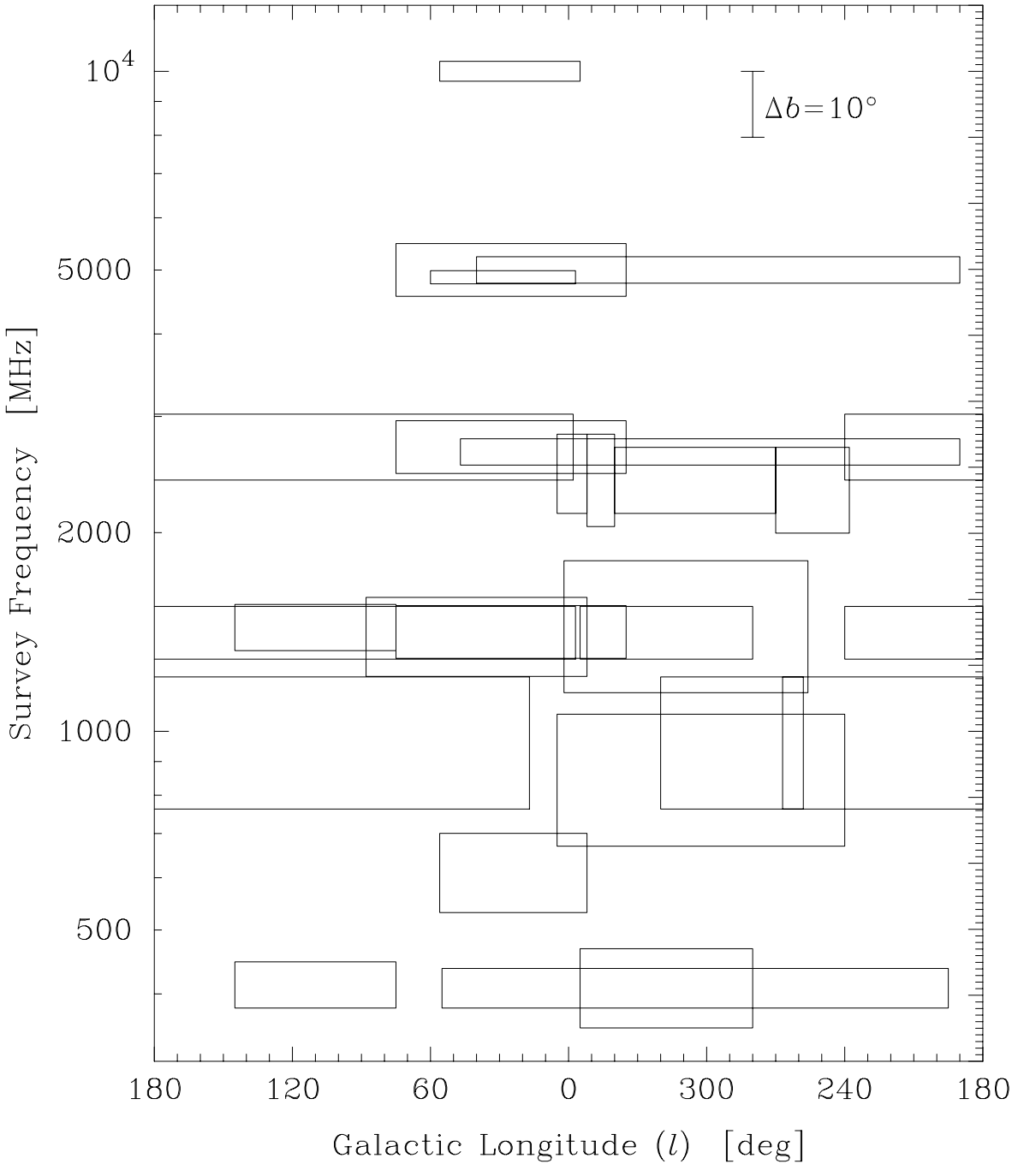

Figure 1.2: A graphical representation of the distribution in frequency and galactic coordinate space of all major galactic plane surveys above 400 MHz. This diagram was constructed using the parameters listed in table 1.2. The width and height of each rectangle represent the galactic longitude and latitude coverage of the associated survey. The small ticks on the right-hand axis are spaced at 1° intervals of galactic latitude. The frequency of each survey is given by the intercept of the horizontal bisector of the relevant rectangle with the left-hand axis.

is sensitive to a wide range of angular scales extending from $\approx 1^\circ$ $(3 \times HPBW)$ to $> 180^\circ$.

The paucity of medium-resolution pencil-beam radio surveys at high frequencies is not particularly surprising. Surveys of this type are long-term undertakings, requiring thousands of hours of telescope time. The observations also place severe demands on the performance of the telescope receivers. Good baseline and gain stability are of particular importance if large-scale emission features are to be rendered reliably in the resulting maps. Environmental factors, such as inclement weather, man-made radio interference, and natural terrestrial radio emission, also present significant challenges to the observer.

It is unlikely that ground-based, extensive radio continuum surveys of this kind will be made in the future. Radio interference from satellite down-links and terrestrial microwave communications systems has severely compromised single-dish continuum observing at many observatories, and this situation is sure to deteriorate. It is also doubtful that the required observing time will be made available by allocation committees.

The following section provides an overview of the work undertaken by the author in pursuance of *SKYMAP* 2326 MHz radio continuum survey project. This work is reported in more detail in the body of the thesis.

1.2 Overview

All of the *SKYMAP* observations were made using the 26-metre antenna at the Hartebeesthoek Radio Astronomy Observatory (HartRAO) near Johannesburg, South Africa. This facility is well-suited to the requirements of the survey because of the $20'$ beam at 2.3 GHz and the relatively uncongested time-allocation schedule. The characteristics of the antenna and observation procedures used to map the ten individual target areas are discussed in chapter 2. The data reduction processes applied to the observation data in order to produce the survey maps are described in chapter 3. The design and implementation of the prototype *SKYMAP* observing procedure and data reduction processes have previously been reported by Mountfort (1989) but various modifications that were effected by the author are described in chapters 2 and 3. The major modifications made to the data reduction software were the replacement of the original batch-oriented procedures with a more interactive processing environment and the implementation of a procedure for combining the ten individual component maps into a single composite map without edge

discontinuities.

Various calibration parameters of the *SKYMAP* survey data need to be known accurately if the map is to be used for any form of quantitative scientific work. Chapter 4 details the procedures that were used to verify the flux and temperature scales of the survey map and determine the uncertainties in these scales. Analyses of the RMS noise level and pointing accuracy of the map are also presented in this chapter.

Chapter 5 is a review of the observations and theoretical models reported in the literature that are relevant to the radio continuum emission of the Milky Way. Topics discussed in this chapter include the spiral structure of the Milky Way, the nature of the galactic interstellar medium (ISM), and the effects of supernova remnants (SNRs) on the various components of the ISM. Current ISM models propose the existence of various SNR-related structures in the ISM that should be discernible in the *SKYMAP* radio continuum map. Searches for these objects in the *SKYMAP* map are described in later chapters. The observable consequences of current theories of galactic cosmic ray diffusion are also discussed.

The investigation of the diffuse galactic background (DGB) radiation presented in chapter 6 has two objectives: (a) the reconciliation of the observed morphology of the DGB with models of the spiral structure of the Milky Way, and (b) the isolation of discrete galactic radio sources from the extended DGB emission in order to emphasize these faint sources and hence facilitate their identification. Both of these objectives require a model of the DGB emission, and a new technique for obtaining an empirical model of the DGB from the *SKYMAP* data is discussed. The familiar galactic loops, and also faint, large-scale loop-like structures that have not been identified previously, are prominent in the DGB-subtracted map. The high-latitude and very extended objects identified in the residual maps are discussed briefly in chapter 6, but their interpretation is held over to chapter 8.

A modern trend in astronomy is to make observations of target objects at a number of different wavelengths and then perform multi-spectral analyses on the resulting data. The various wavelengths probe different physical processes in the object and therefore the multi-spectral analysis permits a broader understanding of the nature of the object. This is certainly true for the Milky Way, and chapter 7 compares the *SKYMAP* 2326 MHz map of the galactic continuum emission with maps at lower and higher radio frequencies, and with far-infrared maps. These analyses include: (a) the calculation of the low-frequency spectral index of the galactic emission in an attempt to test cosmic ray diffusion models, (b) the estimation of the galactic foreground contamination of CMBR measurements,

(c) the identification of galactic HII regions on the basis of their FIR/radio flux ratio, and (d) the correlation between the FIR cirrus emission and high-latitude radio emission features.

SNRs undoubtably play a major role in the dynamics and energetics of the galactic ISM, but current SNR catalogues are known to be statistically incomplete. Statistical tests and Monte Carlo models estimate that only about 10% of the galactic SNRs have been identified. This incompleteness is largely due to source confusion near the galactic plane that makes the identification of SNR candidates difficult. By subtracting the emission associated with the empirical DGB model and the bright galactic HII regions from the *SKYMAP* 2326 MHz map the source confusion near the galactic plane has been reduced quite significantly. As a result, 42 new radio sources with shell-like structures or other morphologies suggestive of SNR emission were identified in the residual 2326 MHz map. These sources are discussed in the context of current ISM theories in chapter 8.

Chapter 9 presents a synopsis of the conclusions drawn from the work presented in this thesis and discusses further observations required to complete the *SKYMAP* project. Although the *SKYMAP* project has produced a 2326 MHz radio continuum map of 67% of the sky there still remain two tasks that need to be performed. These are: (a) the mapping of the small area of sky near to the southern equatorial pole, and (b) the improvement of the accuracy of the baseline of the map. The new techniques and instrumentation required to complete these two experimental procedures are discussed in chapter 9.

Pseudo-colour images of radio brightness and spectral index maps are included as appendix C at the end of this thesis. It was thought that this was a more convenient arrangement than including the plates near to the relevant text in the body of the thesis.

1.3 Current *SKYMAP* Publications

A number of staff members and students in the Department of Physics and Electronics at Rhodes University have contributed to the *SKYMAP* survey project by developing software systems, making observations, reducing the raw data into maps, and performing astrophysical interpretation on the results. Five postgraduate theses have resulted from this work to date (Jonas, 1982; Greybe, 1984; Wright, 1989; Mountfort, 1989; Woermann, 1998). In addition to these theses, a number of results arising from the survey data have been published in the literature (Jonas et al., 1985; Jonas, 1986; Mountfort et al., 1987;

Jonas, 1993; Jonas and Baart, 1995; Jonas, 1998), and the preliminary results of the semi-completed survey have been published recently (Jonas et al., 1998). The appropriate publications are cited wherever results of previously published work are discussed in this thesis.

Chapter 2

SKYMAP Survey Observations

The 2326 MHz *SKYMAP* survey observations were made over a 13 year period, starting in 1980 and ending in 1992. In order to understand the characteristics and limitations of the final survey data, it is necessary to have full knowledge of the equipment used for the observations and the techniques used to obtain the data. For such a long-term experiment it is particularly important to monitor the effects that inevitable changes in the experimental procedure may have had on the data. This chapter covers the description of the equipment, describes the observation technique, and notes changes made to the equipment and technique. Much of this information is used in the following two chapters.

All of the 2326 MHz survey observations were made at the Hartebeesthoek Radio Astronomy Observatory (HartRAO), a National Facility operated by the Foundation for Research Development of South Africa. This chapter includes a brief description of the telescope and the receiver system used for the observations, and lists the telescope parameters that are relevant to the survey observations. The maintenance and development of all of the physical telescope subsystems was undertaken by the observatory staff.

The *SKYMAP* observation procedure was originally conceived, designed and implemented by Mountfort (1989). The characteristics of this observing technique are reviewed briefly, and modifications made by the author to the original observing system are discussed. The systematic effects introduced into the survey data by the observing technique are examined.

The final section of this chapter provides details of the scheduling of the survey observations. Some of the survey observations were supervised by Rhodes University staff, but the automated nature of the observing procedure allowed many of the observations to be made in "absentee mode", i.e. supervised by the observatory staff. This absentee observing proved to be indispensable, given the logistic difficulties imposed by the 1100 km

Longitude	$27°41'$ east
Latitude	$25°53'$ south
Mount geometry	Equatorial
Feed configuration	Cassegrain
Physical diameter	26 m
Half-power beamwidth (FWHM)	$20'$
Point-source sensitivity (PSS)	9.8 Jy/K
Aperture efficiency	53%
Main beam efficiency	55%
Full beam efficiency	69%
Polarization	Linear E–W
Receiver front end	TWT maser (before 8/2/1983) GaAsFET (24/4/1985–16/5/1992) HEMT (after 16/5/1992)
System temperature (at zenith)	30 K (maser) 46 K (GaAsFET) 39 K (HEMT)
Centre frequency	2295 MHz (maser) 2326 MHz (GaAsFET & HEMT)
Pre-detection bandwidth	15 MHz (maser) 40 MHz (GaAsFET & HEMT)

Table 2.1: Parameters and configurations of the HartRAO telescope relevant to the 2326 MHz *SKYMAP* radio continuum survey.

distance between HartRAO and Rhodes University.

2.1 The Telescope and Receiver System

This section discusses characteristics of the HartRAO telescope that are relevant to the observation technique and the survey results. Figure 2.1 is a block diagram of the 13 cm receiver configuration that was used for the survey observations. Individual components of the receiver were upgraded over the 13 year observation period, but the same basic configuration was used for all of the observations. Table 2.1 lists the relevant parameters of this telescope when operating at 2326 MHz, the nominal centre frequency of the $\lambda = 13$ cm receiver system. These parameters remained constant over the observing period, except where explicitly indicated. Some of the antenna parameters are discussed in more detail in chapter 4. Brief descriptions of the individual telescope components are given below.

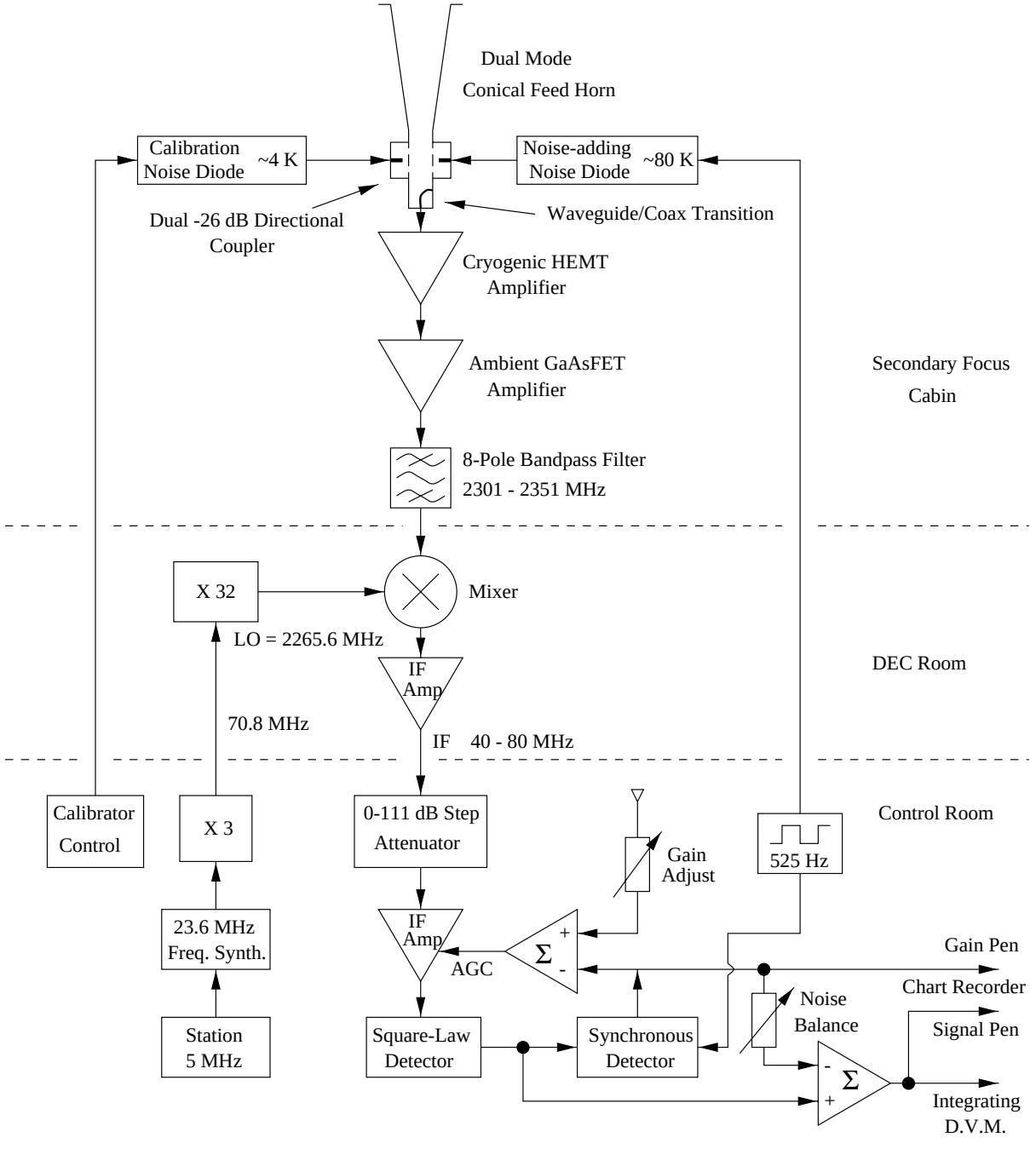

Figure 2.1: A block diagram showing the nominal configuration of the receiver and radiometer system used for the survey observations. Individual components may have been different for various observing epochs, but the overall configuration remained fixed.

2.1.1 The Antenna

The cassegrain optics of the HartRAO telescope consist of a 26 metre-diameter parabolic reflector and a 3 metre-diameter, hyperbolic secondary reflector. The secondary reflector and its four support legs contribute quite significant aperture blockage and scattering, which produces the cross-like sidelobe pattern evident in figure 4.1. The beam pattern and related performance parameters are discussed in detail in chapter 4. The various feed horns and cryogenic receiver packages are enclosed in a feed cabin, which is mounted above the centre of the dish surface. The receiver feed systems have fixed mountings in this cabin, which necessitates that all of the feed horns are offset from the optical axis of the antenna.

The telescope has a polar mount geometry, and both axes are under computer control. The computer control system was initially developed by Mountfort (1989), and the control algorithm was essentially unchanged for the duration of the survey observations. The pointing error map for the two antenna axes was improved over the observation period, and the replacement of the axis shaft encoders with modern optical devices in 1985 markedly enhanced the pointing performance of the antenna. At the time of the survey observations, the support structure did not allow access to the southern equatorial pole (SEP), resulting in the southern boundary of the survey at -83° declination.

2.1.2 The Feed Horn and Waveguide Components

A conical, dual-mode feed horn (Potter, 1963) was used for all of the survey observations. The use of the dominant mode and a higher order mode results in a circular beam with coincident phase centres for orthogonal polarizations. Coupled with exceptionally low sidelobes, it is an ideal feed for cassegrain antennas, although it is limited in bandwidth. All survey observations were made in linear polarization (E-vector East-West) since no quarter-wave transformer was available during the observing period. The polarization orientation remained E-W irrespective of how the telescope was manoeuvred because the telescope has an equatorial mount.

Directional couplers allowed the injection of noise signals from two high-stability noise diodes into the waveguide directly after the feed horn. The excess noise temperature of one of the diodes was adjusted to be about twice the receiver noise temperature. This high-level noise diode was continuously switched at 525 Hz with a 50 percent duty cycle. This modulated signal was recovered by the radiometer for gain and baseline stabilization

(see below). The second noise diode had an effective antenna temperature of 3.95 K, which was close to the expected variation in antenna temperature due to astronomical sources. This low-level noise source was used to calibrate the antenna temperature scale for each observation. The antenna temperature scale is discussed in chapter 4.

The waveguide signal was coupled into the receiver dewar package via a low-loss coaxial line transition. Variations in system temperature due to waveguide and transmission line losses were minimized by regulating the air temperature in the feed cabin to within 1° C. A low pressure supply of dry air ensured that the waveguide and feed horn cavities remained free of condensation.

2.1.3 The Receiver

The first maps (A12D63 and A23D80 in figure 2.6) were made using a travelling-wave maser receiver which required a liquid helium cryostat to achieve a 4 K operating temperature. This receiver package proved to be very temperamental, and all of the subsequent observations were made using FET front-end amplifiers cooled to 17 K by a more robust closed-cycle helium cryostat. The transistor amplifiers had a higher noise temperature than the maser, but this drawback was amply compensated for by their wider operating bandwidth, improved gain stability and excellent reliability. Unfortunately the full bandwidth of the transistor amplifiers could not be utilised because of interference from satellite and terrestrial communication signals. Bandpass filters were inserted in the RF signal path to restrict the pre-detection passband of the receiver to an interference-free region of the S-band spectrum.

An ambient temperature GaAsFET amplifier was used to provide additional gain in the feed cabin, and to buffer the RF signal for transmission to the mixer via low-loss semi-rigid coaxial cable. The mixer and final frequency multipliers in the local oscillator chain were located in the DEC (declination) room, a compartment located directly below the feed cabin and the antenna surface. Low-loss coaxial cables were used to transfer IF and LO signals between the DEC room and the control room.

2.1.4 The Radiometer and Data Recording

The remainder of the receiver instrumentation was housed in the control room, which is located in a building near to the antenna. All of the survey observations were made using a noise-adding, gain-stabilized radiometer, the operation of which is briefly described

below. Detailed analysis of the radiometer operation is available from more authoritative sources (Jelley and Cooper, 1961; Nicolson, 1970). The characteristic of the noise-adding radiometer that made it suitable for the survey observations was the effective suppression of 1/f noise caused mainly by fluctuations in the receiver open loop gain.

The major components of the radiometer are seen in figure 2.1. The first stage of the radiometer was a manually operated step attenuator that was used to adjust the signal level presented to the input of the second IF amplifier. The IF amplifier gain was controlled by an automatic gain control (AGC) feedback voltage (see below). The output of the IF amplifier was rectified by a square-law detector and associated DC amplifier. The switching signal used to modulate the high-level noise diode was also used as a reference signal by a synchronous demodulator in order to retrieve the amplitude of the switched noise signal from the square-law detector output.

This demodulated signal was compared to a fixed preset voltage ("Gain Adjust" in figure 2.1), and the difference signal was used as a negative feedback AGC signal to stabilize the closed-loop gain of the receiver. During *SKYMAP* observations the synchronous detector output ("Gain Pen" in figure 2.1) was recorded on a paper chart together with the radiometer output ("Signal Pen"), which allowed the receiver gain to be monitored and correlated with spurious features in the radiometer output. These chart recordings were used for initial data quality assessment, and formed part of the archival package associated with each observation.

A voltage that was proportional to the level of the demodulated signal was used as an offset voltage to balance out the system temperature component of the radiometer output. With the "Noise Balance" potentiometer adjusted so that the radiometer output was nulled, the radiometer was totally insensitive to gain variations. At the start of each observation the noise balance potentiometer was adjusted so that the radiometer output varied equally about the null point during the initial scans (see figures 2.4 and 2.5). Operating the radiometer near the null point ensured that the radiometer output was optimally insensitive to receiver gain variations.

The post-detection time constant of the radiometer was 0.1 seconds, which was determined by a first-order R-C filter associated with the summing-amplifier (Σ) in figure 2.1. A dual-slope integrating, digital voltmeter (DVM) sampled the radiometer output at a rate of 10 Hz, and the digitized samples were recorded by the controlling computer. Earlier observations used a voltage-to-frequency converter and digital counter in place of the

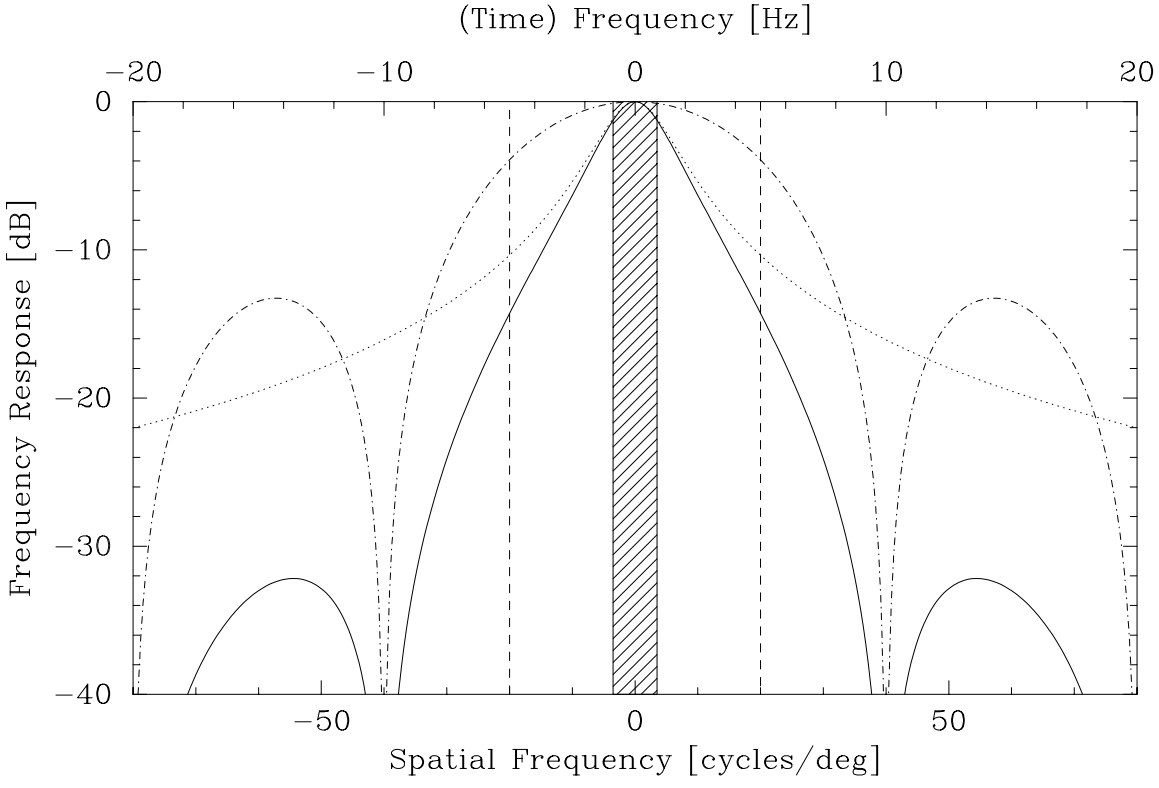

Figure 2.2: The individual and combined time and spatial frequency responses of the radiometer post-detection filter and the integrating DVM. The ratio between the time frequency and spatial frequency scales is determined by the 0.25° s^{-1} declination scan rate. The dotted line traces the frequency response of the first-order post-detection filter associated with the summing-amplifier in the radiometer. The chained line is the effective "sinc function" response of the dual-slope integrating DVM. The solid line is the cascaded response of these two hardware devices. The physical diameter of the antenna is 200λ, so the maximum possible bandwidth of the sky signal was 200 cycles/rad, or 3.5 cycles/deg. This frequency band is represented by the hashed rectangle in the figure. The maximum attenuation of the sky signal was -1.25 dB (or $\times 0.75$) at the edge of this band. Noise signals with frequency components outside the vertical dashed lines were aliased back into the signal band because the DVM sample rate was 10 Hz (or 40 samples/deg). The combined frequency response of the radiometer and DVM attenuated these noise signals by more than -14 dB prior to aliasing.

DVM. The smoothing and noise-filtering effects of the radiometer post-detection filter and the DVM integration are illustrated in figure 2.2, and described in the figure caption.

2.2 The Observation Process

The task of mapping large-scale, continuum emission features at centimetre wavelengths confronts the observer with significant technical challenges. The Rhodes University Radio Astronomy Group had investigated various techniques for mapping extended continuum sources at 2.3 GHz (Baart et al., 1980; Mountfort, 1989) before embarking on the 2326 MHz survey. This experience had demonstrated that the best observing strategy should accom-

modate the principles outlined below (adapted from Mountfort (1989)). The central aim of the observation strategy was to ensure suitable conditions for the reliable observation of low brightness, spatially-extended continuum radio sources.

Night-time observations

Observations had to be made at night, with the sun's emission shielded by the horizon. Besides the unwanted illumination of the stray response pattern of the antenna by the overwhelming solar radio emission, the solar heating of the antenna structure and surroundings caused instabilities in the receiver baseline. Despite starting observations after sunset the recorded antenna temperatures were often affected by a "relaxation" (drift) of the baseline after sunset (see figure 2.5).

Meteorological conditions

Cloudless conditions were required to ensure that atmospheric absorption was at a stable minimum, and that the terrestrial foreground emission remained constant throughout the night. Observations were only initiated if the prospects were good for clear weather throughout the night. Deterioration in the weather conditions was the most common reason for abandoning or rejecting an observation.

Fast scans

Relatively fast scan rates were used in order to reduce the effects of the 1/f noise caused by residual gain variations in the receiver. To ensure that the scan time was short compared to the time-scale of this low-frequency variation in the receiver baseline, the maximum practical scan rate allowed by the antenna was used.

Large target areas

It was impractical to observe the entire southern sky with one monolithic set of scanning observations, so the sky was divided into a number of overlapping regions, termed *target areas* in this thesis. A radio map cannot reliably record emission features that have scale sizes comparable to the extent of the map. It is inevitable that baseline correction procedures have to be applied to the map data, and these subtract out structures extending beyond the map boundaries. For this reason the southern sky was divided into as few target areas as was practically possible. A competing factor was the number of nights required to make the observations required to construct a complete map of a target area. The compromise chosen was to observe

the largest possible area of sky that could be completely observed within a three month observing season. Having fewer large maps, rather than many smaller maps, also facilitated the merging of the constituent maps into a single complete map. The ten target areas selected for the *SKYMAP* survey are listed in table 2.2 and shown schematically in figure 2.6.

Foreground radiation

The excess antenna temperature of the emission due to atmospheric absorption and ground radiation was very dependent on antenna position, particularly the zenith angle. It became apparent that this terrestrial foreground also had a temporal dependence, and it was decided that a unique empirical model of the foreground emission had to be found for each individual observation. These individual models were derived from the *SKYMAP* scan data, rather than supplementary observations, by ensuring that each target area included cold sky. This requirement was met by careful selection of the position and size of the target areas.

Repeated scans

The fast scanning rate and sparse scanning pattern of the *SKYMAP* observing procedure necessitated many nights of observation in order to achieve sufficient integration time and scan density. Having a large number of independent coverages of the target area provided significant data redundancy, which simplified data quality control. Every scan could be compared with completely independent peers, and those scans that were contaminated by interference were edited out of the data set without compromising the completeness of the map.

Spatial oversampling

The physical diameter of the HartRAO antenna is 200λ at 2326 MHz, which corresponds to a spatial frequency cutoff at 3.5 cycles/deg for the "beam transfer function" (see figure 2.2). The maximum scan and sample spacing that would satisfy the Nyquist sampling criterion was therefore $\approx \frac{1}{7}^{\circ}$. In order to allow for subsequent digital image processing, a maximum scan spacing of 0.1° was used for the *SKYMAP* maps. This oversampling also contributed to the data redundancy mentioned above.

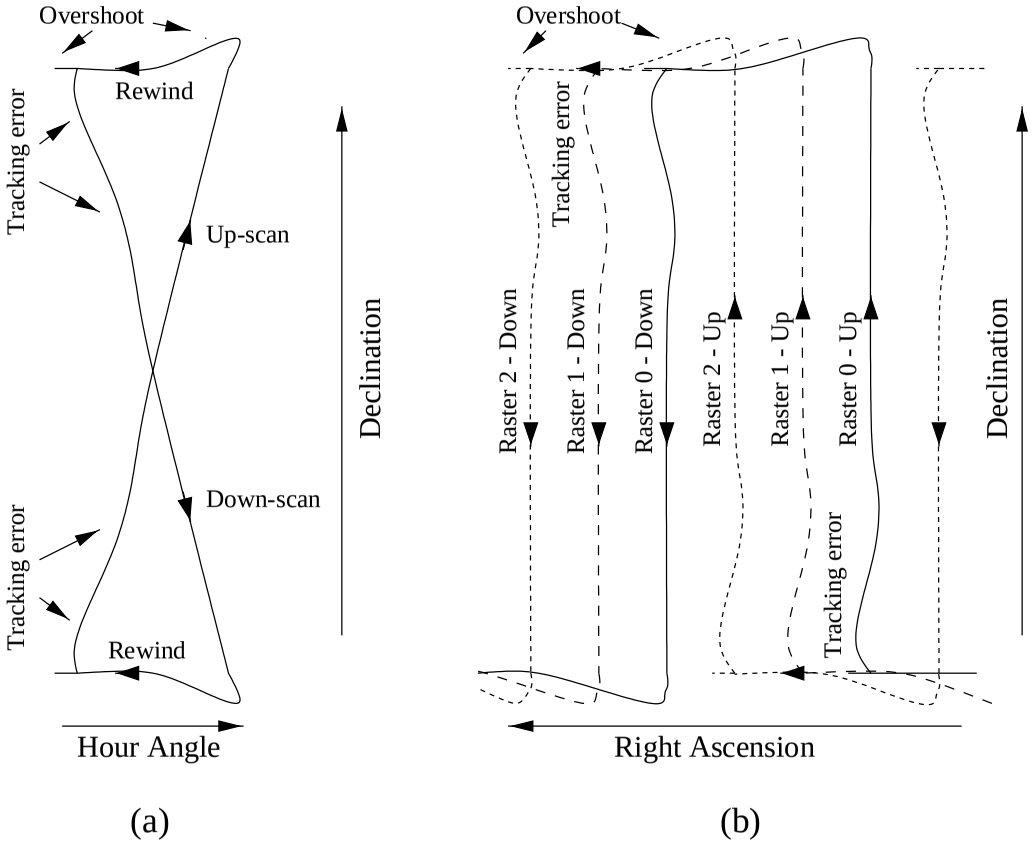

Figure 2.3: (a) The topocentric "figure of eight" scanning pattern used for the *SKYMAP* survey observations. The tracking errors at the start of each scan were exacerbated by the sharing of a common hydraulic pump by the hour angle and declination drive motors. The rewind time at the end of each scan was long enough to allow for adequate damping of the overshoot oscillations. (b) An example of the equatorial (RA/Dec) track for a target area requiring a three-fold interleaving of rasters. The magnitude of the tracking errors was of the order of 0.1° at the start of each scan. This mistracking was corrected for in the subsequent data reduction. Notice that each individual scan pattern is termed a *raster*. For all target areas other than A12D63 the equatorial coordinate system was referenced to the mean equinox of the observation date.

2.2.1 The Scanning Pattern

Many of the previous large-area centimetre and decimetre continuum sky surveys were made using the Dwingeloo, Stockert, Parkes, Jodrell Bank (MkI and MkIa) and Effelsberg telescopes. All of these telescopes have azimuth-elevation mount geometries, which influenced the observation technique used for the surveys. The polar mount geometry and the modest drive system of the HartRAO telescope precluded the use of the constant elevation scanning pattern used for previous high-frequency radio continuum surveys (Berkhuijsen, 1971; Reich, 1982; Reich and Reich, 1986). As a result of this limitation a declination scan pattern was adopted (Mountfort, 1989).

The popular "nodding" scan technique (Haslam et al., 1974; Haslam, 1974) was not used for the *SKYMAP* observations for two main reasons: (a) the relatively low signal-to-

noise ratio of the high frequency, fast-scan *SKYMAP* data did not allow the use of scan intersections to correct for baseline drift, and (b) the *raster* scan pattern (described below) was considered to be a more efficient scanning strategy.

Figure 2.3(a) shows the trajectory of the *SKYMAP* scanning pattern in the topocentric (HA/Dec) coordinate frame. While scanning in declination the telescope was commanded to track a constant right ascension, resulting in the bi-directional raster-scan trajectory in the equatorial (RA/Dec) coordinate frame shown in figure 2.3(b). The sidereal rotation of the earth was used to advance successive scans in right ascension and ensure that the HA/Dec trajectory remained fixed for the duration of the raster. For the rest of this chapter the term *raster* is taken to mean the set of scans that comprise a complete and continuous raster observation.

The minimum possible right ascension spacing of a single raster was determined by the scan duration because of the restrictions imposed by the raster- scanning strategy. The parameters that determined the *minimum* scan duration were the declination extent of the scan, the scan speed, and the antenna rewind time required at the end of a scan to advance to the next scan. For typical scan parameters used in the survey this minimum possible raster scan spacing always exceeded the spacing required to satisfy the Nyquist criterion. In order to achieve the required scan density a set of interleaved rasters had to be observed, as shown in figure 2.3(b). Table 2.2 lists the number of rasters required to complete one coverage of each of the ten target areas.

Each *SKYMAP observation* lasted an entire night (sunset till sunrise) and involved the execution of the scans for a single *raster*. Typically each raster was observed two or three times to achieve the required data redundancy and noise statistics. Therefore the total number of observations (and hence nights) required for the successful coverage of a target area depended on the number of rasters required *and* the number of times each raster was observed.

2.2.2 Systematic Effects

Ground-based radio observations are contaminated by two natural terrestrial sources of radio emission: (a) atmospheric emission due to the absorption spectra of oxygen and water vapour (Hogg, 1959; Howell and Shakeshaft, 1967; Danese and Partridge, 1989; Bersanelli et al., 1995a; Bersanelli et al., 1995b), and (b) emission from the ground that illuminates the extensive near-field pattern of the antenna (Anderson et al., 1991; Landecker et al.,

	Map	RA range	Dec range	Observation period	Nras	Nobs
1)	A12D63	12h00 – 22h00	−63 – −24	162/1980 – 209/1980	8	24
2)	A23D80	23h00 – 07h00	−80 – −61	266/1982 – 338/1982	3	9
3)	A05D63	05h00 – 13h20	−63 – −24	085/1986 – 137/1986	8	23
4)	A14D26	14h00 – 02h30	−26 – +13	182/1986 – 227/1986	8	16
5)	A06D83	06h00 – 18h00	−83 – −61	111/1987 – 124/1987	3	9
6)	A12D11	12h00 – 00h00	+11 – +32	138/1987 – 222/1987	5	11
7)	A14D83	14h00 – 01h00	−83 – −61	177/1989 – 199/1989	3	9
8)	A22D26	22h00 – 07h00	−26 – +13	276/1990 – 015/1991	8	16
9)	A04D26	04h00 – 15h00	−26 – +13	066/1992 – 112/1992	8	18
10)	A21D63	21h00 – 07h00	−63 – −24	330/1991 – 312/1992	8	21

Table 2.2: Extent of the ten constituent maps and the periods over which they were observed. The map names were derived from the starting right ascension and lower declination limit. The dates are given in the form of day number and year. Appendix A gives a detailed listing of the individual observations. The column headed Nras lists the number of interleaved rasters required to completely sample the target area, and the column headed Nobs lists the total number of successful raster observations that were made of the target area.

1991; Lambert and Rudduck, 1992). The excess antenna temperature of the 2.3 GHz atmospheric emission towards the zenith is about 2 K, and this component varies roughly as the secant of zenith angle. The ground emission has a more complex dependence on zenith angle and azimuth, and the excess antenna temperature due to this ground radiation can increase by more than 10 K between zenith angles of 0° and 60°.

In order to reduce the dependence of the antenna temperature on scan angle, constant elevation scanning patterns were used for previous high frequency surveys (Berkhuijsen, 1971; Reich, 1982; Reich and Reich, 1986). Reich (1986) reports an azimuth-dependent antenna temperature variation of 1 K for the Stockert telescope at 40° elevation, indicating that constant elevation scans do not completely eliminate terrestrial foreground effects. The long declination scans employed by the *SKYMAP* observations necessitated large excursions in telescope zenith angle, which resulted in variations in the antenna temperature of up to 7 K for some observations.

Because the topocentric scanning trajectory was repeated almost exactly throughout the night (without sidereal slippage) it was expected that the up-scan and down-scan terrestrial foreground profiles would remain constant for the entire raster. Foreground profiles would differ between observations because they were started at quite arbitrary hour angles.

Figures 2.4 and 2.5 are plots of time-ordered raw data for two typical rasters. The raw

data were smoothed using a digital filter with a 2 second time constant prior to plotting. The graph panels emulate the radiometer output chart records that were obtained for each observation. The antenna temperatures for both rasters are dominated by a periodic modulation caused by the declination-dependent variation in the terrestrial foreground contribution.

Even though the scan length for observation 295 was shorter (22°) than that for observation 318 (39°), the foreground modulation was larger for observation 295. This was a consequence of the declination range for observation 295, which resulted in the raster scans being made at high zenith angles. Examining figure 2.5 it is clear that the foreground profile for this raster was a complex function of declination scan angle. This complex profile probably resulted from ground radiation being scattered into the feedhorn at small zenith angles.

Strong radio sources identified in the time-ordered data have been labelled. Many point sources in the target area covered by the raster will have been missed because of undersampling, or attenuated by the smoothing filter. Typical baseline instabilities have been labelled in figure 2.5, including the evening drift effect, and bumps probably caused by passing clouds. No radio interference can be seen in either of these observations, but many others were affected by man-made transmissions.

2.2.3 The Observing Software

The entire observing process was controlled by computer procedures which virtually removed any chance of operator error, ensured repeatability of the technique, and made efficient use of observing time. An important part of the automatic observing procedure was the self-consistency checks made prior to and during the observations. These checks tested that the telescope instrumentation was in the correct configuration, and that it was operating correctly.

Mountfort (1989) devised and implemented the initial *SKYMAP* observing software. The first area of sky to be successfully mapped by this version of the software was the region designated A12D63 in figure 2.6. Modifications that were made by the author to Mountfort's original observing program are listed below.

Precession

The raster scan pattern that was tracked by Mountfort's original version of the

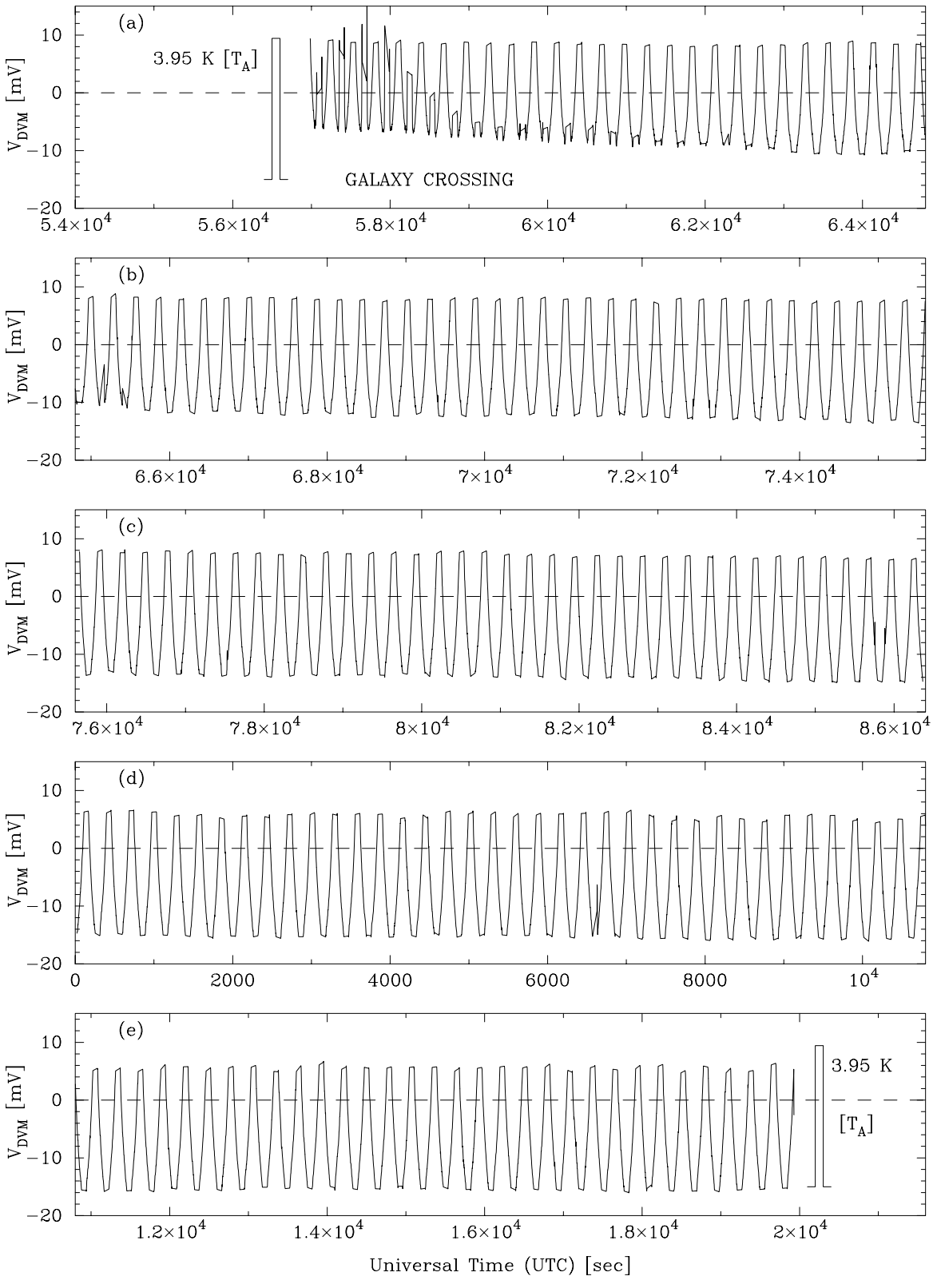

Figure 2.4: A time-ordered representation of the raw raster data for observation 295. A running-mean digital filter with a time constant of 2 seconds was applied to the data prior to plotting. The horizontal axis represents UTC modulo 86400 in units of seconds, and the vertical axis represents the radiometer output voltage as measured by the digital voltmeter (DVM) and written to magnetic tape. The excess voltage caused by activating the 3.95 K calibration noise diode is indicated in the first and last panels.

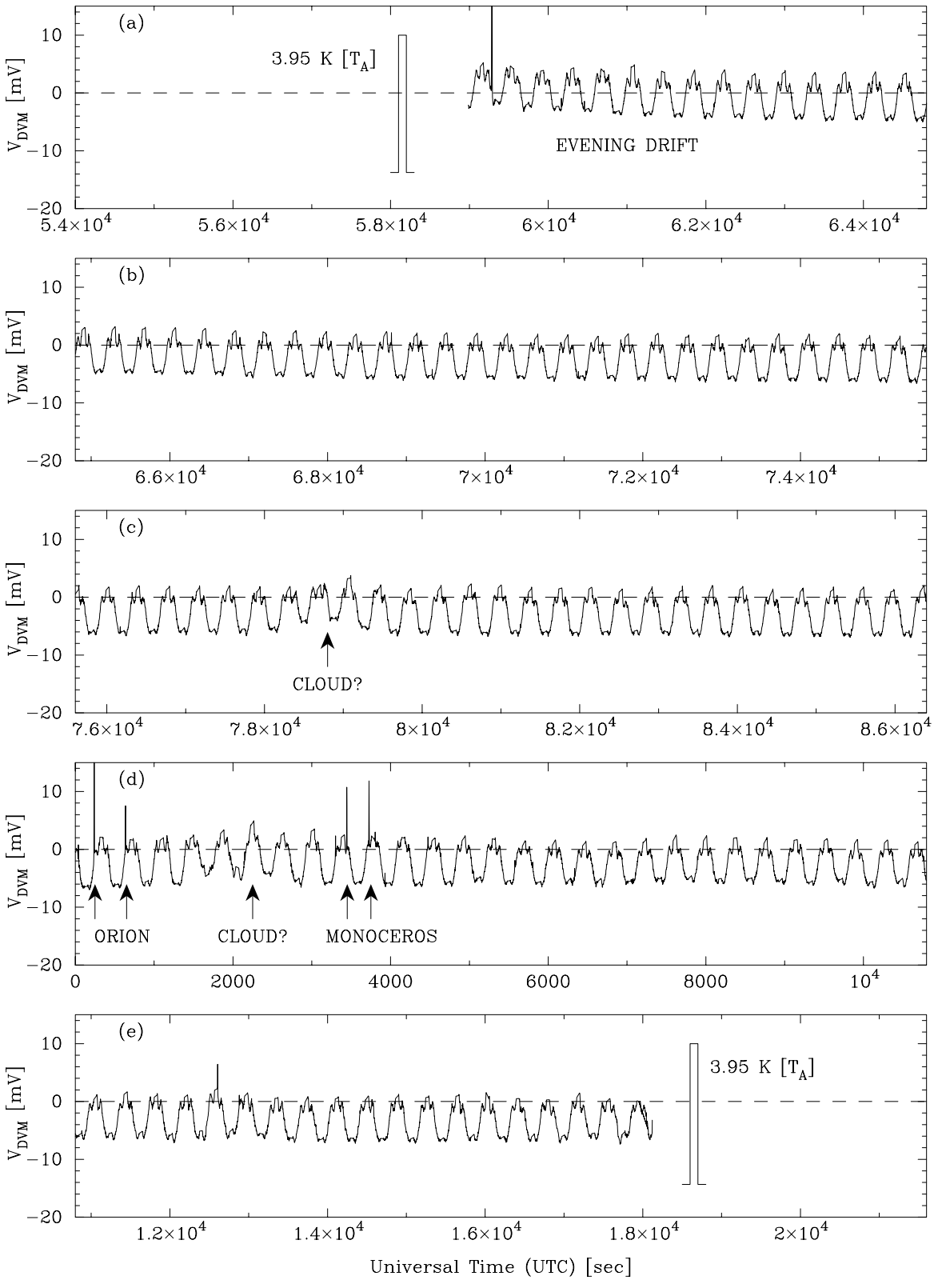

Figure 2.5: A time-ordered representation of the raw raster data for observation 318. A running-mean digital filter with a time constant of 2 seconds was applied to the data prior to plotting. The horizontal axis represents UTC modulo 86400 in units of seconds, and the vertical axis represents the radiometer output voltage as measured by the digital voltmeter (DVM) and written to magnetic tape. The excess voltage caused by activating the 3.95 K calibration noise diode is indicated in the first and last panels.

SKYMAP observing program was referenced to the B1950 standard equinox. The effects of differential precession caused the figure-of-eight topographic scanning pattern to wander slightly in hour angle and declination throughout the night. This resulted in a time variation in the foreground emission, and for all observations following A12D63 the raster coordinate system was referred to the mean equinox at the epoch of the observation.

Calibration

The original *SKYMAP* procedure required the antenna temperature scale to be calibrated manually for each observation. Program code was added to measure the excess radiometer voltage resulting from switching on the calibration noise diode, and the calculated kelvins-per-volt conversion factor was printed out on the observation log. These calibration measurements were made at the beginning and the end of each observation. More frequent calibration measurements were not required because of the intrinsic gain stability of the radiometer.

User interface

Because the *SKYMAP* observing procedure could not tolerate interruptions and often ran unattended, it was essential that the parameters specified by the user at the start of the observation were correct. The user interface was modified to check all of the user input for consistency, and an option to read the parameters from a pre-prepared disk file was included. These precautions eliminated operator error, which was a particularly important consideration for the absentee observations.

Telescope hardware checks

A number of routines that tested various components of the telescope hardware were included in the *SKYMAP* observing program. Again, the main aim of these tests was to reduce the chance of operator error. Before the start of an observation the program checked that the radiometer output was within predetermined nominal levels, and that the antenna could be driven. During the 13 year observation period various telescope hardware subsystems were subjected to computer control. The *SKYMAP* observing program was routinely modified to take advantage of these hardware upgrades, relieving the operator of the responsibility of configuring the relevant subsystems prior to an observation.

Operating system changes

Over the period of the observations the operating system on the Hewlett-Packard on-line computers evolved from RTE-II to RTE-VI. Each time the operating system was upgraded the observing software had to be modified slightly. The real-time aspects of the *SKYMAP* program were modified quite substantially to improve the reliability of the procedure. Mountfort's original design was prone to memory overflow problems.

Data format

When the $\frac{1}{2}$-inch 9-track magnetic tape drives at the observatory were upgraded from 800 bpi to 1600 bpi capability the format of the data blocks written to the tape was changed. Many of the 800 bpi tapes with the original data format proved difficult to read at a later date, but the 1600 bpi tapes with the new format were far more reliable. See table 2.3 for a description of the modified tape record structure.

Off-line data inspection

As can be ascertained from figures 2.4 and 2.5, it was difficult to assess the quality of the data from the radiometer paper chart record. Gross interference could be identified, but more subtle effects, such as low-level receiver instability, emission from light clouds and signals from satellites illuminating the far sidelobes, could not. Because of the demanding data-quality requirements of the survey it was essential that problem observations could be identified at the observatory, thus allowing the prompt scheduling of contingency observations. A suite of software was developed by the author that checked the integrity of the tape data, performed rudimentary foreground emission corrections on the raster data, and produced hardcopy hidden-line maps of the resulting scans. Using this software the data quality could be checked at the observatory immediately after the completion of the observation.

2.2.4 The Observation Schedule

The 2326 MHz continuum survey was observed by independently mapping ten overlapping target areas. The details of these target areas are listed in table 2.2 and their sky coverage is depicted in figure 2.6. This figure shows that the target areas fell within four declination bands. The nomenclature for the maps was determined from the starting right ascensions and southern declinations of the target areas. The survey currently covers 67% of the whole sky. A small polar region representing 1% of the southern sky has not been observed.

Field	Format	Abbreviation	Description
1–6	I6	OBS	Integer observation sequence number
7–10	I4	SCAN	Integer scan number indicating sequence within raster
11–14	I4	BLOCK	Integer magnetic tape block sequence number
15–22	F8.3	RA	Nominal right ascension of current scan [deg]
23–24	I2	RAS	Integer raster number (0 $\leq$RAS$<$NRAS)
25–29	I5	YEAR	Integer year of observation
30–33	I4	DAY	Integer day number at time of data recording
34–36	I3	DIR	Integer direction flag for current scan: $+1$ for northward (up), -1 for southward (down)
37–44	F8.3	STRTHA	Antenna hour angle at start of current scan [deg]
45–52	F8.3	LODEC	Southern declination limit of raster scans [deg]
53–60	F8.3	HIDEC	Northern declination limit of raster scans [deg]
61–66	F6.3	DRA	Desired right ascension spacing of interleaved raster scans [deg]
67–72	F6.3	RATE	Command declination scan rate [deg/sec]
73–74	I2	NRAS	Integer number of rasters required for full coverage
75–78	I4	NSAM	Integer number of data samples that follow this header (NSAM$\leq$ 100)
	F8.3	HA	Hour angle encoder reading [deg]
	F8.3	DEC	Declination encode reading [deg]
	F8.1	UT	Coordinated universal time (UTC) [sec]
	F8.3	DVM1	Voltage read from radiometer DVM [volts]
	F8.3	DVM2	Voltage read from spare DVM [volts]

Table 2.3: The data format used to write observation data to 9-track magnetic tape. Every tape block contained redundant information to lessen the impact of recording errors.

The sometimes competing constraints that guided the selection of the individual target areas are listed below.

- All raster scans were made at hour angles within 45° of the local meridian in order to limit the terrestrial foreground emission to a reasonable level. This restricted the observing season for each target area to three months, which implied a maximum of 30 observation nights of if the project was awarded a generous fraction of the observing time available at HartRAO. In practice weather conditions and equipment failures reduced the number of available nights to less than this number. A maximum raster interleave factor of 8 was chosen to allow three repeat observations of each raster (a total of 24 observations) during the three month observing window. Combining this information with the *SKYMAP* scan parameters, the maximum declination extent of the target areas was calculated to be 39°.

- The duration of the individual observations was limited by the time the sun was below the horizon. In the winter it was possible to obtain reliable data for up to 14 hours, but in the summer this period was reduced to less than 9 hours. Therefore the right ascension extent of the target areas was season dependent.

- The observatory is situated in a summer rainfall region, with most of the rain occurring in the form of violent thunder storms. As a result of this weather pattern the success ratio of summer observations was relatively low, and it was not possible to observe three complete sets of rasters within the three month window for some target areas. All target areas were fully covered at least twice to provide satisfactory data redundancy and noise reduction.

- The technique used to determine the terrestrial foreground profile for each raster required some regions of cold sky at all declinations in the target area. This requirement demanded that the target areas be chosen carefully, and that the areas be as large as possible.

- Once the ten component maps had been completed they had to be combined into a single map of the southern sky. In order to aid this procedure it was necessary that there be generous overlap between adjacent target areas, and that the number of constituent maps be minimized, i.e. the maps were as large as possible.

- Because of meridian convergence towards the southern equatorial pole (SEP), the right ascension spacing required for a true scan spacing of 0.1° increased towards the pole. The right ascension spacing of maps at declinations beyond −60° was increased to 0.2°, and a target area boundary was positioned near this declination.

- The structure of the antenna mount imposed a southern declination limit of −83° on the *SKYMAP* observations. The A23D80 target area was restricted to a southern limit of −80° because the automated antenna control system was still being evaluated at the time of the observations, and a stricter safety margin was imposed.

- The extreme northern declination limit of +32° was determined by the telescope geocentric latitude and the local topology. The ground radiation contribution to the antenna temperature rose steeply beyond this northern declination limit. Only one target area was observed in the most northern declination range. This area was observed in the winter when the weather was stable. It was decided that there was no compelling scientific justification to observe the rest of this declination range for the following reasons: (a) the area was already covered at 408 MHz (Haslam et al., 1982), 820 MHz (Berkhuijsen, 1972) and 1420 MHz (Reich and Reich, 1986), (b) the Galactic emission in this area is not very significant, and (c) increased competition for telescope time made the scheduling of weather-sensitive summer observations difficult.

Raster data from a total of 154 successful nights of observation were used to create the ten constituent maps. At least an equal number of nights of observation were discarded because of inadequate data quality. The details of the successful observations are given in appendix A.

The only region of the southern sky that has not yet been observed is the small area near the southern equatorial pole (SEP). The antenna mount has recently been modified to allow the $\lambda = 13$ cm telescope beam to reach the SEP, and this polar region will be observed once the necessary changes have been made to the telescope control system which will allow the telescope to be driven safely to −90° declination.

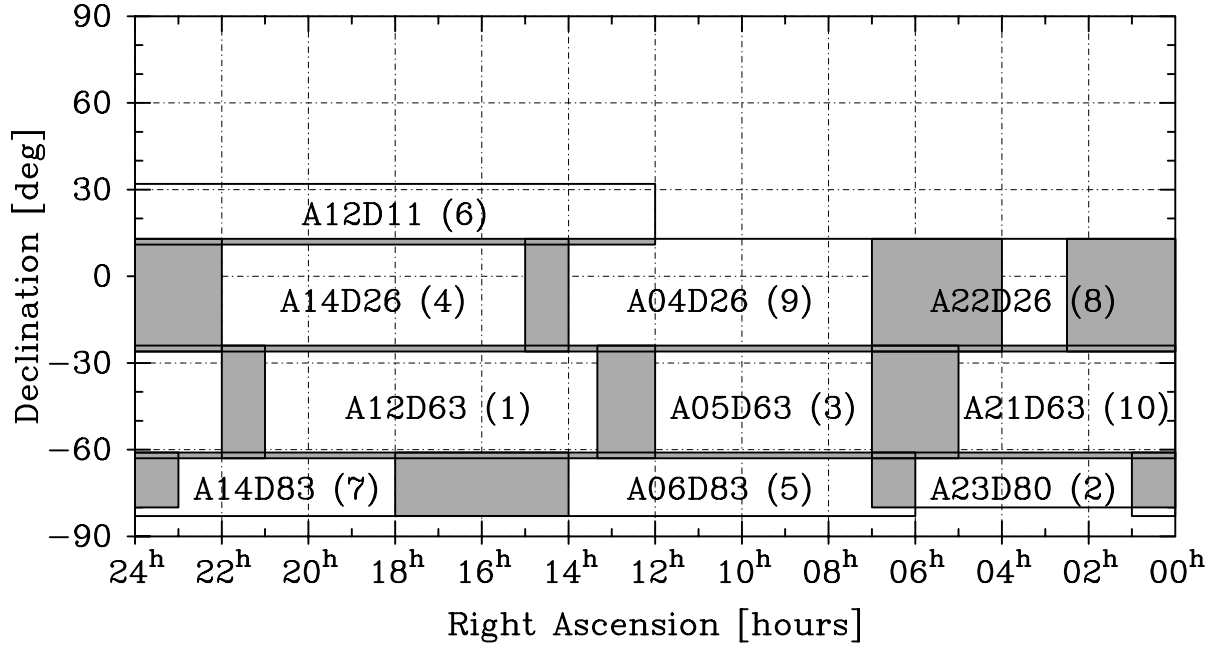

Figure 2.6: The sky coverage of the ten constituent maps. Shading indicates areas of overlap between two or more adjacent maps. The names given to the individual maps are given, and the numbers in brackets indicate the chronological order of the associated observation periods.

Chapter 3

SKYMAP Data Reduction

This chapter describes the three distinct stages in the data processing that were required to convert the raw *SKYMAP* observation data into useful data products. These stages were: (a) the production of maps of individual target areas from the raw observation data, (b) the assembling of the individual component maps into one composite map of the southern sky, and (c) the image processing necessary to manipulate the map data and extract qualitative and quantitative scientific information from the radio survey data.

In 1980 Mountfort developed a set of routines to produce maps from the initial *SKYMAP* observations (Mountfort, 1989). At that time the main computing resource at Rhodes University was an ICL 1904A mainframe computer, which was shared by all sectors of the university community. Applications running on this computer were restricted to very meagre resources (by today's standards): 256 kilo-words of program and data memory, 15 fixed-allocation data files, and a slow central processor. Graphical output was obtainable via a Tektronix T4010 vector graphics terminal or a very slow Calcomp single-pen drum plotter. Mountfort's data reduction software was used to produce the first two survey map (A12D63 and A23D80), and the process proved to be remarkably successful, given the severe limitations imposed by the available computing equipment.

The design philosophy of Mountfort's *SKYMAP* data reduction software was strongly influenced by the available computing hardware (Mountfort, 1989). The tasks were executed in batch-mode, and most processing was done at night when the computer could be run in single-task mode. Robust data processing techniques were used to automatically exclude outlier data, and there was very little user interaction. Since 1980 a number of new computing facilities have become available to the Rhodes Radio Astronomy Group, and the *SKYMAP* data reduction software has evolved to take advantage of these developments. The most significant computer hardware developments were:

- The acquisition of graphics workstations capable of displaying scan data and raster images on demand and allowing interactive data processing.
- The increase in the performance and capacity of the available computer systems. Most notable improvements were the availability of virtual-memory architectures, high-capacity disk-drives, and fast CPU's.
- The use of fast graphics hardcopy devices, such as laser printers, which has speeded up the data reduction processes significantly.

Driven by the improvement in computing technology, and the identification of deficiencies in Mountfort's original data reduction package, the *SKYMAP* reduction software was extensively modified by the author. Section 3.1 describes the modified map-making procedure in some detail.

Rather than covering the whole sky in one monolithic observing effort, the *SKYMAP* observing technique required the independent mapping of a number of overlapping target areas. The map processing for these target areas was also performed in an independent way, which inevitably resulted in the maps having inconsistent base-levels. It was necessary, therefore, to devise a procedure for combining the component maps into one consistent map with no discontinuities at the map boundaries. This process is discussed in section 3.2.

A number of data processing utilities were written to manipulate, analyze and display the radio continuum survey maps. Some of the utilities that were used to obtain the results reported in this thesis are described very briefly in section 3.3.

3.1 *SKYMAP* Data Reduction Software

The data written to magnetic tape by the *SKYMAP* observing procedure required significant processing in order to produce an array of temperatures that was a reliable representation of the sky radio brightness distribution. The recorded data were contaminated by systematic and instrumental effects that resulted from the observation technique and equipment, and these effects needed to be removed from the data. The main tasks of the map-making software were:

- Reformatting of the raw observation data into a format that was convenient for the data reduction processes that were to follow.
- Subtraction of the declination-dependent terrestrial foreground emission.

- Compensation for baseline instabilities caused by receiver gain drift and temporal variations in the foreground emission.
- Adjustment of the base-levels of the raster data from all of the observations to be consistent with a common baseline.
- Merging of the raster data from all of the observations, and interpolation of the corrected temperatures onto a regular rectangular coordinate grid.

Mountfort's PhD thesis (Mountfort, 1989) gives a full description of the prototype *SKYMAP* data reduction package that he developed in 1980. This section describes the modified *SKYMAP* package as designed by the author. The main departures from Mountfort's original design are outlined where appropriate.

Figure 3.1 gives an overview of the final version of the *SKYMAP* data reduction procedures. This processing cycle was applied to all but the first two sets of observations (A12D63 and A23D80). Unfortunately the deterioration of the original observation tapes made it impossible to re-process the early observations using the more sophisticated data reduction package.

The data processing strategy was a balance between interactive processing and more traditional batch processing. User input required by individual stages in the processing pipeline was either entered as a numerical value in a parameter file, or deduced from a graphics cursor associated with an interactive graphical user interface. Successive generations of the raster data were produced in the course of the data reduction cycle, with each later generation having a further correction applied to it. Each major processing step produced some form of graphical output which allowed the user to evaluate the efficacy of the relevant process. Individual stages were repeated using different input parameters until the user was satisfied with the resulting output data. Sometimes it was necessary to go back and repeat earlier processes because of the latent effects of prior parameter choices.

The final VAX/VMS implementation of the *SKYMAP* reduction package provided the user with the simple menu interface shown in table 3.1. Each of the individual data reduction processes listed in table 3.1 are described in more detail in the following sections.

Data file format

It is convenient to describe the formats used to store the main data types before describing the data reduction process in detail. The design of the data structures is intimately linked

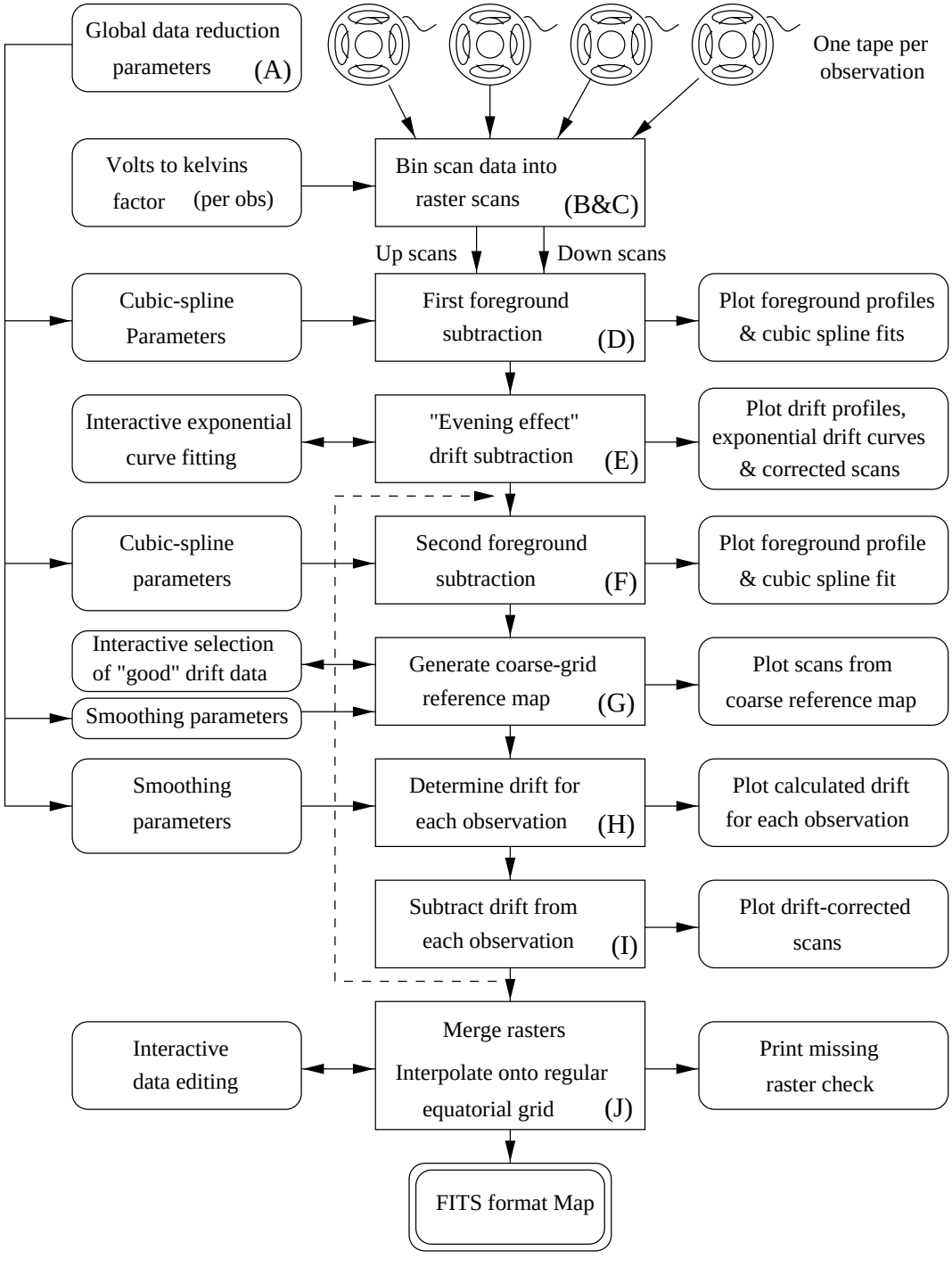

Figure 3.1: A flowchart giving an overview of the *SKYMAP* data reduction procedures. The boxes on the left specify the user input and interaction, those in the centre describe the data reduction procedures, and the boxes on the right indicate what informational output was produced. The letters in brackets are pointers to the associated computer procedures listed in table 3.1. The dashed line indicates a loop that could be used to apply iterative corrections for foreground and drift effects. In practice it was not necessary to perform the iteration for any of the data sets processed to date.

```
        SKYMAP data reduction procedures
        ================================

A ..... Set up data reduction parameters
B ..... Read data from observation tapes
C ..... Concatenate observation data
D ..... First background determination
E ..... Interactive drift removal (Tektronix 4115b)
F ..... Second background determination
G ..... Reference sky determination (Tektronix 4115b)
H ..... Final drift removal
I ..... Interactive bad scan identification (Tektronix 4115b)
J ..... Raster combination to produce map

Q ..... Quit

   Enter letter identifying procedure: _
```

Table 3.1: The top-level menu of the *SKYMAP* data reduction procedures, as presented on the user's screen. Some of these procedures launched batch processes, while those requiring the Tektronix 4115b terminal activated interactive graphical user interfaces. The identifying letters are included in the relevant boxes in figure 3.1 to reveal the structure underlying the data reduction process.

to the data reduction philosophy. Two main data file types were used in the data reduction process, each with its own record format.

Raster scan records were used to store the full-resolution scan data interpolated onto a declination grid with a regular spacing of 0.1°. Each individual scan was stored using the record format detailed in table 3.2. The very first data processing stage produced raster data files from the observation tapes, and the tasks that followed in the processing cycle produced successive generations of raster data files. Systematic and instrumental effects diminished with each successive generation. Associated with the raster data files were two auxiliary files containing: (1) the statistical weight, and (2) the deviation from the nominal scan right ascension of each sample bin in the raster data set. For clarity, these auxiliary files have been excluded from the processing flow diagrams that follow.

Drift scan records were used to store the low resolution data used by the processes that estimated the baseline drift present in nearly all of the observations. Because the timescale of the baseline drift was long compared to the duration of a single

Field	Format	Abbreviation	Description
1–3	A3	KEY	Character code identifying record and data type
4–7	I4	OBS	Integer observation sequence number
8–10	I3	DIR	Integer scan direction flag: +1 for northward (up), −1 for southward (down), 0 if not appropriate
11–14	I4	SCAN	Integer scan number indicating sequence within observation, blank for foreground profiles
15–16	I2	WRAP	Integer flag set to 1 if the raster wraps through 24h00 to 00h00 in right ascension, blank for foreground profiles. Combined with RA when sorting.
17–24	I8	RA	Nominal right ascension of the scan [mdeg], blank for foreground profiles
25–32	I8	DEC	Lower declination limit of the raster or profile [mdeg]
33–38	I6	NBIN	Integer number of declination bins that follow this header
39–EOR	I6	DATA	Integer array of NBIN temperatures [mK]

Table 3.2: The record format used for raster scan data. The declination bin width was 0.1° for all rasters, so the centre declination of bin with index $i \in$[1,NBIN] was $\delta = \mathrm{DEC} \div 1000 + (i-1) \times 0.1°$. A similar record format was used to store the terrestrial foreground profiles.

declination scan, the effects of the drift were essentially independent of declination. The drift processing required only a few representative samples from each scan in an observation in order to characterize the right ascension dependent drift profile for the observation. Raw drift data were obtained from specific generations of the raster data. Median smoothing was used to obtain three to five low resolution samples from each individual raster scan. These samples were stored using the record format detailed in table 3.3

Global parameter input

All of the simple numerical parameters required by the various procedures in the processing cycle were stored in a single file. This ensured that a consistent record of all of the user-defined parameters was kept. A VMS command procedure was written to maintain this parameter file (option "A" in table 3.1). This procedure could be run at any stage in the processing cycle in order to modify existing parameter values. The user had to ensure that the appropriate reduction processes were re-run so that the intended changes were applied to the data.

Field	Format	Abbreviation	Description
1–3	A3	KEY	Character code identifying record and data type
4–7	I4	OBS	Integer observation sequence number
8–10	I3	DIR	Integer scan direction flag: +1 for northward (up), −1 for southward (down), 0 if not appropriate
11–14	I4	SCAN	Integer scan number indicating sequence within observation, or merged sequence number
15–16	I2	WRAP	Integer flag set to 1 if the raster wraps through 24h00 to 00h00 in right ascension
17–24	I8	RA	Nominal right ascension of the sample bin [mdeg]
25–32	I8	DEC	Declination at the centre of the sample bin [mdeg]
33–38	I6	DATA	Integer temperature of the sample bin [mK]

Table 3.3: The record format used to store the drift data samples. Each sample was stored in its own record to allow for the various sorting permutations required by the drift processing.

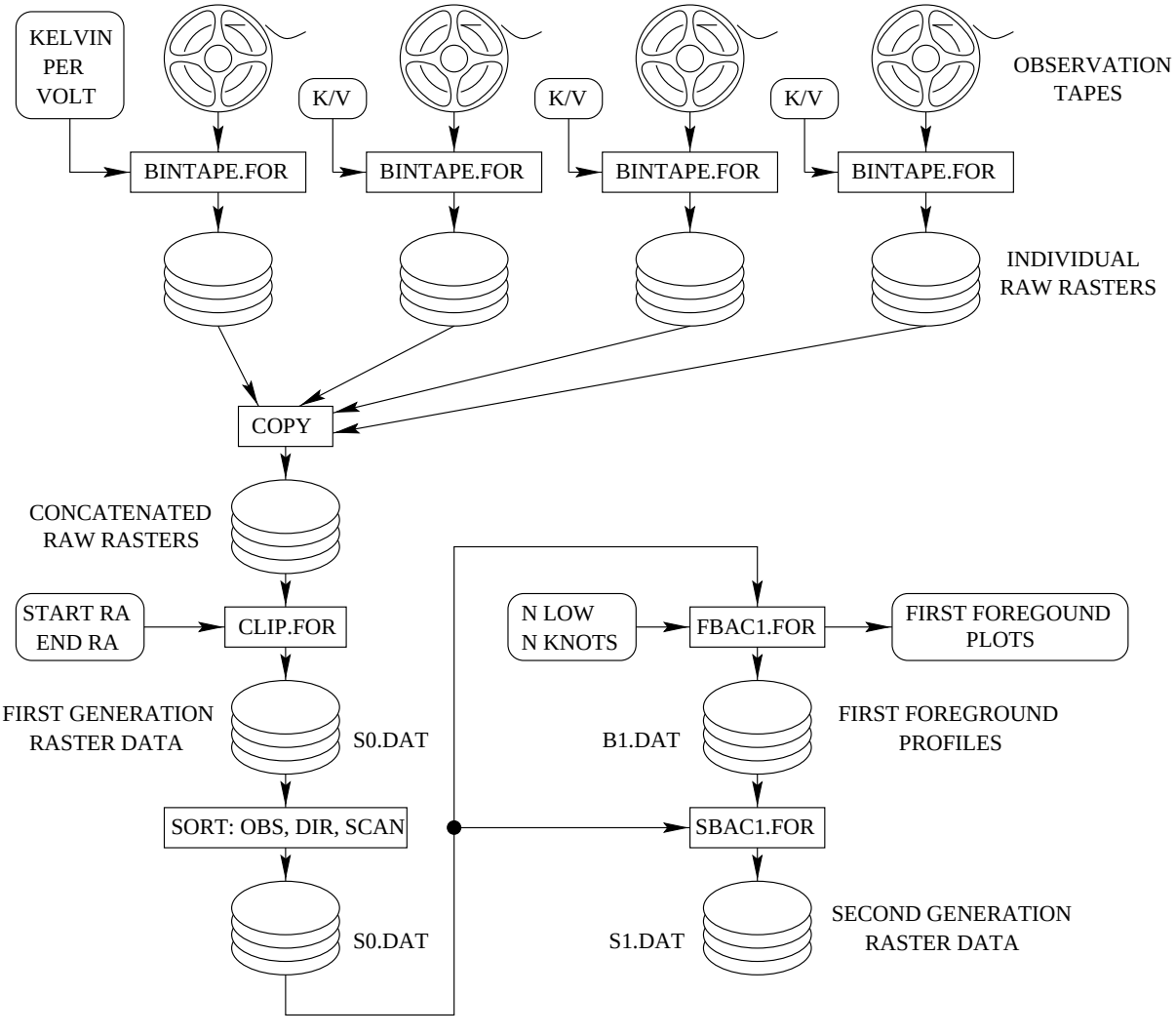

Figure 3.2: A flow diagram illustrating the initial data binning and first foreground subtraction processes. These procedures correspond to options “B”, “C” & “D” in table 3.1.

Initial data binning

Selecting option "B" in table 3.1 activated the first *SKYMAP* data reduction task, which read an observation tape and produced a binned raster scan file for that observation. In addition, auxiliary files containing statistical weighting information and right ascension deviations for each binned sample were also generated at this stage. For clarity, only the raster scan files are shown in the data flow diagram in figure 3.2. The nominal declination interval of the data samples on the tape was 0.025°, which was determined by the 0.25°/sec declination scan rate and the 10 Hz DVM sampling rate. Since the raster scan records had a 0.1° declination interval, the sample density was reduced by a factor of four by this initial binning process.

The program `bintape.for` was written to perform this data reformatting task. The true equatorial coordinates of each sample on the magnetic tape was calculated from the recorded UTC and encoder angles, using the antenna pointing-error map to convert the encoder angles to true topocentric coordinates. The volts-to-kelvins factor reported by the *SKYMAP* observing program was used by `bintape.for` to convert the recorded DVM voltages to antenna temperatures.

Mountfort's original version of this process used a simple running-mean binning algorithm to decimate the raw sample data, and then applied a three-point running-median filter to the binned data. This original decimation algorithm was replaced by a second-order Savitzky-Golay procedure (Savitzky and Golay, 1964) in order to reduce the smoothing effect of the running-mean process, and to improve the noise reduction performance. The combined spatial frequency response of the radiometer hardware and the Savitzky-Golay decimation is shown in figure 3.3. The combined response curve reveals an acceptably low attenuation of −2 dB at a spatial frequency of 3.5 cycles/deg, the highest spatial frequency detected by the antenna beam. Above this threshold frequency the attenuation rises sharply to more than −20 dB. This attenuation was required to reduce the noise components above 5 cycles/deg which were aliased into the signal as a result of the 0.1° declination sampling interval.

The running-median filter in Mountfort's original binning procedure was intended to automatically eradicate interference spikes from the scan data (Mountfort, 1989). Unfortunately this non-linear filter had the undesirable effect of reducing the peak amplitude of radio sources (see chapter 4), and was therefore excluded from the modified procedure.

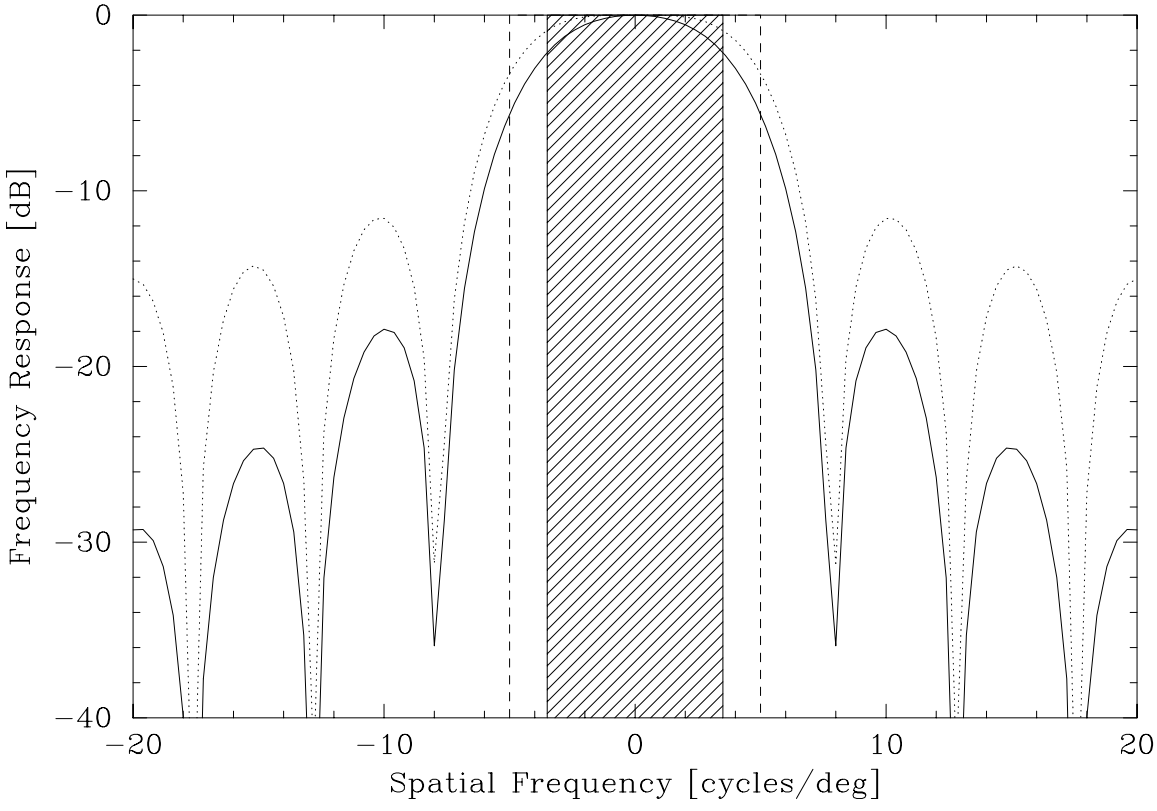

Figure 3.3: The effective one-dimensional spatial frequency response window applied to the antenna temperature data as a result of all of the filtering processes in the signal path. The dotted curve traces the frequency response of the second-order Savitzky-Golay (SG) finite impulse response (FIR) filter used to decimate and interpolate the raw sample data onto a regular declination grid. The solid curve is the frequency response that results from cascading this SG-FIR response with that of the radiometer and DVM (see figure 2.2). The shaded rectangle is the required sky-signal passband as determined by the spatial frequency response of the antenna beam. The declination binning interval was 0.1° for all observations, resulting in an aliasing threshold frequency of ±5 cycles/deg (demarcated by the vertical dashed lines in the figure). Residual noise components outside this Nyquist frequency limit were aliased down into this band by the re-sampling process.

Scans containing interference were manually excluded in a later stage of the processing cycle.

After all of the observation tapes were read successfully, the individual raster data files for all of the observations of a target area were concatenated into a single data file using the VMS COPY command (option "C" in table 3.1). The rasters in the composite data file were cropped to a common right ascension range using the program `CLIP.FOR` and written to the first-generation raster scan file `S0.DAT` (see figure 3.2).

At this early stage in the data reduction the temperature values in the first-generation raster file were assumed to be a superposition of the following components:

$$T_{i,j,k} = \mathrm{Sky}_{i,j,k} + \mathrm{FG}_{j,k}^{\mathrm{up,down}} + \mathrm{Offset}_k + \mathrm{ExpDrift}_{i,k} + \mathrm{Drift}_{i,j,k} \tag{3.1}$$

The interpretation of the symbols used in this equation is given below.

i	Scan sequence number, corresponds to SCAN in table 3.2.
j	Index of the declination bin.
k	Observation number, corresponds to OBS in table 3.2.
$T_{i,j,k}$	Relative antenna temperature recorded in bin j of scan i in observation k.
$\mathrm{Sky}_{i,j,k}$	Antenna temperature due to celestial radio sources.
$\mathrm{FG}_{j,k}^{\mathrm{up,down}}$	Declination-dependent terrestrial foreground emission, different for up and down scans.
Offset_k	Arbitrary isotropic temperature offset related to the radiometer noise-balance setting.
$\mathrm{ExpDrift}_{i,k}$	Right ascension dependent exponential relaxation of the recorded antenna temperature near the start of an observation.
$\mathrm{Drift}_{i,j,k}$	Random drift in the receiver baseline caused by gain fluctuations and weather effects. Most strongly dependent on right ascension (and hence index i), but some weak dependence on declination too.

The processing stages described in the following sections made estimates of the unwanted temperature components ($\mathrm{FG}_{j,k}^{\mathrm{up,down}}$, Offset_k, $\mathrm{ExpDrift}_{i,k}$, $\mathrm{Drift}_{i,j,k}$), and subtracted these from the raster data.

First foreground subtraction

The declination-dependent terrestrial foreground modulation, represented by $\mathrm{FG}_{j,k}^{\mathrm{up,down}}$ in equation 3.1, was the dominant systematic effect present in the raw raster data, and thus was the first effect to be addressed. Mountfort's original processing scheme started with a correction for instrumental drift (Mountfort, 1989), but this step was abolished because of the inaccuracy in the instrumental drift model that was used. The initial foreground

correction procedure was activated by selection option "D" in table 3.1. The sequence of tasks and the data flow for this process are shown in figure 3.2.

The foreground profiles were different between individual observations because the starting hour angle for each observation was quite arbitrary. In addition each observation required two distinct foreground profiles because the "up" (northward) and "down" (southward) raster scans within each observation followed slightly different tracks (see figure 2.3 in chapter 2). For a set of N observations covering a given target area it was therefore necessary to determine $2 \times N$ different foreground profiles. Before calculating the foreground profiles the first-generation raster data were partitioned into contiguous blocks of scans with the same expected foreground profile. This was achieved by using the OBS and DIR fields in the scan record headers as primary and secondary keys in a sorting process (see figure 3.2). The VMS SORT utility was used here and for all sorting operations in the *SKYMAP* data reduction cycle.

The estimation of the terrestrial foreground profiles for each of these blocks of scans was performed by `FBAC1.FOR`. Following Seeger et al. (1965), the foreground profile was determined by finding the declination-dependent lower-envelope for each block of scans. It was assumed that this lower-envelope was representative of antenna temperatures measured towards "cold sky", and was therefore devoid of celestial radio sources. In practice, the lower-envelope was obtained by selecting the 10th lowest temperature at each declination interval. This was done to exclude outliers representing the tail of the gaussian noise probability distribution.

In his original foreground modelling procedure Mountfort fitted a global polynomial to the lower-envelope in order to reduce the effects of noise and the residual influence of discrete radio sources on the profile. It was found that cubic-splines were better suited to the task of modelling the foreground profiles because of the complex shape and number of inflection points in the lower-envelope.

The resulting profiles were written to a data file (`B1.DAT` in figure 3.2), and hardcopy plots of the profiles were produced for visual inspection of the spline fits. Besides the terrestrial foreground, these profiles also contained components due to the instrumental offset term, Offset_k, and the isotropic component of $\mathrm{Sky}_{i,j,k}$ (see equation 3.1). For this reason the temperature scale of the *SKYMAP* map data has a quite arbitrary zero-point. An example of up and down foreground profiles for a *SKYMAP* observation is shown in figure 3.4. The record format used for the background profiles was similar to that used for

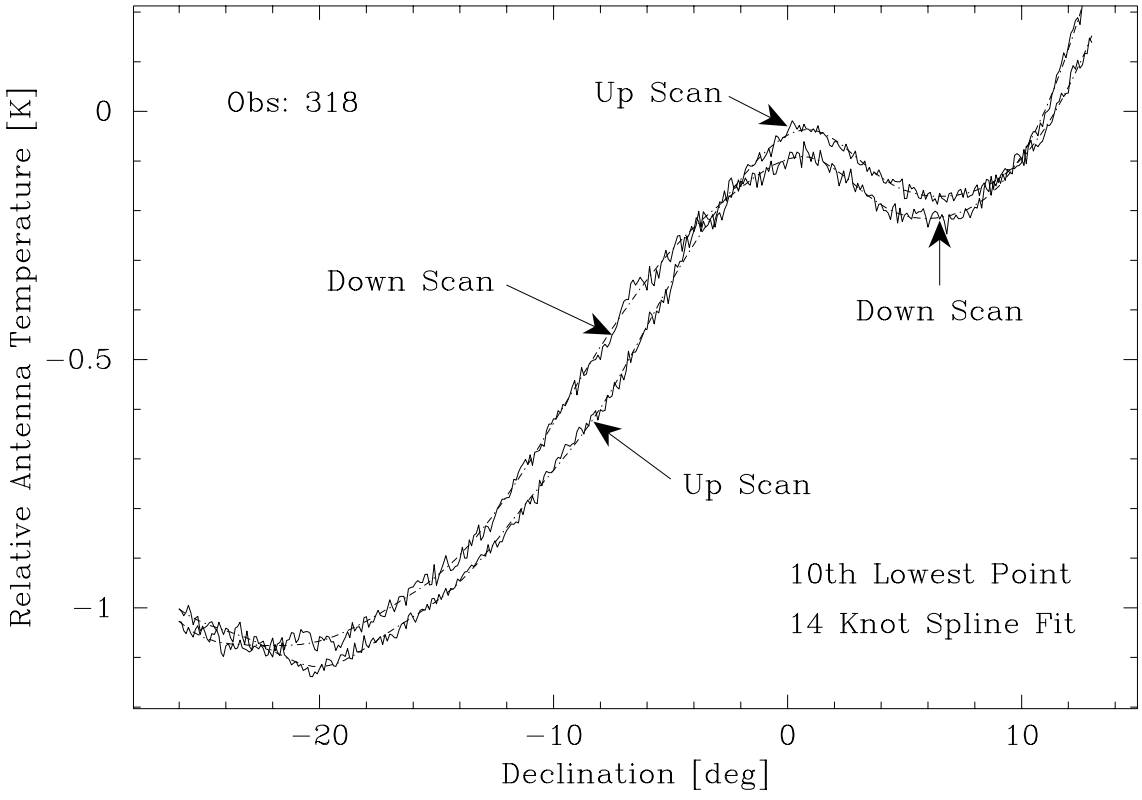

Figure 3.4: An example of the up and down foreground profiles determined from the raster data of a single *SKYMAP* observation. The raw foreground profiles that were determined by the selecting the 10th lowest antenna temperature at each declination bin position are represented by the solid lines. The chained lines trace the cubic spline functions that were fitted to these raw profiles.

the raster data (see table 3.2).

The foreground profiles were then subtracted from the respective sets of raster scan data by program `SBAC1.FOR`, and the residuals were written out to the second generation raster scan file `S1.DAT` (see figure 3.2).

Exponential drift removal

The second most prominent systematic effect in the *SKYMAP* raster data was the downward receiver baseline drift, represented by $\text{ExpDrift}_{i,k}$ in equation 3.1, that affected many observations. Mountfort made no attempt to correct for this relaxation effect, and as a result the effective duration of the observations was reduced because the first few hours of data recorded after sunset had to be discarded.

The data used for the determination of this drift was created from the second-generation raster data in `S1.DAT` by program `DRFBN.FOR` (see figure 3.5). `DRFBN.FOR` divided each scan into three or five (depending on the raster declination range) declination bins and computed the median temperature value for each of these bins. These median values were written out

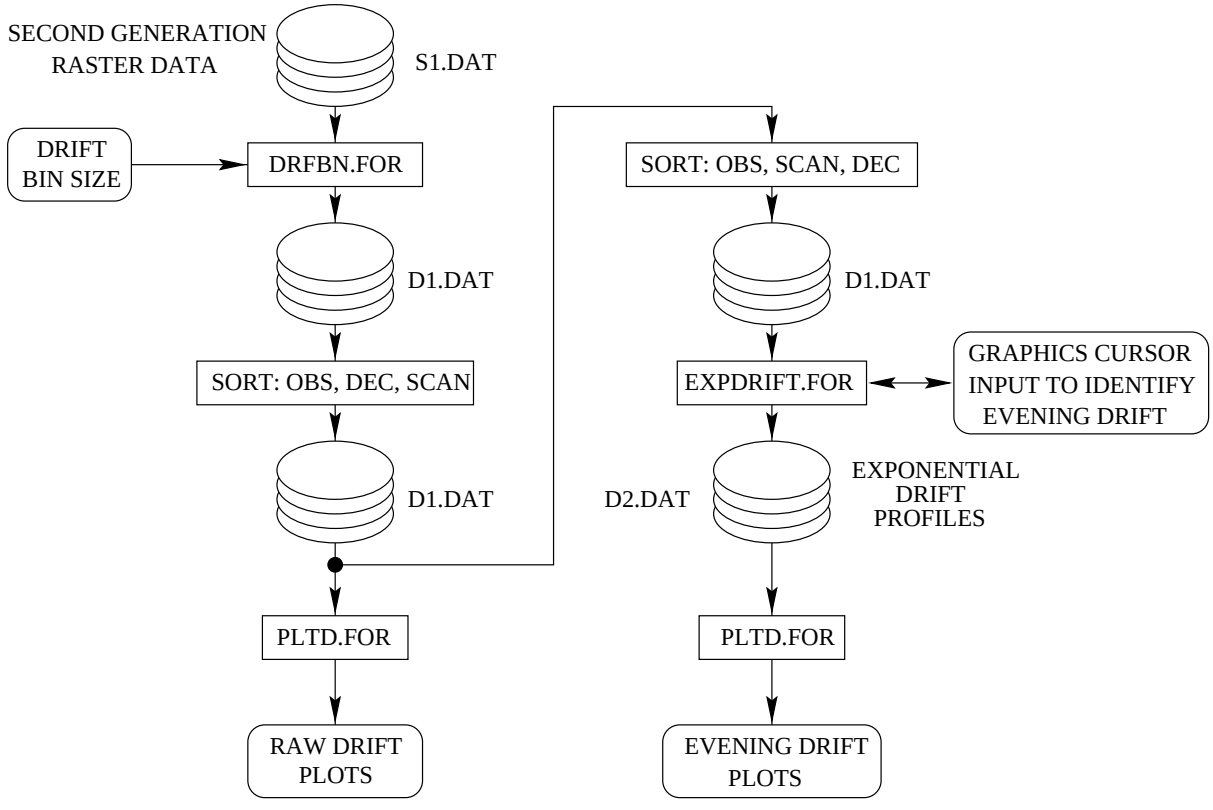

Figure 3.5: A flow diagram illustrating the procedure for determining the exponentially decaying evening drift from individual raster observations. File `D1.DAT` and the associated drift scan plots were produced by the later part of option "D" in table 3.1. The interactive process for specifying the exponential drift was initiated by selecting option "E" in table 3.1. Notice that file names are often repeated (`D1.DAT` on this case) in the flow diagrams in this chapter. These different incarnations of the files contain identical data but the records are sorted on different keys.

to the file `D1.DAT` using the drift scan format described in table 3.3 above, and hardcopy plots of the scans were produced by `PLTD.FOR`. See the curves labelled `D1.DAT` in figure 3.8 for an example of the raw drift profiles for a typical *SKYMAP* raster observation.

By comparing the drift profiles for all of the observations making up a map it was possible identify those affected by baseline relaxation. Selecting option "E" in table 3.1 initiated an interactive graphics procedure that allowed the user to model the relaxation for each observation as the sum of two exponential functions with independent amplitudes and time constants. The function of program `EXPDRIFT.FOR` was to plot out the raw drift scans for each observation on a graphics terminal, and allow the graphics cursor to be used to specify the estimated locus of the relaxation drift profile for each observation. The program used a non-linear least-squares procedure to fit two exponential functions to the manually selected points. This procedure could be repeated for each observation until the user was satisfied with the resulting exponential drift profile. These smooth drift profiles were written out to file `D2.DAT`, and hardcopy plots were produced by `PLTD.FOR`. See the dashed curves in figure 3.8 for an example of the exponential drift determined for observation 295.

The subtraction of these drift profiles from the second-generation raster data in `S1.DAT` was performed as part of option "F" in table 3.1 because the subtraction procedure was better suited to a batch processing environment (see figure 3.6). The resulting third-generation raster data was stored in a temporary data file (`Stemp.DAT in the figure`).

Second foreground subtraction

Having removed the most significant distortions from the raster data, a second foreground profile determination was made. This was an attempt to improve the determination of the $\mathrm{FG}_{i,j,k}^{\mathrm{up,down}}$ term in equation 3.1. The "cold sky" regions of an observation that were necessary for the successful determination of the foreground profiles were often distorted by the effects of the exponential drift. The effects of this distortion were minimized by repeating the foreground determination using the third-generation raster data. The second foreground correction was part of the processing associated with option "F" in table 3.1.

Program `FBAC2.FOR` was used to determine the background profiles for each observation in the third-generation data, and `SBAC2.FOR` produced the fourth-generation raster data by subtracting these profiles from the appropriate rasters. The second foreground determination was very similar to the first, except that the up and down scans within an observation

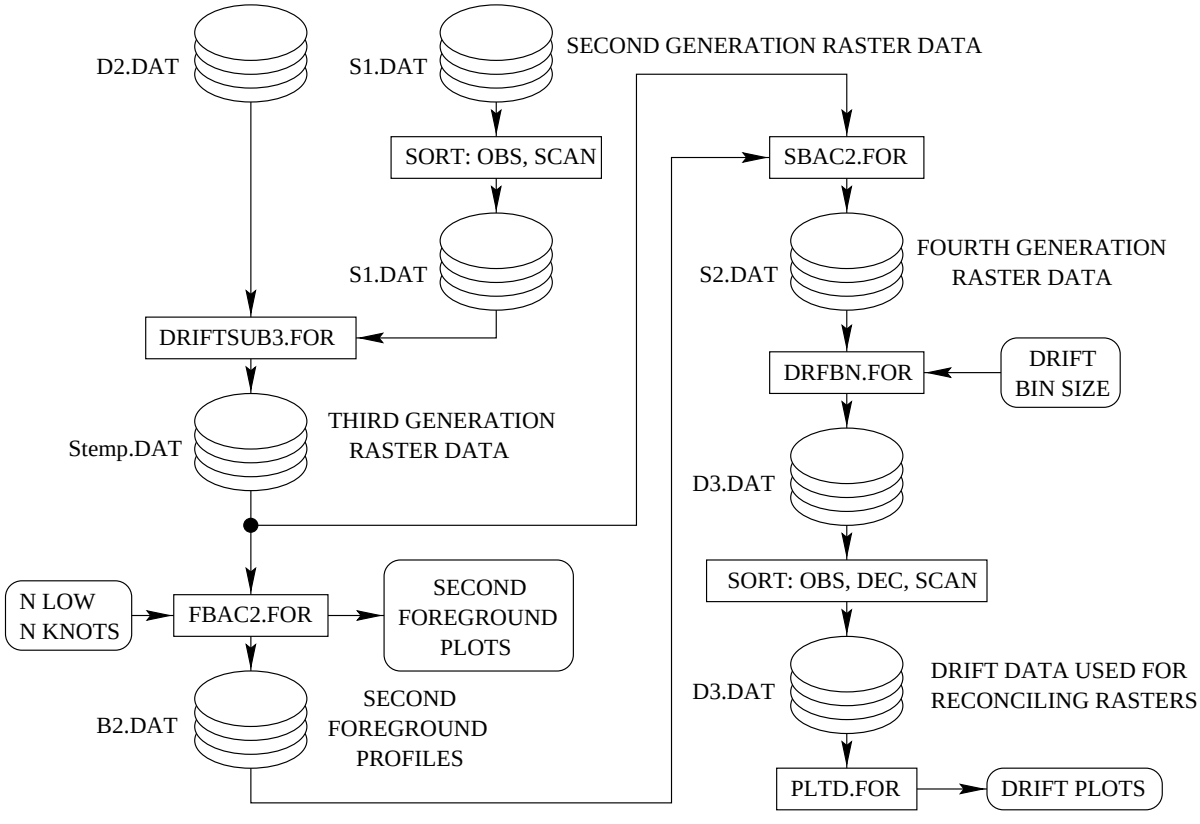

Figure 3.6: A flow diagram illustrating the subtraction of the exponential drift from the scan data, and the determination and subtraction of the second terrestrial foreground profile. These procedures correspond to option "F" in table 3.1.

were not treated separately, and the 20th lowest temperature at each declination interval was selected to represent the raw foreground profile. The second foreground profiles seldom had amplitudes greater than 50 mK, and no examples are given here. Mountfort's data reduction process made no provision for this second foreground correction.

The fourth-generation raster data resulting from this second foreground correction was written to `S2.DAT`, and program `DRFBN.FOR` was used to produce the drift scan data file `D3.DAT` from this raster data. `PLTD.FOR` produced the hardcopy plots of the drift data in `D3.DAT` that were necessary for the next drift correction process.

Raster base-level reconciliation

Small, low-frequency fluctuations in the antenna temperature caused by receiver gain variations, weather effects and temporal variations in the ground spillover radiation were the last distortions to be corrected in the raster data prior to creating the final map. These fluctuations, represented by $\text{Drift}_{i,j,k}$ in equation 3.1, resulted in residual baseline offsets between the observations at the fourth-generation level. If not corrected these offsets would have resulted in "scanning effects" in the final map.

The method that was adopted to reconcile the base-levels of the rasters from the various observations was similar to that devised by Mountfort, but three refinements were added to the original procedure:

- An interactive graphical user interface was developed to facilitate the identification of anomalous drift data.
- Additional linear and non-linear filtering was included in the process to reduce the effects of noise.
- Residual declination-dependent distortions in the raster data were identified and corrected if necessary.

A flow diagram of the full drift-correction procedure is shown in figure 3.7.

Option "G" in table 3.1 initiated an interactive procedure that was used to produce reliable reference drift scans from the individual observation drift data. These reference scans were the best estimates of the true large-scale behaviour of the sky brightness distribution that could be obtained from the independent sets of *SKYMAP* data, and were used to "tie down" the rasters of the various observations to a common base-level.

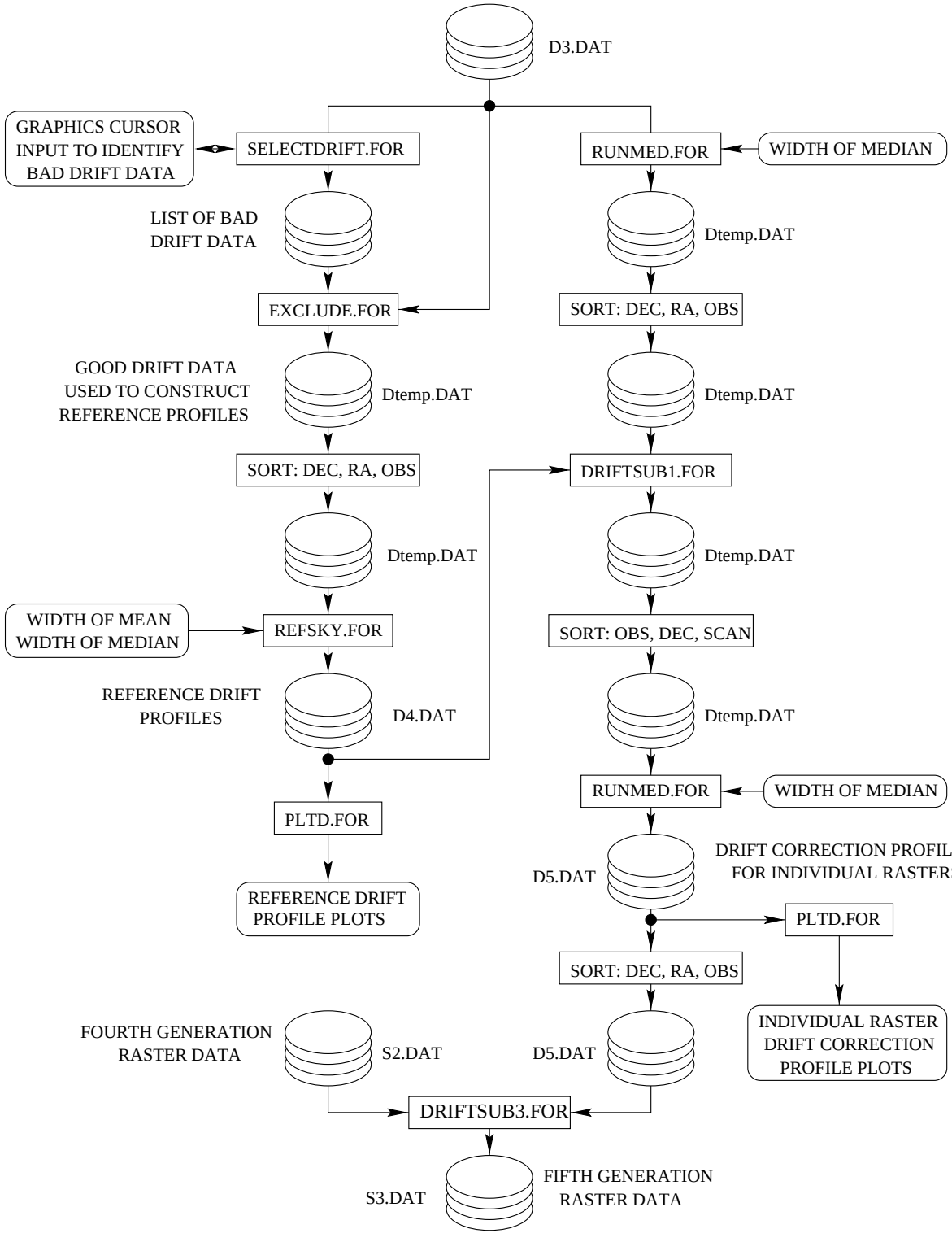

Figure 3.7: Flow diagram of the procedure used to reconcile the base-levels of the different rasters making up a map. The processes and data flow associated with options "G" and "H" in table 3.1 are illustrated in this diagram.

The dotted lines in figure 3.8 represent the `D3.DAT` data for observation 295, which appendix A lists as belonging to map A14D83. By comparing such drift scan plots for all of the observations it was possible to identify right ascension ranges in individual observations that were affected by anomalous baseline drift and interference. The interactive graphics application `SELECTDRIFT.FOR` was used to specify the regions of each observation that had unreliable baselines, and program `EXCLUDE.FOR` edited the relevant drift data out of the `D3.DAT` file. Program `REFSKY.FOR` used median and running-mean filters to combine and smooth the remaining "good" drift data to produce reference drift profiles in file `D4.DAT`. Hardcopy plots of the reference scan profiles were then produced by program `PLTD.FOR`.

This procedure for determining the reference drift profiles was repeated using different selections of input drift data and values for the smoothing parameters until satisfactory results were obtained. The solid lines in figure 3.8 represent the three reference drift scans that were obtained during the processing of map A14D83.

Having determined the reference drift scans it was necessary to determine drift correction profiles for each individual observation, and apply these corrections to the raster data. Option "H" in table 3.1 initiated a batch procedure that performed this task.

Program `RUNMED.FOR` applied a median smoothing filter to the individual drift scans in file `D3.DAT` so that they had the same resolution as the reference scans. `DRIFTSUB1.FOR` subtracted the appropriate reference scans from the individual smoothed drift scans in the temporary file `Dtemp.DAT`, and `RUNMED.FOR` applied a smoothing median filter to the residual scans. These smoothed residual scans were written to `D5.DAT`, and were used as correction profiles for the raster data. The correction profiles applied to observation 295 are shown in figure 3.8.

Program `DRIFTSUB3.FOR` was used to subtract the drift correction profiles in `D5.DAT` from the fourth-generation raster data in `S2.DAT`, and the resulting fifth-generation raster data was written to file `S3.DAT`. Since there were three or five correction profiles spanning the declination range of each raster, it was possible to use linear interpolation and extrapolation to expand the profiles into a drift correction surface.

The correction surfaces were generally dominated by right ascension dependent drift effects, mostly ripples caused by light clouds and receiver gain drift. Sometimes small residuals were apparent in the declination direction, normally causing a twist in the surface. These declination-dependent effects were probably due to temporal changes in the terrestrial foreground profile.

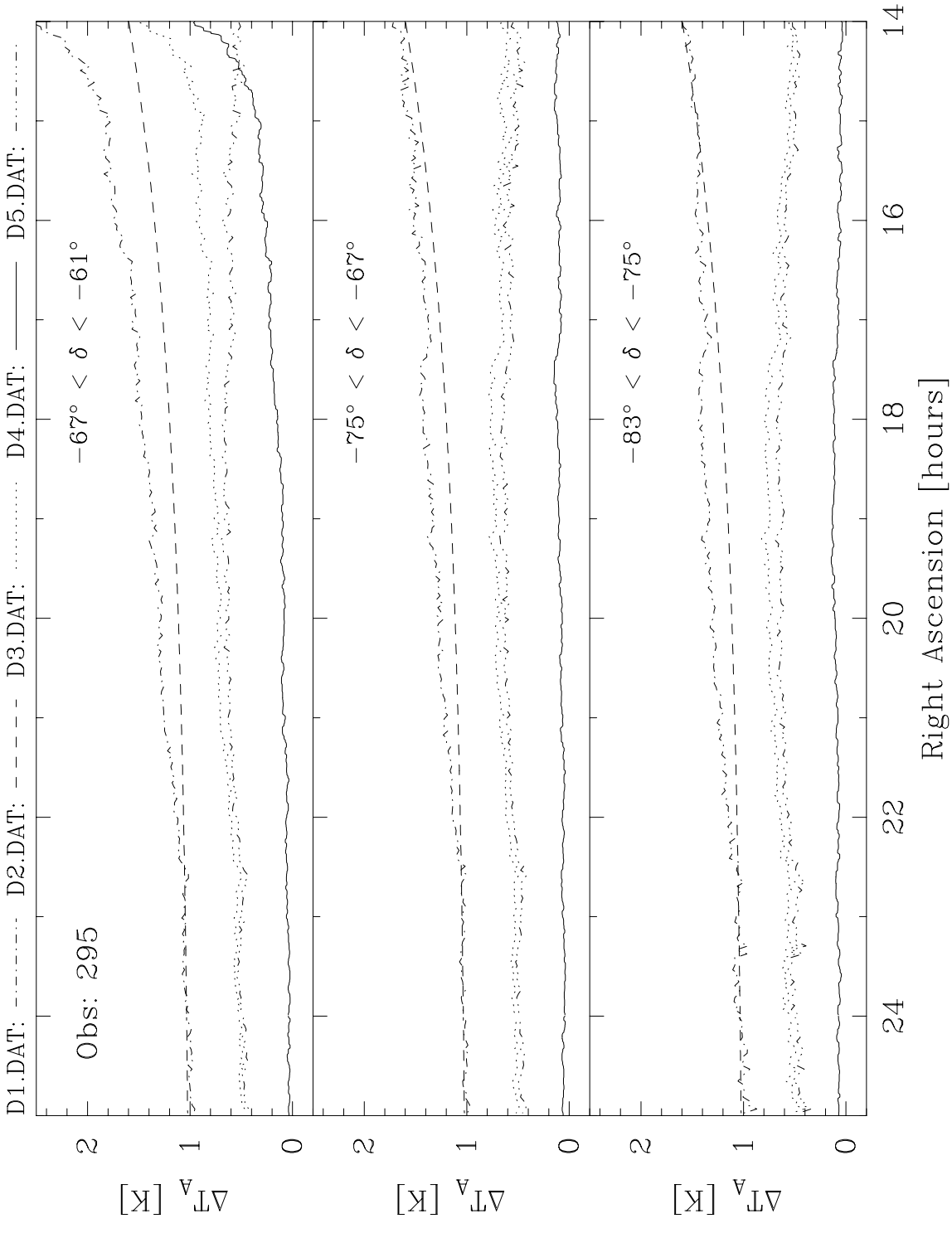

Figure 3.8: Plots of the data used for correcting baseline drifts in an typical *SKYMAP* raster data set. The legend at the top of the graphs associates the line styles with the data files used to create the plots. For the sake of clarity the curves for D3.DAT and D5.DAT are vertically offset by 0.5 K, and those for D1.DAT and D2.DAT by 1 K. Each of the three panels is annotated with the declination range of the median bin associated with it. Note that the scan in the top panel is affected by emission from the Galactic plane. See the text for a full description of the relevance of these graphs. Figure 2.4 in the previous chapter gives the time-ordered representation of the raw data for observation 295.

Raster data editing

Mountfort's original *SKYMAP* data reduction procedure did not allow visual inspection of the raster data, nor was there provision for excluding individual scans that were contaminated by interference or some other deleterious effect. This was not an oversight; the computing facilities necessary for this sort of interactive image processing were not available at the time the original *SKYMAP* reduction procedures were designed.

Option "I" in table 3.1 consisted of two separate procedures: (1) a batch procedure to prepare the raster data in a convenient form for (2) an interactive graphics application that was used to identify scans that were to be excluded from the raster data prior to the construction of the map. Both of these procedures are illustrated in figure 3.9.

The initial batch procedure associated with option "I" consisted of two data reformatting tasks. Program `TOBINARY.FOR` converted each of the fourth-generation rasters into a binary data format so that they could be displayed as pseudo-colour images on a graphics terminal without an inconvenient processing delay. Program `TRIALMAP.FOR` merged the fifth-generation rasters in the correct right ascension order, and averaged congruent scans to create a rough trial map. This trial map was also stored in binary format to reduce the processing required to display it on a graphics terminal.

The identification of scans that were to be omitted from the final map was performed with the aid of the interactive graphics application `BADSCAN.FOR`. Images of both the trial map and the raster data under consideration were simultaneously displayed on the graphics screen, one above the other and with the same scale. This display format was convenient for associating anomalous effects in the trial map with the flaws in the raster data of individual observations. The fourth-generation data were used for the raster images of the individual observations so that the quality of the data prior to the final drift correction could be evaluated. A vertical graphics cursor was used to flag the suspect scans in each observation, and a list of these "bad" scans was written to a data file. Program `EXCLUDE.FOR` was used to remove these scans from the raster data.

It was possible to exclude dubious scans without compromising the final map quality because of the strategies of repeated raster observations and spatial oversampling. At this stage it was important to check that no gaps were created in the final map because of insufficient good data or over-zealous data editing. Program `MISSING.FOR` produced a summary of the scan density after the editing process, and reported possible gaps.

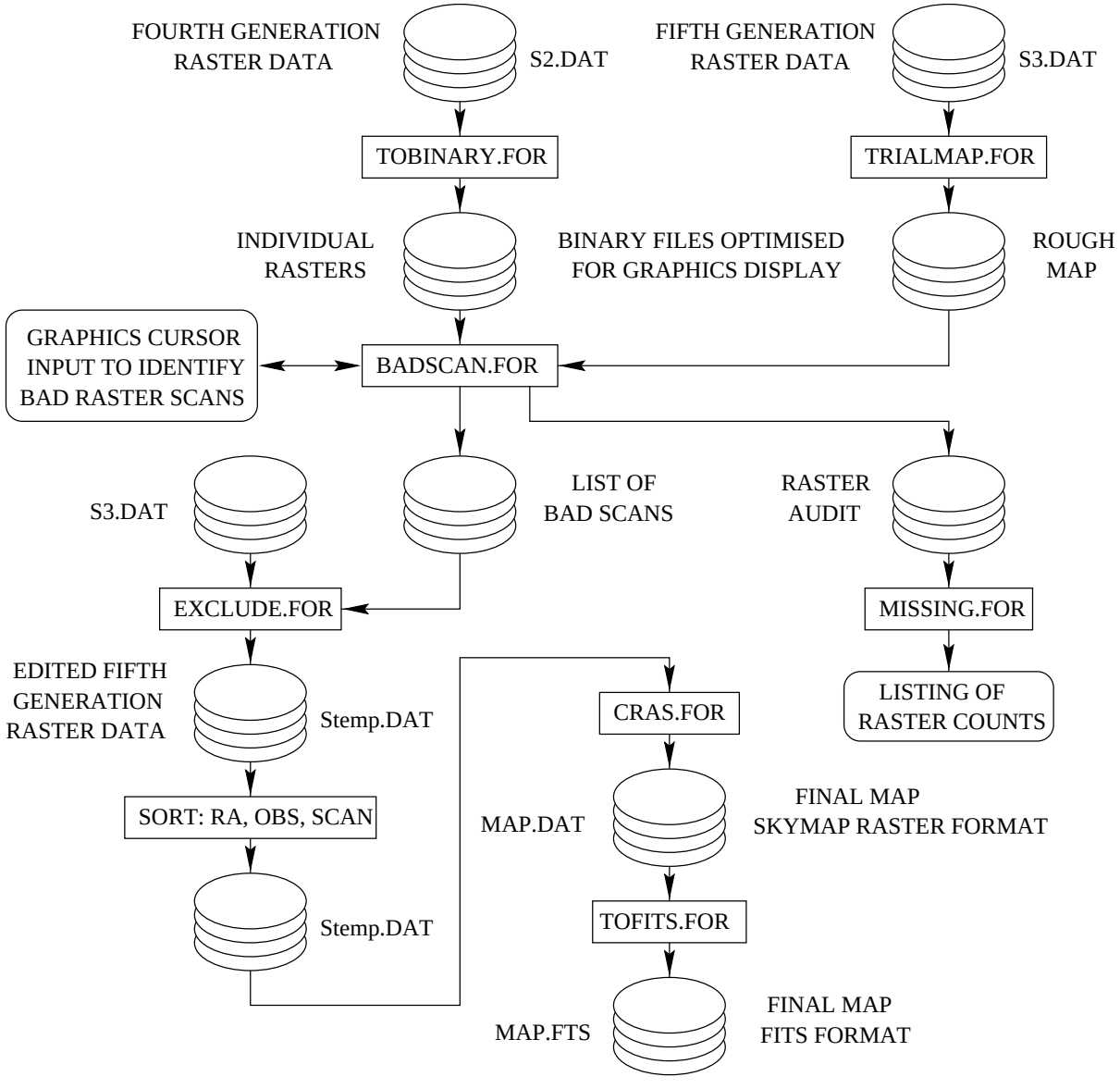

Figure 3.9: A flow diagram of the data editing and final raster merging processes that concluded the *SKYMAP* data reduction cycle. This diagram illustrates the processes associated with options "I" and "J" in table 3.1.

Merging the rasters into a map

The final step in the map making process was initiated by selecting option "J" in table 3.1. The primary purpose of program `CRAS.FOR` (see figure 3.9) was to merge the raster data that had been sorted into the correct right ascension order, and interpolate the temperatures onto a regular equatorial coordinate grid. The initial binning procedure had already set up a regular declination grid, so one-dimensional interpolation in the right ascension direction was required to account for the imperfect tracking of the antenna (see figure 2.3 in the previous chapter). This interpolation was accomplished using a windowed $\frac{\sin x}{x}$ convolution kernel with nulls coinciding with the map scan spacing. A triangular windowing function was applied to the convolution function in order to reduce Gibb's phenomenon effects. Mountfort's original version of this program used simple rectangular binning, which did not produce proper interpolated temperatures.

The map produced by `CRAS.FOR` (`MAP.DAT` in figure 3.9) was stored using the *SKYMAP* raster scan format. To ensure reliable data portability and efficient data storage the program `TOFITS.FOR` was used to create a FITS (Wells et al., 1981) format map with appropriate FITS keywords in the file header.

3.2 Combining the Maps

The relative base-levels of the ten component maps were not expected to be consistent because the maps were observed and processed completely independently. It was necessary to apply additional "DC offset" and "warping" corrections to each of the component maps prior to combining them into a composite all-sky image. The purpose of these corrections was to (a) reduce discontinuities at the map boundaries, and (b) ensure that the composite map was a reliable representation of the large-scale emission features in the sky.

The constant declination scans shown in figure 3.10 were extracted from the ten original maps produced by the *SKYMAP* data reduction process. These scans were interpolated onto a common J2000 equinox coordinate grid to prevent problems caused by differential precession. The scan declinations were chosen to be near the map boundaries so that the base-levels of adjacent maps could be compared. This figure reveals that the relative offsets between the various independent maps never exceed 250 mK T_{FB}, but that simple "DC" offset corrections would not be sufficient to make the maps self-consistent.

In order to force the maps to be consistent it was necessary to construct "master" scans

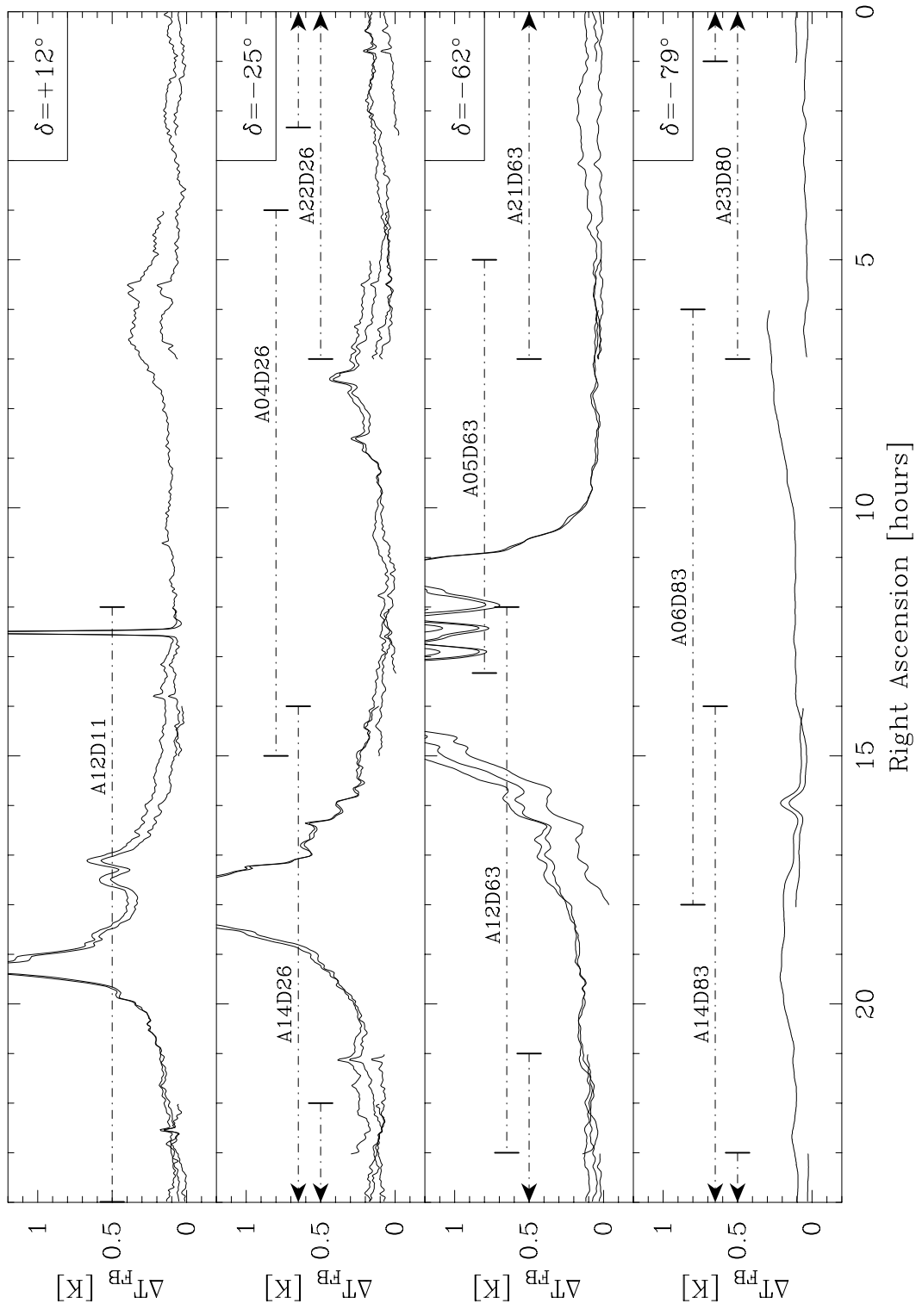

Figure 3.10: Constant declination scans extracted from the northern and southern boundaries of the 10 constituent maps prior to the baseline correction procedure that is described in section 3.2. The right ascension coverage of each of the ten component maps is indicated in the panel representing the lower boundary of the map. The full-beam brightness temperature scale has been used for the vertical axis.

that would best represent the real sky at the four chosen declinations. The original map images were then warped to be consistent with the master scans, and thus consistent with each other.

Construction of the master scans proved to be difficult because of the disparity between the various scans, as seen in figure 3.10. For example, the $\delta = -79^\circ$ scan obtained from A06D83 was particularly problematic. The region between RA=4h00 and RA=10h00 shows an anomalous gradient, which is not present at the northern boundary of the map. Because this declination was near the southern boundary of the survey there was no adjacent map to compare with. This anomaly was presumably due to an unexpected but persistent temporal variation in the terrestrial foreground emission present in all nine observations covering target area A06D83.

An interactive, iterative, non-linear least-squares procedure was developed by the author to produce the master scans at the four declinations from the individual map scans. This procedure was applied independently at each declination. The map scans were too disparate to be averaged directly to construct the master scans, so cubic spline drift-correction profiles were subtracted from the individual map scans prior to their combination. The coefficients of these cubic spline profiles were chosen to minimize the following least-squares criterion:

$$\chi^2 = \sum_k \sum_{k'>k} \sum_i [(S_{k,i} - C_{k,i}) - (S_{k',i} - C_{k',i})]^2 + \lambda_k \sum_k \sum_i C_{k,i}^2 \qquad (3.2)$$

where the $S_{k,i}$ were the drift scans derived from the maps, the $C_{k,i}$ were the correction splines, k and k' were observation indices, i was a right ascension sample index, and the λ_k were Lagrange multipliers. The first term in equation 3.2 ensured that the corrected scans were self-consistent, while the second term had the competing effect of minimizing the amplitude of the correction profiles. A running median filter was used to combine the corrected scans at each declination into the master scan for that declination.

This procedure was repeated in an iterative fashion, with the Lagrange multipliers and the spline control points being varied between each iteration. A graphical user interface was developed to aid the adjustment of these parameters, which were adjusted until the resulting master scan was free of discontinuities and spurious structure. Comparison scans from the 408 MHz survey (Haslam et al., 1982) were used to guide the selection of the parameters, but these scans were not included directly in any numerical calculations.

Once all four of the master scans had been constructed they were subtracted from the

associated map scans in order to generate raw correction profiles for the corresponding maps. These raw correction profiles were smoothed by the fitting of cubic spline functions. All of the maps, except A12D11, had correction curves for both the northern and southern boundaries. The single correction curve for A12D11 was subtracted from the entire declination range of the map, while for the rest of the maps the correction was achieved by linear interpolation between the northern and southern correction curves.

Figure 3.11 illustrates the result of this exercise. The scans in this figure were obtained from the ten component maps after the above bending and warping corrections had been applied. It is apparent that all of the major inconsistencies were removed, as were anomalous gradients. A constant offset was applied to all of the observations in an attempt to re-introduce the Galactic isotropic emission, hence the curves in figure 3.11 are about 200 mK higher than those in figure 3.10. This offset was determined by extrapolating results from the 408 MHz survey. A more accurate determination of the isotropic Galactic emission is given in the next chapter.

3.3 Image Display and Processing

The radio survey maps were stored as computer disk files and thus required visualization tools to display the radio brightness distributions as images. These images were necessary for two main purposes: (a) to allow visual inspection of the quality of the data, and (b) to allow the identification of astronomical objects in the maps. In order to make quantitative deductions from the map data a suite of image processing software was required. This section briefly outlines the software tools that were developed by the author to exploit the scientific value of the radio continuum survey.

3.3.1 Background

Contour diagrams were the primary means used to display the radio survey maps before scientific graphics workstations were available to the Radio Astronomy Group. This classical technique for displaying spatial data had a number of disadvantages:

- The production of contour diagrams was a slow process, particularly when using the Calcomp drum plotter that was available when the first *SKYMAP* observations were made. The slow turn-around time made any form of interactive data processing almost impossible.

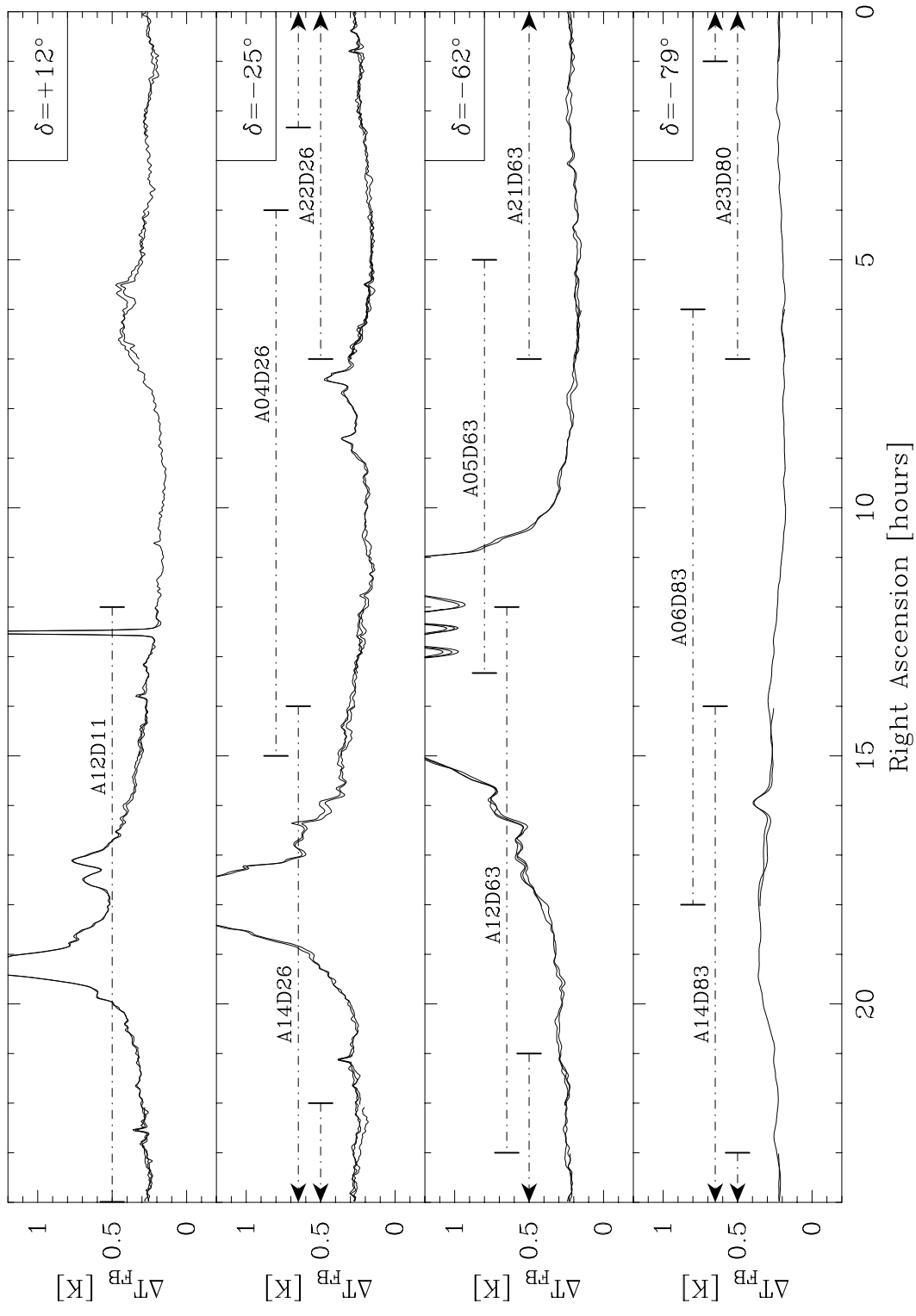

Figure 3.11: Constant declination scans extracted from the northern and southern boundaries of the 10 constituent maps after the baseline correction procedure that is described in section 3.2. The right ascension coverage of each of the ten component maps is indicated in the panel representing the lower boundary of the map. The full-beam brightness temperature scale has been used for the vertical axis.

- Contour diagrams were not suited to the display of faint, spatially extended radio sources. One of the main aims of the survey was to detect such sources.
- The wide dynamic range of the survey data made the choice of contour levels very difficult.

A number of attempts were made to produce grey-scale images of the early survey maps. These efforts included using the existing vector plotting devices, dot-matrix printers, oscilloscopes with custom-built circuitry to scan and modulate the intensity of the electron beam, and the use of early desk-top computers. None of the attempts were particularly successful, but valuable experience in low-level computing and the interfacing of electronic hardware to computers was gained by the author!

The first successful *SKYMAP* map, A12D63, contained more than 700000 samples, or pixels. When the map was produced in 1980 there was no computer available to the Radio Astronomy Group that could simultaneously store the entire map in core memory. Initial image processing applications that were written for the ICL 1904A computer had to make extensive use of temporary scratch files to overcome this memory limitation. Common applications, such as regridding a map onto a different coordinate projection, would run for a number of hours. The arrival of the CDC 825 computer with virtual memory capability and a fast processor alleviated the difficulties associated with processing the survey maps, but the problem of displaying the resultant radio images remained.

3.3.2 The use of graphics workstations

In the early 1980's the VAX/VMS computer architecture was quite dominant in the field of scientific computing, and this held particularly for the processing of astronomical data. In 1981 the Radio Astronomy Group obtained a VAX 11/730 minicomputer, together with a 9-track magnetic tape deck and a Tektronix M4115B colour graphics terminal as peripherals. This computing facility provided the Group (and Rhodes University) with its first scientific graphics workstation. The significant features of this facility were:

- Sufficient disk capacity to store the survey maps, and an efficient means for archiving data.
- Substantial random access memory and a virtual memory system which simplified the development of image processing applications that required the allocation of large data arrays.

- A graphics terminal capable of displaying high-resolution colour images on demand.
- A terminal that allowed the development of graphical user interfaces to be used for interactive data processing.

Over the years this facility has been upgraded, and currently the Group uses a standard Pentium PC running the non-proprietary Linux operating system for the analysis, manipulation and display of astronomical images.

3.3.3 Image display and processing software

The Starlink astronomical data processing package was installed on the VAX computers in order to have access to the DSCL environment (Pearce, 1980) and the ASPIC image processing applications (Hartley, 1983). It was soon discovered that the ASPIC procedures were of limited use for work on the survey data because of two factors: (a) the image display programs were designed to work with an ARGS display unit, not the Tektronix display, and (b) the image processing applications were mostly intended for optical images with small fields of view.

Because of the specialized processing required to manipulate and analyze the survey data, it was decided to develop a local package of data processing software. Initially these applications were written to conform to the Starlink DSCL programming environment, but this practice was stopped when the software was ported to Unix computing platforms. Currently, all of the applications use the FITS format (Wells et al., 1981) for storing images, and extensive use is made of the following proprietary and public-domain software libraries and utilities:

FITSIO a library of routines for reading and writing FITS format files (Pence, 1996)

IMSL a library of numerical analysis techniques and transcendental functions (IMSL, 1978)

Numerical Recipes a useful resource for various numerical methods (Press et al., 1986)

PGPLOT a library of plotting routines with an astronomical bias (Pearson, 1995)

SAOimage an interactive imaging package that displays FITS format astronomical maps (Hilst, 1991)

SLALIB a library of astrometry routines that accompanies the Starlink software collection (Wallace, 1996)

WCS a library of routines that implements the WCS world coordinate system proposal (Greisen and Calabretta, 1993; Greisen and Calabretta, 1997)

WIP a graphics application that produces annotated graphs and images from data in ASCII or FITS data files (Morgan, 1996)

The data processing applications that were developed by the author to analyze the survey data are not reported here in any detail. The list below merely itemizes the applications most relevant to the work reported in this thesis, together with brief comments describing the functions of the programs.

`2point.f` Performs 2-point correlation between two images stored in FITS binary table format using the *COBE* Quadrilateralized Spherical Cube coordinate projection (see chapter 7).

`addimage.f` Forms a linear combination of two congruent FITS images.

`ait.f` Transforms a cylindrical projection FITS image into a Hammer-Aitoff coordinate projection (Greisen and Calabretta, 1997).

`basesub.f` Subtracts a two-dimensional polynomial base surface from a FITS image.

`beampro.f` Performs the analyses of the antenna beam as described in section 4.1 of chapter 4.

`cal.f` Performs the map beam analyses as described in section 4.5 of chapter 4.

`cont.f` Draws contour diagrams of map data using various standard coordinate projections.

`convolve.f` Convolves two fits images.

`ctfm.f` Regrids maps from one coordinate projection to another. The program allows the processing of multiple input maps to construct a single output map. The interpolating kernel function can be selected to be a gaussian profile for degrading the map resolution, or the non-smoothing profile described in section 4.7.2 of chapter 4.

`ctfm_iras.f` A version of `ctfm.f` that operates on the *IRAS* sky-plates (see chapter 7).

`galgauss.f` Models the Galactic disk emission as the superposition of a number gaussian components (see chapter 6).

`hornconv.f` Convolves a FITS image with an extended beam function.

`lxfm.f` Performs a discrete Legendre transform on a sequence of numbers (see chapter 7).

`noise.f` Calculates the RMS noise level for a small region in a FITS format map.

`radiofir.f` Performs discrimination between thermal and non-thermal radio emission by comparing radio and far-infrared (FIR) maps (see chapter 7).

`ratio.f` Creates a spectral index map by dividing one FITS image by another.

`scaleoff.f` Applies a scale factor and offset term to a FITS image.

`rhodes2csc.f` Transforms a cylindrical coordinate projection FITS image into the *COBE* Quadrilateralized Spherical Cube projection (Greisen and Calabretta, 1997; Bennett et al., 1996).

Chapter 4

Calibration and Data Quality

For the survey data to be useful in any quantitative study it is necessary for the measurement process to be well understood, and for procedures to be undertaken to ensure that the data are consistent with accepted calibration standards. It is equally important that the systematic errors in the data are well characterized so that the limitations of the data are clearly evident. This chapter describes the various procedures that were devised to ensure the accurate calibration of the flux and temperature scales of the *SKYMAP* data, and to test the quality of the final data product.

In order to define a useful brightness scale for the survey data it is necessary to understand the characteristics of the telescope beam so that the relationship between measured antenna temperature and intrinsic sky brightness temperature can be established. The results reported in sections 4.1 to 4.5 were obtained by making supplementary observations that were specifically designed to determine the aperture and beam characteristics of the HartRAO telescope. Some standard radio astronomy fundamentals are covered so as to clearly define how the full-beam brightness temperature scale was derived and verified.

Section 4.5 describes the analysis of the beam characteristics as determined from the *SKYMAP* survey maps. This analysis showed that the *SKYMAP* observation and data reduction procedures did not significantly affect the beam pattern, and hence the results obtained from the supplementary beam observations could be applied to the final map. The development of an absolute full-beam brightness scale for the *SKYMAP* survey is described in section 4.6.

The noise level in the radio maps and the accuracy of source positions are important parameters that are used to gauge the quality of radio continuum survey data. The techniques used to measure these parameters, and the results obtained for the individual maps, are presented in sections 4.7 and 4.8.

For convenience, the main results of this chapter are tabulated here in table 4.1.

Half-power Beamwidth	HPBW, FWHM	$20'$
Separation Of First Nulls	FWFN	$48'$
Separation Of Second Nulls	FWSN	$100'$
Point Source Sensitivity	PSS	9.8 Jy/K
Aperture Efficiency	$\eta_{\rm A}$	53%
Main-Beam Efficiency	$\eta_{\rm MB}$	55%
Full-Beam Efficiency	$\eta_{\rm FB}$	69%
RMS Noise Level	Nominal	25 mK $T_{\rm FB}$
	Worst Case	34 mK $T_{\rm FB}$
RMS Pointing Deviation	Nominal RA	$0.75'$
	Worst Case RA	$1.5'$
	Nominal Declination	$0.9'$
	Worst Case Declination	$1.9'$

Table 4.1: A summary of the calibration and data quality parameters derived in this chapter.

4.1 The Beam Pattern

It is necessary to have a good understanding of the beam polar pattern of an antenna used for pencil-beam mapping observations for the following reasons:

1. The width of the main response lobe defines the spatial resolution of the resulting radio brightness images. This resolution determines the scan spacing and map pixel widths that are necessary to satisfy the Nyquist sampling criterion.

2. Knowledge of the beam sidelobe pattern allows the discrimination between true sources and beam artifacts in the radio brightness images.

3. Parameters such as the aperture efficiency and full-beam efficiency are needed to define a meaningful brightness temperature scale for the radio images.

This section describes measurements and calculations that were made to obtain the polar pattern of the HartRAO antenna operating at $\lambda = 13$ cm.

The instrumentation necessary to perform an interferometric measurement (Hartsuijker et al., 1972) of the extended complex beam pattern was not available at HartRAO, so the power response polar pattern was measured by making mapping observations towards a strong point-like cosmic source. Tau A is a convenient cosmic source for this purpose: its

is relatively uncontaminated by Galactic background emission, is very powerful, and has an extent which is small compared to the $20'$ beamwidth of the HartRAO antenna.

A $\lambda = 13$ cm map of a $6^\circ \times 6^\circ$ region of sky centred on Tau A was made at HartRAO in 1984, and again in 1996. The period between these two observations overlaps most of the time window of the *SKYMAP* observations. Both of the resulting maps were made with a scan spacing and binning width of $2'$, thus ensuring generous oversampling of the beam profile. Figure 4.1 is a contour map of the *normalized beam polar pattern*, $P_{\rm N}(\Omega)$, that was derived from the average of the two beam maps. The beam pattern was normalized by dividing the array of antenna temperatures by the value of the central pixel, which corresponds to the peak antenna temperature.

Commonly quoted parameters of the beam pattern were derived from the beam polar plot shown in figure 4.1. The main lobe was circular with a half-power beamwidth, HPBW, (or full-width at half-maximum, FWHM) of $20'$. The sidelobe pattern was strongly influenced by the aperture blockage caused by the four subreflector support legs. The maximum amplitude of the first sidelobe was 2% of the peak beam response. The first null occurred at a radius of $24'$ (FWFN=$48'$), and a well-defined second null at $50'$ (FWSN=$100'$).

Figure 4.2 is an image of the difference between the two beam maps that were made 12 years apart. The mutual residual was normalized with respect to the peak beam response. Differences were detectable in the main lobe and first sidelobe, but these were everywhere less than 2% of the peak response. These small differences were probably caused by the repositioning of the feed horn within the feed cabin when the maser receiver was decommissioned, and caused no significant incompatibilities between survey maps made at differing epochs.

Two parameters that are related to the beam polar pattern are introduced at this stage. These parameters are used in later derivations, but their numerical values are not required.

The *total beam solid angle*, $\Omega_{\rm A}$, is a parameter that is used frequently in subsequent sections of this chapter. It is defined to be the solid angle enclosed under the normalized beam pattern, $P_{\rm N}(\Omega)$ (Kraus, 1966a):

$$\Omega_{\rm A} \equiv \int\int_{4\pi} P_{\rm N}(\Omega)\, d\Omega = \int_0^{\pi}\int_0^{2\pi} P_{\rm N}(\phi,\theta)\, \sin\theta\, d\phi\, d\theta \quad [\rm sr] \tag{4.1}$$

where the peak of the polar pattern is assumed to be at $(\phi = 0, \theta = 0)$. In practice $\Omega_{\rm A}$ cannot be calculated by numerical integration of equation 4.1 because it is not feasible to measure the polar pattern in all directions with sufficient sensitivity.

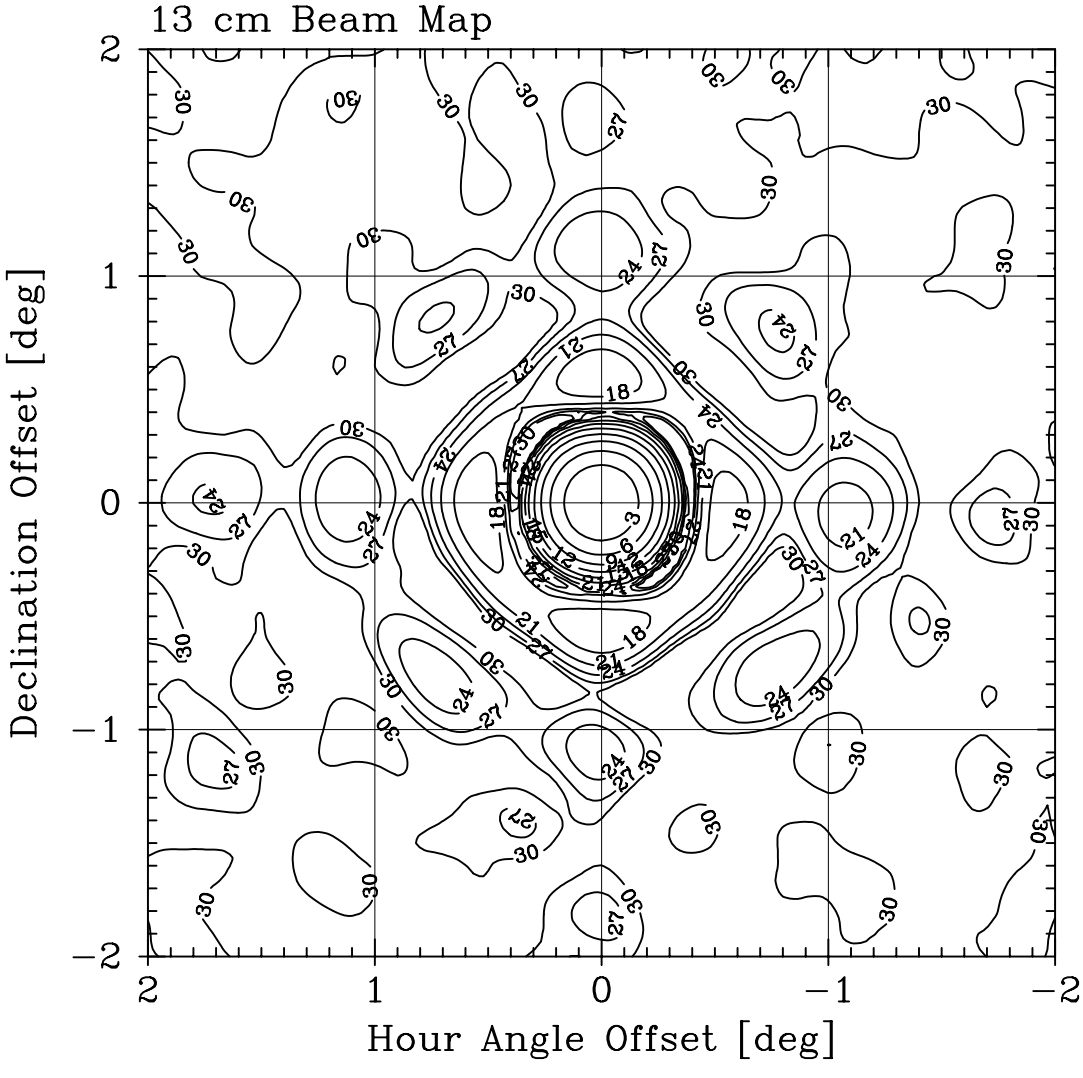

Figure 4.1: A contour diagram of the beam polar pattern for the HartRAO antenna operating at $\lambda = 13$ cm. This map of the beam response was obtained by mapping an area of sky towards the strong point-like radio source Tau A. Contours are drawn at 3 dB intervals, and the contour labels give the attenuation with respect to the central peak. The symmetric sidelobe pattern was a result of the aperture blockage caused by the four subreflector support legs. There is very slight evidence of a north-south coma, which was probably due to the offset position of the feed horn.

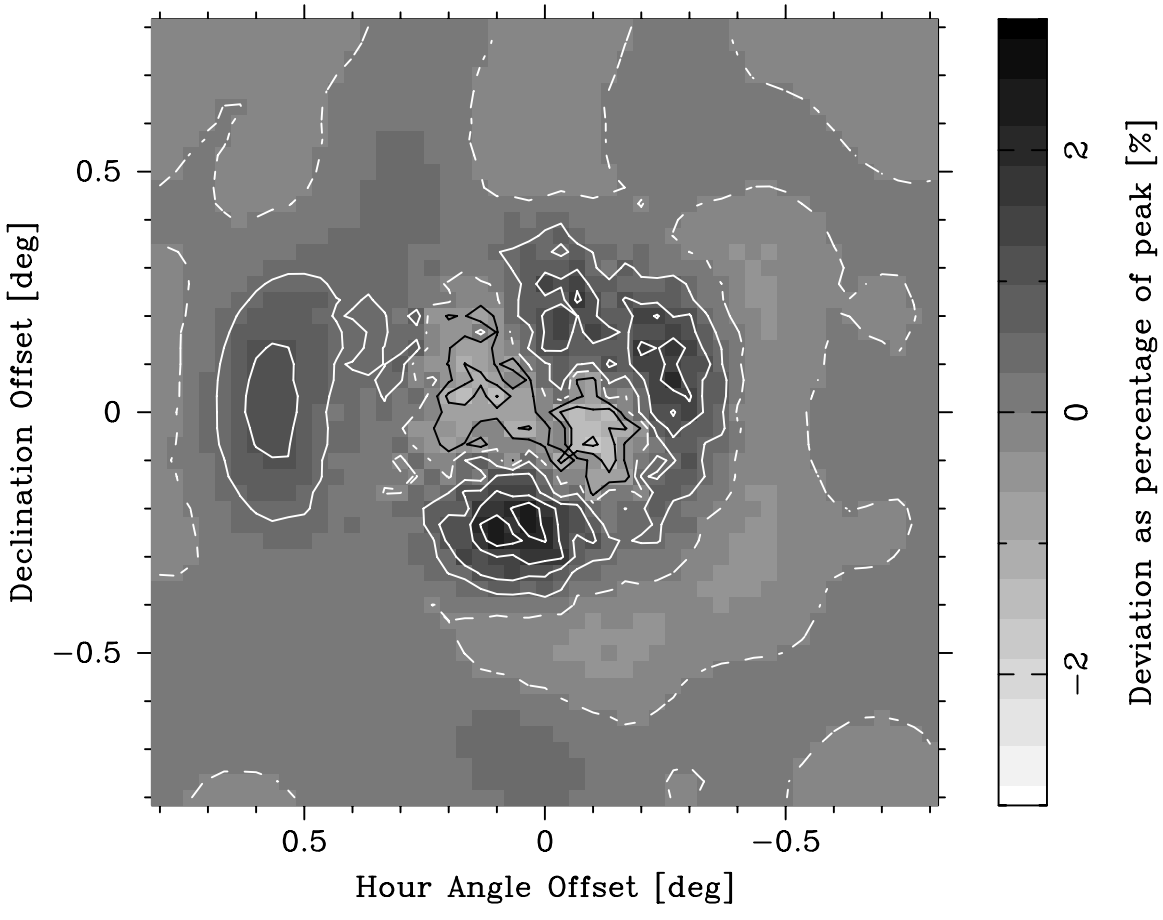

Figure 4.2: The residual remaining after taking the difference between the 1984 and 1996 beam maps. Both the grey-scale and the contours indicate mutual deviation as a percentage of the peak beam response. The dashed white contours represent zero deviation and the solid contours are spaced at 0.5% intervals, white representing positive deviations and black representing negative deviations.

The total beam solid angle is reciprocally related to the *effective geometrical aperture* of the antenna, $A_{\rm G}$, by the equation (Baars, 1973; Kraus, 1966b):

$$\Omega_{\rm A} \times A_{\rm G} = \Omega_{\rm A} \times (\eta_{\rm G} \times A_{\rm P}) = \lambda^2 \quad [{\rm m}^2] \tag{4.2}$$

where $\eta_{\rm G} < 1$ is an efficiency factor relating the geometrical aperture to the physical area of the antenna, $A_{\rm P}$. The effective geometrical aperture (and hence the total beam solid angle) is dependent on the illumination taper provided by the feed horn and subreflector, and on the physical properties of the antenna, such as the aperture blockage and the accuracy of the dish surface. Dissipative losses which have an isotropic effect on the beam pattern, such as feed losses or ohmic losses in the reflectors, do not affect the geometrical aperture.

4.2 The Antenna Temperature Scale

The HartRAO $\lambda = 13$ cm antenna temperature scale is defined by a noise diode that can be activated to inject a reference noise signal into the receiver front-end. The excess antenna temperature, $T_{\rm CAL}$, of this calibration signal was measured to be 3.95 ± 0.2 K (Nicolson, private communication) using the "Y-factor" technique described by Findlay (1966). Hot (373 K) and cold (liquid nitrogen) matched loads were used as absolute noise temperature references for this procedure.

The 5% error in the measurement of $T_{\rm CAL}$ results from the uncertainty in the physical temperatures of the hot and cold reference loads, and unknown line losses and mismatches in the Y-factor measurement setup. The factor $\eta_{\rm CAL}$ is introduced to account for this *systematic* error in the following analysis of the antenna temperature scale.

The radiometer has been tested to have a linear power response over the operating range required for the survey observations, and therefore the *measured* excess antenna temperature, $T_{\rm A}$, due to a radio source transiting the antenna beam is given by the simple ratiometric formula:

$$T_{\rm A} = T'_{\rm A} \times \eta_{\rm CAL} = \frac{\Delta V_{\rm source}}{\Delta V_{\rm CAL}} \times T_{\rm CAL} \quad [{\rm K}] \tag{4.3}$$

where $\Delta V_{\rm source}$ and $\Delta V_{\rm CAL}$ are the excess radiometer output voltages due to the radio source and calibration signal respectively, and $T'_{\rm A}$ is the "true" antenna temperature.

The excess antenna temperature that is *measured* towards the direction Ω_0 as a result of a randomly polarized sky brightness temperature distribution, $T_{\rm B}(\Omega)$, is given by the

following convolution integral (Baars, 1973; Kraus, 1966c):

$$T_{\rm A}(\Omega_0) = \frac{\eta_{\rm R} \times \eta_{\rm CAL}}{\Omega_{\rm A}} \int\int_{4\pi} T_{\rm B}(\Omega)\, P_{\rm N}(\Omega_0 - \Omega)\, d\Omega \quad [{\rm K}] \tag{4.4}$$

The efficiency factor $\eta_{\rm R} < 1$ has been introduced to account for dissipative losses in the antenna and feed system. $\eta_{\rm R}$ is normally very close to unity for radio telescope antennas. Note that equation 4.4 describes the convolution of two spherical distributions so the argument $(\Omega_0 - \Omega)$ implies an Euler rotation rather than the angle between two directions.

The *measured* antenna temperature scale as defined by equation 4.3 is a convenient and consistent intermediate brightness scale to use, as long as the physical and electrical properties of the antenna remain unchanged. For quantitative studies of radio sources it is necessary to determine the factor

$$\frac{\eta_{\rm R} \times \eta_{\rm CAL}}{\Omega_{\rm A}} \tag{4.5}$$

in equation 4.4 in order to relate the measured antenna temperatures to the intrinsic sky brightness temperature.

4.3 The Effective Aperture

It can be shown that for a randomly polarized, point-like source with monochromatic flux S_λ equation 4.4 simplifies to:

$$T_{\rm A} = \frac{\eta_{\rm R} \times \eta_{\rm CAL}}{\Omega_{\rm A}} \int\int_{4\pi} T_{\rm B}(\Omega)\, d\Omega = \frac{\eta_{\rm R} \times \eta_{\rm CAL}}{\Omega_{\rm A}} \times \frac{\lambda^2 \times S_\lambda}{2k \times 10^{26}} \quad [{\rm K}] \tag{4.6}$$

where S_λ is the source flux in jansky and k is Boltzmann's constant. This equation shows that the factor in equation 4.5 can be obtained by measuring the peak excess antenna temperature, $T_{\rm A}$, produced by a point-like source with known flux S_λ transiting the beam. A commonly quoted figure of merit used to characterise the performance of an antenna is the *point source sensitivity* (PSS) which is the ratio of point source flux to excess antenna temperature. Rearranging equation 4.6 and using equation 4.2 results in an expression for the PSS:

$${\rm PSS} = \frac{S_\lambda}{T_{\rm A}} = \frac{2k \times 10^{26}}{\eta_{\rm CAL} \times \eta_{\rm R} \times A_{\rm G}} = \frac{2k \times 10^{26}}{A_{\rm E}} \quad [{\rm Jy/K}] \tag{4.7}$$

where the *effective aperture* of the antenna

$$A_{\rm E} = \eta_{\rm CAL} \times \eta_{\rm R} \times A_{\rm G} = \eta_{\rm CAL} \times \eta_{\rm R} \times \eta_{\rm G} \times A_{\rm P} \quad [{\rm m}^2] \tag{4.8}$$

has been introduced. Defined in this way the effective aperture is a somewhat fictitious measure of area because it contains the error-propagation factor $\eta_{\rm CAL}$; nevertheless, it is a useful quantity since equation 4.4 is conveniently rewritten in terms of $A_{\rm E}$:

$$T_{\rm A}(\Omega_0) = \frac{A_{\rm E}}{\lambda^2} \int\int_{4\pi} T_{\rm B}(\Omega) P_{\rm N}(\Omega_0 - \Omega) d\Omega \quad [{\rm K}] \tag{4.9}$$

Thus the value for the PSS (and hence $A_{\rm E}$) and the form of $P_{\rm N}(\Omega)$ provide sufficient information to determine the relationship between the measured antenna temperature scale and the Rayleigh-Jeans sky brightness temperature scale.

Routine measurements of the $\lambda = 13$ cm PSS were made at HartRAO as part of a long-term programme to monitor the fluxes of variable extragalactic sources. These measurements consistently yielded a PSS value of 9.5 Jy/K (Nicolson, private communication) over the period of the *SKYMAP* observations. This consistency confirms that the changes in the beam shape illustrated by figure 4.2 had no measurable effect on the antenna gain. Although the stepped-pointing technique that was used for the flux monitoring programme produced internally self-consistent results, it was felt that the technique did not yield a precise value for the PSS. In order to obtain a more precise determination of the PSS, mapping observations were made of small areas of sky towards the three strong standard calibrator sources Vir A, Her A and Tau A. These observations were made in June 1996 (the Tau A observations were described in section 4.1).

All of these small-area maps were at least 2° by 2° in extent, so as to include the first two sidelobes of the beam pattern and allow the reliable determination of a background surface. The beam was well-sampled in all cases, with the scan spacing and bin widths being 0.05° or less. The new HartRAO antenna control system (Jonas, 1991) was used for these observations, which allowed the scans to be made in a orthographic coordinate projection (Greisen and Calabretta, 1997) centred on the respective source positions. Three maps were made of Vir A, and one each of Her A and Tau A. The total integration time for each map was chosen so that the relative uncertainty in the peak amplitude was less than 1%.

Maps constructed from these scanning observations were inspected visually, and bad pixels were edited out of the data. Second-order polynomial base surfaces were fitted to the edge regions of the images using a simple least-squares procedure. These base surfaces were then subtracted, and the peak amplitudes of the residual source images were determined by fitting bivariate gaussian surfaces to the central nine pixels of each residual map.

Table 4.2 is a summary of the results obtained from these observations. The assumed source fluxes were calculated from the formulae given by Ott et al. (1994). Small correction factors, $\eta_{\rm SS} > 1$, were applied to the measured antenna temperatures to account for signal attenuation caused by the finite angular extent of the sources. Ott et al. (1994) give angular sizes for Vir A and Her A, and the extent of Tau A was obtained from Baars et al. (1977). The adopted average of 9.8 Jy/K for the PSS was strongly influenced by the Vir A measurements and the low value obtained by Nicolson's long-term monitoring. Using this figure results in an effective aperture of

$$A_{\rm E} = 282 \pm 6 \ \ [{\rm m}^2] \tag{4.10}$$

which corresponds to an aperture efficiency of

$$\eta_{\rm A} = \frac{A_{\rm E}}{A_{\rm P}} = \eta_{\rm CAL} \times \eta_{\rm R} \times \eta_{\rm G} = \frac{282}{531} = 53 \pm 1 \ \ [\%]$$

Source	$T_{\rm A}$ [K]		$\eta_{\rm SS}$		S_λ [Jy]	PSS [Jy/K]
Nicolson's result						9.5
Herc A	2.79	×	1.01	=	28.1	9.9
Vir A (average of 3)	13.68	×	1.03	=	138.2	9.8
Tau A	79.52	×	1.03	=	812.5	9.9
Adopted average						9.8 ± 0.2

Table 4.2: A summary of the measurements made of the point source sensitivity that are described in the text. The source fluxes, S_λ, were derived from the formulae of Ott et al. (1994).

The value for the effective aperture that was obtained using the PSS technique was independently confirmed using the moon as a reference source. An orthographic coordinate projection map of a $2^\circ \times 2^\circ$ region centred on the moon was made using a scan spacing and binning width of $6'$, resulting in a 21×21 pixel image. For comparison, a model image of the $\lambda = 13$ cm lunar brightness distribution was computed by scaling the brightness temperatures of a published $\lambda = 3.55$ cm model of the full moon (Keihm and Gary, 1979). A temperature scaling factor of $\frac{220}{213}$ was determined from tables of disc-averaged lunar brightness temperatures at various centimetre wavelengths (Keihm and Langseth, 1975; Krotikov and Pelyushenko, 1987). The pixel size for this model was $2' \times 2'$.

Numerical calculation of equation 4.9 was performed to convolve the model lunar brightness temperature with the normalized beam pattern shown in figure 4.1. The value quoted in equation 4.10 was used for $A_{\rm E}$. The resulting image, representing the predicted antenna

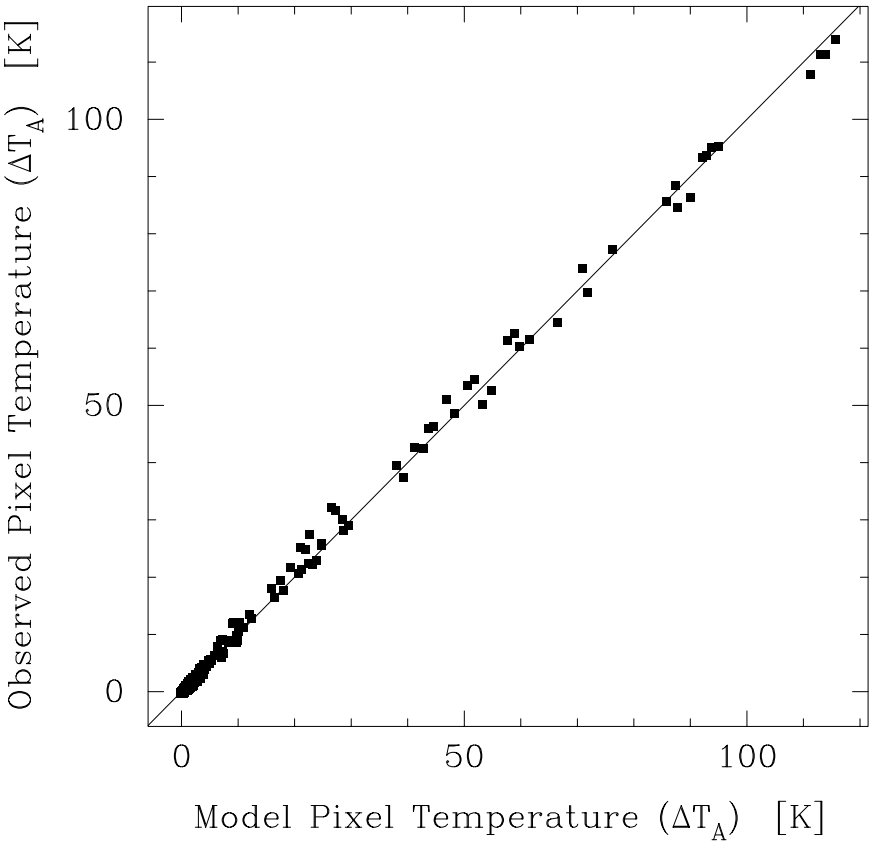

Figure 4.3: A pixel-by-pixel T-T plot of model (predicted) and observed excess antenna temperatures for the moon. A line with a slope of unity has been drawn through the data points.

temperature distribution, was sub-sampled onto a $6' \times 6'$ grid to match the pixel spacing of the observed data array. Figure 4.3 is a pixel-by-pixel comparison (T-T plot) of the model and the observed antenna temperature distributions, indicating excellent agreement between the predicted and measured antenna temperatures. The success of this comparison confirmed that the measurements of $A_{\rm E}$ and $P_{\rm N}(\Omega)$ were reliable.

4.4 The Beam Efficiency

Further examination of the beam polar pattern is required to determine a practical brightness temperature scale for the survey maps. In particular it is necessary to examine how the partial solid angle subtended by the beam pattern increases as a function of radius from the beam centre. For this analysis the *beam efficiency* function is introduced, which is defined to be:

$$\eta_{\Omega}(\theta) \equiv \eta_{\rm R} \times \eta_{\rm CAL} \times \frac{\Omega_{\rm a}(\theta)}{\Omega_{\rm A}} \tag{4.11}$$

where the partial beam solid angle $\Omega_{\rm a}(\theta)$ is defined by equation B.2 in appendix B. This beam efficiency may be measured by the numerical integration of maps of point-like sources

with known flux, since:

$$\eta_\Omega(\theta) = \frac{S(\theta)}{S_\lambda} \tag{4.12}$$

by rearrangement of equation B.10 in appendix B.

The Tau A map described in previous sections was used to examine the behaviour of $\eta_\Omega(\theta)$ out to a radius of integration of 2.5°. Beyond this limit the inevitable uncertainties in the base level of the map caused divergence of the integral as the solid angle limit increased. To explore the behaviour of $\eta_\Omega(\theta)$ beyond this limit required a much stronger source so that baseline errors became negligible. Equation B.13 and its derivation in appendix B provide justification for using the sun as a suitable source for examining the stray response of the beam.

Two orthogonal horizon-to-horizon scans were made through the sun to obtain some knowledge of the stray, forward sidelobes of the beam. From this investigation it was established that a $16° \times 16°$ map centred on the sun would include all of the measurable forward sidelobes, and such a map was observed in June 1996. Special care had to be taken to ensure that the radiometer response remained linear when scanning through the solar disk. Equation B.13 could not be used directly to calculate $\eta_\Omega(\theta)$ from the resulting radio image since the sun does not have a well-defined, constant flux. In order to obtain a reliable estimate of $\eta_\Omega(\theta)$ for $0° < \theta < 8°$ a combined analysis of the Tau A and solar images had to be performed.

The Tau A map and the sun map provided complementary information, but both maps had missing information:

- The 2326 MHz flux of Tau A, S_{Tau}, was known and was calculated using the formula given by Ott et al. (1994). However, the Tau A map had a small unknown base level offset, ΔT_{Tau}, which caused instability in the flux integration required to calculate $\eta_\Omega(\theta)$. If this offset were known then the Tau A map would produce a reliable estimate of $\eta_\Omega(\theta)$ for $\theta < 2.5°$.

- Base level errors for the sun map were negligible because of the strength of the source. However, the flux of the sun, S_{Sun}, was unknown which prevented the use of equation 4.12 for calculating $\eta_\Omega(\theta)$. If the value for the solar flux were known then the sun map would produce a reliable estimate of $\eta_\Omega(\theta)$ for $\theta > 2°$ (see equation B.13).

A least squares solution for the two unknown parameters was found by minimizing the

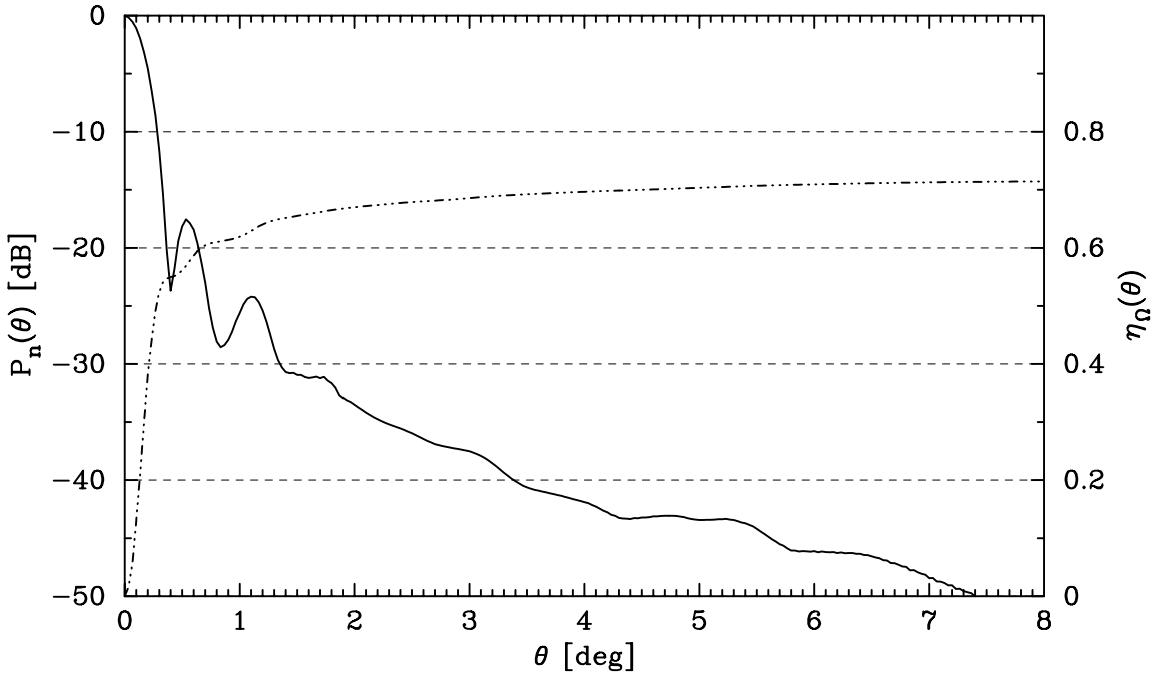

Figure 4.4: The radial characteristics of the HartRAO beam at $\lambda = 13$ cm derived from radio images of Tau A and the sun, as described in the text. The solid line represents the azimuthally averaged beam response, $P_{\rm n}(\theta)$, while the chained line traces the beam efficiency, $\eta_\Omega(\theta)$.

following quantity:

$$\chi^2(S_{\rm Sun}, \Delta T_{\rm Tau}) = \int_{2.0^\circ}^{2.5^\circ} \left[\int_0^\theta \int_0^{2\pi} \left(\frac{T_{\rm Sun}(\Omega)}{S_{\rm Sun}} - \frac{T_{\rm Tau}(\Omega) + \Delta T_{\rm Tau}}{S_{\rm Tau}} \right) d\Omega \right]^2 d\theta \quad (4.13)$$

where $T_{\rm Sun}(\Omega)$ and $T_{\rm Tau}(\Omega)$ were the antenna temperatures from the sun and Tau A maps respectively. This optimization matched the two independent estimates of $\eta_\Omega(\theta)$ over an intermediate range of θ where both maps were capable of providing a reasonable estimate. The solar flux obtained was $S_{\rm Sun} = 590000$ Jy, and the offset in the Tau A map was determined to be $\Delta T_{\rm Tau} = +25$ mK (i.e. 0.03% of the peak antenna temperature).

The graph in figure 4.4 shows the estimate of $\eta_\Omega(\theta)$ that resulted from this combined analysis of the Tau A and solar maps. The Tau A image (including the offset $\Delta T_{\rm Tau}$) was used for $0^\circ \leq \theta \leq 2^\circ$, and the solar image for $2^\circ \leq \theta \leq 8^\circ$. Also shown in this diagram is the azimuthally averaged beam pattern, defined by:

$$P_{\rm n}(\theta) = \frac{1}{2\pi} \int_0^{2\pi} P_{\rm N}(\phi, \theta)\, d\phi \quad (4.14)$$

The *main-beam efficiency* of an antenna is defined to be the value of $\eta_\Omega(\theta)$ for θ equal to the radius of the first null in the beam pattern. For the HartRAO antenna operating at $\lambda = 13$ cm the main-beam efficiency was:

$$\eta_{\rm MB} = 55 \pm 1 \ [\%] \quad (4.15)$$

as determined from the curve in figure 4.4.

From figure 4.4 it is apparent that the curve tracing $\eta_\Omega(\theta)$ becomes nearly horizontal as θ increases beyond 3° and that the sidelobe response traced by $P_{\rm n}(\theta)$ decreases monotonically with θ. The asymptotic trend by $\eta_\Omega(\theta)$ towards a value that is less than unity implies one or more of the following:

1. The beam polar pattern, $P_{\rm N}(\phi,\theta)$, had stray response in the form of diffractive, spillover and scattering sidelobes for $\theta > 8°$. The stray pattern has been well studied for other radio telescopes, and it has been shown (Anderson et al., 1991; Hartmann et al., 1996; Baars, 1973) that it can account for up to 30% of the total beam solid angle.

2. There were dissipative losses in the antenna and feed system, i.e. $\eta_{\rm R} < 1$.

3. The measurement of the excess antenna temperature of the calibration noise diode was in error, i.e. $\eta_{\rm CAL} \neq 1$. This systematic error factor has a similar effect to $\eta_{\rm R}$, and these two efficiency factors can be lumped together.

It will be shown in section 4.6 that it was not necessary to distinguish between these effects in order to determine a useful temperature scale for the survey data.

4.5 The Map Beam

The preceding analysis of the HartRAO telescope beam has relied on supplementary observations and data processing that were independent of the *SKYMAP* observation process. It is necessary to investigate how the *SKYMAP* processes may have affected the beam shape and to check whether the results from the previous sections can be applied to the survey maps. The most convenient way of examining the *map beam* was to analyze the images of the point-like cosmic radio sources present in the maps. In particular the PSS and main-beam efficiency derived from these images were used as diagnostics for comparing the map beam to the actual antenna beam pattern. In this section it will be shown that, except for two maps, the beam characteristics were well preserved by the observation and data processing procedures.

The *SKYMAP* survey was designed to study extended radio sources, rather than point sources, so the effective integration time for individual sources of small angular extent was very short. There are only six sources in the Ott et al. (1994) list of flux density calibrators

Source	Parkes Flux [Jy]	Ott et al. Flux [Jy]	Ratio Ott et al. / Parkes
0624-058	12.55	12.68	1.01
0915-118	26.78	26.64	0.99
0945+076	4.59	4.92	1.07
1228+126	137.36	136.96	1.00
1648+050	26.77	27.74	1.04
1717-009	39.24	36.63	0.98

Table 4.3: A comparison of the 2326 MHz fluxes calculated for six standard calibrator sources using two different methods: (a) Quadratic interpolation of the 1410 MHz, 2700 MHz and 5000 MHz fluxes quoted in the Parkes catalogue (PKSCAT90, 1990). (b) Evaluation of the formulae given by Ott et al. (1994).

that fall within the survey limits, therefore any parameters derived from images of these few sources would be subject to large statistical errors, and not every map would be covered. To improve the measurement statistics, all Parkes sources (PKSCAT90, 1990) with fluxes above a 3 Jy threshold that fell within the boundaries of the survey were used as reference sources.

A quadratic continuum spectrum was fitted to each source in the Parkes catalogue that had 1410 MHz, 2700 MHz and 5000 MHz fluxes recorded. Sources that did not have measurements for all three frequencies and sources that lay outside the survey limits were discarded at this stage. This quadratic spectrum was used to interpolate a nominal value for the 2326 MHz flux of each remaining source and those with fluxes above a 3 Jy threshold were extracted. Many of the sources are intrinsically variable, but the effects of this variability should have been averaged out because of the large source populations that were used.

Table 4.3 uses six standard calibrator sources to compare the 2326 MHz flux scale derived from the Parkes catalogue with the Ott et al. (Ott et al., 1994) scale. This comparison shows that the two flux scales are equivalent to the required precision.

A FORTRAN program, `CAL.FOR`, was written to analyze the images of the selected Parkes sources in each of the ten *SKYMAP* maps. Each map was processed independently so that systematic differences between the maps could be measured. Sub-images of the selected Parkes sources were extracted from the maps, and these sub-images were noise-filtered and flat-fielded (see sections 4.7 and 4.8 for descriptions of these processes). The peak antenna temperature was obtained for each sub-image by fitting a gaussian beam

surface to the central nine pixels. The "main-beam" partial flux for each source was computed by numerical integration of the sub-image out to a small-circle radius of 0.4° (i.e. the first null of the beam).

4.5.1 Point Source Sensitivity

Figure 4.5 shows scatter plots of measured peak antenna temperature versus Parkes flux for the ten *SKYMAP* maps. For each plot the solid diagonal line is the expected locus for PSS = 9.8 Jy/K, the value obtained for the point source sensitivity in section 4.3. The dashed lines above and below the solid line indicate the effects of a variation of ±10% in this value.

Apart from the map A12D63, there is good agreement between the effective map PSS and the intrinsic antenna PSS. This implies that the mapping process causes very little smoothing of the beam, which would have had the effect of broadening the beam shape and reducing the peak height. The reduction in the peak temperatures that is evident in the A12D63 map is due to a running median filter that was present in Mountfort's early version of the data reduction software (see section 3.1). This non-linear digital filter had the effect of truncating the peaks of point sources without broadening the beam shape.

4.5.2 Main-Beam Efficiency

Figure 4.6 is a compilation of scatter plots of the measured main-beam partial flux versus Parkes flux for the ten survey maps. The diagonal line in each plot corresponds to $\eta_{\mathrm{MB}} = 55\%$, the value obtained for the main-beam efficiency in section 4.4. The dashed lines above and below this line represent a variation of ±10% in this efficiency value.

All of the maps except A23D80 appear to be consistent with a main-beam efficiency of 55%. This implies that the beam shape has not been significantly changed by the data processing, and that no systematic change has been made to the flux scale. The apparent excess in the main-beam efficiency for the A23D80 map results from the broadening of all of the point sources in the declination direction. This broadening probably results from residual antenna pointing errors that existed for the low declination range at the time of the observations. Note that the clipping of the beam for the A12D63 map has not affected the main-beam efficiency. This is to be expected since very little flux is lost by the attenuation of just one pixel in the main-beam.

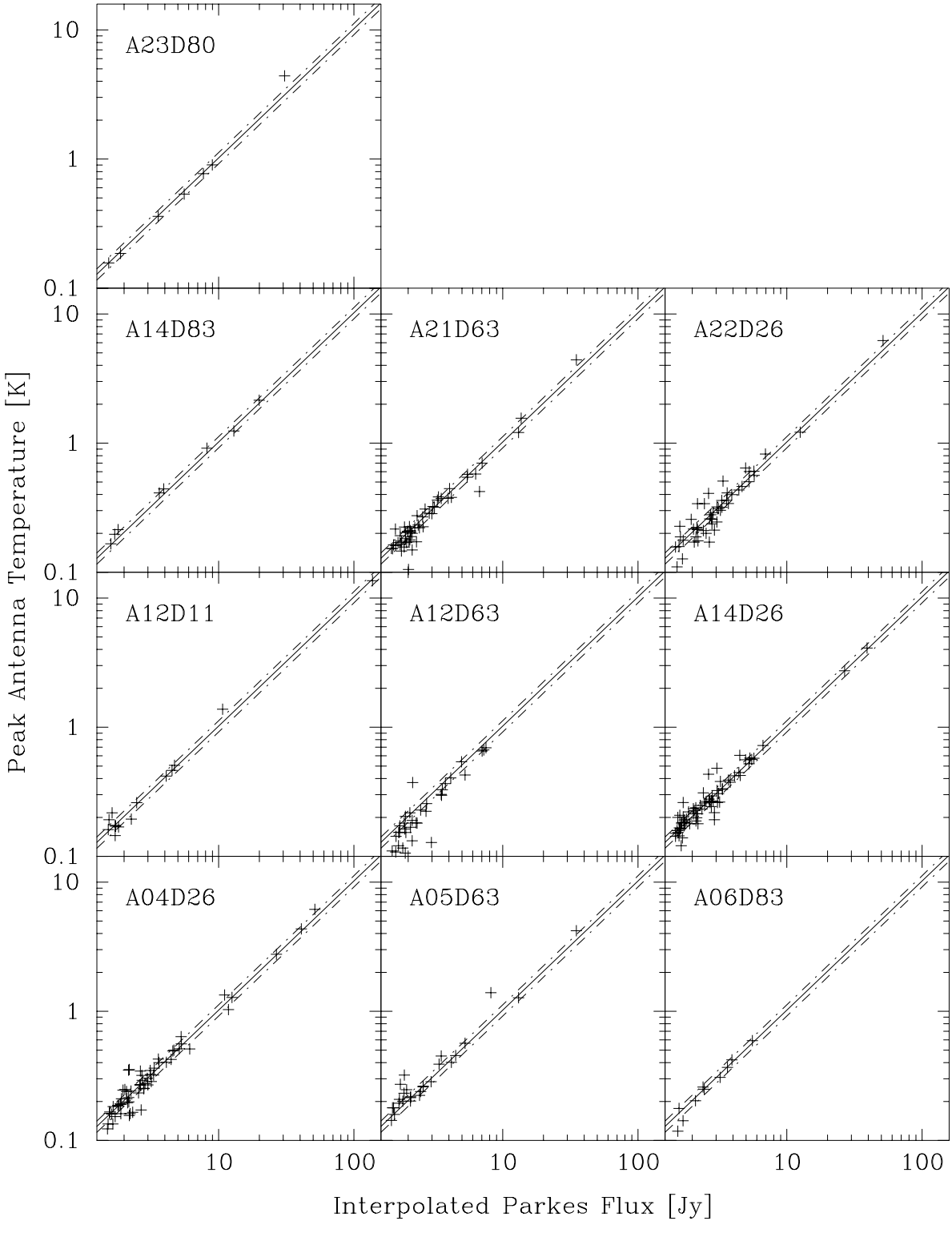

Figure 4.5: Scatter plots of measured excess antenna temperature versus nominal source flux for point sources in the 10 *SKYMAP* maps. Sources with 2326 MHz fluxes above a threshold of 3 Jy were extracted form the Parkes catalogue for this analysis. The solid diagonal line represents a point source sensitivity (PSS) of 9.8 Jy/K. The dashed lines indicate a ±10% variation on this value. Logarithmic scales have been used for both the flux and temperature axes to help equalize the distribution of data points.

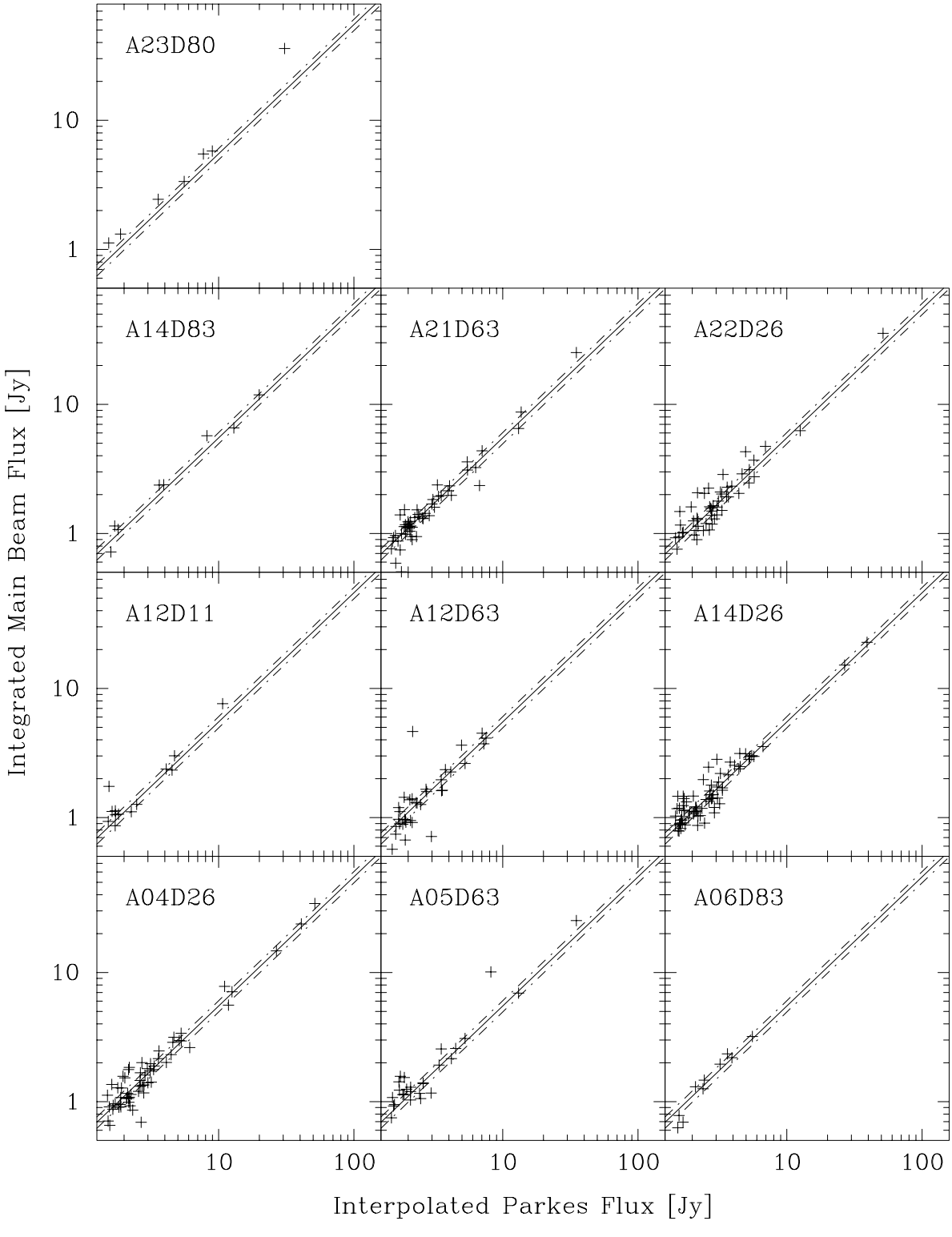

Figure 4.6: Scatter plots of measured main-beam partial flux versus nominal source flux for point sources in the 10 *SKYMAP* maps. Sources with 2326 MHz fluxes above a threshold of 3 Jy were extracted form the Parkes catalogue for this analysis. The solid diagonal line represents a main-beam efficiency of 55%. The dashed lines indicate a ±10% variation on this value. Logarithmic scales have been used for both the flux and temperature axes to help equalize the distribution of data points.

4.6 The Full-Beam Temperature Scale

The excess antenna temperature scale used during the observation and initial data reduction of the *SKYMAP* survey has two serious shortcomings:

- The relationship between the antenna temperature and intrinsic sky temperature is very telescope-dependent.
- The observing and data reduction procedures subtract out an arbitrary base level, which eliminates all absolute brightness information from the radio images.

It is common practice to define a *full-beam brightness temperature* scale for radio continuum maps, which attempts to address these problems. This section describes the development of the full-beam brightness temperature scale appropriate for the *SKYMAP* 2326 MHz survey.

The transformation between the relative antenna temperature scale and the absolute full-beam temperature scale is assumed to have this simple linear form:

$$T_{\rm FB}(\Omega_0) = \frac{T_{\rm A}(\Omega_0)}{\eta_{\rm FB}} + T_{\rm OFF} \quad [\rm K] \tag{4.16}$$

where $\eta_{\rm FB}$ and $T_{\rm OFF}$ are two parameters that need to be determined. $\eta_{\rm FB}$ is a factor that corrects for instrumental effects such as dissipative losses in the antenna and feed system, mis-calibration of the noise diode, and extended structure in the beam pattern. $T_{\rm OFF}$ is an offset that reinstates the isotropic temperature distribution due to the cosmic microwave background, unresolved extragalactic sources and the diffuse Milky Way emission.

4.6.1 Determination of $\eta_{\rm FB}$

The inversion of the convolution integral in equation 4.4 to obtain intrinsic sky brightness temperatures is neither feasible nor necessary for most quantitative astrophysical investigations, although early low-resolution surveys did attempt such deconvolution (Bolton and Westfold, 1950; Allen and Gum, 1950; Turtle and Baldwin, 1962; Pauliny-Toth and Shakeshaft, 1962; Landecker and Wielebinski, 1970). A working compromise is to define a temperature scale ($T_{\rm FB}$) that has the following properties:

- The brightness temperature of extended radio sources is given directly by $T_{\rm FB}$.

- The flux of any radio source may be obtained by numerical computation of the following integral:

$$S_\lambda = \frac{2k \times 10^{26}}{\lambda^2} \iint_{\Omega_{\rm Int}} T_{\rm FB}\, d\Omega \quad [\rm Jy] \tag{4.17}$$

where $\Omega_{\rm Int}$ extends beyond the intrinsic source solid angle by no more than a few beamwidths.

Such a temperature scale allows consistent and meaningful numerical comparison with other astrophysical brightness distribution maps (including other radio continuum surveys), irrespective of the resolution of the comparison maps. This consistency is particularly important when determining the spectral index of the extended galactic emission and examining the galactic contamination of cosmic microwave background data.

Examination of figure 4.4 reveals that for $\theta > 3.5°$, the average beam response of the HartRAO antenna falls below -40 dB, and that the partial beam efficiency increases very slowly beyond this radius. This inner region of the beam pattern is traditionally called the *full-beam* which is a rather ambiguous term. The remainder of the beam pattern is called the *stray pattern.*

Defining the radius of the full-beam to be $\theta_{\rm FB}$, the integral in equation 4.4 may be split into two components:

$$\begin{aligned} T_{\rm A}(\Omega_0) &= \frac{\eta_{\rm R} \times \eta_{\rm CAL}}{\Omega_{\rm A}} \int_0^{\theta_{\rm FB}} \int_0^{2\pi} T_{\rm B}(\Omega)\, P_{\rm N}(\Omega_0 - \Omega)\, d\Omega \\ &+ \frac{\eta_{\rm R} \times \eta_{\rm CAL}}{\Omega_{\rm A}} \int_{\theta_{\rm FB}}^{\pi} \int_0^{2\pi} T_{\rm B}(\Omega)\, P_{\rm N}(\Omega_0 - \Omega)\, d\Omega \quad [\rm K] \end{aligned} \tag{4.18}$$

After some substitution (see appendix B) this equation may be rewritten:

$$T_{\rm A}(\Omega_0) = \left[\frac{\eta_\Omega(\theta_{\rm FB})}{\Omega_{\rm a}(\theta_{\rm FB})} \int_0^{\theta_{\rm FB}} \int_0^{2\pi} T_{\rm B}(\Omega)\, P_{\rm N}(\Omega_0 - \Omega)\, d\Omega \right] + T_{\rm STRAY}(\Omega_0) \quad [\rm K] \tag{4.19}$$

where the first term is the response of the full-beam to the sky brightness distribution and $T_{\rm STRAY}(\Omega_0)$ is the response of the stray beam to the sky brightness distribution. If the extent of the full-beam is sufficient to include all significant sidelobe structures then the spatial variation of $T_{\rm STRAY}(\Omega_0)$ resulting from the response to celestial sources is very small because of the nearly isotropic distribution and very attenuated response of the stray beam. In practice $T_{\rm STRAY}(\Omega_0)$ is strongly dependent on antenna elevation angle because of the illumination of the stray pattern by the ≈ 300 K emission from the ground surrounding the antenna. The *SKYMAP* data reduction processes described in chapter 3 subtracted out the position-dependent terrestrial foreground emission together with all of the isotropic

contributions to the antenna temperature. As a result, the composite *SKYMAP* map of the southern sky resulting from the processing described in chapter 3 can be represented by the following slightly modified form of equation 4.19:

$$T_{\rm A}(\Omega_0) = \left[\frac{\eta_\Omega(\theta_{\rm FB})}{\Omega_{\rm a}(\theta_{\rm FB})}\int_0^{\theta_{\rm FB}}\int_0^{2\pi} T_{\rm B}(\Omega)\, P_{\rm N}(\Omega_0-\Omega)\, d\Omega\right] - T_{\rm ISO} \quad [{\rm K}] \tag{4.20}$$

where $T_{\rm ISO}$ is an unknown isotropic temperature component. By choosing:

$$\eta_{\rm FB} = \eta_\Omega(\theta_{\rm FB}) \tag{4.21}$$

for the value of the temperature conversion factor in equation 4.16 and performing some manipulation, the following relationship results:

$$T_{\rm FB}(\Omega_0) = \left[\frac{1}{\Omega_{\rm FB}}\int_0^{\theta_{\rm FB}}\int_0^{2\pi} T_{\rm B}(\Omega)\, P_{\rm N}(\Omega_0-\Omega)\, d\Omega\right] + \left[T_{\rm OFF} - \frac{T_{\rm ISO}}{\eta_{\rm FB}}\right] \quad [{\rm K}] \tag{4.22}$$

where

$$\Omega_{\rm FB} = \Omega_{\rm a}(\theta_{\rm FB}) \tag{4.23}$$

is conventionally called the *full-beam solid angle*. Using results from appendix B it may be shown that the relationship between $T_{\rm FB}$ and $T_{\rm B}$ given in equation 4.22 satisfies the temperature and flux requirements stated at the beginning of this section.

There is no single consistent definition for the extent of the full-beam in the literature. Seeger, Westerhout and van de Hulst (1956) suggested a circle with diameter 5 times the half-power beamwidth (HPBW), a convention that was used in other early surveys (Westerhout, 1958; Mathewson et al., 1962a). Reich (1982) estimated that the full-beam of the Stockert antenna at $\lambda = 21$ cm extended out to a diameter of 7°, or 12 times the HPBW, when calibrating the Bonn 1420 MHz survey. Berkhuijsen (1972) used Higgs' (1967) dimensions of $7.2° \times 10.0°$ for the full-beam of the Dwingeloo antenna when calibrating her 820 MHz survey of the northern sky, which corresponds to an extent of more than 7 times the HPBW. Definition of the full-beam for the 408 MHz survey was more difficult because three different telescopes were used, but the full-beam of the Jodrell Bank Mark I antenna was assumed to extend to where the polar pattern dropped below −26 dB (Haslam et al., 1970).

A full-beam diameter of 7° was adopted for the *SKYMAP* survey because this value satisfies the following criteria which are necessary for the above analysis to be valid:

- All of the major diffraction sidelobes and small-scale structures of the $\lambda = 13$ cm beam are contained within a radius of $\theta = 3.5°$.

- The partial beam efficiency, $\eta_\omega(\theta)$, increases very slowly beyond $\theta = 3.5°$.

This value is also consistent with the full-beam extent used for the 1420 MHz survey of the northern sky. The beam efficiency curve in figure 4.4 yields a full-beam efficiency of $\eta_{\rm FB} = 69\%$ for a full-beam radius of $\theta_{\rm FB} = 3.5°$. This results in a temperature scale conversion factor of:

$$\frac{1}{\eta_{\rm FB}} = \frac{1}{0.69} = 1.45 \pm 0.03 \tag{4.24}$$

for the *SKYMAP* data. The error estimate corresponds to a 2% uncertainty in the computation of $\eta_\Omega(\theta)$.

4.6.2 Determination of $T_{\rm OFF}$

Having determined the value of the scaling factor, it was necessary to obtain a value for the temperature offset term in equation 4.16. From equation 4.22 it is clear that the required value for the offset temperature is:

$$T_{\rm OFF} = \frac{T_{\rm ISO}}{\eta_{\rm FB}} \tag{4.25}$$

There was no way of using the *SKYMAP* data to determine $T_{\rm ISO}$, so the data from independent observations had to be used to measure $T_{\rm OFF}$.

Bersanelli et al. (1994) have made absolute sky temperature measurements at 2 GHz from the geographic south pole using a horn antenna with well-behaved sidelobes (Bersanelli et al., 1992). Their results include an absolute temperature measurement of the southern equatorial pole (SEP) and drift scans made at $-40°$, $-50°$ and $-60°$ declination. These drifts scans were recorded as brightness temperatures relative to the SEP. A joint analysis of the *SKYMAP* data and these absolutely calibrated measurements was used to determine an absolute temperature scale for the survey data.

The 2326 MHz *SKYMAP* map was scaled to a 2 GHz full-beam brightness scale by assuming a Galactic synchrotron spectral index of $\beta_{\rm syn} = 2.75$. These scaled data were convolved with the beam pattern of the "extended horn" used for the South Pole experiment (Bersanelli, private communication). The thermal sources in the Galactic plane were estimated to introduce errors of less than 5% in the scaled data because of their flatter spectra. A simple least-squares procedure was used to adjust the zero-point of the survey data to match that of the differential drift scan data. This base level adjustment resulted in a temperature scale with its zero point at the SEP. These adjusted data were called

the SEP-referenced survey data. Figure 4.7 compares the adjusted survey data with the differential horn measurements. The two data sets are seen to be in fair agreement, particularly at $-60°$ declination. Deviations at the other declinations indicate a maximum baseline error of 50 mK T_{FB} in the SEP-referenced survey data.

The T-T plots in figure 4.8 show that the relative temperature scales of the two data sets are mutually consistent (assuming $\beta_{syn} = 2.75$), providing further independent confirmation of the reliability of scale factor determined in section 4.6.1. The plots clearly show that the relative temperature scales of the two independent data sets are very compatible, if the assumed synchrotron spectral index is correct. Even if this index were in error by ± 0.1, the slope of the lines drawn in figure 4.8 would only change by $\pm 1.5\%$.

The residual baseline offsets in the survey data that are evident in figure 4.7 are also evident in these T-T plots: the points lie in straight lines with the expected slope, but there is no unique intercept that all of these lines would pass through. The baseline errors are seen to increase northwards from $\delta = -60°$. This trend is to be expected given the procedure described in section 3.2 that was used to correct the baselines of each of the ten constituent maps. The southern boundary of the *SKYMAP* survey encloses a very small patch of unobserved sky that is relatively cold and featureless. Errors on the baseline at this extreme southern declination are unlikely to be large. It is quite likely that the efficacy of the terrestrial foreground subtraction technique was compromised by the lack of true cold sky, which would result in anomalous gradients in the resulting maps. These twists and gradients in the maps amplify the baseline uncertainty towards the north, particularly when crossing the Galactic plane. Absolute measurements of the sky temperature at 2297 MHz have been made at $+34°$ declination with an uncertainty of 0.77 K (Otoshi and Stelzried, 1969a; Otoshi and Stelzried, 1969b; Otoshi and Stelzried, 1975), but these measurements lack the required accuracy and are too far beyond the northern limit of the *SKYMAP* survey for meaningful baseline comparisons to be made.

Bersanelli et al. (1994) have determined the non-cosmological component of the SEP sky temperature to be 0.32 K at 2 GHz. This value is the sum of a 0.29 K Galactic component and a 0.03 K contribution from unresolved extragalactic sources. Assuming $\beta_{syn} = 2.75$, the Galactic component scales to 0.19 K at 2326 MHz. This value was added to the SEP-referenced survey data. The zero-point of the resulting temperature scale was therefore offset by the absolute temperature of the isotropic radiation due to the cosmic microwave background and unresolved extragalactic sources. A conservative estimate of

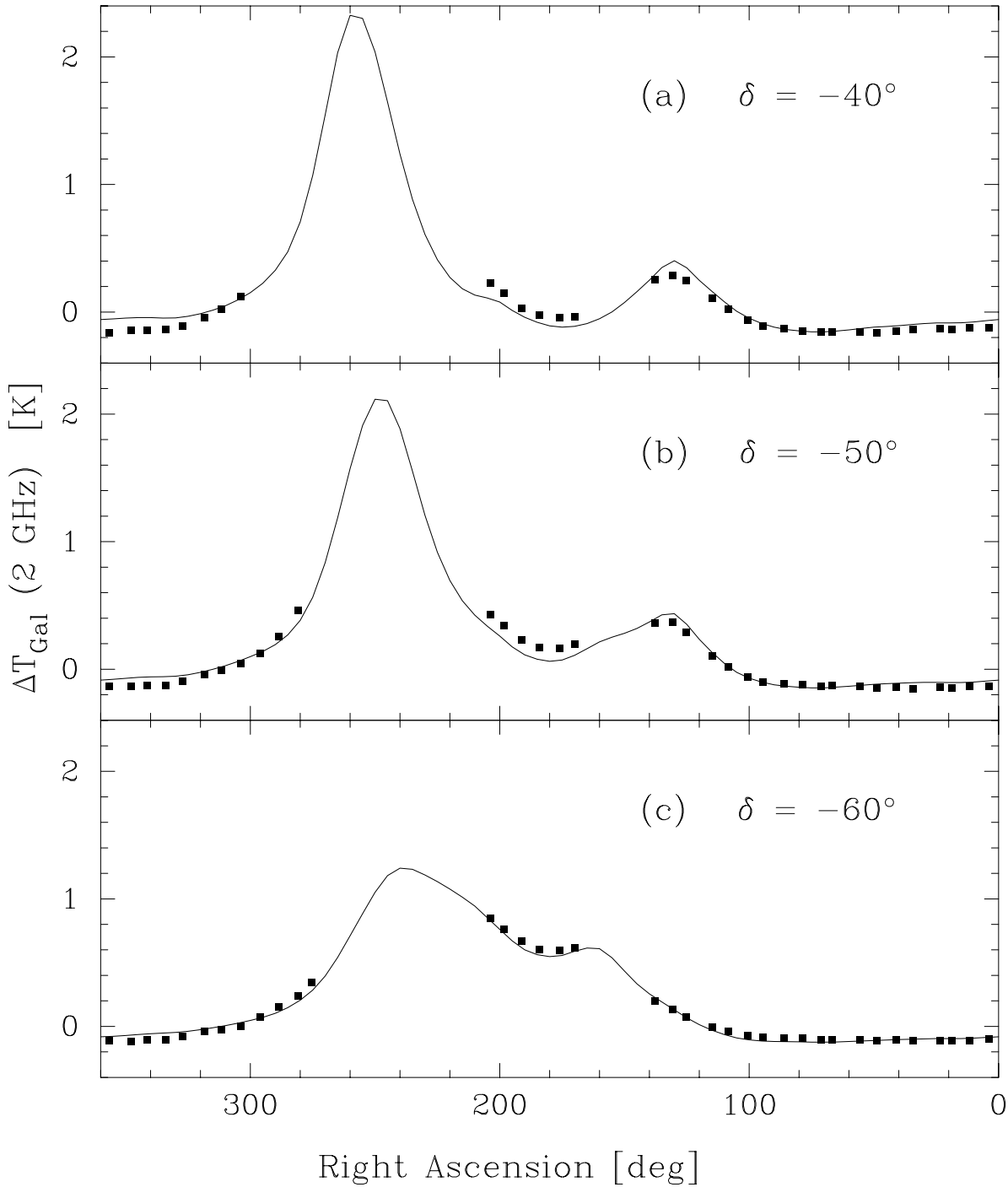

Figure 4.7: Differential Galactic emission at 2 GHz between $\delta = -90°$ and (a) $\delta = -40°$, (b) $\delta = -50°$, and (c) $\delta = -60°$. The filled squares are the differential sky temperatures measured by Bersanelli et al. (1994) using their "extended horn" antenna. The solid line was obtained by scaling the SEP-referenced survey data to 2 GHz (assuming $\beta_{\rm syn} = 2.75$) and numerically convolving the scaled data with the horn antenna beam pattern. The gaps in the right ascension coverage of the horn data are due to solar interference and equipment failure.

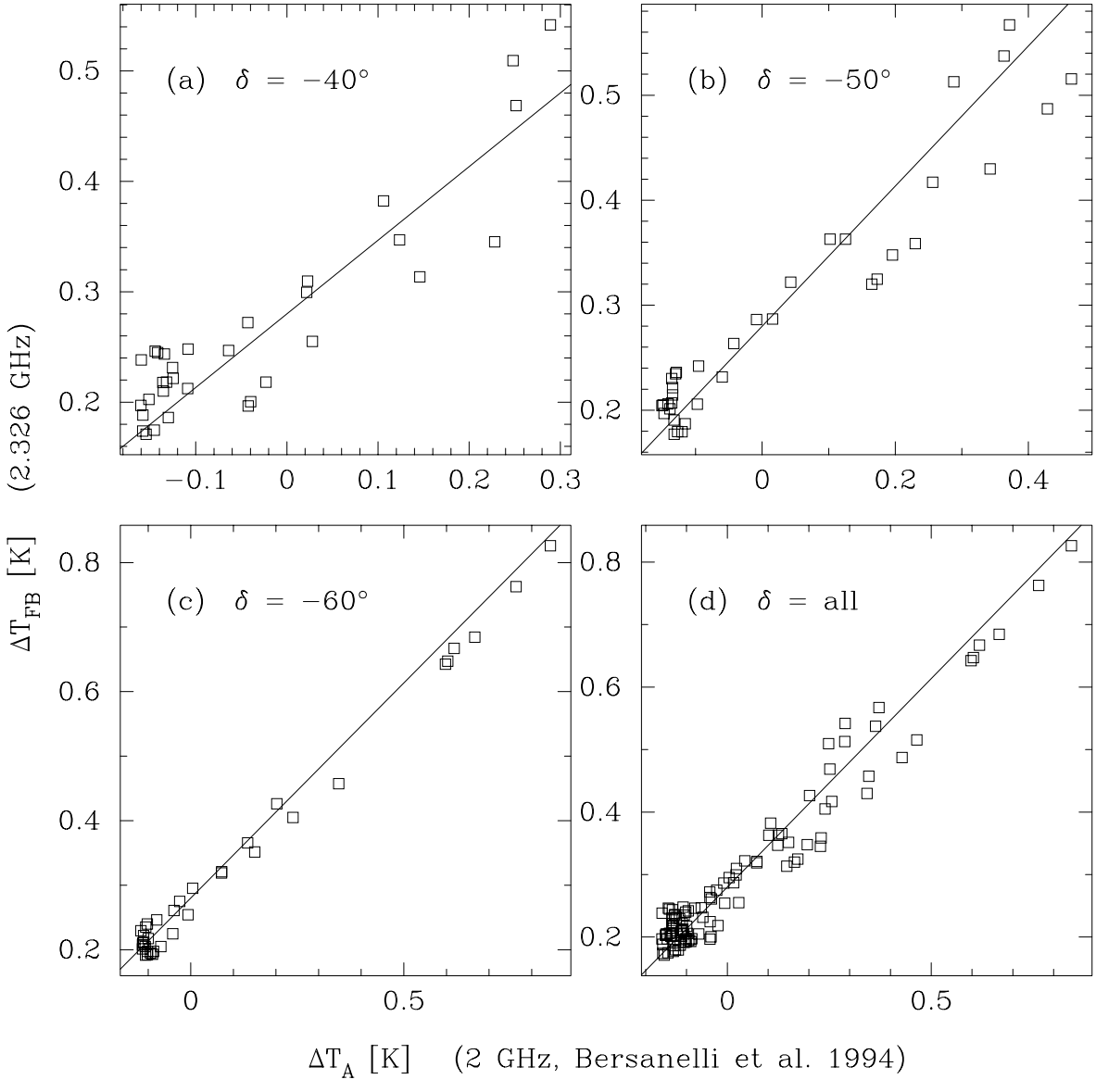

Figure 4.8: T-T plots comparing the differential Galactic emission at 2 GHz as measured by Bersanelli et al. (1994) with the 2.3 GHz survey data smoothed to the same resolution as the horn data. The first three panels represent scans at declinations of: (a) $\delta = -40°$, (b) $\delta = -50°$, and (c) $\delta = -60°$, while panel (d) is a compilation of all three declinations. In all panels the diagonal line is the locus expected for a galactic synchrotron spectral index of $\beta_{\rm syn} = 2.75$. These lines are not regression lines.

the baseline uncertainty for the current version of the survey data is 80 mK. This value was obtained by compounding the estimated baseline errors in the SEP-referenced 2326 MHz data and the systematic errors in the 2 GHz absolute sky temperature measurement.

A continuing experiment that was devised to attempt to reduce these residual errors in the survey baseline is described in the conclusion (chapter 9).

4.7 Noise

This section describes the measurement of the noise level for each individual survey map, and compares the results with the expected values. There is also a discussion of the noise filtering that was applied to the map data in order to improve the signal-to-noise ratio without compromising the spatial resolution. This filtering was possible because of the strategy of oversampling embraced by the observing procedure.

4.7.1 Receiver Noise Fluctuations

The RMS measure of the random fluctuations in the output of a continuum radiometer is related to the system temperature, $T_{\rm SYS}$, by (Dicke, 1946; Kraus, 1966d):

$$\Delta T = \frac{K_{\rm RAD} \times T_{\rm SYS}}{\sqrt{\Delta\nu_{\rm IF} \times \tau_{\rm PD}}} \quad [\rm K] \tag{4.26}$$

where $\Delta\nu_{\rm IF}$ is the aggregate pre-detection bandwidth of the IF subsystem, $\tau_{\rm PD}$ is the post-detection time constant of the radiometer, and $K_{\rm RAD}$ is a figure of merit that depends on the radiometer type. For the noise adding radiometer used for the *SKYMAP* observations this performance factor is given by (Nicolson, 1970; Jelley and Cooper, 1961):

$$K_{\rm RAD} = 2 \times \left(1 + \frac{T_{\rm SYS}}{T_{\rm ND}}\right) \tag{4.27}$$

For optimal noise performance and gain stability the excess antenna temperature of the noise-adding noise diode, $T_{\rm ND}$, was adjusted to be about double the nominal system temperature, resulting in $K_{\rm RAD} \approx 3$ for the HartRAO $\lambda = 13$ cm radiometer.

4.7.2 Noise Filtering

In order to use equation 4.26 to predict the pixel noise in a radio image it is necessary to replace $\tau_{\rm PD}$ by the effective pixel integration time, which is given by:

$$\tau_{\rm PIXEL} \ [\rm sec] \ = \frac{\text{Effective pixel Area } [\rm deg^2] \times \text{No. of scan repeats}}{\text{Scan rate [deg/sec]} \times \text{Scan spacing [deg]} \times \cos\delta} \tag{4.28}$$

The effective pixel area required by this equation is determined by the interpolation kernel, or spatial filter, used for regridding and filtering the radio images. A FORTRAN program, `CTFM.FOR` was written to perform all the regridding and filtering operations required for analyzing the *SKYMAP* data. This program provided a number of different convolution kernels, including one which approximated an ideal noise filter. The design of this filter is briefly described below.

Because the diameter of the HartRAO telescope is $200 \times \lambda$ for $\lambda = 13$ cm, the convolution of the sky brightness distribution by the beam filters out all spatial frequencies above 200 cycles/rad, or 3.5 cycles/deg. The ideal noise reduction filter for the survey images would therefore cut out spatial frequencies above this limit without attenuating the lower spatial frequencies.

It was not practical to use Fourier domain techniques for filtering and interpolating the survey data, because it was impossible to project the large-scale *SKYMAP* maps onto a rectangular Euclidean surface without introducing unacceptable geometrical distortions. Program `CTFM.FOR` performed filtering and interpolation functions by using the following spatial domain convolution which was computed numerically:

$$T_{\rm OUT}(\ell_0, b_0) = \int\int_{r<r_{\rm max}} I(r)\, T_{\rm IN}(\ell_0 - \ell, b_0 - b)\, \cos b\, d\ell\, db \quad [\rm K] \tag{4.29}$$

where (ℓ, b) are celestial coordinates, $I(r)$ is the radial profile of the circularly symmetric interpolation kernel function, and r is the small-circle distance between (ℓ_0, b_0) and (ℓ, b).

The radial profile of the interpolation kernel function was chosen to have the form:

$$I(r) = \frac{3.5 \times J_1(2\pi \times 3.5 \times r)}{r} \times \exp\left(-\frac{1}{2} \times \left[\frac{2.5 \times r}{r_{\rm max}}\right]^2\right) \times \prod\left(\frac{r}{2 \times r_{\rm max}}\right) \tag{4.30}$$

This function, which is traced by the solid line in figure 4.9(a), is a truncated and windowed variant of an ideal (but physically unrealizable) interpolation kernel. The rectangle function truncates this profile at a small-circle radius of $r_{\rm max} = \frac{19.62}{2\pi \times 3.5}{}^\circ = 0.89^\circ$. The seemingly arbitrary numeric value of 19.62 in the argument of the rectangle function corresponds to the sixth zero of the first order Bessel function, J_1 (Abramowitz and Segun, 1968). This ensured that the convolution mask was continuous at its outer limit. The gaussian window function has a value of 0.04 at the edge of the mask, which provided enough tapering of the profile to prevent Gibb's phenomenon effects. These windowing parameters were decided by trial-and-error.

This convolution mask subtends a small solid angle, and it is not significantly distorted by projection onto a flat Euclidean coordinate plane. The filtering action of the

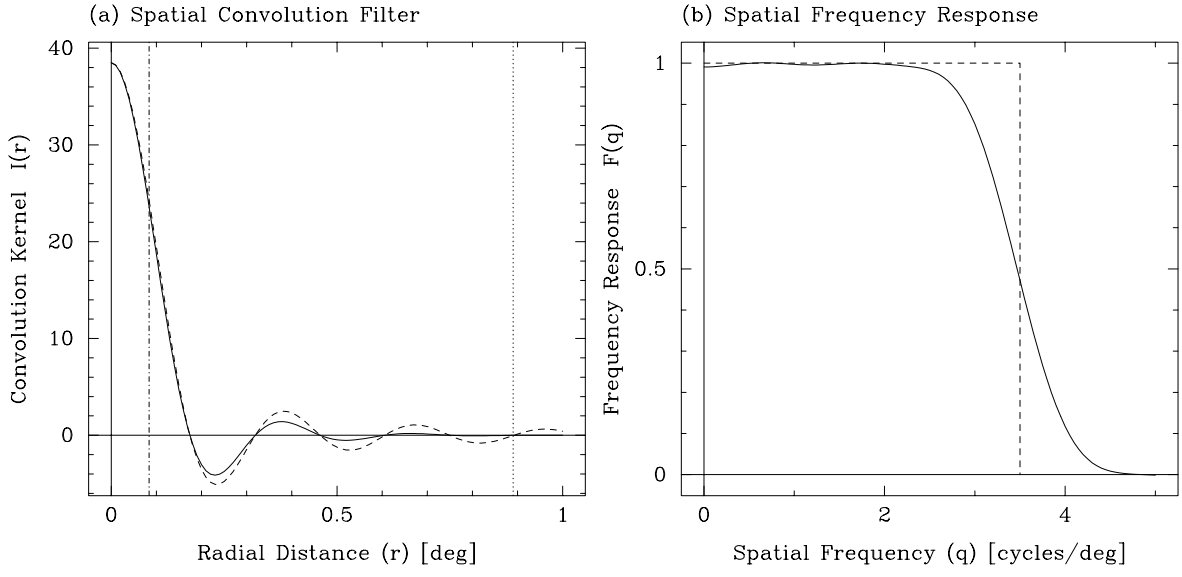

Figure 4.9: Radial profile representations of the circularly-symmetric two-dimensional spatial filter function and its effective spatial frequency response. (a) The solid line traces the radial profile of the spatial domain interpolation kernel given by equation 4.30. The dashed line is the function $\frac{3.5 \times J_1(2\pi \times 3.5 \times r)}{r}$ which is the shape of the unweighted profile that would be required for an ideal low-pass filter with infinite support. The vertical dotted line on the right represents the small-circle radius of the convolution mask, $r_{\max}$. The vertical chain line on the left represents the effective radius of the interpolation kernel. (b) The Hankel transform of the spatial filter profile, as given by equation 4.31, is traced by the solid line. Note that the passband is very flat for spatial frequencies below 2.5 cycles/deg. The dashed line represents $\prod\left(\frac{q}{2 \times 3.5}\right)$, which is an ideal low-pass filter with a spatial frequency cut-off of 3.5 cycles/deg.

convolution mask over small areas of sky can, therefore, be conveniently examined in the Fourier domain. The Hankel transform (Bracewell, 1965a) of the interpolation kernel in equation 4.30 is:

$$F(q) = \frac{2\pi r_{\max}^3}{2.5^2} \prod \left(\frac{q}{2 \times 3.5} \right) * \exp \left(-\frac{1}{2} \times \left[\frac{2\pi \times r_{\max} \times q}{2.5} \right]^2 \right) * \frac{J_1 \left(2\pi \times r_{\max} \times q \right)}{q} \tag{4.31}$$

where q is the radial spatial frequency variable with units of cycles/deg, and $[*]$ represents two-dimensional convolution (Bracewell, 1965b). The shape of this filter function is traced by the solid line in figure 4.9(b). The ideal low-pass filter function, $\prod \left(\frac{q}{2 \times 3.5} \right)$, is degraded by the two convolutions in equation 4.31, particularly by the gaussian function. Nevertheless, most of the out-of-band noise is attenuated and the passband is not overly compromised.

The effective pixel area that results from this interpolation kernel is:

$$\Omega_{\text{PIXEL}} = 2\pi \int_0^{r\max} \left[\frac{I(r)}{I(0)} \right]^2 r \, dr = 0.0222 \quad [\text{deg}^2] \tag{4.32}$$

which corresponds to an effective diameter of 0.17° for circular pixels (see vertical chained line in figure 4.9(a)), or sides of 0.15° for square pixels. This effective pixel area was used in equation 4.28 to calculate the effective integration time for pixels in the survey images.

4.7.3 Individual Map Noise

The expected RMS pixel noise for the *SKYMAP* maps was predicted by using τ_{PIXEL} as a post-detection time constant in equation 4.26. The RMS noise level was expected to vary from map to map because of the different receiver characteristics and observation parameters that were applicable to the various maps. The noise level also varied within each map because of the $(\cos \delta)^{-1}$ dependence of τ_{PIXEL} indicated by equation 4.28.

Two representative sub-images were extracted from each of the ten survey maps in order to characterize the RMS noise fluctuations. The pairs of sub-images were positioned near the northern and southern edges of the maps where there was little evidence of radio source structure. Each sub-image was regridded onto an orthographic coordinate projection, using the interpolation kernel described in section 4.7.2, and a second-order least-squares polynomial base surface was subtracted from the filtered result. The RMS noise level for each sub-image was obtained by calculating the variance of the residual pixels values. Table 4.4 lists the results obtained from this noise analysis, together with the noise levels predicted using equation 4.26. The predicted noise level also includes a component due

Map	Sym	RA [°]	Dec [°]	Size [°] × [°]	T_{SYS} T_A [K]	$\Delta\nu_{IF}$ [MHz]	τ_{PIXEL} [sec]	ΔT_{PRED} T_{FB} [K]	ΔT_{MEAS} T_{FB} [K]
A04D26	I	137.5	+6.7	11.8 × 8.6	30	15	1.8	27.1	26.4
A04D26	I	65.5	−23.5	5.7 × 3.4	30	15	1.9	26.2	25.0
A05D63	C	89.8	−55.5	6.9 × 5.9	30	15	4.7	18.5	23.6
A05D63	C	169.6	−28.2	7.7 × 5.2	30	15	3.0	21.8	24.4
A06D83	E	126.7	−64.1	15.4 × 5.4	46	40	3.0	20.7	21.5
A06D83	E	150.9	−80.0	9.0 × 4.4	46	40	7.7	15.2	15.6
A12D11	F	228.8	+29.8	4.5 × 4.1	46	40	2.0	24.3	26.7
A12D11	F	357.7	+13.2	3.8 × 3.0	46	40	1.8	25.5	25.7
A12D63	A	183.2	−30.9	5.5 × 5.5	46	40	3.1	20.6	17.8
A12D63	A	326.0	−59.2	7.4 × 6.4	46	40	5.2	17.1	18.0
A14D26	D	14.9	+10.5	6.4 × 4.4	46	40	1.8	25.6	24.3
A14D26	D	32.5	−19.6	8.3 × 3.9	46	40	1.9	25.1	23.2
A14D83	G	352.1	−63.0	9.8 × 3.8	46	40	2.9	21.0	28.7
A14D83	G	355.6	−80.3	10.4 × 3.9	46	40	7.9	15.1	22.1
A21D63	J	45.1	−26.8	7.1 × 3.8	46	40	2.5	22.4	23.3
A21D63	J	56.0	−60.0	7.6 × 3.4	46	40	4.4	18.0	17.7
A22D26	H	49.6	−22.5	7.8 × 4.9	46	40	1.9	24.9	30.0
A22D26	H	15.3	+9.4	5.6 × 6.1	46	40	1.8	25.6	34.2
A23D80	B	32.4	−62.7	12.8 × 3.3	46	40	2.9	21.1	16.7
A23D80	B	76.7	−77.8	9.4 × 3.2	46	40	6.3	16.1	13.3

Table 4.4: Table of predicted and measured noise fluctuations for the ten constituent survey maps. The letter in the second column is the identifying symbol used in figure 4.10. Columns 3, 4 and 5 specify the position and extent of the rectangular area used to calculate ΔT_{MEAS}, the measured noise fluctuations. Columns 6 to 8 contain the parameters used to calculate ΔT_{PRED}, the noise fluctuations predicted from the receiver parameters and pixel integration time.

to extragalactic source confusion, which is estimated to have an RMS level of 10 mK T_{FB} (Nicolson, private communication).

Figure 4.10 is a graphical comparison of the predicted and measured noise levels listed in table 4.4. Most of the points lie near the line representing agreement between predicted and measured noise levels. The two early maps, A12D63 and A23D80 (A and B in the figure), have noise levels that are slightly better than expected. This effect is probably due to a running-median filter that was included in the early version of the observing program. This non-linear filter was disabled for the later observations because it clipped the peaks of radio sources. Maps A05D63, A14D83 and A22D26 (C, G and H in the figure) are somewhat noisier than predicted. These regions were observed during periods of unstable weather, which had the effect of contributing additional 1/f noise in the recorded antenna temperatures. The symptoms of these excess low-frequency variations in antenna temperature were striations parallel to the scanning direction in the resulting maps. These

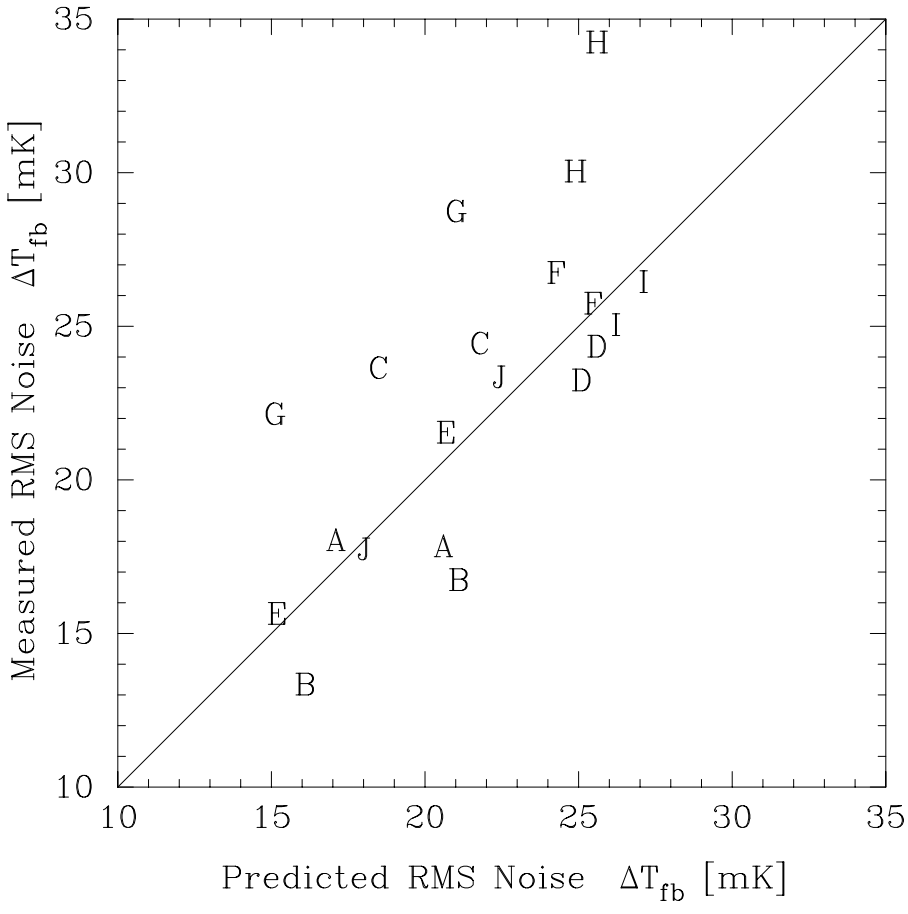

Figure 4.10: Plot of measured versus predicted noise fluctuations for the ten survey maps. The ordinates for both axes are scaled as full-beam brightness temperatures. The symbols A to J are used to identify the maps (see table 4.4). The diagonal line is the expected locus of the points. Most of the points lie in the upper-left half of the diagram, indicating that the associated maps are noisier than expected.

"scanning effects" had non-gaussian statistics and contributed significantly to the measured RMS noise level.

From the table and figure it is clear that for most of the individual survey maps the RMS noise level was less than 30 mK $T_{\rm FB}$. When the maps were combined into a composite image this noise figure was reduced for regions where adjacent maps overlapped.

4.8 Pointing Accuracy

The positional accuracy of the survey data was established by measuring the apparent positions of point sources in the survey data and comparing these measurements with the positions listed in the Parkes Catalogue (PKSCAT90, 1990). The technique and results of this exercise are given below.

All sources with nominal 2.3 GHz fluxes greater than 1.5 Jy and positions that fell

within the boundary of the survey observations were extracted from PKSCAT90. A sub-image surrounding the catalogue position of each of these selected sources was extracted from the survey data. Each of these $2^\circ \times 2^\circ$ sub-images was interpolated onto an orthographic coordinate projection that was centred on the catalogue position in order to reduce the geometrical distortion of the beam shape. A fine pixel grid spacing $2' \times 2'$ was used to ensure that the angular resolution of the position measuring algorithm was adequate.

A least-squares procedure was used to fit a second-order polynomial base surface to the sub-image data outside of the expected boundary of the first sidelobe of the source image. After subtracting the base surface, the rows and columns of the sub-image were summed to create two orthogonal, one-dimensional marginal distribution profiles. A least-squares procedure was used to fit the height, width and position of a gaussian model to these profiles. Discarding the height information, this procedure yielded two orthogonal beamwidths, and two orthogonal position offsets for each selected catalogue source. Excess deviation of the fitted beamwidths from the expected value of $20'$ was assumed to result from a bad model fit, probably resulting from source confusion. The results from these bad model fits were discarded from the tables of small-circle offsets that were compiled for each of the 10 constituent maps.

Two sources of error contributed to the measured position offsets that were obtained using the analysis described above: (a) real position errors in the survey data, and (b) errors introduced by the source-fitting algorithm, which were expected to decrease for stronger sources. This trend is apparent in figure 4.11, which summarises the combined results from the ten survey maps. This figure shows the dependence of the measured RMS pointing deviation on the flux threshold used to select the reference source sample population. Above a threshold flux of 4 Jy the RMS deviations for right ascension and declination approach plateau values of $0.75'$ and $0.9'$ respectively. Above a threshold flux of 7 Jy the RMS pointing deviations continue to decrease but, since the sample populations consist of less than 27 sources above this flux threshold, it was decided to use the conservative plateau values to characterise the RMS pointing errors inherent in the survey data.

Table 4.5 summarises the RMS pointing errors that were determined for each of the ten individual survey maps. The pointing residuals tend to be better for the later maps for two reasons: (a) the replacement of the original electro-mechanical axis-angle encoders with modern optical encoders and (b) the improvement in the reliability of the axis-error map used by the antenna control software. From table 4.5 it is apparent that the unweighted

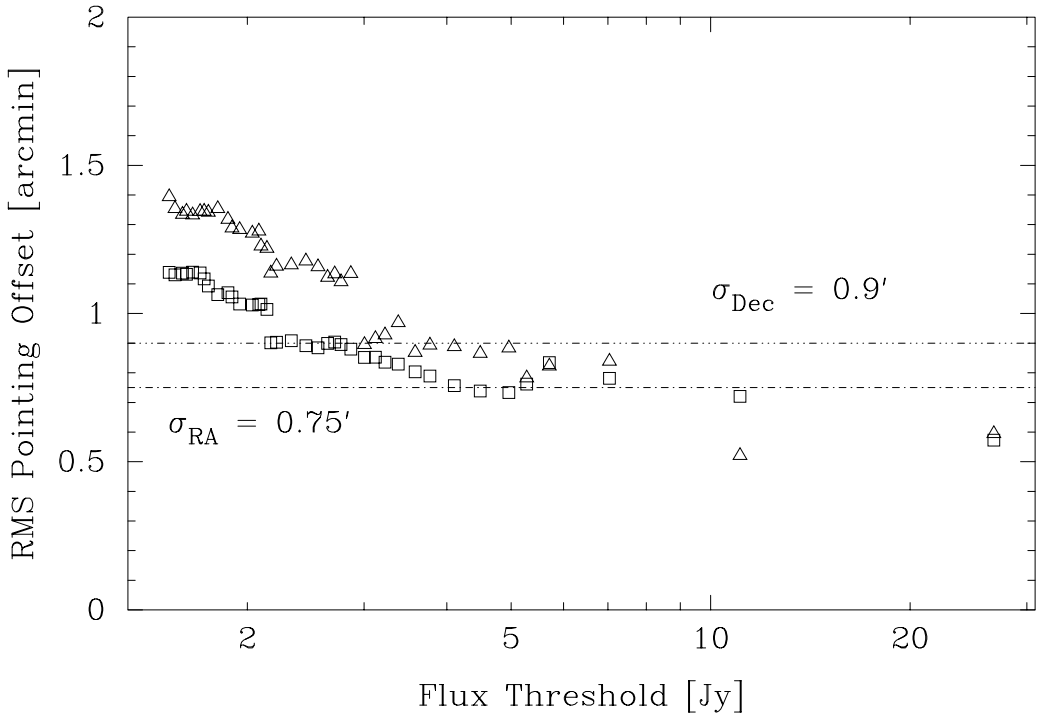

Figure 4.11: The dependence of the measured RMS pointing deviation on the flux threshold chosen for the reference sources. The open squares represent the right ascensions offsets and the open triangles represent the declination offsets. Both right ascension and declination offsets are measured as great-circle angles. The horizontal lines indicate the adopted RMS pointing errors for the survey.

Map	σ_{RA} [′]	σ_{DEC} [′]
A12D63	1.1	1.8
A23D80	0.7	0.7
A05D63	0.85	1.9
A14D26	0.55	0.45
A06D83	1.5	1.0
A12D11	0.9	0.9
A14D83	1.2	0.65
A22D26	0.9	0.55
A04D26	0.65	0.65
A21D63	0.6	0.75
Maximum	1.5	1.9
Unweighted Mean	0.85	0.95
Combined	0.75	0.9

Table 4.5: The RMS right ascension and declination pointing dispersions measured for the ten component maps of the 2326 MHz survey. The dispersions represent small-circle arcs in units of arcminutes. The values in the second-last row are the unweighted means of the ten RA and DEC dispersions listed in the table, while the last row reflects the dispersions obtained by analyzing the final composite map.

mean of the individual RMS measurements implies a larger deviation than that obtained by analyzing the results from the combined maps. This is because the unweighted mean is skewed by the relatively poor pointing performance of the southern declination maps, which contain considerably fewer test sources than the other maps.

These measurements show that the pointing accuracy of the survey data is everywhere better than 10% of the full-width at half-maximum of the survey beam. For most of the surveyed area the pointing accuracy is better than 5% of the survey beamwidth. There was no evidence of systematic offsets in right ascension or declination for any of the maps.

Chapter 5

A Review of the Milky Way and its Radio Continuum

The primary objectives of the *SKYMAP* project are the study of the diffuse, extended galactic emission and the identification and classification of individual galactic radio sources superimposed on this diffuse background. This chapter presents a review of the observations and theories published in the literature that have relevance to this study of the galactic radio continuum emission. The subsequent three chapters describe the investigations that were made into the nature of the galactic emission using the *SKYMAP* survey data.

To set the context of the review, this chapter starts with a brief digression into the early observational studies of the galactic radio continuum and then presents a preview of the map produced from the *SKYMAP* data.

The galactic radio continuum emission is largely influenced by the following factors:

- The large-scale structure of the galaxy.
- The composition of the galaxy, particularly the interstellar medium.
- The sources of energy in the galaxy.

The remainder of this chapter is a survey of theories and observations that relate to these characteristics of the galaxy. In particular, this review demonstrates that supernovae and their remnants are important factors in the evolution of the interstellar medium, and hence help determine the structure of the galaxy and the nature of the radio continuum emission.

5.1 Historical Perspective

The 1958 Paris Symposium on Radio Astronomy (Bracewell, 1959) included a session on the large scale structure of galaxies, with most of the presentations concentrating on the

Milky Way. In a classical paper presented at this symposium, Mills (1959) identified three components of the metre-wavelength Galactic radio continuum emission: (1) a narrow ridge of emission near the Galactic equator (the disk), (2) discrete sources embedded in this ridge (HII regions and SNRs), and (3) a more diffuse distribution of emission extending to high Galactic latitudes (the corona or halo). He also recognised that the step-like features in the longitude distribution of the disk component are a result of the spiral structure of the galaxy.

Since 1958 the extended galactic radio continuum emission has been investigated at wavelengths ranging from 10 metres down to millimetres. As the angular resolution of the surveys has improved over time, it has become apparent that there is a wealth of structure in all three of the galactic radio continuum components identified by Mills.

5.2 Overview of the *SKYMAP* Map

The *SKYMAP* 2326 MHz survey is the highest resolution large-scale radio continuum survey currently available. As such, it is well suited to identifying new radio emission features with angular scales ranging from tens of degrees down to less than a degree. It is also the highest frequency survey of this type, and therefore provides valuable information on the spectral characteristics of the galactic radio sources.

Plate C.1 in appendix C is a pseudo-colour representation of the complete 2326 MHz *SKYMAP* survey data displayed using the Hammer-Aitoff equal-area coordinate projection. For display purposes the resolution of the original map data has been smoothed to 51 arcmin, which is identical to the resolution of the 408 MHz survey (Haslam et al., 1982). The zero-point of the temperature scale has been set to exclude all isotropic extragalactic contributions (see section 4.6.2).

The three components of the galactic emission identified by Mills (1959) are clearly evident in plate C.1. The galactic plane is traced by a bright ridge of emission which is quite symmetric about the galactic equator. Both the central brightness and width of this ridge vary with galactic longitude and a number of step-like structures are evident. Some compact, discrete sources are discernible along the galactic equator, but many of the small-scale sources are concealed by the brightness gradient of the galactic ridge. The high-latitude galactic emission appears to be a continuation of the ridge emission, and this extended component becomes nearly isotropic towards the galactic poles.

A most striking extended emission feature in the map is the North Polar Spur (NPS) extending northwards out of the galactic plane near $\ell \approx 30°$. This was one of the first coherent structures detected at high latitudes in early radio continuum surveys, and was discovered to be part of a large, almost continuous loop of emission (Hanbury Brown et al., 1960). Three more large galactic loops were subsequently identified (Large et al., 1962; Quigley and Haslam, 1965), and it is now generally accepted that these large loops are old supernova remnant (SNR) shells (Yates, 1968; Berkhuijsen et al., 1971; Spoelstra, 1973; Berkhuijsen, 1973). The small-circle loci of galactic radio loops I, II and IV are indicated by white dashed lines in plates C.1, C.2 and C.3 (appendix C). Published parameters were used for the centres and diameters of these loops (Berkhuijsen et al., 1971). Being a northern hemisphere object, loop III does not intersect with the sky covered by *SKYMAP* .

The diffuse galactic ridge and the numerous superimposed loop, spur and filamentary structures discernible in the *SKYMAP* map are discussed in more detail in the chapters following this one.

5.3 The Milky Way - a Warped Spiral Galaxy

Early HI observations by the Leiden and Sydney groups confirmed that the Milky Way has a spiral structure (Kerr et al., 1957; Oort et al., 1958). It is now generally believed that the spiral structure in disk galaxies is caused by a gravitational instability, as described by the spiral density wave theory proposed by Lin and Shu (1964). The spatial distribution of the galactic HI gas has been modeled quite accurately to a radius beyond the solar circle. The application of the density wave theory and a galactic rotation model was necessary to obtain distance information from the raw HI observations (Kerr et al., 1968; Burton, 1970; Burton, 1971; Verschuur, 1973). Using such an HI model, Henderson (1977) produced a mathematical model for the spiral structure the Milky Way which has four trailing arms following a logarithmic spiral with a pitch-angle of 13°, and with the position of the sun being about half-way between the Perseus and Carina arms. This model is similar to many of the more recent models listed by Vallée (1995). Burton (1988b) also provides a relatively recent review of galactic structure as deduced from HI observations.

Other tracers, besides HI gas, have been used to map the spiral pattern of the galaxy. Georgelin and Georgelin (1976) used the positions and velocity dispersions of galactic HII

regions to determine a spiral structure that is consistent with the HI data. Although radio continuum maps do not provide a distance measure to emission features it is possible to compare the observed continuum distribution with that predicted by a given spiral emissivity model. Price (1974) proposed that a disk-plus-two-arm emissivity model for the galaxy was consistent with a 150 MHz map of the galactic plane. Paul et al. (1976) extended this analysis to include cosmic ray and magnetic field data. Both of these works placed the sun near the inner edge of one of the two spiral arms.

French and Osborne (1976) showed that the multi-armed spiral models developed by the Georgelins (Georgelin and Georgelin, 1976) and Verschuur (1973) could be reconciled with the galactic synchrotron emissivity distribution as determined from 150 MHz and 408 MHz radio continuum maps. Phillipps et al. (1981a; 1981b) and Beuermann et al. (1985) have used iterative inversion techniques to "unfold" the 408 MHz sky brightness distribution to independently obtain three-dimensional emissivity models for the galactic synchrotron radiation. Both of these models suggest a four-arm model for the galactic structure.

Current models of the spiral structure that are consistent with both observational evidence (galactic magnetic field, dust, gas and stars) and with theoretical hydrodynamical modelling seem to favour a four-arm spiral (Vallée, 1995) or a superposition of two-arm and four-arm components (Amaral and Lépine, 1997). A recent dissenting view is presented by Han and Qiau (1994), who have constructed a bisymmetric spiral model for the galactic magnetic field from measurements of rotation measure towards pulsars and extragalactic sources.

The common features of the models proposed by Vallée (1995) and Amaral and Lépine (1997) suggest that the spiral structure is present between galactic radii of 2.8 and 12.8 kpc, with a pitch-angle of $\approx 12^{\circ}$. Figure 5.1 is a schematic representation of the spiral structure of the Milky Way derived by combining these two models. Density wave theory permits only two of the spiral arms to reach the inner boundary of the spiral structure (which is near the "molecular ring"), and the Milky Way probably has a similar appearance to the Sc galaxy M101 (NGC 5457). Although not flocculent, the spiral pattern probably exhibits many small-scale features such as inter-arm links. The sun appears to be situated near the Orion spur, a local feature that extends out of the Perseus arm and possibly forms a link with the Carina-Sagittarius arm.

The Milky Way is not perfectly symmetric about the galactic equatorial plane. From

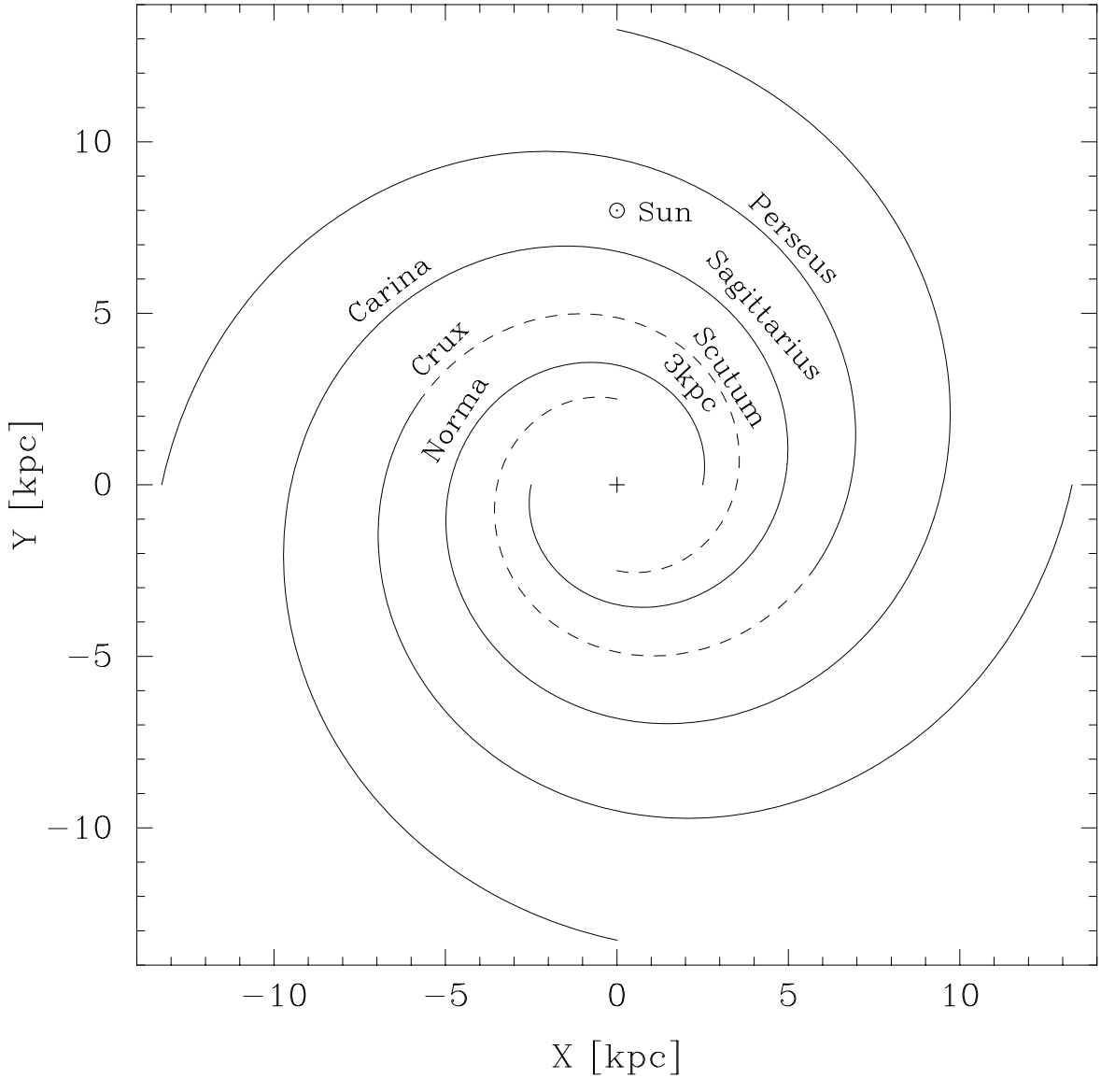

Figure 5.1: A schematic representation of a four-arm realization of the spiral structure of the Milky Way as derived from two recently published models (Vallée, 1995; Amaral and Lépine, 1997). The pitch-angle for the spiral arms is 12°. A four-arm model is not valid inside the inner Lindblad resonance, and two of the arms have been represented by dashed lines in this region. The position of the sun is shown at a galactocentric radius of 8 kpc, and the arms have been labelled with their common names. For clarity, the local "Orion spur" has been excluded from this diagram.

our viewing position within the galaxy large-scale global distortions and small-scale local asymmetries are clearly evident in survey observations at various wavelengths. Two of the distortions visible in the radio continuum are reported here.

The outer region of the disk of the Milky Way is distorted by a large-scale warp which has its line of nodes nearly coincident with a line running from the galactic centre through the position of the sun. This warp was apparent in early HI observations (Burke, 1957; Kerr et al., 1957; Westerhout, 1957; Oort et al., 1958; Kerr, 1962) and Burton (1988a) provides a review of more recent HI observations of the warp. It was also recently detected in the *COBE–DIRBE* maps of the galactic far-infrared emission (Freudenreich et al., 1993).

The Gould Belt (Davies, 1960; Clube, 1967; Lesh, 1968; Stothers and Frogel, 1974) is a local galactic feature that, because of its proximity, appears as an asymmetric distortion in the disk of the galaxy. The Gould Belt is a system of stars that have a flattened ellipsoidal distribution centred near the sun. The age of the star system is 30–40 Myr and it is inclined at $\approx 20^\circ$ to the galactic plane (Lindblad et al., 1997). The most prominent components of the system are the Orion and Scorpius-Centaurus associations. Molecular cloud complexes have also been related to the Gould belt (Pöppel et al., 1994).

5.4 The Galactic Synchrotron Emission

Diffuse non-thermal synchrotron emission is ubiquitously associated with the disks of spiral galaxies. Lequeux (1971) has shown that for both our galaxy and external galaxies the distribution of the continuum emission is strongly correlated with the positions of extreme population I objects. In an early investigation of the diffuse galactic emission Davies and Hazard (1962) speculated that both the magnetic field and the cosmic rays necessary for this synchrotron emission result from supernova remnants (SNRs). It has been proposed that the synchrotron background is entirely due to the confused emission from the radiative shells of old SNRs (Sarkar, 1982), but it appears likely that at least some fraction of the emission is due to electrons that have diffused away from the confines of the SNR (Ilovaisky and Lequeux, 1972a; Dickel, 1974; Boulares, 1989). This diffusion is aided by the stochastic nature of the galactic magnetic field (Jokipii and Parker, 1969).

The extreme population I objects that are thought to provide the energy and material for the cosmic rays are distributed in a disk with a z half-width of ≈ 100 pc, but there appears to be a cosmic ray halo that extends to distances of $z \approx 10$ kpc above and below the

galactic plane (Price, 1974; Webster, 1975; Phillipps et al., 1981b; Beuermann et al., 1985). Current theories speculate that there is in fact a cosmic ray "wind" that emanates from the galactic plane, driven by population I objects such as SNRs (Lerche and Schlickeiser, 1982; Dröge et al., 1987; Pohl and Schlickeiser, 1990).

Further evidence that the diffuse galactic synchrotron emission cannot be entirely due to SNR shells is the fact that the median flux spectral index for SNRs is $\alpha = 0.5$ while for bright spiral galaxies the figure is $\alpha = 0.74$ (Dröge et al., 1987). This difference is attributed to a change in the energy spectrum of the cosmic ray as they propagate from the SNR shells into the interstellar medium.

Extended thick disks, or halos, are evident in other phases of the galactic ISM besides cosmic rays:

- Outside of a galactocentric radius of 3.5 kpc there exists a high-z HI halo (Lockman, 1984; Lockman, 1991). The kinetic temperature of the interstellar gas is far too low to support the observed HI layer and the additional pressure is attributed to turbulent gas motion (Lockman and Gehman, 1991). Ti II interstellar absorption lines have been observed at $z = 8.7$ kpc (Albert et al., 1994) which indicates that diffuse HI gas may extend well beyond the traditional HI disk.

- Both a thin and a thick disk are seen in the distribution of molecular clouds as traced by CO observations (Dame and Thaddeus, 1994).

- The scale height of free electrons is ≈ 1500 pc (Reynolds, 1989) and diffuse ionised gas has been detected at $|z| > 500$ pc (Reynolds, 1990). A significant fraction of the combined power output from population I sources (OB stars and supernovae) is required to maintain this extensive "warm ionised medium" (WIM).

Although these halos are not necessarily related, it is evident that radiation and various phases of matter are ejected in a direction perpendicular to the galactic plane. Figure 5.2 is a schematic representation of the Milky Way in cross section, showing the distributions of the various high-z components described above.

Besides the diffuse ridge of emission, the large-scale galactic radio continuum is characterized by spurs extending out of the galactic plane. The most notable of these features are associated with the giant radio loops identified in section 5.2. Although these spurs are now generally accepted to be parts of nearby SNR shells (Berkhuijsen et al., 1970; Berkhuijsen, 1971; Berkhuijsen et al., 1971; Ilovaisky and Lequeux, 1972b), it must be mentioned

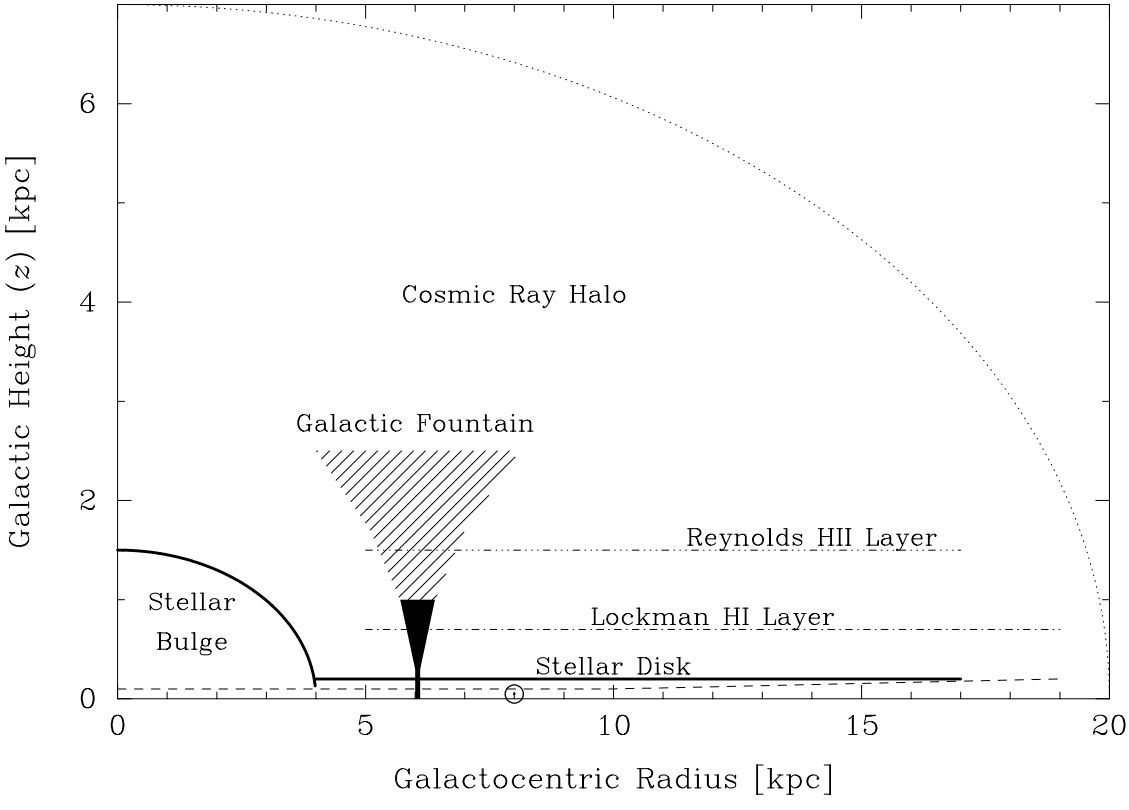

Figure 5.2: A schematic representation of the Milky Way in cross-section, showing the extent of the high-z components of the galaxy. Assuming symmetry, only one quadrant of the cross section is shown. No attempt has been made to illustrate the galactic warp. The position of the sun is marked at a galactocentric radius of 8 kpc. The dashed-line near $z = 0$ indicates the thickness of the "traditional" disk HI layer. Population I objects, such as molecular clouds and SNRs, have a narrower distribution than this HI layer. Objects such as superbubbles and worms have linear sizes of the order of 100 pc, and are too small to represent effectively on this diagram.

that there are competing theories for these large-scale structures which consider the spurs to be high-z manifestations of large-scale galactic structure, rather than emission from discrete, nearby objects. Mathewson considered the spurs to be tracers of a large-scale helical galactic magnetic field (Mathewson, 1968), while Sofue used the apparent positional coincidence of the spurs with the tangent directions of spiral arms to support a theory that the spurs are inclined extensions of the galactic spiral arms (Sofue, 1973; Sofue and Tosa, 1974; Sofue, 1976). The loop morphology, association with surrounding HI shells (Berkhuijsen et al., 1971) and enclosed hot gas (Heiles et al., 1980) is, however, considered to be convincing evidence that the galactic loops and spurs are SNR shells.

5.5 The Effect of SNRs on the ISM

From the above discussion it is clear that the evolution of the ISM is largely controlled by population I objects, with supernovae and their remnants being particularly important energy sources. Brand and Zealey (1975) pointed out that observations of all phases of the ISM indicate a dominance of loop and filamentary structures. They proposed that these structures were a result of the ISM being processed by supernova blast waves. This view is consistent with the calculations of Haslam et al. (1971) showing that a substantial amount of energy would be injected into the ISM if the large loops observed in radio continuum maps represent a common class of object in the galaxy. Since the late 1960's the study of the effects that supernova remnants have on the ISM has been an active field of theoretical and observational research.

An early model of the ISM (Field et al., 1969) proposed two phases for the interstellar gas: cool neutral clouds surrounded by a warm blanketing cloud. It was assumed that the warm gas is heated by diffuse cosmic rays, and that SNRs have no important local effects on the ISM gas. The realization that expanding SNR shells contain hot gas (Jones, 1973; Cox and Smith, 1974; Heiles, 1976a) lead to the classical McKee and Ostriker three-phase model (McKee and Ostriker, 1977; McCray and Snow, 1979). They proposed that about 70% (by volume) of the ISM consisted of hot gas with a temperature of $\approx 10^6$ K. This hot gas would be contained in shells "blown" by the SNRs and in tunnels formed by the merging of SNRs (Cox and Smith, 1974), while the warm gas phase occurred at the interface of the hot gas and neutral material. All three of the gas phases were assumed to be in hydrostatic equilibrium.

Because the hot gas would be buoyant it would rise and possibly feed gas into the galactic halo (Jones, 1973). This line of enquiry lead to the theory of "galactic fountains" (Shapiro and Field, 1976; Bregman, 1978) which proposed that hot gas would rise into the halo, cool, and fall back down onto the galactic plane.

Revisions to this classical model have been driven by four main constraints imposed by observations and theoretical modelling:

- The ISM supports processes, such as supernova and stellar winds from hot stars, that create gas structure far from hydrostatic equilibrium (Bregman, 1998). This disequilibrium leads to large, disordered motions in the interstellar gas.

- Magnetic fields and high-z gas result in an ISM pressure that is higher than originally assumed (Cox, 1988).

- Type-II SNe are spatially and temporally correlated (Norman and Ikeuchi, 1989) rather than randomly distributed throughout the disk.

- Soft X-ray observations of the halos of the Milky Way and other spiral galaxies are not consistent with the fluxes predicted by strong galactic fountains (Cox, 1981; Heiles, 1987).

As a result of these constraints the currently accepted models of the ISM are characterized by the following features:

- The expansion of SNR shells is constrained by magnetic pressure which results in a filling factor of $\approx 20\%$, or less, for the hot gas contained within these shells. This view is supported by a large body of theoretical modelling of the ISM using MHD codes and semi-analytic techniques (Norman and Ikeuchi, 1989; Spitzer, 1990; Cox, 1990; Cox, 1991; Bregman and Ashe, 1991; Slavin and Cox, 1992; McKee, 1993; Slavin and Cox, 1993; Cox, 1995; Slavin and Cox, 1996; Bregman, 1996; Elmegreen, 1997).

- Because the SNRs are spatially correlated there is no network of tunnels of hot gas formed by SNR mergers. The hot gas morphology is, instead, characterized by isolated superbubbles created by multiple "simultaneous" supernovae (Norman and Ikeuchi, 1989; Spitzer, 1990; Tenorio-Tagle et al., 1990).

- The combined effects of magnetic pressure and high-z gas reduce the efficiency of galactic fountains. Only superbubbles driven by multiple supernova remnants are capable of breaking out of the galactic disk into the halo (Cox, 1988; Norman and Ikeuchi, 1989; Różyczka, 1989; Kahn, 1989; Heiles, 1989; Tenorio-Tagle et al., 1990; Tomisaka, 1991; McKee, 1993; Kamaya et al., 1996).

- The morphology of the neutral gas phase is better represented by a diffuse layer with holes and shells, rather than the previous model of discrete cool clouds (Li and Ikeuchi, 1990; Bregman and Ashe, 1991; Bregman et al., 1993).

- The distribution of the warm ionized gas phase (WIM) is as extensive as the cool atomic gas and extends to large z-heights (Reynolds, 1989; Slavin and Cox, 1992; Lockman et al., 1996; Heiles et al., 1996a; Heiles et al., 1996b; Slavin and Cox, 1996). The source of ionizing photons for this diffuse HII is somewhat enigmatic (Reynolds et al., 1995; Reynolds, 1996; Reynolds, 1997). It appears that ionizing photons are able to escape the classical Strömgren spheres surrounding OB stars and penetrate the HI gas, even beyond the galactic disk. Various ISM morphologies (not necessarily mutually exclusive) have been proposed that allow the diffusion of ionising photons through the ISM. These include overlapping Strömgren volumes (Miller and Cox, 1993), chimneys (Dove and Shull, 1994) and fractal distributions (Elmegreen, 1997).

5.6 Observable Consequences of the Turbulent ISM

The model of the ISM outlined above results from observations of morphological and spectral features seen at wavelengths ranging from the radio to γ-rays. In particular, the morphology and kinematics of the galactic HI gas have been used extensively to probe the structure and dynamics of the neutral phase of the ISM. The above ISM model also predicts features that should be observable at various wavelengths, and the confirmation and quantification of these features is necessary to validate and refine the model, and determine its physical parameters. With regard to the *SKYMAP* survey, the distribution and spectrum of the diffuse and large-scale galactic radio continuum emission are useful probes for studying the effects of SNRs on the morphology and dynamics of the ISM. The following sections describe features to search for in the galactic continuum which may be consequences of the current ISM models.

5.6.1 Shells

Expanding cavities in the HI gas, termed shells and supershells, have been observed over a wide range of latitudes and longitudes in the Milky Way and other galaxies (Heiles and Habing, 1974; Heiles, 1976b; Cleary et al., 1979; Heiles, 1979; Colomb et al., 1980; Hu, 1981; Brinks and Bajaja, 1986). It appears that these objects fall into two categories:

- The larger and more energetic shells, or "supershells", which are probably the result of collisions between infalling high-velocity gas clouds (HVC's) and gas in the galactic plane (Tenorio-Tagle et al., 1987b; Tenorio-Tagle and Bodenheimer, 1988; Mirabel, 1991). With sizes up to 1000 pc and energies up to 10^{54} ergs (Tenorio-Tagle and Bodenheimer, 1988) it is difficult to conceive of any other physical process, including multiple supernovae and radiation pressure (Elmegreen and Chiang, 1982), that could produce these structures. Supershells do not appear to be spatially correlated with population I objects or associations (Brinks and Bajaja, 1986; Tenorio-Tagle and Bodenheimer, 1988), further supporting the hypothesis that multiple SNRs are not the energy source. It is unlikely that supershells are significant non-thermal radio continuum sources because, even though the magnetic field in the shell may be amplified by compression of the shell gas, there is no local source of relativistic electrons.

- There is evidence that the smaller, less energetic HI shells are related to the multiple SNR "superbubbles" discussed in the previous section. Positional coincidences between HI "holes" smaller than 300 pc and OB associations have been observed in M31 (Brinks and Bajaja, 1986), and possible spatial correlations between SNRs and HI shells in our own galaxy have been noted (Sofue and Tosa, 1974; Hu, 1981; Maciejewski et al., 1996). Extensive numerical modelling of multiple SNRs and the associated superbubbles predicts that they should have a limb-brightened appearance in the radio continuum that is similar to single SNRs (Bodenheimer et al., 1984; Tenorio-Tagle et al., 1987a; Franco et al., 1993). X-ray evidence suggests that own solar system is contained within such a superbubble (Innes and Harquist, 1984; Cox and Reynolds, 1987).

This scenario provides justification for searching for extended loop-like structures in the galactic radio continuum. Important parameters describing the galactic structure and

dynamics, such as the galactic supernova rate and the prevalence of multiple SNRs, can be constrained by the identification and classification of shells of continuum emission.

5.6.2 Worms, Chimneys & Fountains

An important, but still unknown, parameter of the galactic morphology is the number of superbubbles that are able to break out into the halo. There is evidence from HI maps that superbubbles (and supershells) reach up to high galactic latitudes, but observations of the X-ray emission from galactic halos of spiral galaxies indicate that relatively little hot gas is released from these bubbles into the halo. This is probably because of the smothering effect of magnetic pressure and the high-z neutral gas (Cox and McCommon, 1986; Li and Ikeuchi, 1990). A hierarchy of structures, termed "worms", "chimneys" and "fountains", have been proposed to describe the various stages of superbubble breakout.

By spatial filtering HI maps Heiles has identified elongated structures, which he has termed worms, that extend out of the galactic plane but apparently do not open out into the halo (Heiles, 1984). These worms are thought to be superbubbles that have been restrained by magnetic and gas pressure and have not broken out into the halo. The terms chimney and fountain are not uniquely defined in the literature. In the context of this thesis chimneys are assumed to be worm-like structures that have reached the halo and are conduits of hot gas to the halo. Fountains are the structures formed on top of the chimneys by this hot gas rising and then cooling and falling back onto the galactic plane.

Searches for worm-like features in HI, far-infrared (FIR) and radio continuum maps have yielded about 120 candidate objects (Koo et al., 1991; Koo et al., 1992; Reach et al., 1993), with about 30% apparently having radio continuum structures associated with them (Koo et al., 1991). Contrary FIR evidence is provide by Waller and Boulanger (1993) who claim that the structure of the interstellar dust does not have chimney or worm structures, but has a frothy morphology instead. Galactic chimney (and associated fountain) candidates observed at various wavelengths include Stockert's chimney in Serpens (Kundt and Müller, 1987) and apparent breakout features in Perseus (Normandeau et al., 1996) and Aquilla (Maciejewski et al., 1996).

Heiles has recorded radio recombination lines from diffuse HII regions that he claims are radiated from the walls of galactic worms and chimneys (Heiles et al., 1996b). These observations support his theory that the walls of a worm are ionized by photons from surviving hot stars in the OB association that produced the multiple supernovae responsible

for the worm. The apparent spatial coincidence of population I objects with the bases of worms and chimneys provides independent support for this theory (Kundt and Müller, 1987; Reach et al., 1993). Worms and chimneys could, therefore, be the conduits which provide ionizing photons to the diffuse ionized gas at high latitudes (the "Reynolds layer").

A search for radio continuum emission features that are aligned in a direction perpendicular to the galactic plane is necessary to corroborate or refute the sometimes contradictory evidence for worms and chimneys. Chapters 6 and 8 describe searches for such objects in the *SKYMAP* data.

5.6.3 Radio Spectral Index

In this thesis the following conventions are used for temperature (β) and flux (α) spectral indices:

$$T_{\rm B}(\nu) \propto \nu^{-\beta} \quad ; \quad S(\nu) \propto \nu^{-\alpha} \quad ; \quad \beta = \alpha + 2$$

Frequency Dependence

It was apparent from very early measurements of the spectral index of the diffuse disk and halo radio emission that the source mechanism was of a non-thermal nature. This spectral signature and the observed linear polarization of the diffuse emission provide convincing evidence that the responsible source mechanism is synchrotron emission of relativistic electrons with kinetic energies greater than 1 GeV, trapped in the galactic magnetic field.

Figure 5.3 provides a summary of measurements made since 1960 of the spectral index of the diffuse galactic continuum. Clearly evident in this diagram is a trend towards a steeper spectrum at higher frequencies. This steepening is to be expected as a result of the synchrotron loss rate increasing with electron energy. Excess spectral flattening at low frequencies could result from the onset of thermal and synchrotron self-absorption.

All of the spectral indices represented in figure 5.3 were obtained using differential techniques operating on data sets at two distinct frequencies, such as T-T plots (Turtle et al., 1962) or cross-correlation analyses (Kogut et al., 1996a). For all of the results at least one of the data sets had a frequency less than 3 GHz. Because the synchrotron emission dominates in this low-frequency regime (Hirabayashi, 1974) these spectral indices are representative of the non-thermal emission.

The spectral index of the extended galactic emission at 2326 MHz is investigated in

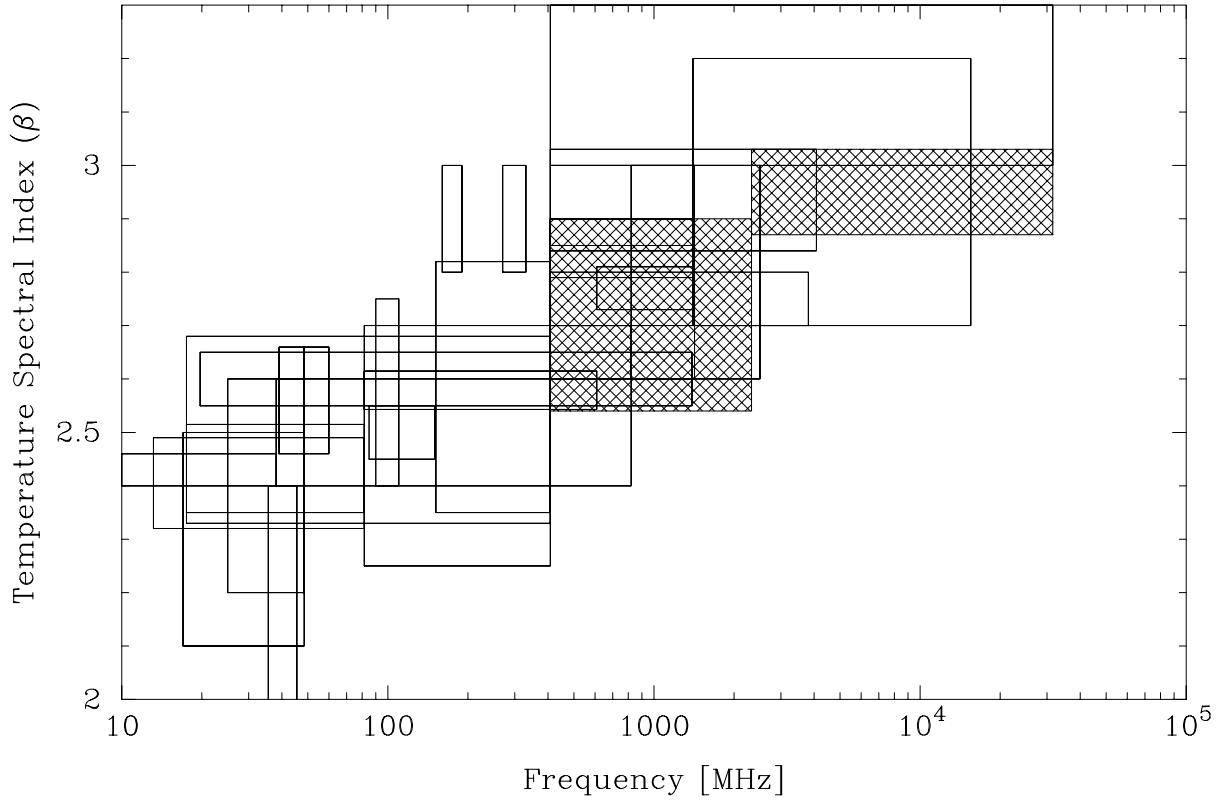

Figure 5.3: A summary of the published measurements of the spectral index of the diffuse galactic emission. The frequency span of each measurement is represented by the width of the associated rectangle, while the height of the rectangle indicates the uncertainty in the spectral index. This uncertainty contains components due to spatial variation and measurement error. The information for this graph was obtained from selected primary references (Komesaroff, 1961; Turtle et al., 1962; Penzias and Wilson, 1966; Andrew, 1966; Yates and Wielebinski, 1966; Bridle, 1967; Wielebinski et al., 1968; Howell, 1970; Sironi, 1974; Webster, 1974; Hirabayashi, 1974; Sironi and Bonelli, 1986; Lawson et al., 1987; Reich and Reich, 1988a; De Amici et al., 1990; Kogut et al., 1996a). Results obtained in chapter 7 of this thesis are represented by the cross-hatched rectangles.

chapter 7 by comparing the *SKYMAP* data with both high- and low-frequency maps of the galactic emission.

Spatial Variation

The spatial distribution of the continuum spectral index can be used to study the evolution of cosmic rays as they diffuse from the galactic plane out into the cosmic ray halo. Synchrotron emission from the halo is expected to have a steeper spectrum than the disk because of the synchrotron losses experienced by the electrons and the weaker ambient magnetic field. Many observations at high galactic latitudes support the existence of this steep spectrum halo (Penzias and Wilson, 1966; Howell, 1970; Webster, 1975; Webster, 1978), but the emission is very weak and may be contaminated by steep spectrum emission from the galactic loops (Webster, 1974; Lawson et al., 1987).

SNRs are probably the source for most cosmic ray electrons (Boulares, 1989), but physical processes within the ISM can change the energy spectrum of the electrons after they have diffused away from the SNR shells. During their lifetime cosmic ray electrons encounter about 10 supernova-induced shock waves from which they can derive energy via the second-order Fermi acceleration process (Axford, 1980; Dröge et al., 1987). These encounters can have the effect of flattening the cosmic ray spectrum with increasing z-distance from the galactic plane (Lerche and Schlickeiser, 1982; Dröge et al., 1987; Pohl and Schlickeiser, 1990; Schlickeiser, 1991). Reich and Reich (1988a; 1988b) claim to detect a flattening of the galactic spectral index with increasing latitude which they associate with the flattening of the cosmic ray spectrum with height above the plane. The uncertainty in the baselines of the 408 MHz and 1420 MHz surveys used for this analysis may cast doubt over this result (Kogut et al., 1996a). An attempt to determine the distribution of the galactic radio continuum spectral index using the *SKYMAP* data is presented in chapter 7 of this thesis.

Besides providing information about the galactic cosmic rays, the spatial variation of galactic spectral index has very important implications for the analysis of cosmic microwave background radiation data (Banday and Wolfendale, 1991; Davies et al., 1996; Tegmark, 1998).

Chapter 6

The Morphology of the Diffuse and Extended Galactic Emission

The most prominent features in the 2326 MHz radio continuum map presented in plate C.1 of appendix C are the stepped, diffuse ridge of emission aligned with the disk of the Milky Way and the large-scale loops, spurs and filaments that extend out of this ridge. In this chapter these large-scale structures are isolated, identified and their morphologies analyzed.

The loops, spurs and discrete patches of emission have a wide range of angular scales and intensities, and often these features are masked by the brightness gradient of the galactic ridge. Referring to the 85 MHz survey, Yates noted that

> *"... a fundamental difficulty encountered is the identification and isolation of the spurs of emission projecting from the Galactic plane ..."* (Yates, 1968)

At high radio frequencies all extended Galactic radio sources are optically thin, and the brightness distribution observed towards a certain position in the sky is thus the superposition of all foreground and background source brightness distributions in that direction. This low opacity prevents background emission features from being obscured, but also results in very significant source confusion.

The analysis of the large-scale galactic emission presented in this chapter required the discrimination between the diffuse galactic "background" emission and the superimposed "foreground" sources. This discrimination was achieved by constructing an empirical model of the diffuse galactic background (DGB) emission from the 2326 MHz data. This model was subtracted from the *SKYMAP* data to produce a residual map with reduced dynamic range, in which the faint superimposed sources were more distinct.

6.1 An Empirical DGB Model

In the context of this thesis there are two functions for a model of the diffuse, smoothly varying galactic emission:

- The comparison of the 2326 MHz DGB emission with existing theoretical and empirical models of the galactic structure and synchrotron emissivity.
- The establishment of a reference brightness distribution that could be subtracted from the original galactic image in order to reduce the dynamic range and thereby accentuate the faint filamentary emission features extending from the midplane to high galactic latitudes.

In pursuance of these aims it was decided that an empirical model of the DGB was preferable to a parametric model based on a restrictive mathematical description for the galactic structure. The following properties are forced upon the model in order to instil some physical reality into it:

- The latitude-dependent profiles (i.e. cross-sections perpendicular to the galactic plane) of the model are constrained to peak near the galactic equator and are forced to decrease monotonically with increasing latitude, $|b|$. This constraint is based on the assumption that the sun is close to the galactic equatorial plane, and that the radio emissivities of all components of the galaxy decrease with galactic height, $|z|$. Any brightening of the galactic emission with increasing latitude is assumed to be indicative of a discrete radio source.
- The overall model is not constrained to be north-south symmetric: the latitude profiles are constructed from gaussian basis functions which can be displaced north or south of the galactic equator. This constraint is based on the assumption that the spiral arms are north-south symmetric about their own midpoints, but that the midpoints do not necessarily coincide with the galactic equatorial plane.
- The DGB model must be smooth with no small-scale structures that are indicative of discrete sources rather than diffuse background emission. This smoothness criterion is achieved by using gaussian basis functions for the latitude profiles.
- The DGB model has to be a true lower-envelope of the observed sky brightness distribution, i.e. the brightness of the model is everywhere less than the observed

sky brightness. This ensures that no "negative sources" are created in the residual map that is formed by subtracting the DGB model from the original map.

The technique used to derive the empirical DGB model from the skymap data is described in the next section.

6.1.1 The Model Fitting Technique

The technique used to derive the DGB model presented in this thesis is based on an algorithm that was originally developed by Flanagan (1981). Her original technique modelled the diffuse galactic emission by fitting a gaussian profile to latitude scans through the galactic plane, but this did not guarantee a lower-envelope DGB model. The modifications made to the original Flanagan algorithm include:

- The fitting of multiple gaussian components at each latitude.
- Lower-envelope fitting of the profiles, rather than standard least-squares fitting.
- An interactive graphical user interface which allows some manual control over the profile fitting procedure.

The modelling procedure consists of two stages: (1) the creation of smooth, lower-envelope latitude profiles at discrete galactic longitudes separated by a pre-determined spacing and (2) the use of cubic-spline interpolation between these profiles to create a lower-envelope surface (the DGB model). `GALGAUSS.F` is an interactive computer program with a graphical user interface that was written to implement this procedure, and its operation is described below.

Consider the original radio map to be binned into a rectangular array, $\mathrm{MAP}_{i,j}$, using a simple Cartesian projection (Green, 1998) of the galactic coordinate system. If the longitude and latitude grid spacings for this map are $\Delta\ell$ and Δb then the galactic coordinate of pixel (i, j) is $(i \times \Delta\ell, j \times \Delta b)$. The FORTRAN convention for rows and columns is used in this discussion, i.e. i indices the columns and j indices the rows.

The first stage of the processing is to pass a decimating, running-minimum filter along each row of the map array. Mathematically this is represented by:

$$\mathrm{RAW}_{k,j} = \min\left(\mathrm{MAP}_{i,j}; |(i \times \Delta\ell) - (k \times \mathrm{StepWidth})| \leq \mathrm{MinWidth}/2\right) \qquad (6.1)$$

MinWidth and StepWidth are independent parameters chosen experimentally to produce the best final results for a given input map. Usually StepWidth is chosen to be

$\approx \frac{1}{2}$ MinWidth. The output array $\mathrm{RAW}_{k,j}$ has fewer columns than $\mathrm{MAP}_{i,j}$ because of the decimation by a factor of (StepWidth/$\Delta\ell$) implied by equation 6.1. The running-minimum filter is the first of two mechanisms used to ensure the model is a true lower-envelope of $\mathrm{MAP}_{i,j}$

An interactive procedure is then used to fit a second order polynomial and up to five gaussian profiles to each column of $\mathrm{RAW}_{k,j}$. The functional form of the resulting profiles is therefore:

$$\mathrm{PRO}_k(b) = A_k + B_k b + C_k b^2 + \sum_{n=1}^{5} D_{k,n} \exp\left(\frac{(b - E_{k,n})^2}{2F_{k,n}^2}\right) \tag{6.2}$$

where up to 18 parameters are to be determined in the fitting procedure. As a second measure to ensure that each resulting profile, $\mathrm{PRO}_k(b)$, is a lower-envelope of the corresponding column in $\mathrm{RAW}_{k,j}$ the following modified least-squares cost-function is used:

$$\begin{aligned} \chi_k^2 = \textstyle\sum_{j=\min(j)}^{\max(j)} & \quad [\mathrm{RAW}_{j,k} - \mathrm{PRO}_k(j \times \Delta b)]^2 \times W_{k,j} \\ W_{k,j} = 1 & \quad \text{if} \quad [\mathrm{RAW}_{j,k} - \mathrm{PRO}_k(j \times \Delta b)] > 0 \\ W_{k,j} = 20 & \quad \text{if} \quad [\mathrm{RAW}_{j,k} - \mathrm{PRO}_k(j \times \Delta b)] < 0 \end{aligned} \tag{6.3}$$

The non-linear optimization required for this fitting procedure is implemented using a standard quasi-Newton technique provided by the IMSL subroutine library (IMSL, 1978). The gaussian basis functions ensure that the latitude profiles are smooth and that they decrease monotonically with increasing $|b|$ (outside of a small region near the galactic plane). The polynomial is required to account for offsets and very large scale gradients in the map.

The interactive interface provided by `GALGAUS.F` allows the user to "guide" the fitting procedure by specifying initial values for the gaussian profile parameters and the number of gaussian components to be fitted. An interactive, sequential fitting procedure is necessary because of the many local minima in the χ^2 surface. The quadratic polynomial and a single gaussian profile are fitted first to model the very high latitude sections of the RAW scan. Up to four additional gaussian profiles are then fitted sequentially, starting with the modelling of the broad "wings" of the galactic ridge and progressing towards the narrow structures near the galactic equator.

Once the profiles have been generated at every required longitude step, a fully-sampled background model, $\mathrm{BKG}_{i,j}$, is constructed by using one-dimensional cubic splines along

constant-latitude lines to interpolate intermediate profiles at longitude intervals of $\Delta\ell$ between the $\mathrm{PRO}_k(b)$ profiles.

In order to create a residual map with low dynamic range in which the faint, extended galactic radio sources are emphasized the following simple arithmetic subtraction is applied to the original map:

$$\mathrm{RES}_{i,j} = \mathrm{MAP}_{i,j} - \mathrm{BKG}_{i,j} \tag{6.4}$$

6.1.2 The Resulting DGB Model

The above procedure was applied to a map of the entire *SKYMAP* survey data set (plate C.1 in appendix C) smoothed to a resolution of 51-arcmin to match the resolution of the 408 MHz survey data (Haslam et al., 1982). After some experimentation to determine how to achieve the best discrimination between the galactic background and discrete foreground sources, values of 10° and 5° were assigned to the MinWidth and StepWidth parameters respectively .

Figure 6.1 is a contour plot representation of a limited region of the DGB model that resulted from this procedure. A pseudo-colour representation of the entire model is shown in plate C.2 of appendix C. Step-like changes in the equatorial brightness and latitudinal extent of this model are quite evident in these graphical representations. These morphological features of the DGB model are discussed below with reference to theories of galactic structure and other studies of the DGB.

6.1.3 The Longitude Dependence of the Model

Figure 6.2 illustrates how the brightness of the galactic ridge varies as a function of galactic longitude for longitudes within the first and fourth galactic quadrants (i.e. the inner galaxy). The three lines in the graph represent the average brightness within a latitude range of ±3° determined from three different DGB models. The profiles represented by the solid and dashed lines were derived from DGB models created using the procedure described above. The solid line represents the *SKYMAP* 2326 MHz result while the dashed line represents the result obtained from the 408 MHz survey. The dotted line is the result obtained by Beuermann et al. using and independent analysis of the 408 MHz data. The brightness temperature scale of the 408 MHz profiles has been adjusted as described in the figure caption.

The three profiles match each other quite well, and also share similar features with the

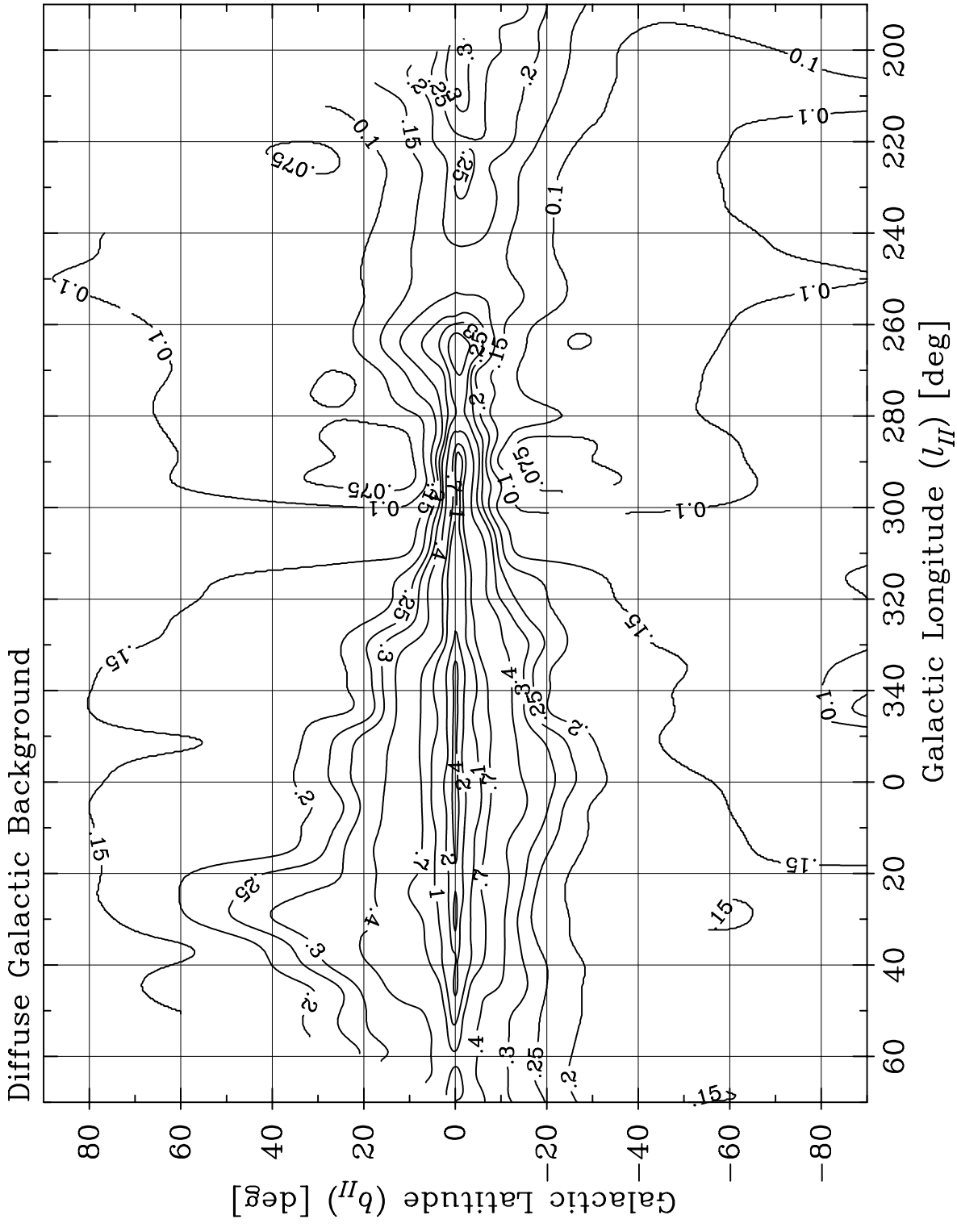

Figure 6.1: A contour map of the brightness distribution of the large-scale diffuse Galactic background model that was derived from the 51-arcmin resolution *SKYMAP* 2326 MHz survey data. The longitude range of this plot has been limited to a region where there is sufficient sky coverage to justify confidence in the model ($190° \leq \ell \leq 70°$). Contours are labelled at full-beam brightness temperatures of 0.075, 0.1, 0.15, 0.3, 0.25, 0.3, 0.4 0.7 1, 2, 4 K. A pseudo-colour rendition of the entire background model is presented in plate C.2 in appendix C.

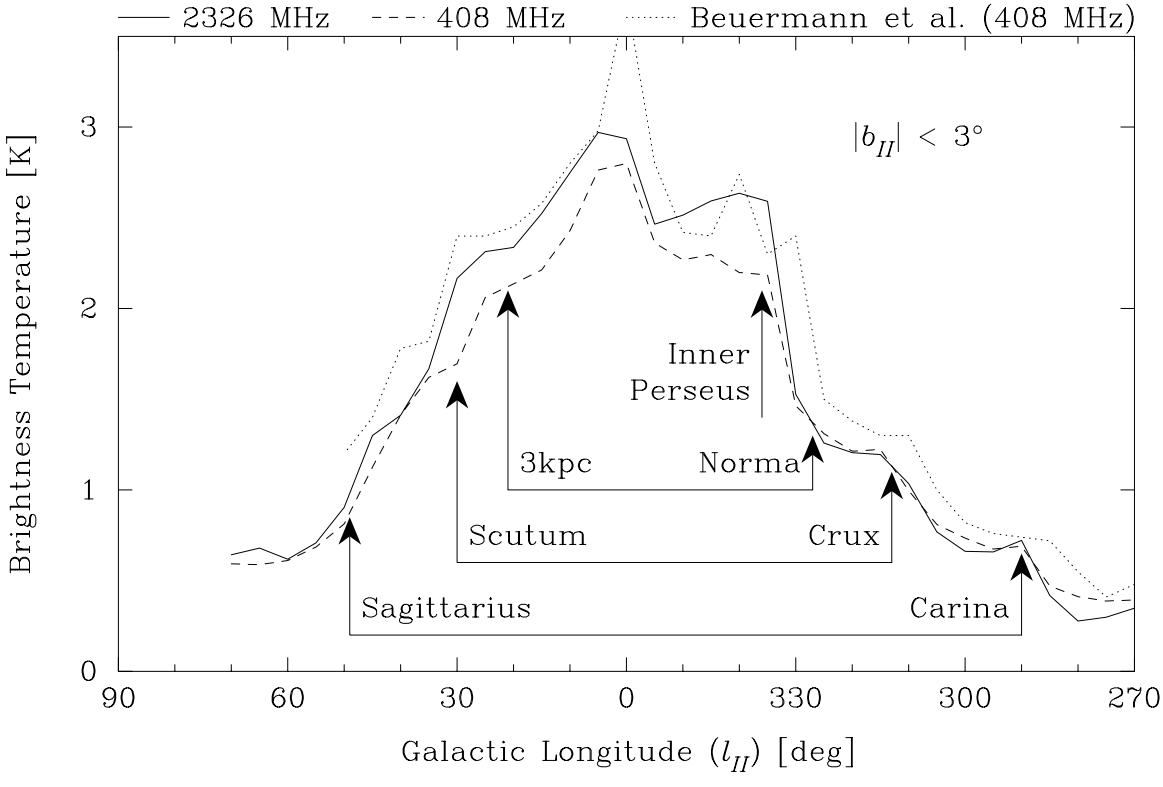

Figure 6.2: Galactic longitude dependence of the equatorial brightness of three different empirical DGB models obtained using different methods and data sets. The longitude profiles were obtained from three different background models, each averaged over the latitude range $|b_{II}| \leq 3°$. The solid and dashed profiles were determined from galactic background emission models obtained using the technique described in the text. The dotted line is the profile that Beuermann et al. (1985) obtained from their 408 MHz diffuse background model ($T_0(\ell)$ in their figure 1.). The brightness temperatures for the 408 MHz profiles have been scaled down by a factor of 101, which corresponds to a temperature spectral index of $\beta = 2.65$ for the frequency span between 408 MHz and 2326 MHz. The vertical arrows indicate the zero-phase tangent-points of the galactic spiral arms as determined by Vallée (1995). A horizontal line joining two arrows indicates that the associated tangent points are the left and right edges of the same spiral arm.

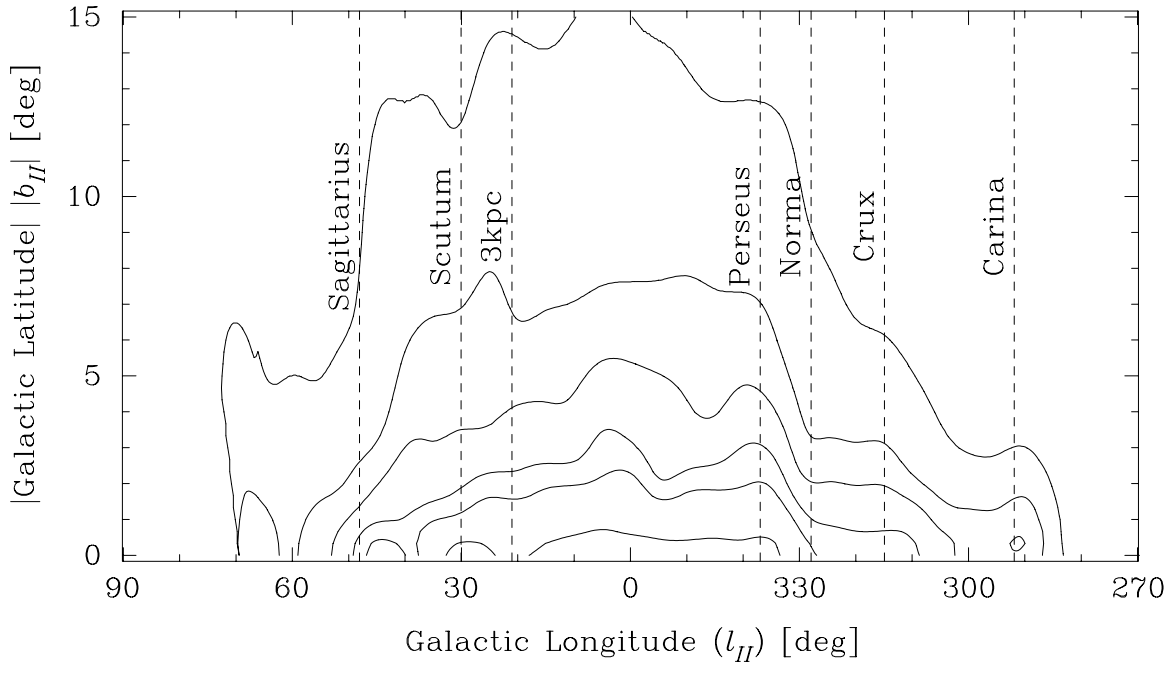

Figure 6.3: A contour map of the hemisphere-averaged brightness distribution of the 2326 MHz DGB model obtained by averaging the northern and southern galactic hemisphere data shown in figure 6.1. The map covers the inner two quadrants, but there are no data for $\ell_{II} > 70°$. The contour levels at 0.4, 0.7, 1, 1.5, 2 and 4 K were chosen to accentuate the steps in the width of the DGB model. The vertical dashed lines indicate the zero-phase tangent-points of the galactic spiral arms as determined by Vallée (1995) (see figure 6.2).

$b = 0°$ profile obtained by Phillipps et al (1981a) from the 408 MHz data. The fact that the solid and dashed lines in figure 6.2 follow each other quite closely indicates that the scaling of the 408 MHz data, and hence the assumed spectral index of $\beta = 2.65$, is probably representative of the galactic ridge emission.

Distinct steps in amplitude that suggest that the galactic disc has ring or spiral structures are apparent in the profiles, particularly in the fourth galactic quadrant. Comparison of the locations these steps can be made with the tangent directions of the spiral arms of the galactic model represented in figure 5.1 of chapter 5. The arrows in figure 6.2 indicate the longitudes of the zero-phase tangents of the various spiral arms and should therefore correspond to horizontal or slightly peaked sections of the profiles if the spiral model is consistent with the DGB models.

In the fourth galactic quadrant good correlations are apparent for the Inner-Perseus, Crux and Carina arms, but the Norma arm does not appear to be represented in the data. The situation in the first quadrant is less certain, presumably because the spiral structure is more crowded in this quadrant.

Figure 6.3 is the result of folding the 2326 MHz DGB model about the galactic equator

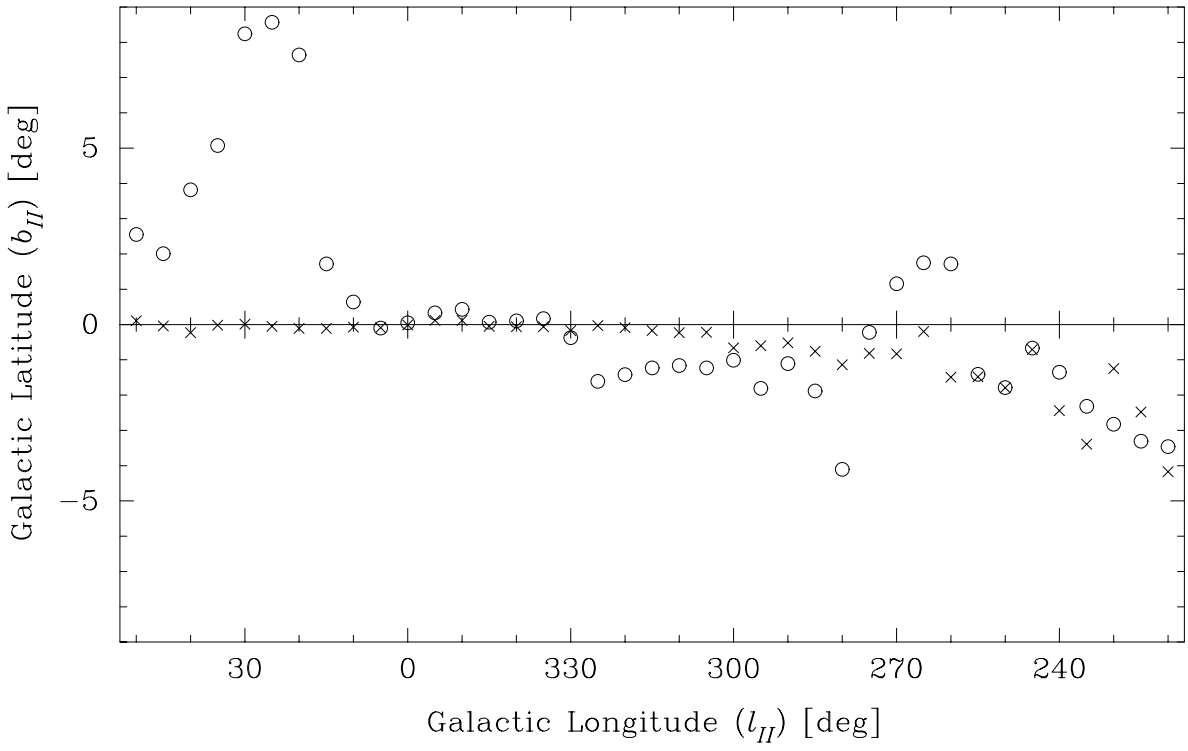

Figure 6.4: Galactic longitude dependence of latitude asymmetries in the 2326 MHz empirical DGB model. The crosses depict the positions of the maxima of the $\mathrm{PRO}_k(b)$ profiles fitted at 5° longitude intervals. The open circles demarcate the positions of the centroids calculated for each $\mathrm{PRO}_k(b)$ latitude distribution.

and averaging the northern and southern galactic hemispheres. The contour levels were chosen to accentuate the steps in the latitude-width of the DGB, and the expected positions of the spiral arm tangent directions are indicated. In the fourth quadrant the expected positions of the Inner-Perseus, Crux and Carina arms are near step-like features in the latitude extent of the DGB, matching the result for the equatorial brightness profile. Again the Norma tangent direction has no apparent feature associated with it. There is some evidence that the low-brightness contours in the first quadrant reveal the Sagittarius and Scutum arms.

The equatorial brightness profile and latitude distribution of the DGB are broadly consistent with the spiral model presented in figure 5.1 but the logarithmic spiral is perhaps an oversimplification of the global galactic structure, particularly in the first quadrant. In contradiction with figure 5.1 it appears that the inner extension of the Perseus arm continues into the two-arm region, while the Norma arm is truncated.

Figure 6.4 depicts the longitude dependence of north-south asymmetries in the $\mathrm{PRO}_k(b)$ profiles used to generate the 2326 MHz DGB model. From the longitude distribution of the peak positions (represented by the crosses) it is clear that the inner part of the galactic

plane is coincident with the galactic equator, but that for $220° \leq \ell \leq 300°$ there is a definite trend towards southern latitudes. This displacement is consistent with the galactic warp seen in the atomic, molecular and dust phases of the ISM and discussed in chapter 5.

The open circles in figure 6.4 represent the latitudes of the centroids calculated for each DGB profile. The centroid is sensitive to the faint, high-latitude wings of a DGB profile, and is therefore a diagnostic for local asymmetries in the galactic structure that are represented in the DGB model. The feature centred on $\ell = 25°$ that extends to positive latitudes is a consequence of the contamination of the DGB model by the emission from the North Polar Spur (NPS). This contamination is unavoidable because of the large extent of the NPS in both longitude and latitude. The trend towards negative latitudes for $\ell < 260$ is a result of the large-scale emission associated with the Orion complex. Assuming that the NPS is a remnant of a supernova (or multiple supernovae) in the Sco-Cen association, both of these asymmetries can be attributed to the Gould Belt system discussed in chapter 5.

6.1.4 The Latitude Dependence of the Model

Figure 6.5 presents a representative selection of the $\mathrm{PRO}_k(b)$ profiles determined from the 2326 MHz data using the technique described in section 6.1.1. The gaussian basis functions proved to be well-suited to the task of matching the shape of the lower-envelope profiles ($\mathrm{RAW}_{j,k}$) derived from the data and a conscious effort was made to use the minimum number of gaussian components necessary to achieve a satisfactory fit. It is apparent from figure 6.5 that towards the inner galaxy the latitude distribution of the galactic disk is the superposition of a number of gaussian components with different scale-widths.

This multi-component model for the galactic disk challenges the assumption by Beuermann et al. (1985) that only two gaussian components are necessary for a satisfactory model of the latitude distribution of the disk emission. They interpret the two gaussian components that they fitted to the disk profile as the synchrotron emission from a thin disk of cosmic rays associated with the "conventional" galactic disk and a more extended thick disk corresponding to the cosmic ray halo. They estimate that within the solar circle the equivalent widths of the thin and thick disks are 250 pc and 2.3 kpc respectively.

The analysis presented in this thesis suggests that the emission from the thin disk is actually composed of a number of components rather than just one, and that the thick disk emission identified by Beuermann et al. is not fundamentally different from the components of the thin disk. The various gaussian components are probably a manifestation of

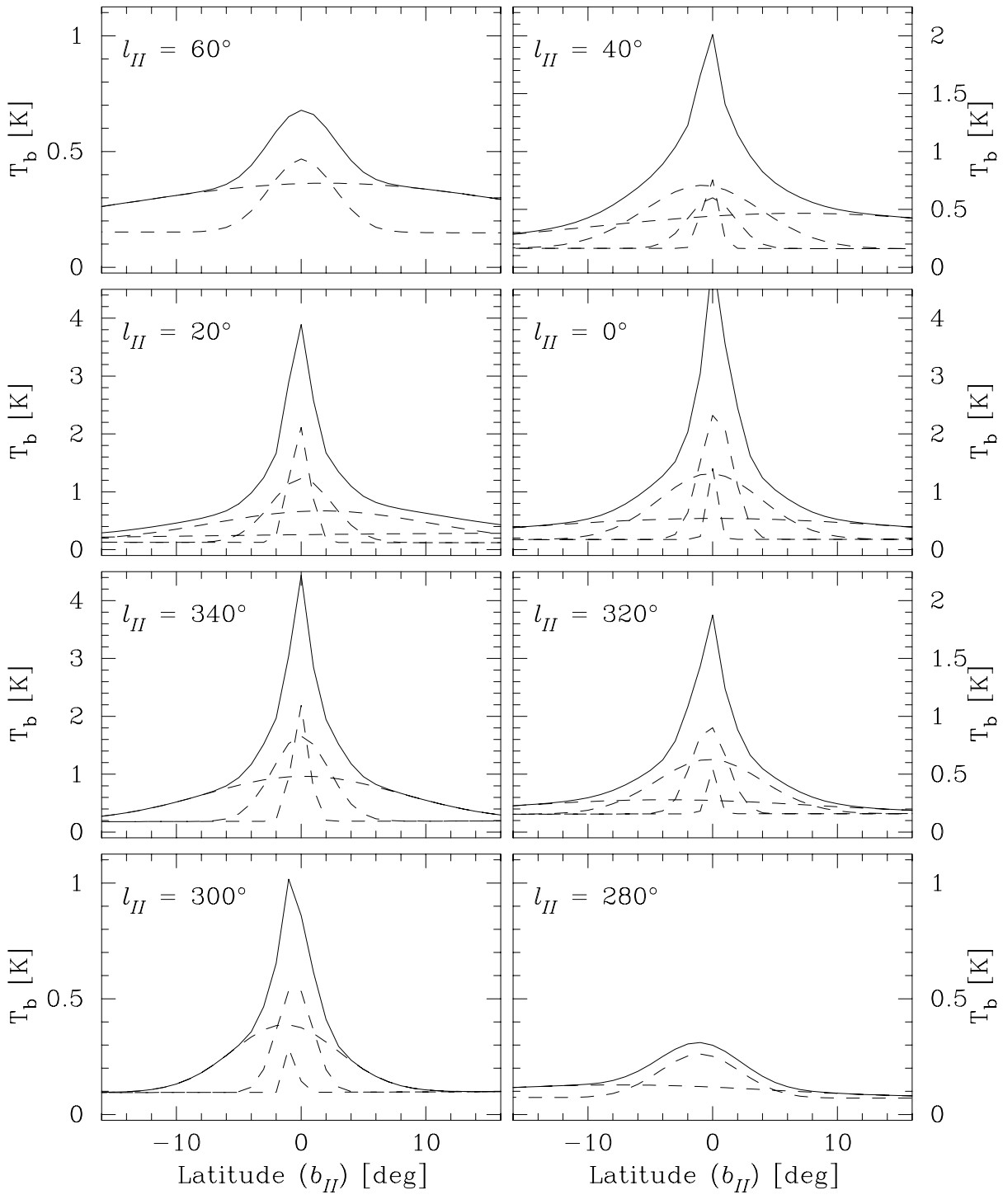

Figure 6.5: Latitude distributions at selected longitudes of the diffuse galactic emission model described in the text. Notice that the latitude range of the plots has been restricted to $|b| \leq 13°$, but that the $\mathrm{PRO}_k(b)$ profiles were fitted over the entire range of latitudes covered by the *SKYMAP* data. The solid lines represent the profiles derived from the 2326 MHz data at eight representative longitudes. The dashed lines are the individual gaussian components that were superimposed to construct the 2326 MHz profile at each longitude.

perspective with the thick disk component identified by Beuermann et al. being emission from a local feature and the more distant arms having a narrower angular extent.

The distribution of the halo emission across the sky is probably well-approximated by a monopole and a dipole component because of our viewing position inside the large and nearly-homogeneous cosmic ray halo. This very large scale emission is represented in the $\mathrm{PRO}_k(b)$ profiles by the quadratic polynomial in equation 6.2. The halo component appears as an almost constant offset in the graphs of figure 6.5 because of its very broad latitude extent and the restricted latitude range of the abscissa.

A simple analysis was devised to test the hypothesis that the distinct gaussian components of the $\mathrm{PRO}_k(b)$ profiles represent the emission from individual spiral arms being viewed in perspective. Assuming that the spiral arms have a gaussian z-distribution for their synchrotron emissivity with a full-width at half-maximum (FWHM) of Z pc, the heliocentric distance to an arm can be estimated from the *angular* FWHM, θ, of the gaussian profile:

$$R_\odot = \frac{Z}{2\tan(\theta/2)} \tag{6.5}$$

Figure 6.6 shows the results obtained using this simple analysis with $Z = 250$ pc, the width of the thin disk calculated by Beuermann et al. (1985). The overall distribution of the filled triangles matches the extent of the main spiral features in the model and, although no claim is made that the points lie along the model spiral pattern, there is a tantalizing association between the filled triangles and the spiral lines. The cluster of points round the position of the sun is probably a manifestation of the local Orion arm, but this analysis is too crude to determine the shape or structure of this feature.

6.2 The Residual Map

Plate C.3 in appendix C is a pseudo-colour image of the residual map resulting from the subtraction of the DGB model (plate C.2) from the original 2326 MHz map data (plate C.1). Plate C.4 represents the residual map obtained by repeating the identical DGB procedure on the Fourier filtered map generated by Davies et al. (1996) from the 408 MHz survey (Haslam et al., 1982). This filtered map has a much lower level of non-gaussian noise (striations) than the original data. The half-power resolution of all of these images is 51-arcmin. Generally, the two residual maps look quite similar, but differences are apparent when details in the morphology are studied.

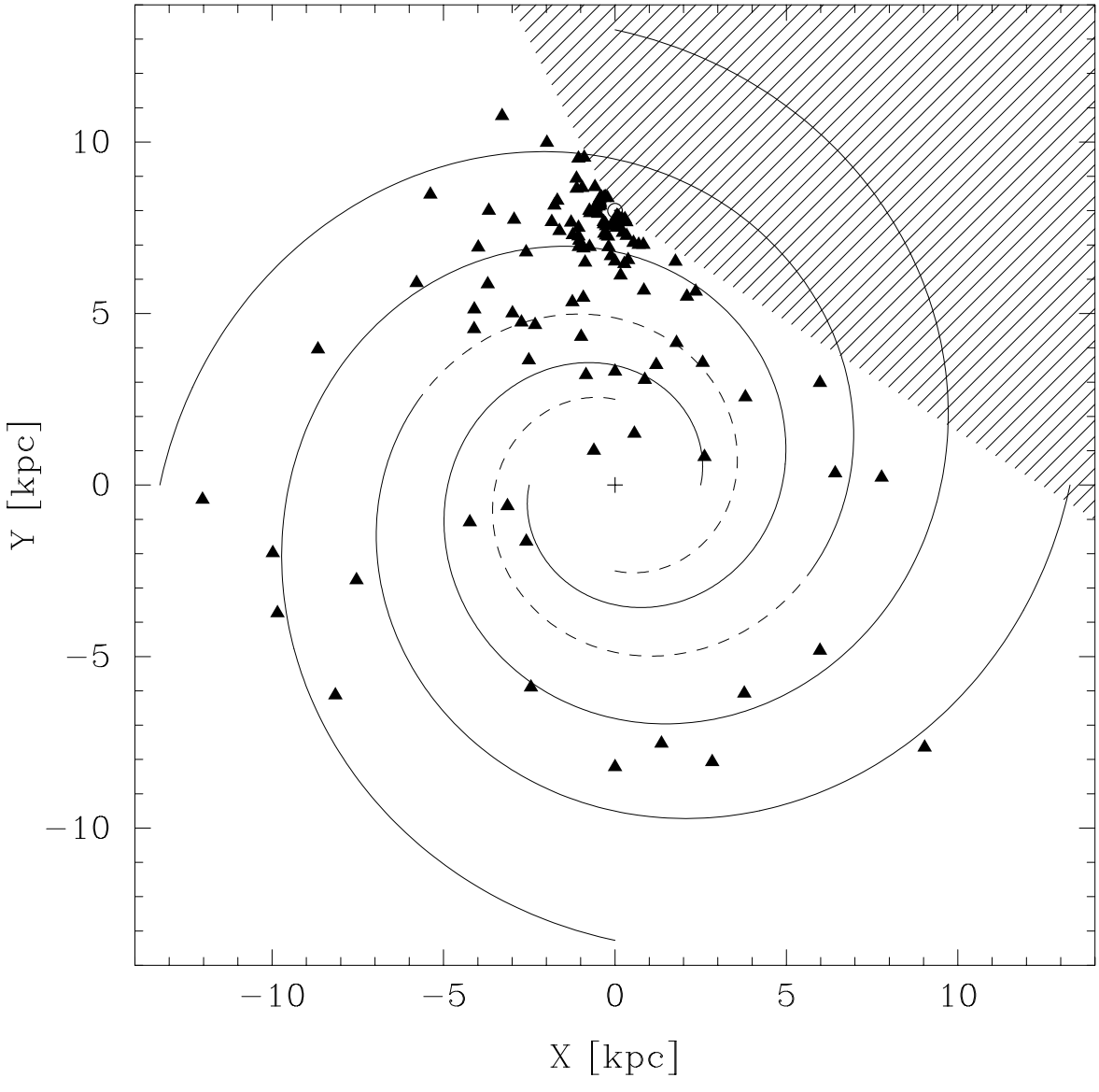

Figure 6.6: The filled triangles mark the positions of spiral arms determined from the widths of the individual gaussian profiles used to construct the DGB model. The distances from the sun were calculated using the simple assumption that the synchrotron emission associated with the spiral arms has a half-width of 250 pc over the entire face of the galaxy. The solid and dashed lines tracing the model spiral structure are the same as those in figure 5.1 of chapter 5. The hatched region of the plot represents the area of sky that the *SKYMAP* survey does not cover.

The effect of the contrast enhancement achieved by the diffuse background subtraction is immediately apparent in both the 408 MHz and 2326 MHz residual maps. Numerous low-brightness features that were not discernible in the original maps become visible in the residual images because of the reduction in the dynamic range of the brightness distributions.

The high contrast residual images reveal the good quality of the *SKYMAP* survey data. "Scanning effect" striations and baseline instability are inevitable in such large-scale maps because of the susceptibility of long scans to ground spillover and weather effects. Davies et al. (1996) have discussed the effects of such artifacts in the 408 MHz (Haslam et al., 1982) all-sky survey and 1420 MHz (Reich, 1982; Reich and Reich, 1986) northern hemisphere survey. They emphasize the need for high-quality, low-frequency ($\nu < 10$ GHz) surveys which can be used for subtracting Galactic contamination from cosmic microwave background data. Even with the modest smoothing applied to the image in plate C.3, there is little evidence of striations parallel to the scanning direction. There are some very faint, broad striations that appear to radiated out from the SEP. These artifacts are symptoms of baseline instabilities which probably result from temporal variations in the terrestrial foreground emission.

The temperature scale for the 408 MHz residual map is 100 times less sensitive than that for the 2326 MHz map. This temperature ratio corresponds to a temperature spectral index of $\beta = 2.65$ which is near the median value for SNRs. Objects appearing more prominently in the 2326 MHz map are likely to be thermal sources, while those appearing more prominently in the 408 MHz map are very steep spectrum sources.

6.3 Very Large-scale Structures

This section discusses very large scale and high latitude structures that have been identified in the residual 408 MHz and 2326 MHz maps. There are numerous structures visible in the residual map at low and intermediate latitudes ($|b| < 15°$), but these are somewhat confused because of the relatively low resolution of the map and the density of sources near to the galactic plane. The identification of these sources using a higher resolution version of the 2326 MHz residual map will be discussed in chapter 8.

There are no immediately obvious large-scale radio continuum structures in the residual maps that suggest objects such as galactic worms, chimneys or fountains. Although there

are a great number of faint structures extending out of the galactic plane, most of these structures are curved and loop-like, rather than linear and perpendicular to the plane, as would be expected for worms and chimneys. Most of the visible structures are probably the emission from single or multiple SNR shells. There is some evidence that the incomplete shells open out towards higher latitudes, which may indicate some form of breakout process.

Both previously known and newly identified large-scale/high-latitude sources seen in the residual maps are discussed individually below. The "G$\ell \pm b$" naming convention has been used for the new sources. Small-circles identifying the new loop-like structures have been drawn as solid white lines on the colour plates. Barnard's Loop and the Lupus Loop are also shown as solid white circles and the classical galactic loops are represented by dashed white circles.

The Galactic Loops

These objects were discovered in early radio continuum maps and are believed to be old SNR shells (Hanbury Brown et al., 1960; Berkhuijsen et al., 1970; Berkhuijsen et al., 1971; Heiles et al., 1980). The small-circle parameters determined by Berkhuijsen et al. (Berkhuijsen et al., 1971) were used to plot the dashed lines tracing these galactic loops in plates C.1–C.5 in appendix C. Loop III does not intersect with the region of sky covered by the *SKYMAP* survey.

- **Loop I and the NPS**

  Loop I is an incomplete ring of emission that includes the North Polar Spur (NPS) and is the largest angular-diameter loop-like feature in the sky. The NPS is the bright, curved ridge extending northwards out of the galactic plane at $\ell \approx 25^\circ$ in the original and residual maps, and can also be seen as a contaminating feature in the DGB model (plate C.2). The NPS appears to "fracture" where it meets the galactic plane (Jonas, 1993), and the southern extension of the Loop I shell lies inside the small-circle fitted to the northern part of the shell. The southern extension appears to be braided, with a number of concentric filaments lying inside the outer edge of the shell. The NPS also has a faint concentric filament which is best seen near $\ell = 15^\circ$ between $b = +10^\circ$ and $b = +30^\circ$. Plate C.7 in appendix C presents a higher resolution image of the fracture region which shows a smaller spur at $\ell \approx 20^\circ$ extending from $b = +3^\circ$ to $b = +15^\circ$. Faint filaments of emission link the NPS to this smaller spur, confirming their physical association. Sofue and Reich (1979) have made a detailed

map of the NPS at 1420 MHz, but the region they mapped did not include the smaller, displaced spur. The fracture in the NPS/Loop I is a feature that is often seen in other SNR shells (Velusamy, 1988), and is presumably the result of the shell colliding with a dense clump of ISM material. A large high-velocity HI cloud (HVC) is situated in the direction of the fracture, but this is probably a chance alignment of unrelated phenomena (Jonas, 1993).

- **Loop II**

  There is very little evidence of 2326 MHz emission associated with Loop II in the residual map in appendix C. Patches of emission at $\ell = 45°$, $b = -40°$ and $\ell = 60°$, $b = -70°$ lie close to the dashed line tracing Loop II, but they do not have the curved morphology that would be expected for fragments of the Loop II shell. It is more likely that the patch at $\ell = 45°$, $b = -40°$ is part of G27.5−21.0 which is indicated by a solid white circle and is discussed below. The implied faintness of the Loop II shell at 2326 MHz confirms its steep spectral index, which is a characteristic of old SNR shells. There is also no evidence for thermal radio emission associated with the H-α filaments discovered near the southern extension of the loop (Johnson, 1978).

- **Loop IV**

  Loop IV is visible in the residual maps as an 40° diameter incomplete shell of emission centred on $\ell = 315°$, $b = +48°$. The northern part of the shell is confused with part of the Loop I shell, and near $\ell = 350°$ the rather diffuse shell emission lies outside the fitted small-circle.

The Orion Complex

The 2326 MHz emission from the Orion complex of radio sources lying within the region $218° \geq \ell \geq 190°$, $-30° \leq b \leq -5°$ is shown as a pseudo-colour image in figure 6.7. This image was extracted from the residual map shown in plate C.3. All of the sources in this region can be assumed to be thermal because they appear much more prominently in the 2326 MHz residual map than the 408 MHz map. Reich (1978) mapped this region at 1420 MHz and has described the radio properties of these sources in some detail. The bright compact sources Orion A and Orion B are encircled by Barnard's Loop which has a diameter of 12.4° and is centred on $\ell = 206.5°$, $b = -19.0°$. The small-circle with these parameters is drawn on the residual maps. The thermal nature of Barnard's Loop is confirmed by

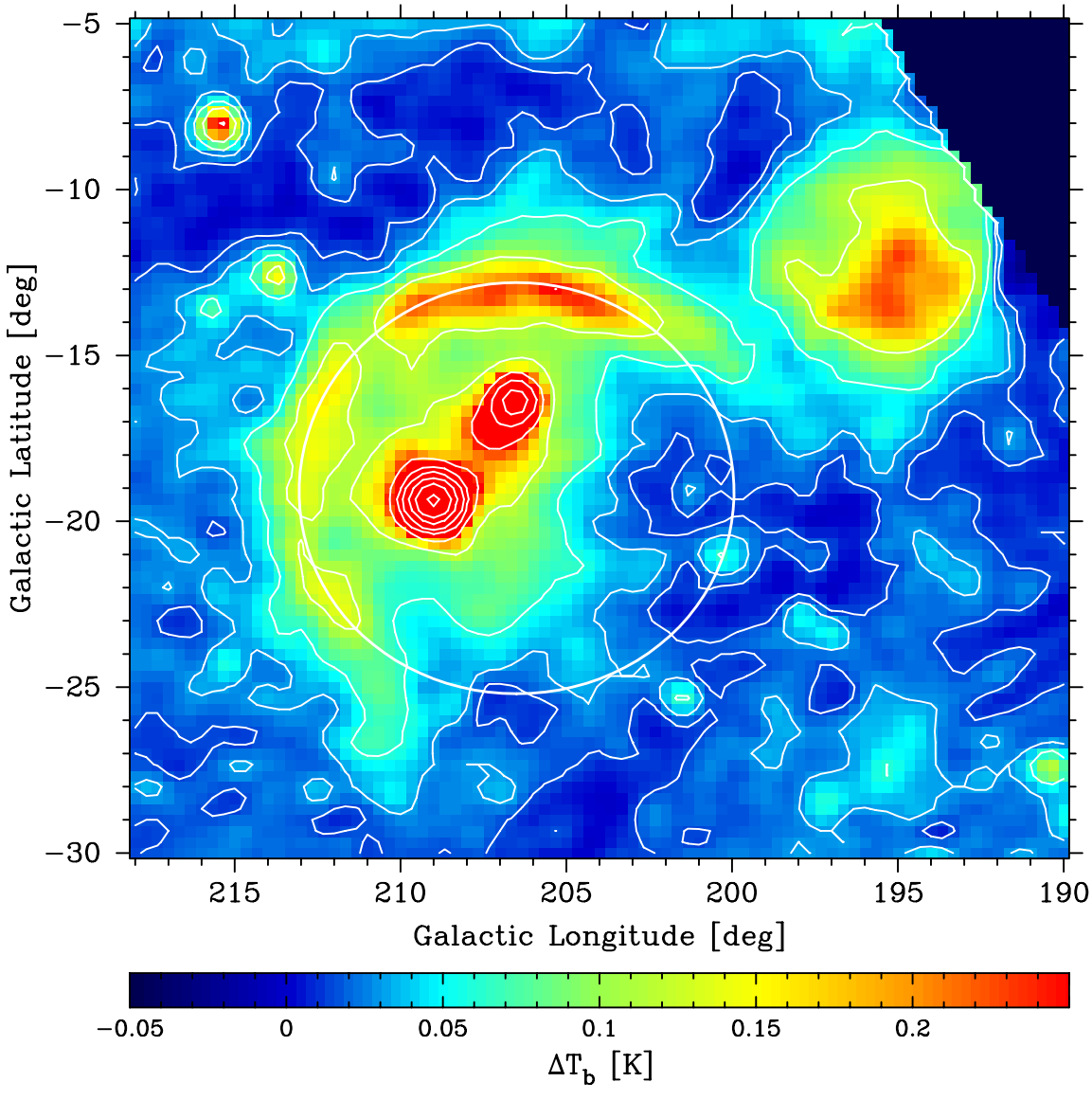

Figure 6.7: A pseudo-colour image of the residual emission from the Orion region. The relationship between brightness temperature and colour is indicated by the bar below the image. Contours of full-beam brightness temperature are drawn as white lines at levels of 0.015, 0.03, 0.06, 0.12, 0.25, 0.5, 1, 2, 4 and 8 K. The white circle traces the loop of emission associated with Barnard's Loop.

the detection of the H-142α recombination line from this semi-circle of emission (Gaylard, 1984a). The extended patch of thermal emission at $\ell = 195°$, $b = -12.5°$ is λ Orionis.

Loop in Apus/Circinus/Triangulum (G314.0−11.0)

This newly discovered feature is an indistinct shell of emission with a diameter of about 26° that is seen in both the 408 MHz and 2326 MHz residual maps. The residual 2326 MHz emission from this structure is shown as a pseudo-colour image in figure 6.8. The shell is not easily traced though the galactic plane, but the arcs extending below the plane form a coherent loop-like structure. The large diameter and high latitude of this object imply that it lies near the sun, and its morphology suggests that it is a SNR shell. A number of high-latitude pulsars are enclosed within the shell of emission, indicating that the object may be a multiple SNR bubble.

Loop in Centaurus/Lupus (G319.8+17.3)

The identification of this object as a SNR shell is rather speculative, but the semi-circular ridge of emission seen at both 408 MHz and 2326 MHz follows a small-circle with a diameter of 13° rather well. The residual 2326 MHz emission from this semi-circular structure is shown as a pseudo-colour image in figure 6.9. Haslam et al. (1981) discovered the spur of emission that extends from $\ell = 314°$, $b = +12°$ towards the emission from Cen A at $\ell = 311°$, $b = +18°$ in the 408 MHz survey, but did not link it with the arc of emission in Lupus near $\ell = 325°$, $+11° < b < +20°$. More recently Combi et al. (1998) have mapped the "Centaurus Spur" at 1420 MHz, which they claim is the superposition of a number of individual non-thermal sources rather than the emission from a single loop-like object. Unfortunately their map did not include the emission near $\ell = 325°$. If the apparent arc of emission is an incomplete shell of a SNR then the pulsar PLS1419−3920 near $\ell = 321°$, $b = +20.5°$ is a good candidate for the associated stellar remnant. The fact that the incomplete section of the loop is directed away from the galactic plane may indicate that the shell has broken out of the galactic gas layer.

The Lupus Loop (G330.0+15.0)

This SNR shell, which can be seen as a diffuse patch of emission in figure 6.9, has been well studied in the radio continuum (Milne, 1971; Milne and Dickel, 1974), HI line (Colomb and Dubner, 1982) and X-rays (Riegler et al., 1980), and is only included here for completeness.

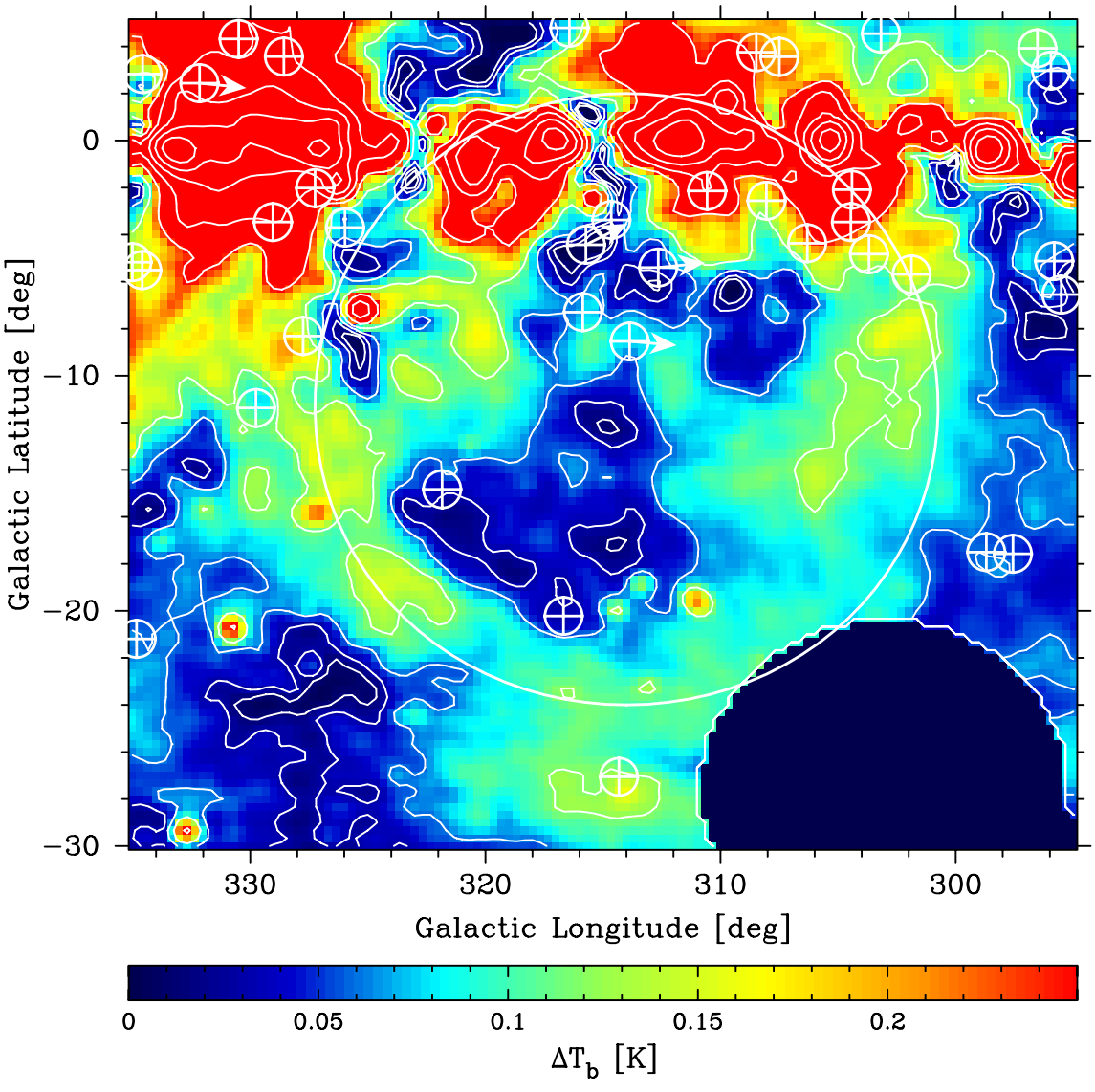

Figure 6.8: A pseudo-colour image of the residual emission from the Apus/Circinus/ Triangulum-Australe region. The relationship between brightness temperature and colour is indicated by the bar below the image. Contours of full-beam brightness temperature are drawn as white lines at levels of 0.015, 0.03, 0.06, 0.12, 0.25, 0.5, 1, 2, 4 and 8 K. The white circle traces the loop of emission associated with G314.0−11.0. The ⊕ symbols represent the positions of known pulsars (Taylor et al., 1993). The direction of pulsar proper motion is indicated by an arrow if it has been measured.

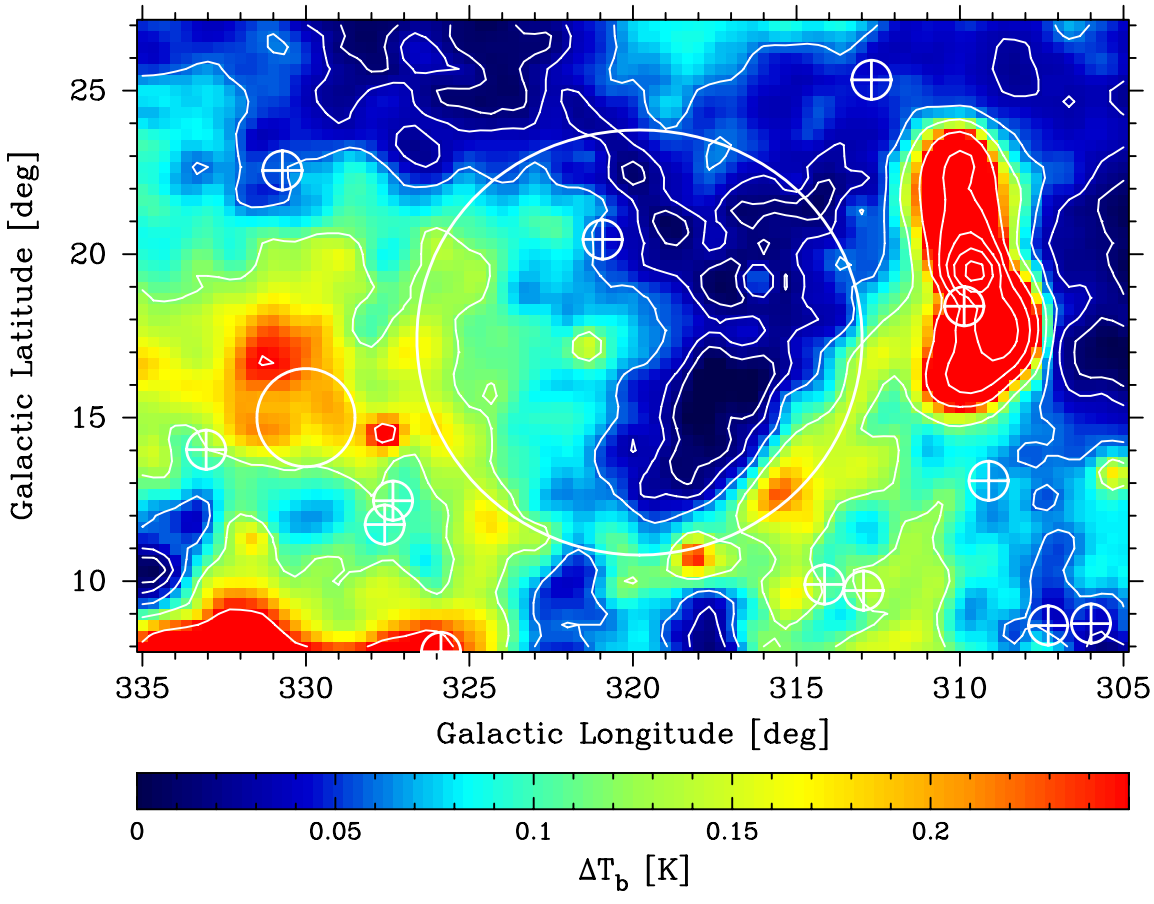

Figure 6.9: A pseudo-colour image of the residual emission from the Centaurus/Lupus region. The relationship between brightness temperature and colour is indicated by the bar below the image. Contours of full-beam brightness temperature are drawn as white lines at levels of 0.015, 0.03, 0.06, 0.12, 0.25, 0.5, 1, 2, 4 and 8 K. The smaller white circle is used to identify the given position of the Lupus Loop (G330.0+15.0) while the larger white circle traces the loop of emission associated with G319.8+17.3. The $\oplus$ symbols represent the positions of known pulsars (Taylor et al., 1993). The direction of pulsar proper motion is indicated by an arrow if it has been measured.

Diffuse emission extending above the catalogued extent of the SNR (Green, 1998) is visible in the pseudo-colour image (see figure 6.9).

The Scorpius/Ophiuchus Region

The radio continuum emission from this region has been encircled in both the 408 MHz and the 2326 MHz residual map colour plates to aid identification, but the circle is not intended to imply a loop morphology for the emission. Much of the emission from this area is associated with HII regions that are part of the Gould Belt system. The mixture of thermal and non-thermal sources in this area causes marked differences in the morphology of the emission at the two frequencies. Figure 6.10 is a pseudo-colour image of the residual 2326 MHz emission extracted from plate C.3.

The extended object that is centred on $\ell = 6°$, $b = +24°$ is the thermal emission associated with S27, the HII region surrounding ζ-Ophiuchi. Comparisons between the radio continuum and optical H-α emission for this object have revealed that the morphology is very similar at radio and optical wavelengths (Celnik and Weiland, 1988; Wright, 1989).

The 2326 MHz continuum emission from the Sco OB2 region is prominent in the right-half of the circle in figure 6.10. These sources have been studied extensively by others at 2326 MHz (Baart et al., 1980) and 1430 MHz (Combi et al., 1995), and H-142α recombination lines have been detected towards the HII regions associated with the stars σ Sco and τ Sco (Gaylard, 1984b).

Examination of the 408 MHz residual map (plate C.4) reveals a curved spur of emission extending out of the galactic plane near $\ell = 1°$. The upper section of this feature was discovered by Baart et al. (1980) in their 2326 MHz map of the Sco OB2 region. Sofue et al. (1989) speculated that this spur may be a jet from the galactic nucleus, but more recently Combi et al. (1995) made the more plausible interpretation that it is associated with a shock front caused by a single or multiple SNRs. This later interpretation is supported by evidence that an expanding HI shell surrounds the Scorpius region (Sancisi and Van Woerden, 1970; Olano and Pöppel, 1981; Combi et al., 1995), which is presumably driven by the population I objects in the local OB association.

The morphology of the feature at 2326 MHz is quite different from the structure seen at 408 MHz. Closer examination of the spur at higher resolution in the 2326 MHz data reveals that it may not be a single object, but rather the chance superposition of at least two separate spurs. In chapter 8 the lower section of the spur is identified as part of a SNR

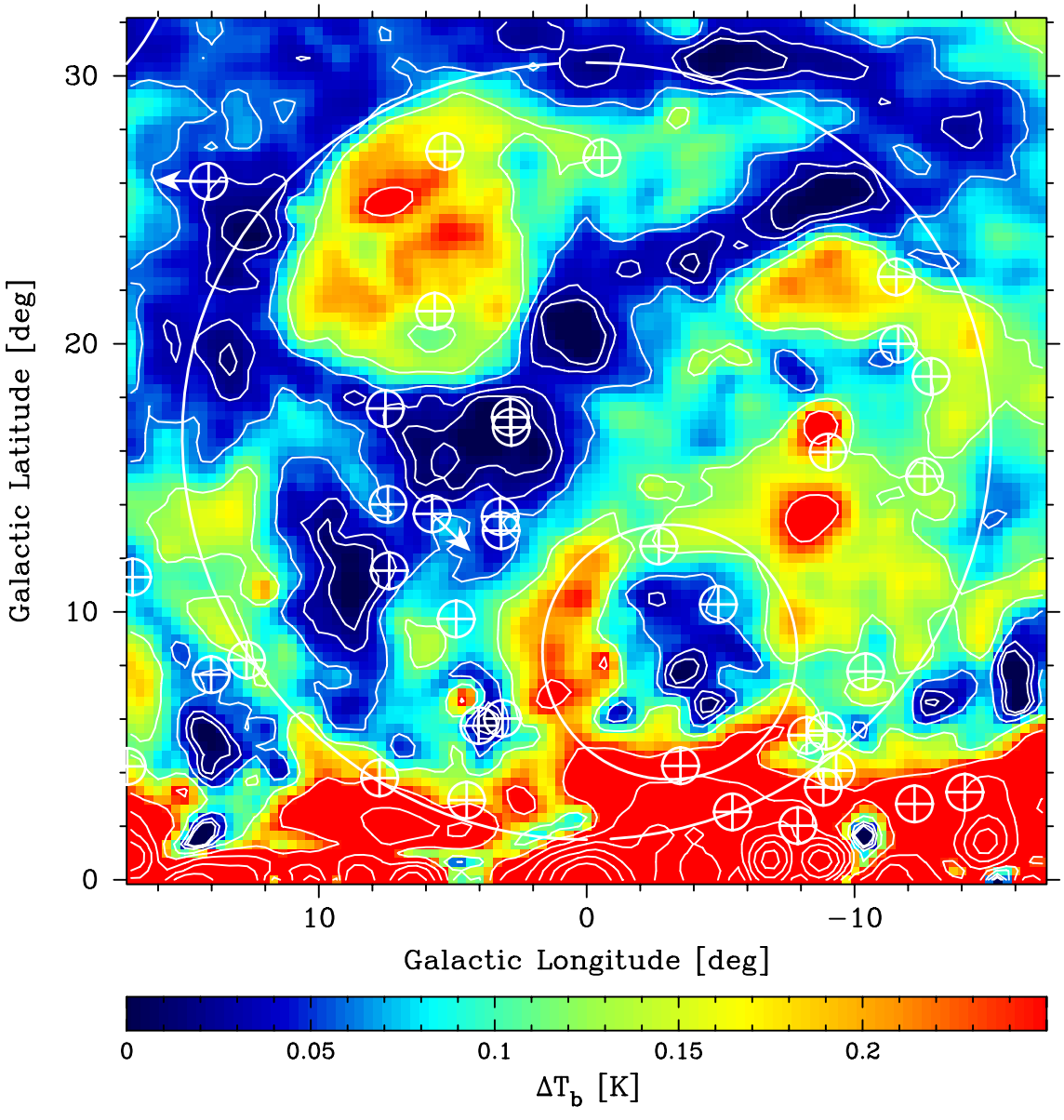

Figure 6.10: A pseudo-colour image of the residual emission from the Scorpius/Ophiuchus region. The relationship between brightness temperature and colour is indicated by the bar below the image. Contours of full-beam brightness temperature are drawn as white lines at levels of 0.015, 0.03, 0.06, 0.12, 0.25, 0.5, 1, 2, 4 and 8 K. The larger white circle encloses the various thermal emission features associated with ζ-Ophiuchi and the Sco OB2 association, while the smaller circle locates the SNR candidate G356.9+8.5 identified in chapter 8. The $\oplus$ symbols represent the positions of known pulsars (Taylor et al., 1993). The direction of pulsar proper motion is indicated by an arrow if it has been measured.

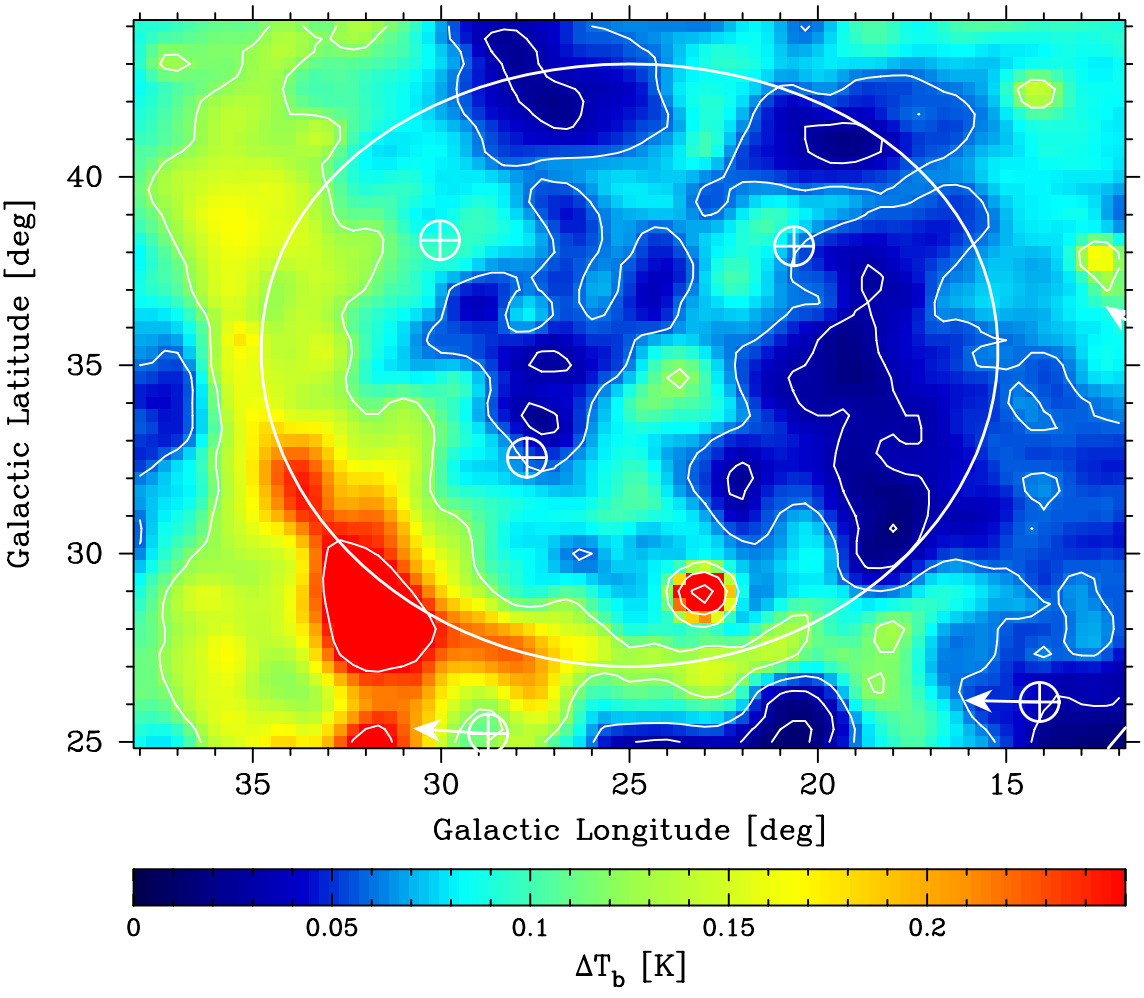

Figure 6.11: A pseudo-colour image of the residual emission from the Hercules region. The relationship between brightness temperature and colour is indicated by the bar below the image. Contours of full-beam brightness temperature are drawn as white lines at levels of 0.015, 0.03, 0.06, 0.12, 0.25, 0.5, 1, 2, 4 and 8 K. The white circle traces the loop of emission associated with G25.0+35.0. The $\oplus$ symbols represent the positions of known pulsars (Taylor et al., 1993). The direction of pulsar proper motion is indicated by an arrow if it has been measured.

candidate, G356.9+8.5, with a diameter of 9.5°. A circle tracing this source is drawn in figure 6.10.

Loop in Hercules (G25.0+35.0)

The emission associated with this semi-circular structure with a diameter of 16° is clearly visible in both the 408 MHz and the 2326 MHz residual maps. This structure was previously assumed to be part of the NPS. If this loop is a distinct SNR shell then its progenitor was probably a member of the Sco/Cen stellar association. Figure 6.11 shows that three known pulsars fall within the boundary of this very high latitude shell, indicating that this may be a multiple SNR bubble. The incompleteness of the shell towards higher latitudes may indicate that this bubble has broken through the disk gas into the halo.

Loop in Aquila (G31.0−11.0)

The 12°-diameter circle drawn in figure 6.12 represents a very speculative identification of a loop-like source below the galactic plane. The main motivation for the identification is the bright arc of emission at $\ell = 28°$, $b = -15°$ and the faint emission extending from this source towards the galactic plane. This feature has the same morphology in both the 408 MHz and 2326 MHz residual maps. It is quite possible that the bright arc is a more compact source rather than a segment of a large shell, but its position at such a high latitude is intriguing. There is no obvious association between known pulsars and the proposed shell or the bright arc.

Loop in Sagittarius (G27.5−21.0)

This faint, patchy loop of emission that traces a small-circle with a diameter of 44° is seen in both the 408 MHz and 2326 MHz residual maps in appendix C. Because of source confusion the apparent shell cannot be traced through the bright emission features associated with the galactic plane and the southern extension of Loop I. The pulsar PLS1944-1750 is positioned very close to the centre of this loop at $\ell = 22.3°$, $b = -19.4°$, and a number of other high-latitude pulsars are enclosed by the shell. The loop of emission appears to be quite continuous, even at high latitudes, so no breakout phenomenon is proposed for this object.

The "Heiles Bubble"

In a recent paper Heiles (1998) has presented tenuous evidence for a superbubble towards the Gum/Orion region. This highly speculative identification is based on faint signatures seen in large-scale HI, radio continuum, far-infrared and low-energy X-ray maps. He claims that a very faint, diffuse arc of emission that extends from below the Gum nebula ($\ell = 255°$, $b = -20°$) towards $\ell = 290°$, $b = -55°$ in both the 2326 MHz and 408 MHz residual maps (not evident in plates C.3 and C.4) is part of the superbubble shell. The sense of the curvature in this faint feature implies that it is more likely to be part of Loop I, rather than part of a shell surrounding the Gum/Orion region.

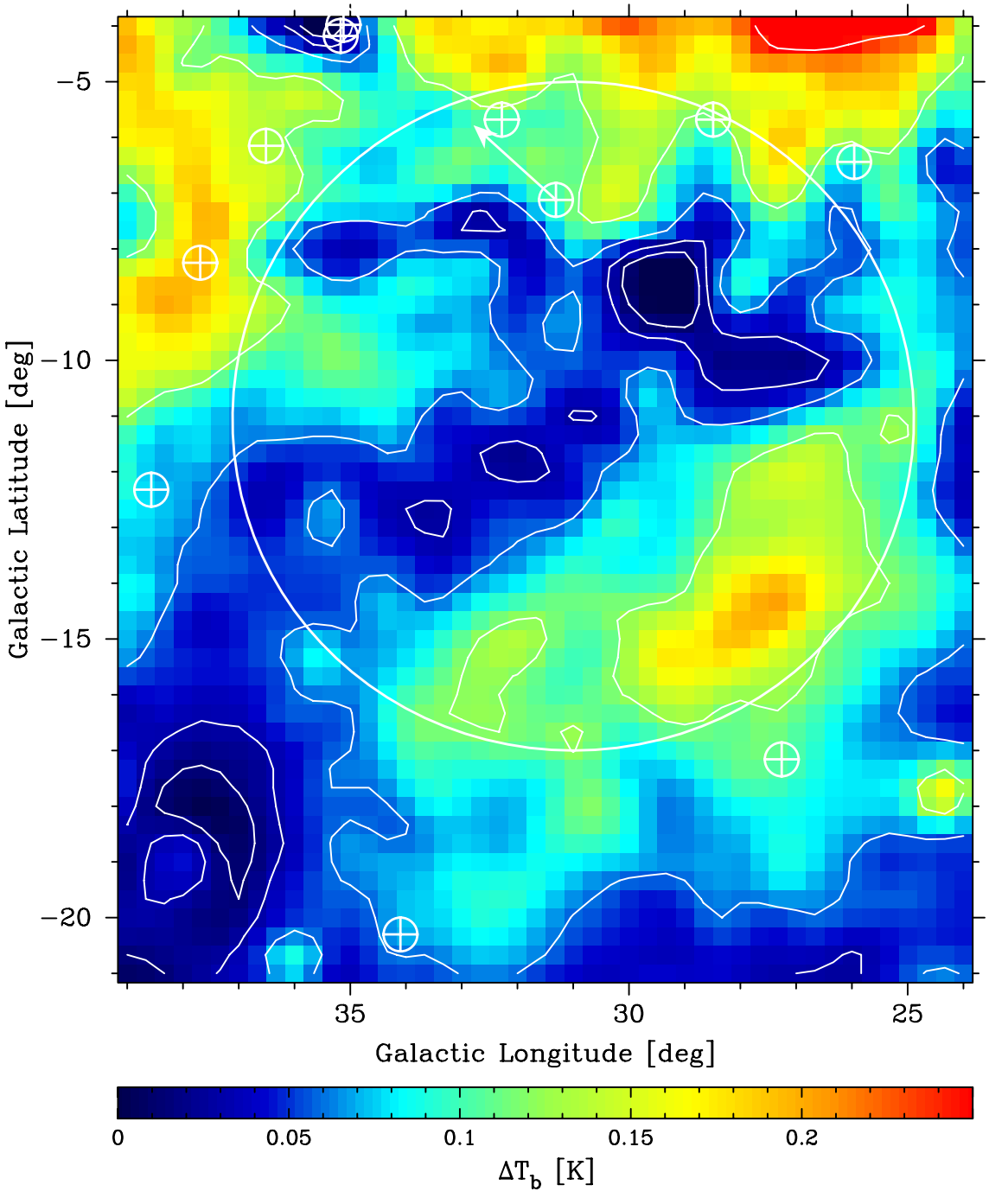

Figure 6.12: A pseudo-colour image of the residual emission from the Aquila region. The relationship between temperature and colour is indicated by the bar below the image. Contours of full-beam brightness temperature are drawn as white lines at levels of 0.015, 0.03, 0.06, 0.12, 0.25, 0.5, 1, 2, 4 and 8 K. The white circle traces the loop of emission associated with G31.0−11.0. The ⊕ symbols represent the positions of known pulsars (Taylor et al., 1993). The direction of pulsar proper motion is indicated by an arrow if it has been measured.

6.4 Summary of the Large-scale Morphology

The main conclusions drawn from the analysis of the morphology of the diffuse and large-scale galactic emission presented in this chapter are listed below.

- The diffuse galactic background emission has two components. The ridge component is associated with a synchrotron disk with a FWHM of ≈ 250 pc that traces the galactic spiral structure. The more isotropic component is associated with an extended, homogeneous cosmic ray halo.

- The brightness distribution of the ridge emission is consistent with current two-plus-four arm spiral models for the large-scale galactic structure.

- Both the galactic warp and Gould Belt are seen as asymmetries in the 2326 MHz galactic radio continuum emission.

- The high-latitude emission features that are identified as discrete sources, rather than components of the diffuse background, have a predominantly loop-like morphology, and are most probably nearby, large SNR shells. There is no convincing evidence for large-scale structures perpendicular to the galactic plane that may be associated with outflow mechanisms, but the incomplete shells of some of the SNR candidates may indicate breakout phenomena. This supports results from recent numerical MHD models that predict magnetic confinement of superbubbles if the scale-height of the galactic magnetic field exceeds that of the dense galactic gas (Tomisaka, 1998).

The SNR candidates identified in this chapter are carried forward to the statistical analysis of newly discovered SNRs in chapter 8.

6.5 Other Background Subtraction Techniques

Previously published background subtraction techniques that have been applied to radio continuum maps fall into three broad categories: Fourier filters, spatial filters and lower-envelope models. The characteristics of these techniques are discussed below and compared to the method used in this thesis.

The Fourier filter technique for background subtraction requires that a numerical two-dimensional Fourier transform be applied to the map under consideration. The large-scale features in the map are represented by low frequency components in the two-dimensional

Fourier transform (u-v) plane and can be attenuated by applying a suitable multiplicative filter to the Fourier data. A reverse transform returns the resulting residual spatial map. This technique has been used to enhance faint radio objects near the galactic equator (Müller et al., 1987). Edge effects and ringing are major problems associated with Fourier techniques that can only be avoided by the careful choice of filter window functions. There is also no way to ensure that the residual map does not have non-physical negative temperature structures.

Spatial filters are usually implemented using a mask function which is passed over the input map. A standard convolution filter results if the mask function is a simple linear combination of the pixel values enclosed by the mask. Convolution filters are functionally equivalent to Fourier filters, and suffer the same problems. Non-linear mask functions are often used in order to overcome or mitigate the shortcomings of Fourier filters. Median filters have been particularly popular and have been used to emphasize the filamentary structures in HI, radio continuum, far-infrared and optical data (Koo et al., 1991; Reach et al., 1993; Waller and Boulanger, 1993).

The "Background Filter" (BGF) method developed by Sofue and Reich (1979) is a lower-envelope background modelling technique that has been used to emphasize radio continuum structures obscured by the gradient of the diffuse galactic emission (Sofue and Reich, 1979; Sofue, 1988; Sofue et al., 1989; Wright, 1989). This technique uses a linear mask operator in conjunction with a non-linear, iterative procedure in order to ensure that the residual map temperatures are everywhere positive. A drawback of this technique is that the limited extent of the mask results in a lower-envelope model that is contaminated by foreground sources.

The advantage that the background subtraction technique described in this thesis has over all of the above methods is that it has some foundation in physical reality. The specifications for the technique that were outlined in section 6.1 provide some measure of confidence that the derived DGB model is representative of the galactic background emission, and that the residual map contains only foreground sources and no artifacts generated by the technique.

Frequency [MHz]	Polarization?	Reference
19.7	no	(Shain, 1958)
85.5	no	(Sheridan, 1958)
406	no	(Cooper et al., 1965)
408	no	(Haslam et al., 1981)
960	yes	(Cooper et al., 1965)
1410	yes	(Cooper et al., 1965)
1435	no	(Combi and Romero, 1997)
2326	no	(Jonas et al., 1985)
2650	yes	(Cooper et al., 1965)
2700	yes	(Gardner and Whiteoak, 1966)
4750	yes	(Junkes et al., 1993)
5000	yes	(Gardner and Whiteoak, 1971)
5000	no	(Haynes et al., 1983)

Table 6.1: A list of maps of the extended emission from Centaurus A (NGC 5128). The centre column indicates whether linear polarization measurements were made.

6.6 Extragalactic Sources

This thesis is concerned with the radio emission from the Milky Way, but the most prominent extragalactic objects visible as extended emission features in the residual map are discussed briefly here.

6.6.1 Centaurus A

The radio galaxy Centaurus A, which is very prominent at $\ell \approx 310°$, $b \approx +20°$, was first associated with the peculiar elliptical galaxy NGC 5128 by Bolton et al. (1949). Table 6.1 lists published radio continuum maps of the extended radio lobes emanating from this conspicuous extragalactic source. Combi and Romero (1997) have used their 1435 MHz map in combination with other published data to determine a spectral index map for the extended lobe emission.

6.6.2 The Magellanic Clouds

The Large Magellanic Cloud (LMC) is quite prominent at $\ell \approx 280°$, $b \approx -32°$ in plate C.1. The Small Magellanic Cloud (SMC) is seen as a relatively faint extended source at $\ell \approx 300°$, $b \approx -45°$. Table 6.2 lists the recently published continuum maps of these nearby irregular companions to the Milky Way.

These maps have been used extensively in the analysis of the thermal and non-thermal

Frequency [MHz]	LMC	SMC	Pol?	Reference
45	yes	no	no	(Alvarez et al., 1987)
408	yes	yes	no	(Haslam et al., 1981)
1400	yes	yes	SMC	(Haynes et al., 1986)
2326	yes	yes	no	(Mountfort et al., 1987)
2450	yes	yes	LMC	(Haynes et al., 1991)
4750	yes	yes	LMC	(Haynes et al., 1991)
8550	yes	yes	no	(Haynes et al., 1991)

Table 6.2: Recent radio continuum maps of the Large and Small Magellanic Clouds. The second and third columns indicate which objects were mapped and column 4 indicates which objects, if any, were mapped in linear polarization.

emission from these galaxies (Loiseau et al., 1987; Klein et al., 1989), and for the study of the relationship between the radio and far-infrared (FIR) emission (Xu et al., 1992).

The Magellanic Stream (MS) is a bridge of gas linking the Magellanic Clouds to the Milky Way. It has been observed in the HI line (Mathewson et al., 1974), and diffuse optical H-α emission towards the MS provides evidence that some of the gas is ionized (Johnson et al., 1982). It is estimated that the emission measure of this ionized gas is less than 1.0 cm^{-6}.pc (Weiner and Williams, 1996), which translates to a brightness temperature of 1 mK at 2326 MHz. No evidence is seen in the *SKYMAP* maps for any radio continuum structures that correlate with the neutral or ionized MS gas.

Chapter 7

Spectral Analysis of the Galactic Emission

A modern trend in astronomy is to compare data from observations made at widely varying wavelengths. This chapter describes quantitative comparisons that were made between the *SKYMAP* 2326 MHz map and published brightness distribution data at other radio frequencies and at far-infrared (FIR) wavelengths. These comparisons were carried out in order to investigate the spectral characteristics of the galactic radiation.

The comparison data sets used in these investigations include:

- the 408 MHz all-sky radio continuum survey (Haslam et al., 1982)
- the 1420 MHz northern sky radio continuum survey (Reich, 1982; Reich and Reich, 1986)
- the 31 GHz and 53 GHz *COBE-DMR* maps (Bennett et al., 1996)
- the 60 μm *IRAS* FIR map (Neugebauer et al., 1984; Beichman et al., 1988)
- the 60 μm, 100 μm, 140 μm and 240 μm *COBE-DIRBE* FIR maps (Hauser et al., 1997).

The quantitative comparisons between these various data sets and the *SKYMAP* data were used for the following investigations of the galactic radio continuum emission:

- The testing of theories of cosmic ray transport and acceleration in the galactic disk and halo.
- The estimation of the galactic synchrotron foreground contamination in cosmic microwave background radiation (CMBR) measurements.

- The discrimination between thermal and non-thermal radio sources in the galactic plane.
- The estimation of the contribution of thermal emission to the high-latitude radio continuum emission.

The limitations imposed on these investigations by systematic errors in the data sets are discussed where appropriate.

7.1 Low Frequency Spectral Index

A review of the theoretical considerations relevant to the spectral index of the diffuse galactic emission was presented in chapter 5. That chapter also presented a summary, in the form of figure 5.3, of existing measurements of the galactic spectral index. The following section of the current chapter discusses an investigation of the centimetre-wavelength spectral index of the diffuse galactic emission that was made using the *SKYMAP* 2326 MHz map and other maps at lower frequencies.

7.1.1 Spectral Index using T-T plots

Attempts to determine the galactic spectral index by applying the equation:

$$\beta_{i,j} = - \frac{\log [T_{i,j}(\nu_1)/T_{i,j}(\nu_2)]}{\log(\nu_1/\nu_2)} \tag{7.1}$$

directly to absolute brightness temperatures derived from radio maps are extremely vulnerable to offsets in the map temperature scales (see section 7.1.2 below). These offsets are systematic errors that are introduced into the data from two sources:

- Observation and data reduction techniques that are not suited to the measurement of absolute sky temperatures.
- Ignorance of the extragalactic background contribution to the absolute sky brightness.

The effects of unknown offsets on the determination of the spectral indices of radio sources can be eliminated by using a differential technique such as the T-T plot method (Turtle et al., 1962). T-T plots are, nevertheless, susceptible to three sources of error:

- Errors in the full-beam brightness temperature scale factor (see section 4.6 in chapter 4).

- Anomalous brightness gradients in either or both of the maps at the two frequencies.
- Statistical errors for regions of the maps where the variance of the signal is less than the variance of the noise.

The last of these sources of error makes it impossible to use T-T plots to determine the spectral index of the galactic emission at high latitudes and towards the galactic anticentre where the galactic emission is nearly isotropic (i.e. where the signal variance is very small).

T-T plot analyses of the intermediate-latitude galactic emission were used to test the consistency of the temperature scales and baselines of the 408 MHz (Haslam et al., 1982), 1420 MHz (Reich, 1982; Reich and Reich, 1986) and 2326 MHz *SKYMAP* maps. These tests were made using three non-overlapping regions of sky which were covered by all three surveys and were not affected by thermal emission from the central disk or steep-spectrum emission from the galactic loops. Three spectral indices were derived for each region by comparing the three possible pairings of the maps. The three-way T-T plots for the three different regions are shown in figures 7.1 to 7.3. A comparison these T-T plots reveals the following:

- The spectral indices fitted to the 408/2326 MHz T-T plots have a smaller range of values ($2.66 \leq \beta \leq 2.78$) than the other two frequency pairings.
- The intercepts of the lines fitted to the 408/2326 MHz T-T plots are more consistent than the regression lines obtained for the other frequency pairings.
- The galactic spectral index is not expected to flatten at higher frequencies (see figure 5.3), but there is a consistent ranking of the spectral indices for all three regions: $\beta_{1420/2326} < \beta_{408/2326} < \beta_{408/1420}$

The following conclusions are drawn from these observations:

- The southern region of the 1420 MHz map that overlaps with the *SKYMAP* survey has anomalous baseline offsets and gradients which cause erroneous variations in the spectral index. This deduction is confirmed by an independent analysis by the *COBE* consortium (Kogut et al., 1996a).
- If the absolute base-level of the 408 MHz map is correct then the base-level of the 2326 MHz map is 15 ± 5 mK too high. The 2326 MHz-axis intercepts computed

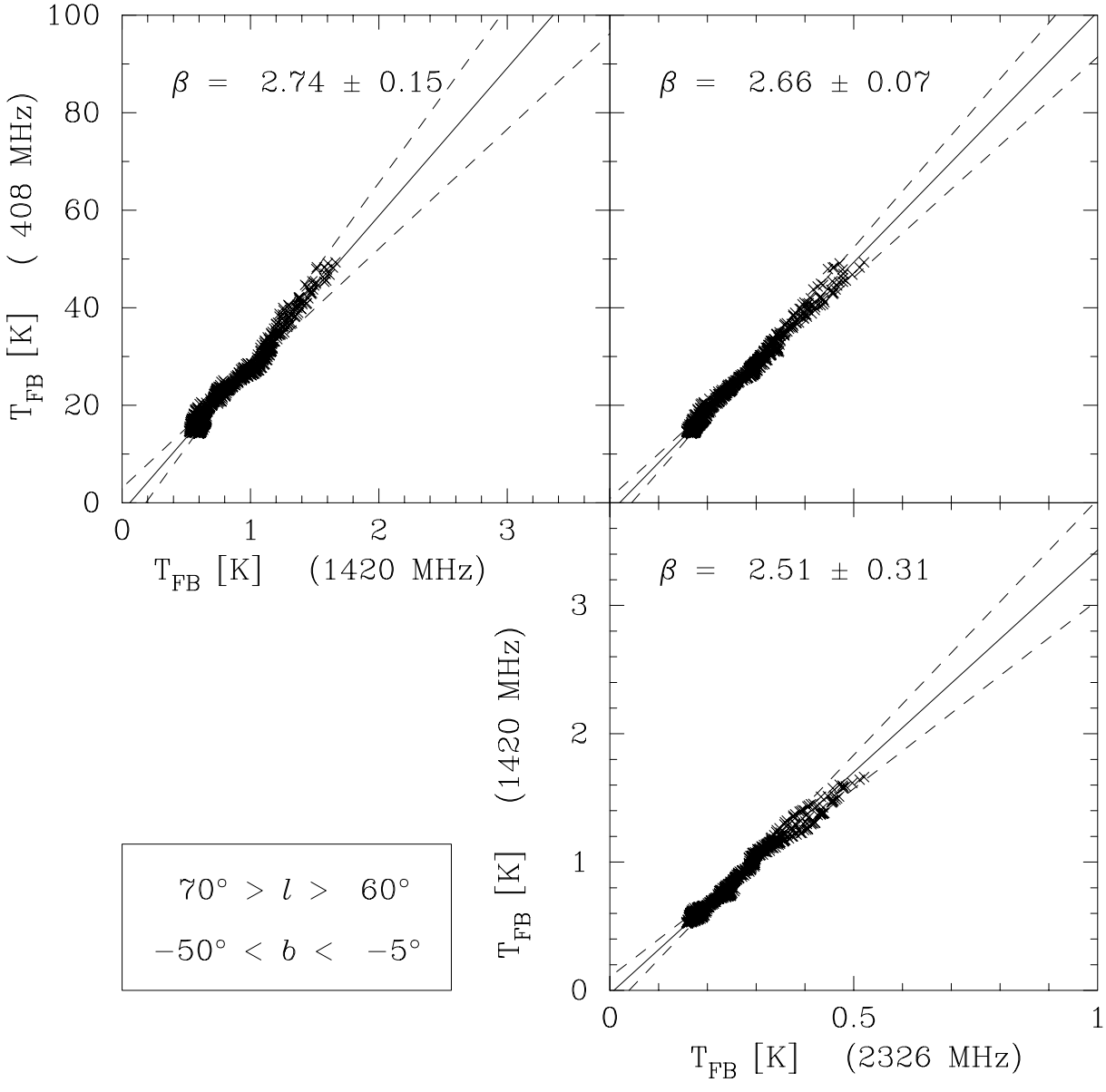

Figure 7.1: A three-way T-T plot of a region of sky common to the 408 MHz all-sky survey (Haslam et al., 1982), the 1420 MHz northern sky survey (Reich, 1982; Reich and Reich, 1986) and the *SKYMAP* 2326 MHz southern sky survey. The solid straight lines drawn through the data points represent the orthogonal regression (Isobe et al., 1990) solutions for each pair of frequencies. The dashed lines represent the $\pm 1\sigma$ spectral indices. Each plot is annotated with the fitted spectral index and associated formal error.

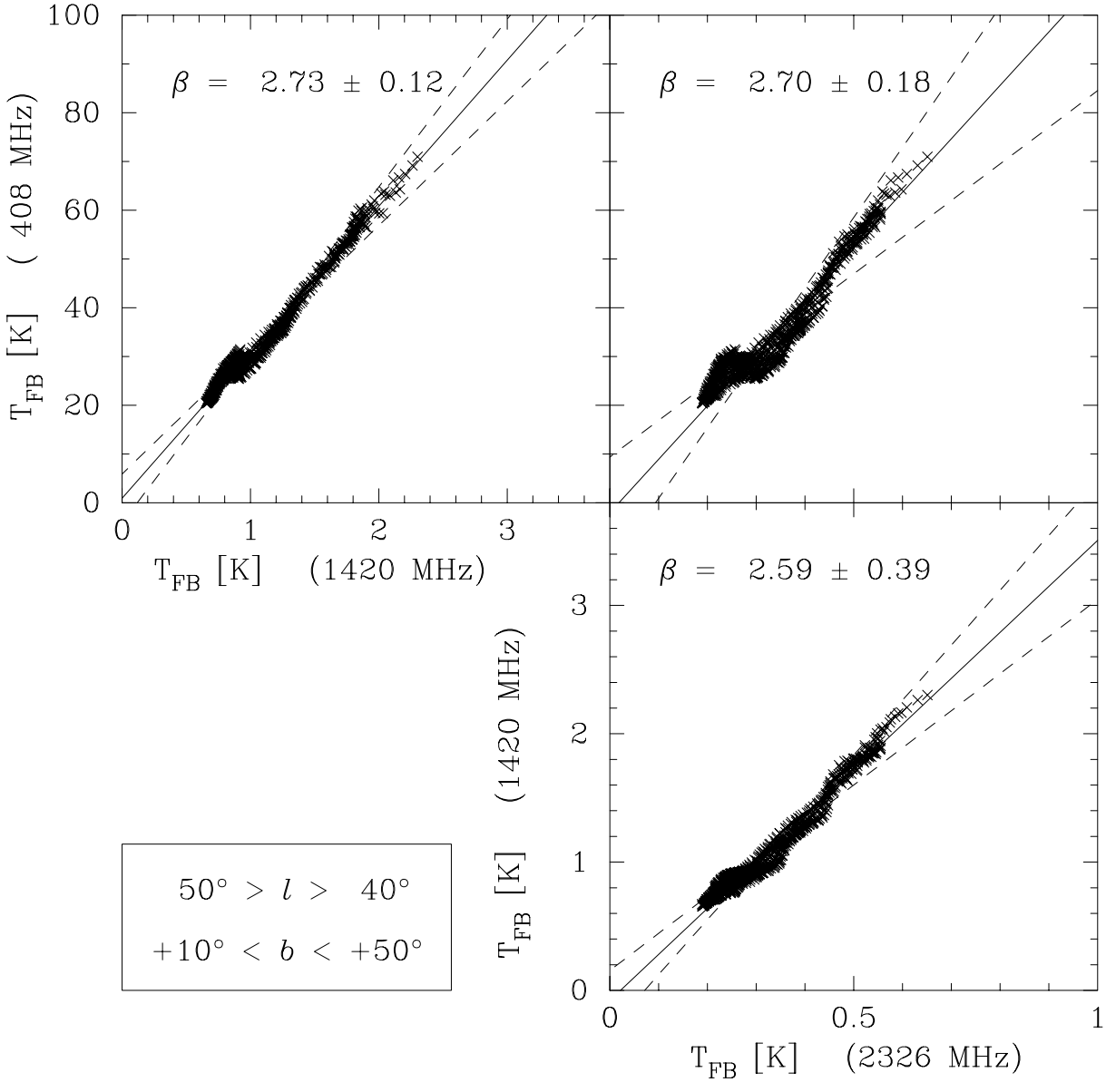

Figure 7.2: A three-way T-T plot of a region of sky common to the 408 MHz all-sky survey (Haslam et al., 1982), the 1420 MHz northern sky survey (Reich, 1982; Reich and Reich, 1986) and the *SKYMAP* 2326 MHz southern sky survey. The solid straight lines drawn through the data points represent the orthogonal regression (Isobe et al., 1990) solutions for each pair of frequencies. The dashed lines represent the $\pm 1\sigma$ spectral indices. Each plot is annotated with the fitted spectral index and associated formal error.

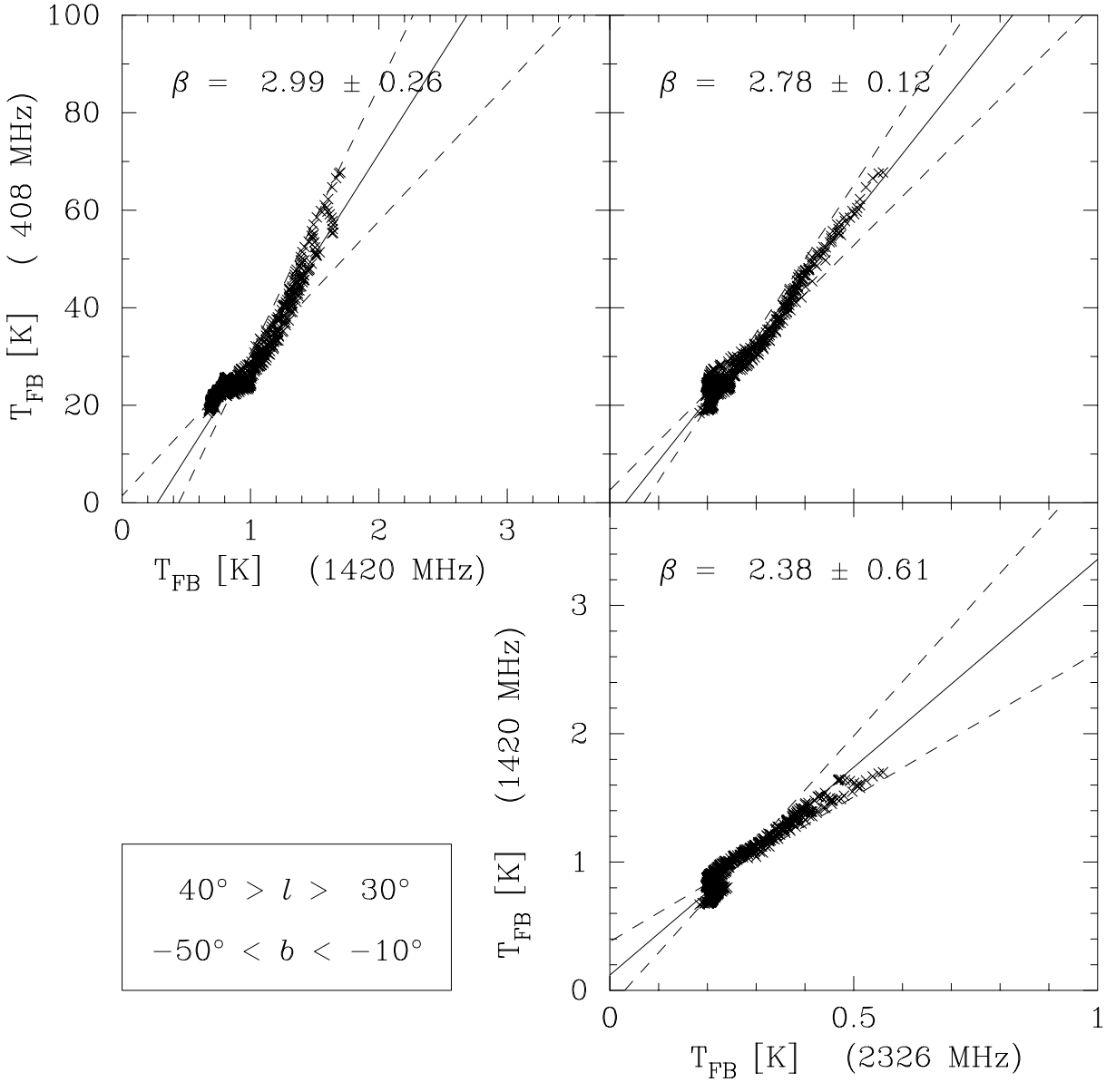

Figure 7.3: A three-way T-T plot of a region of sky common to the 408 MHz all-sky survey (Haslam et al., 1982), the 1420 MHz northern sky survey (Reich, 1982; Reich and Reich, 1986) and the *SKYMAP* 2326 MHz southern sky survey. The solid straight lines drawn through the data points represent the orthogonal regression (Isobe et al., 1990) solutions for each pair of frequencies. The dashed lines represent the $\pm 1\sigma$ spectral indices. Each plot is annotated with the fitted spectral index and associated formal error.

using the 408/2326 MHz regressions were used to estimate this offset. This offset is only valid for the northern region of the 2326 MHz map used in this T-T plot analysis. T-T plots made using data extracted from other regions of the 408 MHz and 2326 MHz maps produce a range of intercept values, both positive and negative, that are well within the conservative 80 mK upper limits on the *SKYMAP* baseline uncertainty determined in section 4.6 of chapter 4.

- The anomalous flattening of the computed spectral index at higher frequencies implies that either the full-beam temperature scale for the 2326 MHz map is too high by $\approx 7\%$ or that the scale for the 1420 MHz map is too low by $\approx 5\%$. It is unlikely that an error in the 408 MHz temperature scale is the cause of the anomaly because unrealistic spectral indices would result from such an error. The independent confirmation (see section 4.6 in chapter 4) of the 2326 MHz temperature scale by the 2 GHz South Pole measurements (Bersanelli et al., 1994) indicates that the 2326 MHz temperature scale is reliable. Although this discrepancy in the 1420 MHz and 2326 MHz temperature scales has not yet been fully resolved (P. Reich, private communication), it appears that the calibration procedures used for the 1420 MHz map may be the cause.

The mean spectral index of the intermediate-latitude galactic emission derived from the three 408/2326 MHz T-T plots is $\beta = 2.71 \pm 0.05$. The three regions used for the T-T plots represent only a small fraction of the diffuse galactic emission. A larger region of sky needs to be analyzed in order to characterize the spectral index of the diffuse galactic emission more reliably. Figure 7.4 shows a T-T plot analysis that was made using the 408 MHz and 2326 MHz DGB models described in chapter 6.

The $\pm 1\sigma$ range in spectral index obtained from this T-T analysis is $2.54 < \beta < 2.90$. This is a wider spread in β than would be expected to result from offset and gradient errors in either or both of the maps, and therefore represents an intrinsic variance in the galactic spectral index. Figure 5.3 of chapter 5 compares this result with previous determinations of the galactic spectral index, and it is seen to be consistent with the almost linear trend exhibited in this graph. The next section of this chapter describes an attempt to map the spatial distribution of this spectral index variation of the galactic emission.

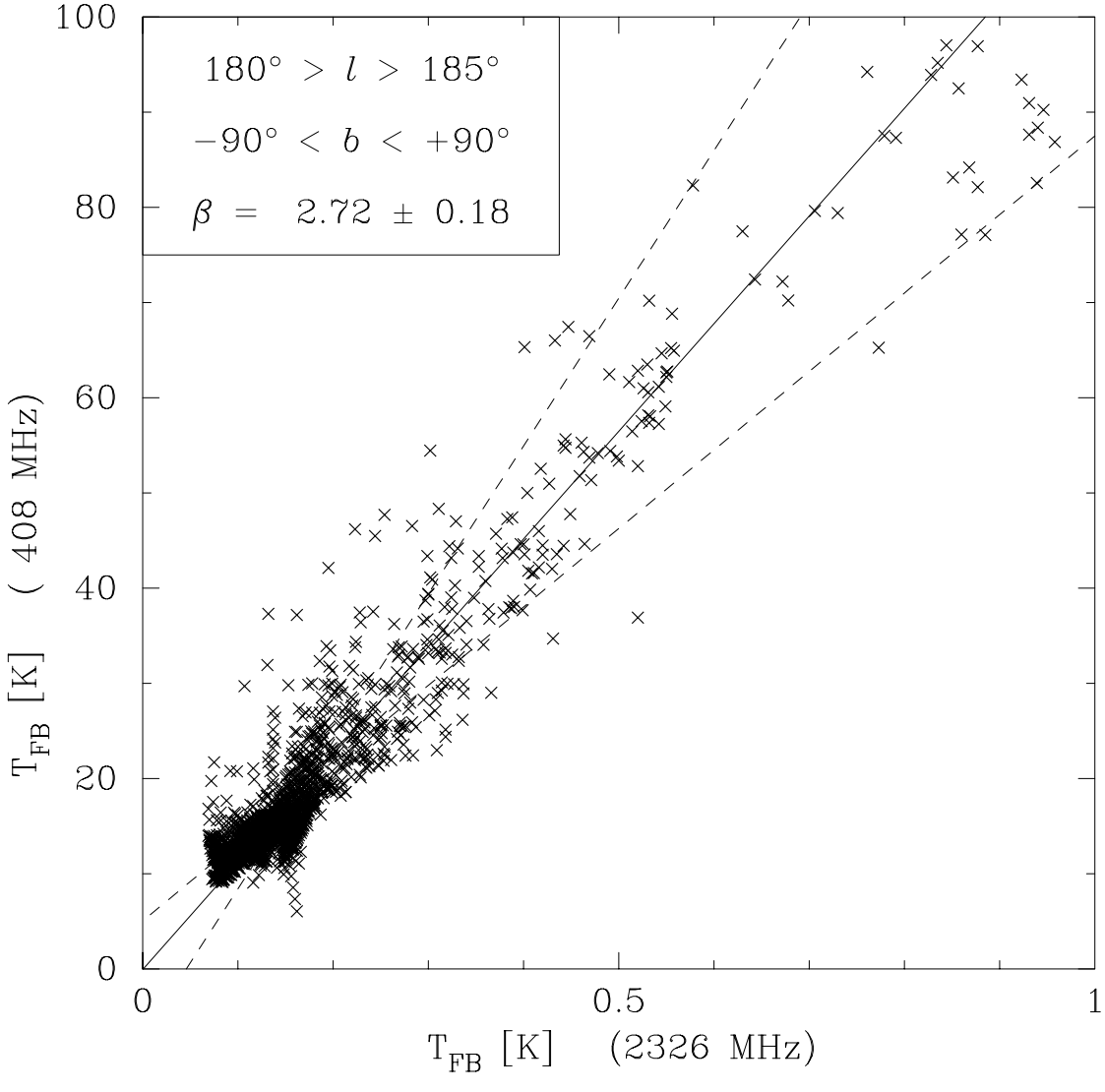

Figure 7.4: A T-T plot comparing the brightness temperatures of the 2326 MHz and 408 MHz diffuse galactic background (DGB) models derived in chapter 6. The solid line was fitted using orthogonal regression (Isobe et al., 1990) and the dashed lines represent the $\pm 1\sigma$ limits on the slope. An average spectral index of 2.72 and a 1σ range of 0.18 are derived from the regression analysis.

7.1.2 Spatial Distribution of the Spectral Index

The results derived from figure 7.4 imply that there is an intrinsic spatial variation in the spectral index of the galactic emission. Reich & Reich (1988a) produced a map of the spatial distribution of the spectral index of the northern sky by calculating pixel-by-pixel ratios between their 1420 MHz map and the 408 MHz all-sky survey. An attempt to map the spatial distribution of the spectral index of the southern sky by performing a similar analysis using the *SKYMAP* 2326 MHz map and the 408 MHz survey is described here.

Preparation of the Maps

The calibration of the *SKYMAP* full-beam brightness temperature scale and the subtraction of the extragalactic emission component was detailed in section 4.6 of chapter 4. The 408 MHz data was destriped using the Fourier technique described by Davies et al. (1996), and following Reich & Reich (1988a) an isotropic offset of 3.7 K was subtracted from 408 MHz survey data. The 408 MHz and the 2326 MHz maps were smoothed to a FWHM resolution of 2° using a gaussian convolution mask in order to reduce the pixel noise and standardize the map beamshapes. The smoothed maps were regridded onto a galactic Hammer-Aitoff equal-area projection.

The Results and Errors

Plate C.5 in appendix C is a pseudo-colour image of the spectral index map obtained by applying equation 7.1 to corresponding pixel pairs in the 408 MHz and 2326 Mhz maps. The small-circles used to demarcate the large-scale features discussed in chapter 6 are superimposed on this image as dashed and solid white lines.

Obvious thermal features in the spectral index map include the discrete HII regions tracing the galactic plane, the Orion complex and the HII region 30 Doradus in the LMC. Besides these discrete thermal sources, the galactic emission appears to be steeper than $\beta = 2.5$ over most of the area covered by the map.

Unfortunately the uncertainty in the base-level of the 2326 MHz data leads to large errors in this spectral index map. The error in each spectral index pixel is determined by the local baseline uncertainties in the two maps. The error propagation equation relating the offset uncertainties to a spectral index uncertainty is:

$$\Delta\beta_{408,2326} \approx 1.32 \times \sqrt{\left(\frac{\Delta T_{2326}}{T_{2326}}\right)^2 + \left(\frac{\Delta T_{408}}{T_{408}}\right)^2} \tag{7.2}$$

The high-latitude diffuse 2326 MHz galactic emission has brightness temperatures in the range 70–200 mK. If the worst-case offset in the 2326 MHz map is assumed, i.e.:

$$\Delta T = \pm 80 \quad \text{mK}$$

then equation 7.2 implies that $\Delta\beta > 1$ for large areas of the spectral index map. The contribution to $\Delta\beta$ by the ≈ 3 K baseline error in the 408 MHz data (Reich and Reich, 1988a) can be assumed to be negligible compared to the contribution by the 2326 MHz data because the minimum temperature in the 408 MHz map is about 10 K.

A very steep spectral index ($\beta > 3$) is exhibited by an approximately rectangular region of sky ($325^\circ \geq \ell \geq 280^\circ$, $+5^\circ \leq b \leq +30^\circ$) surrounding Cen A. A somewhat similar extended region of steep-spectrum emission has been reported in the Cassiopeia-Perseus region ($175^\circ \geq \ell \geq 90^\circ$) of the northern sky (Kallas et al., 1983), but this anomaly is restricted to $|b| \leq 10^\circ$. The apparent steepening of the spectrum in Centaurus region can be explained by an offset of less than 80 mK in the 2326 MHz map, and it is most likely that the anomalous spectral index is an artifact.

The value of 80 mK is probably a generous over-estimate for the baseline error, and it is unlikely that such large baseline errors extend beyond local problem areas in the map. The Centaurus anomaly appears to be the worst artifact of baseline uncertainty. The uncertainties in β derived using equation 7.2 with this value are almost certainly very conservative upper limits for most regions of the map. Improvements in the baseline quality of the *SKYMAP* survey data will hopefully be achieved in the near future by using independent, high-quality measurements of the 2326 MHz sky temperature. Experiments and instruments that are being planned in order to make these measurements include the horn antenna described in chapter 9, the GEM project (De Amici et al., 1993; De Amici et al., 1994; Torres et al., 1996) and the DIMES satellite (Shafer et al., 1995; Shafer et al., 1996).

Despite the unknown uncertainties in the spectral index map, a number of conclusions can be drawn from the image in plate C.5:

- The emission along the galactic ridge ($|b| < 5^\circ$) has a flatter spectrum than the diffuse emission at higher latitudes. This is a result of the mixing of the galactic synchrotron emission with thermal emission from diffuse HII regions in the galactic plane (Mathewson et al., 1962b; Hirabayashi, 1974).

- There is no clear evidence for a systematic variation with latitude in the spectral index of the diffuse galactic emission. The errors in the spectral index map are too large to confirm or refute the spectral flattening at high latitudes reported by Reich & Reich (1988b). It has been suggested that the spectral variations seen by Reich & Reich may be due to baseline errors in the 1420 MHz survey (Kogut et al., 1996a). There is also no evidence for the spectral steepening with galactic latitude that is observed at low frequencies (Howell, 1970; Webster, 1975; Webster, 1978). The conservative conclusion is that the base-levels of all existing centimetre-wavelength radio surveys are not reliable enough to test for the spectral variations in the high-latitude galactic emission that are predicted by various cosmic-ray models.

- A steepening of the spectral index is seen in plate C.5 towards sections of Loop I. This steepening, which has been reported in previous spectral index studies (Lawson et al., 1987; Reich and Reich, 1988b), is particularly apparent towards the upper part of the NPS. T-T plots of the upper and lower parts of the NPS are shown in figure 7.5(a+b), confirming that the spectrum becomes very steep ($\beta \approx 3.1$) towards the upper arch of the NPS. Figure 7.5(a) clearly indicates that two emission components are being sampled: the steep spectrum NPS emission and the flatter spectrum DGB emission. The lower section of the NPS has a typical SNR spectral index of $\beta \approx 2.65$.

- None of the other large SNRs discussed in chapter 6 have obvious signatures in the spectral index map. A T-T plot of the large loop $G27.5 - 21.0$ discovered in Sagittarius is shown in figure 7.5(c). The spectral index of 2.75 that is derived for this loop is somewhat steep for a galactic SNR, but the emission associated with this loop is too faint to affect the bulk spectral index of the diffuse galactic emission.

- The Gum nebula region between longitudes of 245° and 270° shows evidence of spectral flattening, which probably results from a thermal component in the emission. A T-T plot of the emission from the lower part of the Gum nebula is shown in figure 7.5(d). This plot clearly shows that the emission has both thermal and non-thermal components. The 2326 MHz emission from the Gum nebula and Vela SNR has been described in detail by Woermann in her PhD thesis (Woermann, 1998).

- A comparison of the image of the Sco/Oph region shown in figure 6.10 of chapter 6 with the spectral index map in plate C.5 reveals that the thermal sources in the radio

brightness map correlate spatially with flatter spectral features, but the brighter non-thermal background emission dominates the gross spectral index.

7.2 High Frequency Spectral Index

No ground-based radio surveys at frequencies above 2326 MHz have ever been made of the entire sky. To date the only all-sky radio maps at frequencies higher than 2326 MHz are the 31 GHz, 53 GHz and 90 GHz maps observed by the Differential Microwave Radiometer (*DMR*) instrument on the *COBE* satellite. This section describes correlation analyses performed between a composite 2326 MHz map of the whole sky and the 31 GHz and 53 GHz *COBE-DMR* maps. The purpose of this analysis was to determine the spectral index of the galactic emission above 2.3 GHz.

The determination of the spectral index of the galactic emission at high frequencies is useful for the study of galactic cosmic rays, but in the context of this thesis the purpose of this analysis was to quantify the contamination of cosmic microwave background radiation (CMBR) measurements by the high-latitude galactic foreground emission. For this reason the following sections digress into a discussion of the CMBR.

7.2.1 Measuring the CMBR Anisotropy

Ever since the detection of the CMBR (Penzias and Wilson, 1965; Howell and Shakeshaft, 1966) there has been a succession of experiments designed to search for brightness anisotropies in the spatial distribution of this primordial radiation. Spatial fluctuations in the temperature of the CMBR are the signatures of primordial inhomogeneities in the early universe. The spatial frequency spectrum of these fluctuations can be used to derive many of the principal parameters of the universe (Bond and Efstathiou, 1987; Jungman et al., 1996; Bond et al., 1997).

The one-year results from the *COBE-DMR* experiment that were announced in 1992 were the first positive detection of the CMBR anisotropy. The *COBE-DMR* was sensitive to angular scales ranging from the dipole down to the beamwidth of 7° (Smoot et al., 1992). Since 1992 *COBE-DMR* has produced a further three years of data (Bennett et al., 1996; Górski et al., 1996; Hinshaw et al., 1996a; Hinshaw et al., 1996b; Tegmark, 1996; Wright et al., 1996) and a number of balloon and ground-based experiments have made confirmatory detections of the CMBR anisotropies at a wide range of angular scales (Wat-

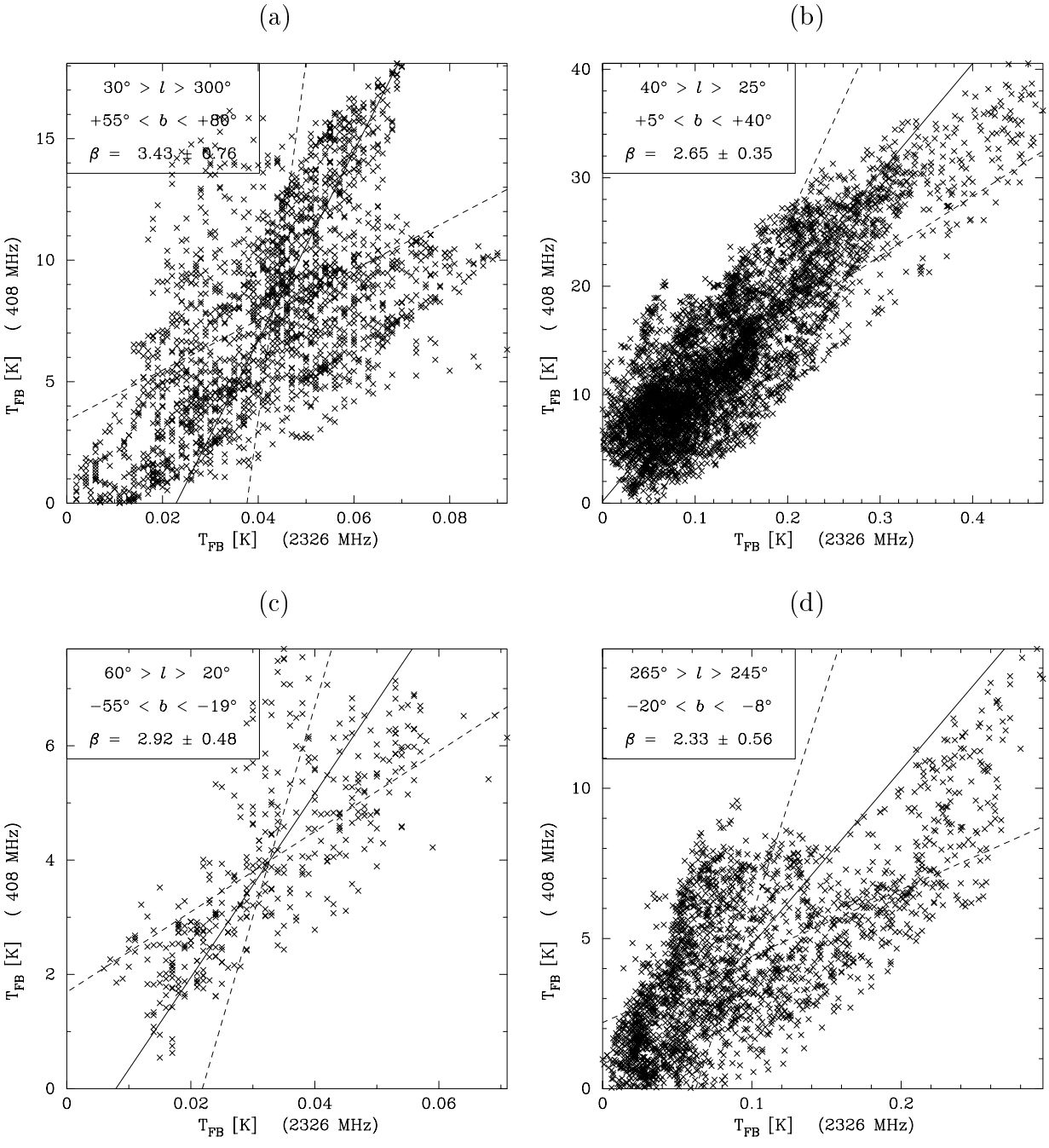

Figure 7.5: T-T plots made using selected extracts from the 51′ FWHM resolution 408 MHz and 2326 MHz residual maps shown in plates C.4 and C.3. The solid lines were fitted using the orthogonal regression method (Isobe et al., 1990) and the dashed lines represent the $\pm 1\sigma$ limits of the slope. Each graph is annotated with the galactic coordinates of the rectangular region that was extracted for the T-T plot, the spectral index that corresponds to the slope of the solid line, and the formal error in the spectral index (corresponding to the dashed lines). (a) The upper region of the NPS; (b) The lower region of the NPS; (c) The lower part of the large loop in Sagittarius (G27.5−21.0 in chapter 6); (d) The lower extension of the Gum nebula.

son et al., 1992; Ganga et al., 1993; Dragovan et al., 1994; Ganga et al., 1994; Hancock et al., 1994; Lineweaver et al., 1995; Davies et al., 1996; Hancock et al., 1997; Gutiérrez et al., 1997; Cheng et al., 1997; Partridge et al., 1997; Platt et al., 1997). Tegmark (1998) provides a contemporary summary of the frequencies and angular scales covered by current and planned CMBR anisotropy experiments, both terrestrial- and space-based.

7.2.2 Galactic Contamination of CMBR Measurements

All measurements of the CMBR are contaminated by the synchrotron, brehmsstrahlung and thermal dust foreground emission from the Milky Way (Bennett et al., 1992; Kogut et al., 1996b; Dodelson, 1997). As a result all CMBR work is carried out at high galactic latitudes ($|b| > 20°$) to avoid the strong thermal and non-thermal emission associated with the galactic disk. At low frequencies the positive spectral index components (synchrotron and bremsstrahlung) dominate the high-latitude foreground contamination. Below about 30 GHz the galactic synchrotron component is stronger than the free-free component because of its steeper spectral index. Above about 100 GHz the temperature fluctuations of the thermal dust emission with an approximately $\nu^{+1.5}$ flux dependence dominate the foreground emission. The CMBR has a Planck-law spectrum with a characteristic temperature of 2.728 ± 0.004 K (Fixsen et al., 1996) which peaks at 160.4 GHz by the Wien displacement law.

The 408 MHz all-sky survey data and the 1420 MHz northern sky survey have been used in most of the published work on galactic synchrotron contamination of CMBR measurements (Banday and Wolfendale, 1990; Banday et al., 1991; Banday and Wolfendale, 1991; Readhead and Lawrence, 1992; Bennett et al., 1992; Witebsky et al., 1993; Davies et al., 1996; Lineweaver et al., 1996; Kogut et al., 1996a; Kogut et al., 1996b; Banday et al., 1997). The *COBE-DMR* consortium used the 408 MHz and 1420 MHz surveys to extrapolate a predicted model of the galactic synchrotron emission at 53 GHz (Bennett et al., 1992; Bennett et al., 1994; Bennett et al., 1996). This model was used in an attempt to remove the galactic synchrotron emission from the *DMR* data. The T-T plot shown in figure 7.6 compares the high-latitude emission of this model to the *SKYMAP* survey data which has been appropriately smoothed with the *DMR* beam. This T-T plot clearly shows that the 53 GHz synchrotron model is inadequate in the southern hemisphere, probably because of the use of only the 408 MHz survey for the extrapolation to 53 GHz.

The following sections describe how a composite all-sky 2326 MHz map was created

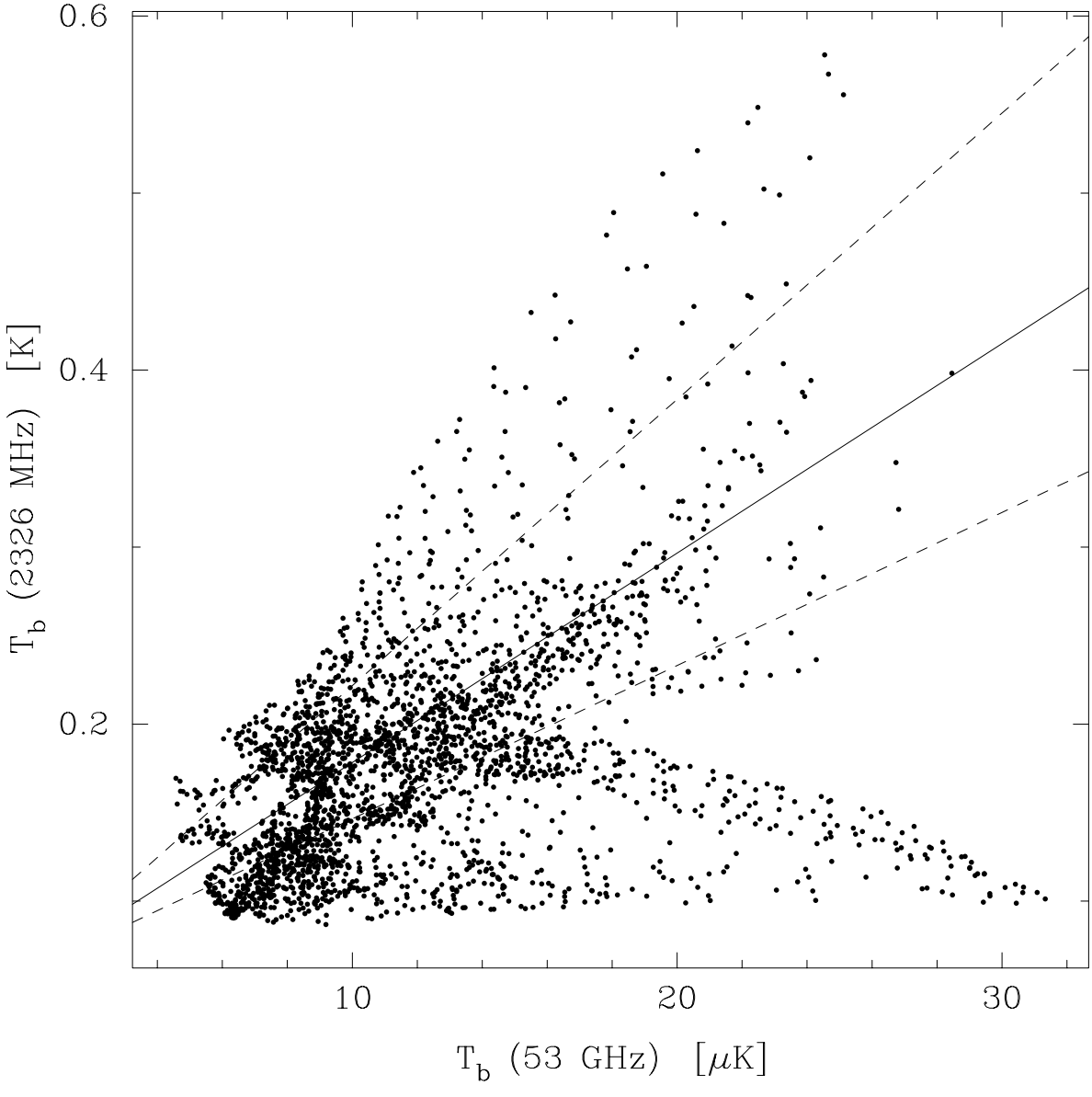

Figure 7.6: A T-T plot comparing the *SKYMAP* 2326 MHz map with the 53 GHz galactic synchrotron emission model extrapolated from the 408 MHz and 1420 MHz surveys (Bennett et al., 1992; Bennett et al., 1994). The *SKYMAP* map was smoothed to match the 7°-FWHM resolution of the model by numerical convolution with the *COBE-DMR* beam. Both data sets were binned using the *COBE* Quadrilateralized Spherical Cube (CSC) coordinate projection (Bennett et al., 1996). The solid line represents a spectral index of +3.0 and the dashed lines represent spectral indices of +2.9 and +3.1. These lines were not obtained by any formal regression method, they are merely intended to emphasize the wide and anomalous dispersion of the points.

and used in a correlation analysis with the *COBE-DMR* data. This analysis was used to estimate the high-frequency spectral index of the galactic synchrotron foreground emission and determine the degree of contamination of the *COBE-DMR* results by this synchrotron emission. The results of these investigations can be used to develop an improved galactic synchrotron foreground model for use in CMBR studies. The sub-degree resolution of this galactic foreground model will be necessary for the new generation of experiments that are currently being planned to probe the CMBR at angular scales relevant to the predicted "doppler peak" feature in the angular spectrum. The MAP (Bennett et al., 1997) and Planck Surveyor (Lawrence and Lange, 1997) satellite missions are the most ambitious of these planned experiments.

7.2.3 Preparation of the Composite 2326 MHz Map

Banday et al. (1997) devised the "*COBE* custom galaxy cut" which excludes the low-latitude pixels from the *DMR* maps that are contaminated by excessive foreground emission associated with the galactic disk. Only data lying outside of this exclusion region have been used for CMBR work reported in the literature. The comparison of the *DMR* maps with the 2326 MHz data was also restricted to this high-latitude region, which significantly reduced the area of sky that could be used for the analysis.

Even at the lowest *DMR* frequency of 31 GHz the high-latitude galactic signal is expected to have amplitudes of $\Delta T_{\rm synch} < 11$ μK if the synchrotron spectral index steepens to $\beta_{\rm synch} = 2.9$ above 2.3 GHz (Kogut et al., 1996a). Because of this small signal amplitude and the restricted sky coverage it was decided to supplement the *SKYMAP* 2326 MHz data with a suitably scaled extract from the 1420 MHz northern sky survey in order to improve the statistics of the analysis. This northward extension of the sky coverage also allowed the investigation of low-order multipole components of the galactic signal that would have been affected by severe aliasing if only the southern sky were considered in the analysis. The aliasing caused by the custom galaxy cut is described by Wright et al. (1996).

The composite map was created by using all of the *SKYMAP* data and an extract from the 1420 MHz survey that overlapped the *SKYMAP* sky coverage by 2°. Following Reich & Reich (Reich and Reich, 1988a) an extragalactic background component of 2.8 K was subtracted from the 1420 MHz data, and the residual pixel temperatures were scaled by a factor of 0.277. This factor was derived using the T-T plot shown in figure 7.2 and

corresponds to a spectral index of $\beta = 2.6$ for the high-latitude emission. This rather flat spectral index is a result of the apparent inconsistency in the calibration factors of the two maps that was discussed in section 7.1.1. Implicit in the use of this scale factor is the rather chauvinistic decision that the temperature scale of the *SKYMAP* 2326 MHz survey is more reliable than that of the 1420 MHz survey. In practice, the wide frequency separation between the 2.3 GHz and 31 GHz maps makes the choice of preferred low-frequency temperature scale irrelevant.

The maps were combined, smoothed using the *DMR* beam (Wright et al., 1994), and regridded onto a galactic Quadrilateralized Spherical Cube (CSC) projection to match the *COBE-DMR* Project Data Sets and Analyzed Science Data Sets (Bennett et al., 1996). The resulting map contained 3859 pixels, which is significantly less than the full sky coverage of $32^2 \times 6 = 6144$ pixels because of the effects of the custom galaxy cut and the lack of *SKYMAP* data near the SEP.

7.2.4 Angular Spectrum of the CMBR

The comparison between observations of the CMBR and cosmological models is usually made in the angular frequency domain. The cosmological models predict a power spectrum for the angular distribution of the CMBR fluctuations (Bond and Efstathiou, 1987; Jungman et al., 1996; Bond et al., 1997) and this is compared to the angular power spectrum calculated from the CMBR measurements. This spectral comparison is necessary because of the stochastic nature of the CMBR fluctuations; it is not possible to predict the actual spatial distribution of the CMBR fluctuations, only their (spatial) spectral characteristics. Any sky temperature distribution may be synthesized as a spherical-harmonic series:

$$T(\Omega) = \sum_{\ell=0}^{\ell\text{-max}} \sum_{m=-\ell}^{+\ell} a_\ell^m \, Y_\ell^m(\Omega) \quad [\mathrm{K}] \tag{7.3}$$

where the $Y_\ell^m(\Omega)$ are the standard orthonormal spherical-harmonic basis functions. The angular power spectrum of this temperature distribution is related to the harmonic coefficients a_ℓ^m:

$$T_\ell^2 = \frac{1}{4\pi} \sum_{m=-\ell}^{+\ell} |a_\ell^m|^2 \quad [\mathrm{K}^2] \tag{7.4}$$

T_ℓ^2 is the signal power contained in the spherical multipole of order ℓ. A multipole of order ℓ represents structures with a scale-size of $\approx (360/\ell)^\circ$ in the spherical temperature distribution.

For the low values of ℓ ($2 \leq \ell < 40$) probed by the *DMR* where only the Sachs-Wolfe (scalar) effects are important, the multipole components of the angular power spectrum of the CMBR are predicted to have the following expectational values (Bond and Efstathiou, 1987):

$$\langle T_\ell^2 \rangle = \frac{2\ell+1}{5} Q_{\rm rms}^2 \frac{\mathbf{\Gamma}(\ell + (n-1)/2)\mathbf{\Gamma}((9-n)/2)}{\mathbf{\Gamma}(\ell + (5-n)/2)\mathbf{\Gamma}((3+n)/2)} \quad [\mathrm{K}^2] \tag{7.5}$$

where n is the wavenumber spectral index of the primordial density inhomogeneities at the epoch of last-scattering and $Q_{\rm rms} = \langle T_{\ell=2}^2 \rangle^{1/2}$ is the RMS quadrupole ($\ell = 2$) component of the CMBR angular power spectrum. This power spectrum simplifies to:

$$\langle T_\ell^2 \rangle = Q_{\rm rms}^2 \frac{6(2\ell+1)}{5\ell(\ell+1)} \quad [\mathrm{K}^2] \tag{7.6}$$

for the scale-invariant (Harrison-Zel'dovich) case where $n = 1$. This scale-invariant scenario is advocated by most of the recent CMBR experiments. Because of the stochastic nature of the CMBR there is an intrinsic variance in the expectational values of the power spectrum multipole components which is dependent on the multipole order:

$$\Delta T_\ell^2 = \sqrt{\frac{2}{2\ell+1}} \langle T_\ell^2 \rangle \quad [\mathrm{K}^2] \tag{7.7}$$

This *cosmic variance* (White et al., 1993), which cannot be defeated by improved measurement statistics, is a consequence of our inability to observe more than one universe, i.e. it is impossible for us to observe an ensemble of universes drawn from a parent population.

7.2.5 The Galactic Quadrupole

A consequence of cosmic variance is that the quadrupole component of the CMBR may never be determined with any accuracy because equation 7.7 implies that:

$$\Delta T_2^2 = \sqrt{\frac{2}{5}} \langle T_2^2 \rangle \quad [\mathrm{K}^2] \tag{7.8}$$

i.e. the cosmic variance is 63% of the expected quadrupole power. As a result the CMBR quadrupole is inferred by extrapolating the $\ell = 2$ component of a power-law spectrum fitted to higher order multipoles that are less affected by cosmic variance, rather than by direct measurement. The amplitude of this extrapolated quadrupole component is usually called $Q_{\text{rms-PS}}$ and the current best estimate of its value is 18 μK (Górski et al., 1996; Hinshaw et al., 1996a; Hinshaw et al., 1996b; Tegmark, 1996; Wright et al., 1996).

Despite the effects of cosmic variance, the *measured* CMBR quadrupole is an important empirical value, but the difficulty of its measurement is compounded by the fact that the

Map	Q_1	Q_2	Q_3	Q_4	Q_5	$Q_{\rm rms}$	
408 MHz[a]	−6.6	+3.4	−0.1	+5.5	−1.8	4.5	K
408 MHz[b]	−6.8	+3.2	+0.2	+5.4	−2.2	4.6	K
Combined 2326 MHz	−56.7	+20.0	−5.0	+56.0	−11.6	40.4	mK
β(408 MHz[b]/2326 MHz)	2.75	2.91	–	2.62	3.01	2.72	
DMR 31.5 GHz[a]	−29.1	+27.0	+2.1	+4.5	+5.3	15.6	μK
DMR 31.5 GHz[b]	−27.8	+36.6	+9.7	+4.3	−1.8	23.3	μK
DMR 53 GHz[a]	−13.6	+9.5	+3.8	0.0	+3.5	4.4	μK
DMR 53 GHz[b]	−7.4	+9.7	+4.8	−0.8	+1.0	6.5	μK

Table 7.1: The quadrupole components of the 408 MHz survey, the composite 2326 MHz survey and the *COBE-DMR* 31.5 GHz and 53 GHz (A + B)/2 maps. The quadrupole basis functions are the same as those used by Bennett et al. (1992). The RMS quadrupole amplitude is given by $Q^2_{\rm rms} = 4/15[(3/4)Q_1^2 + Q_2^2 + Q_3^2 + Q_4^2 + Q_5^2]$. The superscript [a] refers to the results obtained by Kogut et al. (1996a) while the superscript [b] refers to the results obtained using the program `mdqfit.f`. The row labelled β(408 MHz[b]/2326 MHz) contains the spectral indices calculated for the galactic synchrotron quadrupole signal.

galaxy is a strong quadrupolar source (Stark, 1993; Kogut et al., 1996a). The galactic foreground quadrupole needs to be modelled accurately in order to recover the intrinsic CMBR quadrupole from sky temperature maps. Kogut et al. (1996a) have produced synchrotron, free-free and dust models of the galactic foreground quadrupole. Their synchrotron model relies almost exclusively on the 408 MHz survey. The quadrupole component of the composite 2326 MHz map was measured in order to test whether there were any significant differences between the quadrupole characteristics of the 408 MHz and 2326 MHz sky temperatures.

Program `mdqfit.f` was written to simultaneously fit monopole, dipole and quadrupole basis functions to maps stored in the CSC projection. The basis functions (in galactic coordinates (ℓ,b)) matched those used in most CMBR analyses (Bennett et al., 1992):

$$\begin{aligned} Q(\ell, b) &= Q_1(3\sin^2 b - 1)/2 + Q_2 \sin 2b \cos \ell + Q_3 \sin 2b \sin \ell + \\ &\quad Q_4 \cos^2 b \cos 2\ell + Q_5 \cos^2 b \sin 2\ell \end{aligned} \tag{7.9}$$

Table 7.1 lists the quadrupole parameters and amplitudes that were obtained using this program with the 408 MHz survey, the composite 2326 MHz map and the 31 GHz and 53 GHz *DMR* maps (A and B channels averaged). As can be seen from the table, the 408 MHz, 31 GHz and 53 GHz results obtained using `mdqfit.f` compare well with those obtained by Kogut et al. (1996a) using a different technique.

The results in table 7.1 show that the *shape* of the galactic quadrupole measured at 2326 MHz is not significantly different from that obtained from the 408 MHz map, i.e. the relative amplitudes of the quadrupole components for the two maps are quite similar. The spectral indices obtained for the RMS and individual component amplitudes are consistent with the spread of spectral indices obtained for the diffuse galactic emission earlier in this chapter. It is apparent from the magnitudes and signs of the dominant Q_1 and Q_2 components that the 31 GHz quadrupole is closely aligned to the low frequency quadrupole. A similar alignment is not apparent in the 53 GHz data, implying that the quadrupole in the 31 GHz data is due to the galactic foreground, but at 53 GHz the galactic quadrupole is swamped by other quadrupole signals (including the CMBR). Kogut et al. (1996a) have determined that the intrinsic CMBR quadrupole is in fact counter-aligned to the galactic quadrupole signal and has an RMS amplitude of $Q_{\rm rms} = 10.7 \pm 7.1\ \mu$K. This value is within one cosmic variance of the current best estimate for $Q_{\rm rms\text{-}PS}$.

7.2.6 Two-point Correlation

This section describes the techniques and results of a comparison between the higher order multipole components of the composite 2326 MHz map and the *COBE-DMR* 31 GHz and 53 GHz maps (A and B channels averaged). The 2-point correlation technique, which has become ubiquitous in the analysis of CMBR data, is used for this analysis. The aim of the analysis was to quantify the amplitude of the galactic foreground signal in the *COBE-DMR* maps.

Mathematical Background

The 2-point correlation function provides an alternative means to equation 7.4 for determining the angular power spectrum of a spherical distribution. The *continuous* 2-point auto-correlation function of a spherical temperature distribution, $T(\Omega)$, is defined to be (Peebles, 1973):

$$C(\theta) = \iint_{4\pi} \iint_{4\pi} T(\Omega)\, T(\Omega')\, \delta(\cos(\Omega - \Omega') - \cos\theta)\, \frac{d\Omega\, d\Omega'}{8\pi^2} \quad [\mathrm{K}^2] \tag{7.10}$$

This function may be decomposed into a linear combination of Legendre polynomials:

$$C(\theta) = \sum_{\ell=0}^{\ell\text{-max}} T_\ell^2\, P_\ell(\cos\theta) \quad [\mathrm{K}^2] \tag{7.11}$$

As implied by the nomenclature, the discrete coefficients T_ℓ^2 may be shown to be equivalent to the angular power spectrum components of the spherical distribution, as defined by

equation 7.4 (Peebles, 1973). These spectral coefficients may be calculated using:

$$T_\ell^2 = \frac{2\ell+1}{2}\int_{-1}^{+1} C(\theta)\, P_\ell(\cos\theta)\, d(\cos\theta) \quad [\mathrm{K}^2] \tag{7.12}$$

Equations 7.11 and 7.12 define the "Legendre transform" which has similar function to the familiar Fourier transform. Assuming that the temperature distribution has been sampled using an equal-area pixelation scheme, the correlation in equation 7.10 may be performed using the following discrete approximation:

$$C(\theta_k) = C(k \times \Delta\theta) = \frac{\sum_i \sum_j T(\Omega_i)\, T(\Omega_j)\, W(\Omega_i, \Omega_j, \theta_k)}{\sum_i \sum_j W(\Omega_i, \Omega_j, \theta_k)} \quad [\mathrm{K}^2] \tag{7.13}$$

where

$$W(\Omega_i, \Omega_j, \theta_k) = 1 \quad |(\Omega_i - \Omega_j) - \theta_k| \leq \Delta\theta/2 \tag{7.14}$$

$$= 0 \quad |(\Omega_i - \Omega_j) - \theta_k| > \Delta\theta/2 \tag{7.15}$$

Numerical quadrature applied to the integral in equation 7.12 may be used to determine the power spectrum coefficients of this discrete correlation function.

The 2-point correlation technique is a numerically stable and reasonably efficient way of obtaining the angular power spectrum of a spherical distribution, and it is easily generalized to perform cross-correlation and cross-spectral analysis. A program called `2point.f` was written to perform 2-point cross-correlation between two maps gridded using the CSC coordinate projection. A separate program called `lxfm.f` was developed to perform a Legendre transform (equation 7.12) on the discrete correlation function produced by `2point.f`.

Application of the Method

Figure 7.7 shows the 2-point correlation functions obtained using `2point.f` to cross-correlate the composite 2326 MHz map with both the 31 GHz and 53 GHz *COBE-DMR* maps, and to auto-correlate the 2326 MHz map with itself. In order to test the significance of the cross-correlation functions it was necessary to determine a statistical measure of a chance correlation between the CMBR and galactic signals for each lag angle, θ. A Monte Carlo experiment was devised in which 100 synthetic *DMR* maps were constructed and correlated with the 2326 MHz data, and the variance of the resulting correlations functions was calculated at each lag angle.

The synthetic maps were generated using a procedure that is commonly used in the analysis of CMBR 2-point correlations (Banday et al., 1994; Bennett et al., 1994; Wright

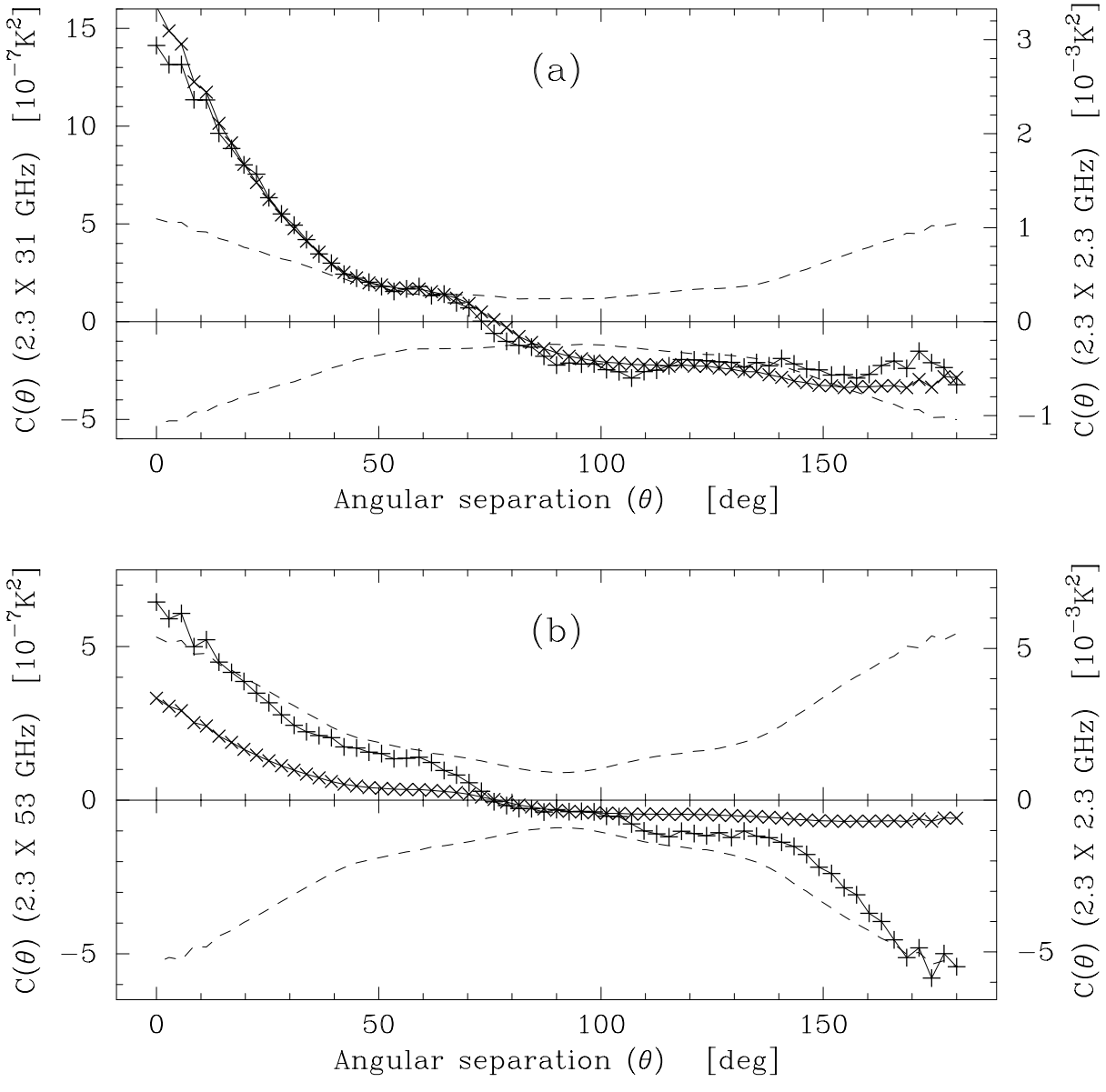

Figure 7.7: The results of the cross-correlation between the composite 2326 MHz map and the averaged A and B channel *COBE-DMR* maps, and the auto-correlation of the 2326 MHz map with itself. The results for the 31 GHz and 53 GHz analyses are shown in panels (a) and (b) respectively. The pluses (+) represent the cross-correlation data and are associated with the scale on the left-hand axis. The crosses (×) represent the auto-correlation of the 2326 MHz data, and are associated with the scale on the right-hand axis. The relative scaling between the cross- and auto-correlation functions has been selected so that they would coincide if the *DMR* maps contained only a galactic signal with a spectral index of $\beta = 2.95$, i.e. were proportional to the 2326 MHz maps. The dashed lines show the $\pm 1\sigma$ limit on chance correlation between the *DMR* and 2326 MHz maps which was computed using the Monte Carlo simulations described in the text.

et al., 1994). The steps involved in producing each individual synthetic CMBR map are outlined below:

1. Realizations of the multipole components, $a_{l,m}$, of a Harrison-Zel'dovich anisotropy with $Q_{\text{rms-PS}} = 18$ μK were generated using a gaussian random number generator in conjunction with equations 7.4, and 7.6.

2. The multipole components were windowed using the Legendre coefficients of the average *DMR* beam (Wright et al., 1994) in order to simulate convolution by the *DMR* beam.

3. Brightness temperature distributions were constructed by using the windowed multipole coefficients in a spherical harmonic synthesis (equation 7.3).

4. The Planck brightness temperatures were converted to the Rayleigh-Jeans antenna temperature scale appropriate to the frequency required (31.5 GHz or 53 GHz).

5. Random pixel noise with the same statistical characteristics as the real *DMR* pixel noise was added to complete the synthetic map.

The dashed lines in figure 7.7 trace the $\pm 1\sigma$ distribution of the 100 correlation functions obtained using these synthetic maps that contained no explicit galactic signal. Cross-correlation results (using real signals) that lie within these bounds are very likely to be chance correlations between the galactic foreground and intrinsic CMBR signals.

The computed cross-correlation function in panel (a) of figure 7.7 shows that for lag angles less than 50° the 31 GHz *DMR* data is significantly correlated with the galactic synchrotron signal in the 2326 MHz map. In addition, the cross-correlation function closely matches the auto-correlation function of the galactic signal, indicating that the 31 GHz *DMR* data contains a strong galactic signal.

These is some evidence for very weak correlation between the 2326 MHz and 53 GHz *DMR* data in panel (b) of figure 7.7, but the correlation is not significant. Signal components other than galactic synchrotron dominate the 53 GHz map.

Program `lxfm.f` was used to obtain the low-order ($\ell \leq 10$) Legendre coefficients of the auto- and cross-correlation functions shown in figure 7.7. These coefficients, which are plotted in figure 7.8, represent the power-spectrum of the 2326 MHz map ($\times$) and the cross-spectrum of the 2326 MHz and *DMR* maps (+). It is clear that the 31 GHz

map contains a galactic synchrotron signal, particularly in the low-order multipoles of its power-spectrum, but that the 53 GHz map is dominated by other signals.

The power-spectrum of the galactic signal as represented by the composite 2326 MHz map falls off quite rapidly above $\ell = 6$. This high-frequency roll-off is partly due to the *DMR* beam which severely attenuates multipole components above $\ell \approx 30$ (Wright et al., 1994), but is mostly a result of the intrinsic angular spectrum of the galactic synchrotron emission. For $\ell > 10$ it appears that the RMS amplitudes of the galactic synchrotron multipoles are below ≈ 10 mK at 2.3 GHz. Extrapolating this upper limit to 31 GHz and 53 GHz using a spectral index of $\beta = 2.9$ results in RMS amplitudes of 5.5 μK and 1.1 μK respectively. Galactic foreground components of this magnitude will need to be accounted for if the doppler peak in the CMBR spectrum is to be characterized properly.

7.2.7 Galactic Synchrotron Spectral Index

From the results of the correlation and spectrum analyses above it is quite certain that at high latitudes the 31 GHz *DMR* map contains a galactic synchrotron signal. The high latitude 2326 MHz data is completely dominated by galactic synchrotron emission, therefore the following relationship between the 2326 MHz and 31 GHz maps may be proposed:

$$T_{31}(\Omega) = \left(\frac{2.326}{31.5}\right)^{\beta} \times T_{2.3}(\Omega) + N(\Omega) \quad [\mathrm{K}] \tag{7.16}$$

where $N(\Omega)$ is the signal component of the 31 GHz map that is independent of the galactic synchrotron emission. $N(\Omega)$ is probably dominated by the CMBR signal, galactic free-free emission and receiver noise. The cross-correlation between the 2326 MHz and 31 GHz maps results in:

$$\begin{aligned} \langle T_{31}(\Omega)T_{2.3}(\Omega')\rangle(\theta) &= \left(\frac{2.326}{31.5}\right)^{\beta} \times \langle T_{2.3}(\Omega)T_{2.3}(\Omega')\rangle(\theta) + \langle N(\Omega)T_{2.3}(\Omega')\rangle(\theta) \quad [\mathrm{K}^2] \\ &= \left(\frac{2.326}{31.5}\right)^{\beta} \times \langle T_{2.3}(\Omega)T_{2.3}(\Omega')\rangle(\theta) + \epsilon(\theta) \quad [\mathrm{K}^2] \end{aligned} \tag{7.17}$$

where the cross-correlation of the 2326 MHz map and $N(\Omega)$ is assumed to result in small values, $\epsilon(\theta)$, for the range of lag angles, θ, being considered. Performing the Legendre transformation on equation 7.17 results in:

$$T_\ell(2.3) \times T_\ell(31.5) = \left(\frac{2.326}{31.5}\right)^{\beta} \times T_\ell^2(2.3) + \epsilon_\ell \quad [\mathrm{K}^2] \tag{7.18}$$

where ϵ_ℓ is assumed to be small for all multipoles of interest. Equations 7.17 and 7.18 imply that simple linear regression may be applied to the correlation and spectral data

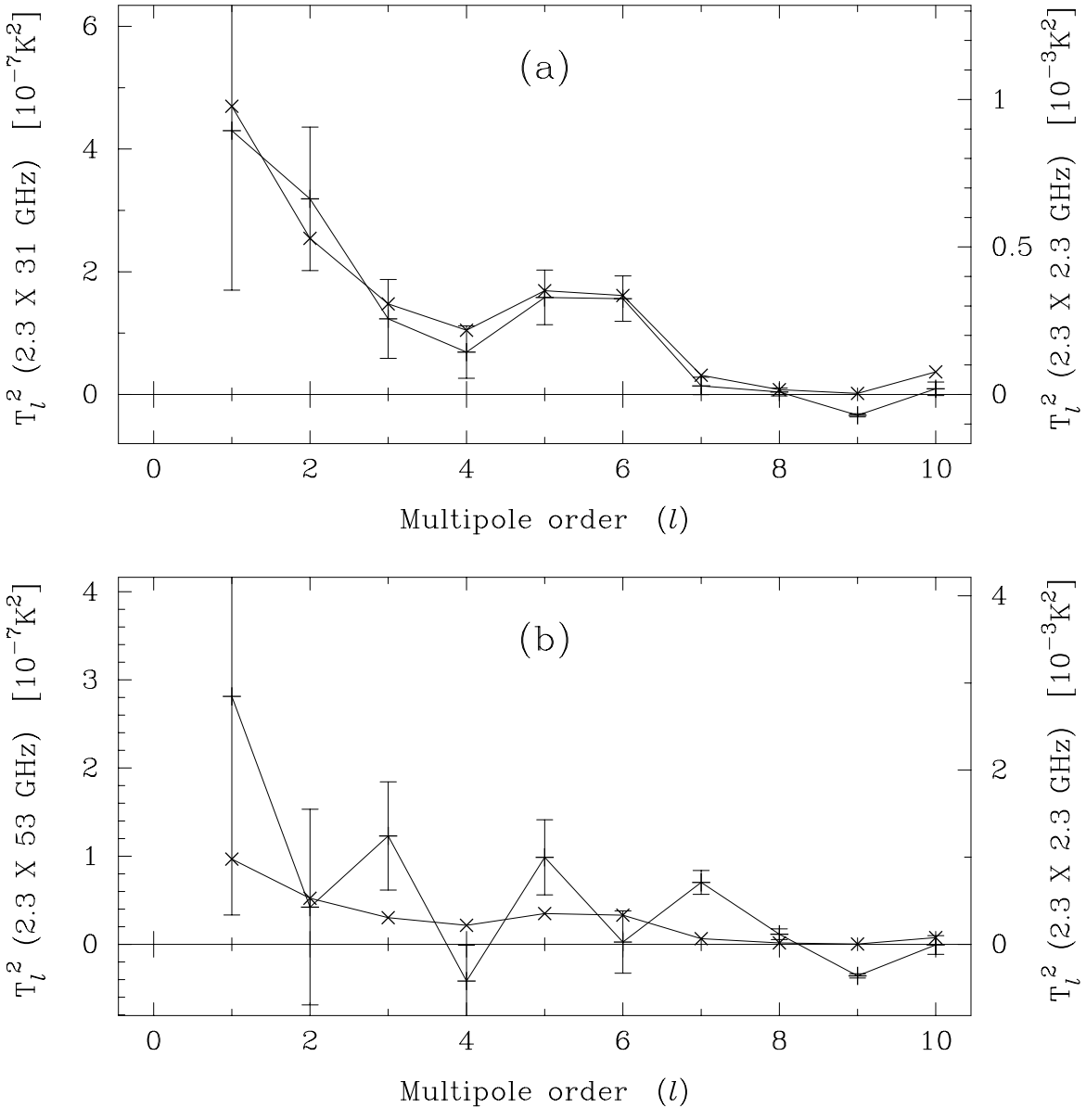

Figure 7.8: The cross- and power-spectra derived from the correlation functions shown in figure 7.7. The results for the 31 GHz and 53 GHz analyses are shown in panels (a) and (b) respectively. The pluses (+) represent the cross-spectrum data and are associated with the scale on the left-hand axis. The crosses (×) represent the power-spectrum of the 2326 MHz data, and are associated with the scale on the right-hand axis. The error bars on the cross-spectrum points are an indication of the magnitude of the expected chance correlation at each multipole. The relative scaling between the power- and cross-spectrum functions has been selected so that they would coincide if the *DMR* maps contained only a galactic signal with a spectral index of $\beta = 2.95$ (i.e. were proportional to the 2326 MHz maps).

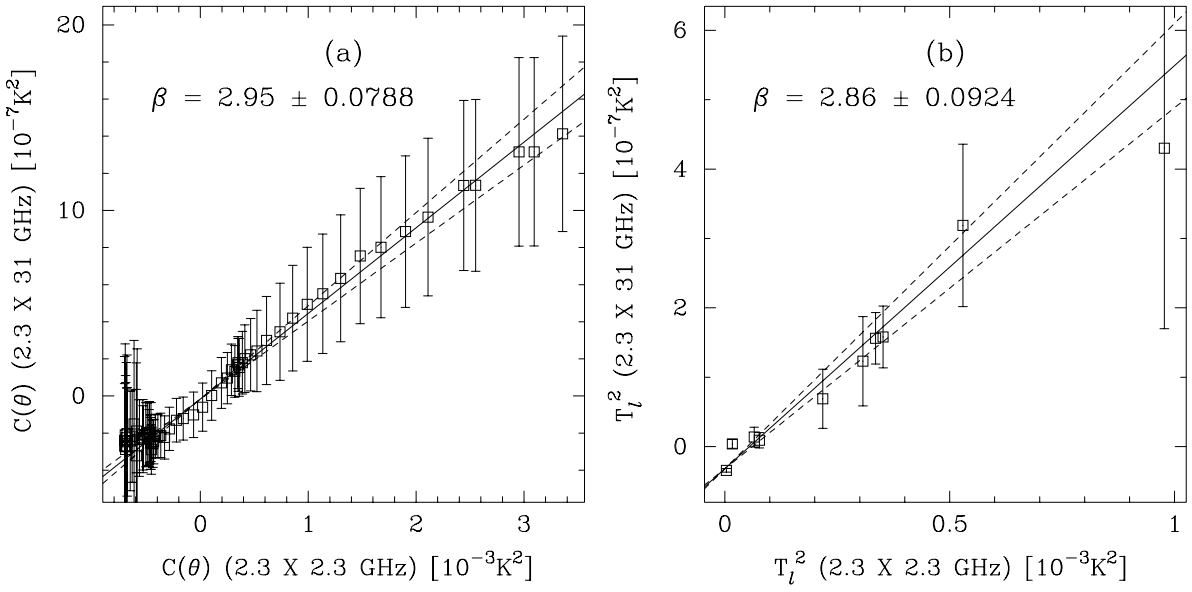

Figure 7.9: "T^2-T^2 plots" comparing (a) the auto- and cross-correlation functions shown in figure 7.7(a) and (b) the power- and cross-spectra shown in figure 7.8(a). The spectral indices and associated formal errors resulting from the ordinary least-squares linear regression are shown in the graphs. The solid and dashed lines represent the regression line and formal errors in the slope respectively.

shown in figures 7.7 and 7.8 in order to determine the spectral index, β. There will be no statistical bias in the estimate of β if the assumption that ϵ_ℓ and $\epsilon(\theta)$ are random variables with zero mean is correct. This assumption is partly based on the reported non-correlation of the synchrotron emission and *DIRBE* far-infrared dust emission (Kogut et al., 1996b).

The graphs in figure 7.9 are similar to the T-T plots used earlier in this chapter, except that the ordinates and abscissa have dimensions of temperature-squared. The high-frequency spectral index of the high-latitudes synchrotron emission that is derived from figure 7.9(a) is $\beta_{2.3/31.5} = 2.95 \pm 0.08$. This determination of the galactic spectral index is included in the compilation of measurements shown in figure 5.3 of chapter 5. This new value is clearly consistent with previous work. No significant variations in the spectral index with multipole order are seen in figure 7.9(b).

7.2.8 A Search for a Galactic Signal in the *COBE* Result

The *COBE-DMR* Analyzed Science Data Sets (Bennett et al., 1996) contain both the "correlation" and "combination" CMBR anisotropy maps generated from the *DMR* data by the *COBE* consortium (Górski et al., 1996; Hinshaw et al., 1996a; Hinshaw et al., 1996b). It is of interest to test whether these maps correlate with any other astronomical phenomena because a significant correlation with astronomical objects at redshifts less than

$z \approx 5$ would imply that the anisotropies in the maps are not of primordial cosmological origin. Negative results have been reported for correlations between the CMBR data and catalogues of rich clusters and radio, far-infrared and X-ray sources (Banday et al., 1996; Kneissl et al., 1997).

Figure 7.10 shows the results of 2-point correlations between the composite 2326 MHz map and the "correlation" and "combination" CMBR maps. The dashed lines represent the $\pm 1\sigma$ bounds for chance correlation that were calculated using Monte Carlo simulations in conjunction with synthetic CMBR maps as described in the previous section. No significant correlation is seen for either version of the CMBR map, but both correlation functions display a negative trend for lag angles near 180°. This apparent negative correlation is probably due to the contra-alignment of the galactic and CMBR quadrupoles.

7.3 Radio/Far-infrared Correlation

The infrared radiation from the Milky Way is emitted by interstellar dust that consists mainly of graphite and silicate grains with a power-law size distribution (Mathis et al., 1977). Most of this dust is associated with neutral atomic gas and molecular gas (Bloemen et al., 1990). In the far-infrared (FIR) wavelength band ($\lambda \geq 60$ μm) the opacity of the dust is determined primarily by the optical properties of the graphite grains, and the opacity (and hence emissivity law) has a λ^{-2} dependence (Draine and Lee, 1984). The grains are heated by various means, primarily the absorption of starlight (Cox et al., 1986; Sodroski et al., 1989), and are in approximate thermal equilibrium (i.e. have a Planck-law source function).

The extended FIR emission of the Milky Way has been mapped comprehensively by the *IRAS* and *COBE* space observatories. The *IRAS* satellite (Neugebauer et al., 1984; Beichman et al., 1988), with bolometric detectors in the 12, 25, 60 and 100 μm bands, provided the first all-sky maps of the entire galaxy at FIR wavelengths (Hauser et al., 1984). The principal FIR imaging devices on the *COBE* satellite were the *DIRBE* detectors which operated at wavelengths of 1.25, 2.2, 3.5, 4.9, 12, 25, 60, 100, 140 and 240 μm (Boggess et al., 1992; Hauser et al., 1997). Although *COBE* was designed to study the cosmic background radiation, the galactic maps obtained from the *DIRBE* data have been used to study the galactic interstellar dust (Sodroski et al., 1994). *COBE* also carried the *FIRAS* spectrometer which operated from FIR wavelengths ($\lambda = 104$ μm) through to

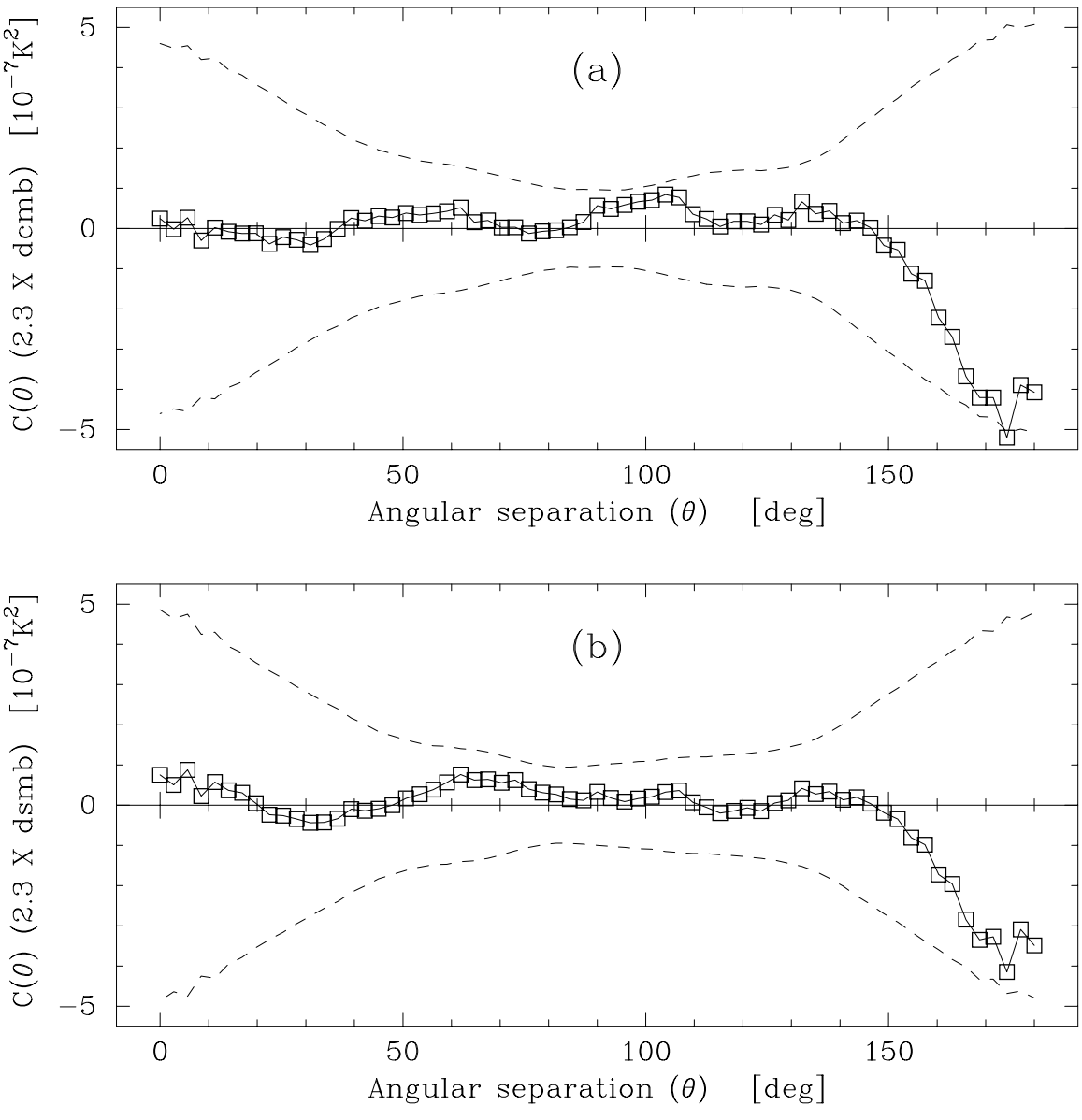

Figure 7.10: 2-point correlation functions between the composite 2326 MHz map and the two versions of the *COBE* CMBR maps. Panel (a) is the result for the "correlation" version (dcmb) and panel (b) is the result for the "combination" version (dsmb). The dashed lines represent the $\pm 1\sigma$ bounds for chance correlation that were calculated using Monte Carlo simulations in conjunction with synthetic Harrison-Zel'dovich CMBR maps.

the millimetre radio region ($\lambda = 10$ mm). The data from this instrument have been used to show that the diffuse galactic interstellar dust is dominated by a warm component with temperatures in the range 16–21 K and a ν^2 emissivity law (Reach et al., 1995; Boulanger et al., 1996). Although radio continuum emission results from the acceleration of thermal and non-thermal electrons and has no direct dependence on the properties of the interstellar dust, there may be common influences that cause correlations between the radio and FIR emission from the galaxy. This section describes the methodologies and results of comparisons that were made between the *SKYMAP* 2326 MHz radio map and selected *IRAS* and *DIRBE* FIR maps.

7.3.1 Total FIR and Radio Luminosity

It is now well-known that the integrated fluxes of the FIR and predominantly non-thermal radio continuum emissions from spiral galaxies exhibit a tight, linear correlation (De Jong et al., 1985; Beck and Golla, 1988). This correlation between two seemingly unrelated emission mechanisms may be explained by the intimate connection of both mechanisms with the young stellar population in the galaxies (Chi and Wolfendale, 1990; Rengarajan and Iyengar, 1990; Xu, 1990; Xu et al., 1994; Lisenfeld et al., 1996). The FIR emission originates from dust that has been heated by the young, hot OB stars (Cox et al., 1986), and the synchrotron electrons are provided by the supernova and supernova remnants that result from these fast-evolving stars (Hummel et al., 1988).

The radio and FIR luminosities of a spiral galaxy are dominated by the diffuse components of the emission. The correlation of these integrated luminosities does not necessarily imply a tight *spatial* correlation between the diffuse FIR and non-thermal radio emission for spiral galaxies, and indeed none is observed in the Milky Way or other similar galaxies. There is, however, a superficial similarity in the distribution of the diffuse radio and FIR emission for spiral galaxies. The longitude distributions of both the diffuse FIR and radio emission are loosely correlated with the younger galactic populations (i.e. the spiral arms), while the latitude distribution of the diffuse FIR is slightly broader than that of the radio continuum emission (Sodroski et al., 1987).

No comparison between the large-scale FIR distribution and the diffuse radio continuum emission is presented in this thesis since this topic has been extensively covered in published work by others (Sodroski et al., 1987).

7.3.2 Galactic HII Regions

There is a very tight correlation between the spatial distribution of the *thermal* radio and 60–100 μm FIR emission associated with discrete galactic HII regions situated close to the galactic equator (Haslam and Osborne, 1987; Fürst et al., 1987; Broadbent et al., 1989). The physical basis for this correlation is well-understood: the heating of the dust grains and the free-free emission are both directly dependent on the Lyman-continuum flux of the OB stars embedded in the HII regions. The free-free radio flux depends largely on the number of free electrons in the nebula, which in turn is dependent on the ionizing flux of the OB stars. As a result, the radio flux is quite predictably related to the Lyman-continuum flux from the stars. Each hydrogen atom that is ionized by a Lyman-continuum photon inevitably emits a Lyman-α photon that is trapped in the cloud (Mezger et al., 1974). These Lyman-α photons are eventually absorbed by dust grains, which become heated. The flux of the FIR emission emitted by the dust in HII regions always exceeds the heating power available from trapped Lyman-α photons by some factor called the infrared-excess, or IR-excess. The IR-excess for galactic HII regions normally lies in the range 2 to 10, and therefore the ratio of the FIR flux to radio flux is expected to vary in a similar way to the IR-excess. Typical FIR/radio flux ratios reported in the literature lie in the range 500 to 1500 (Reich et al., 1987), which corresponds to an IR-excess range of 3 to 5.

In the context of this thesis the motivation for comparing the FIR and radio emission from galactic HII regions was to devise a technique for discriminating between thermal and non-thermal radio sources near the galactic plane. This separation of the radio emission into two components was used to reduce the source confusion near the galactic plane and reveal the faint, extended supernova remnants discussed in chapter 8. The technique relies on the fact that the FIR/radio flux ratio for a typical SNR is less than 20 (Dwek and Arendt, 1992) compared to ≈ 1000 for HII regions, which allows the use of the FIR emission as a tracer of thermal radio emission. The thermal/non-thermal source discrimination technique described below is not the same as published techniques that assume a constant value of ≈ 1000 for the FIR/radio ratio (Fürst et al., 1987; Broadbent et al., 1989), or use the FIR colours to identify SNRs (Arendt, 1989; Saken et al., 1992).

Separating Thermal and Non-thermal Sources

The thermal/non-thermal source discrimination described here was restricted to the galactic latitude range $|b| \leq 15^\circ$ and the longitude range $70^\circ \leq \ell \leq 195^\circ$ because this was the region to be searched for new SNR candidates. The FIR map used for the analysis was constructed by combining and regridding the relevant 60 μm maps from the *IRAS* Sky Survey Atlas CD-ROM set (Wheelock et al., 1994). Program `ctfm_iras.f` was written to perform this coordinate transformation task on the *IRAS* sky-plates which use an equatorial gnomonic projection. The 60 μm channel was chosen to remain consistent with the published work (Fürst et al., 1987; Broadbent et al., 1989).

Both the FIR and *SKYMAP* data were smoothed to a FWHM resolution of 24-arcmin using gaussian convolution filters in order to ensure that both maps had similar beamshapes. The regridded maps were slightly oversampled with a pixel spacing of $\frac{1}{7}^\circ$. Appropriate scaling factors were applied to the maps to convert them to a common Jy.Beam^{-1} brightness scale. The background-fitting procedure described in chapter 6 was applied to both maps in order to subtract out the diffuse, extended emission from both maps. This was done in an attempt to remove the diffuse synchrotron emission from the radio map and the diffuse emission from the interstellar dust and the extended, low-density HII region from the FIR map.

Program `radiofir.f` was written to derive a model of the non-thermal, synchrotron emission from the prepared radio and FIR maps. The procedure used to produce each pixel in the synchrotron model is illustrated in the flow-diagram shown in figure 7.11. The philosophy of the program is to detect local areas where the radio and FIR data correlate very closely. The locally-calculated FIR/radio ratio is used in conjunction with the FIR and radio maps to produce the (non-thermal) synchrotron model. Where there is no significant correlation between the radio and FIR maps the radio emission is assumed to be entirely non-thermal synchrotron emission and the FIR map data are ignored. The transfer function shown in the flow-diagram relating "Weight" to "Corr" is necessary to prevent discontinuities in the resulting maps. All of the parameters shown in the flow-diagram were selected by trial-and-error.

The efficacy of this technique may be judged by consulting plates C.6 to C.14 in appendix C. The lower panels of these plates represent images of the non-thermal radio model produced by `radiofir.f`. The upper panels are maps of the thermal radio emission

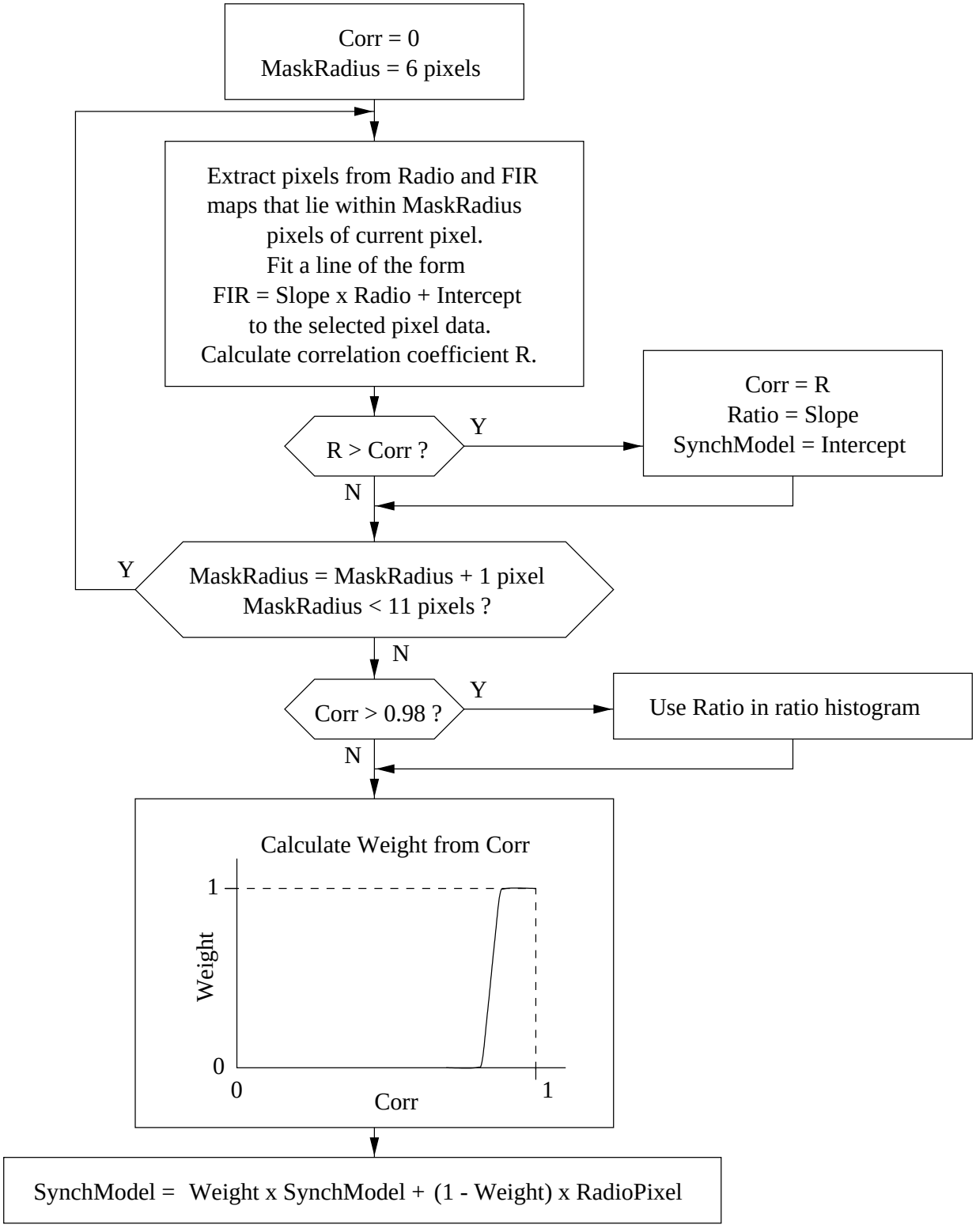

Figure 7.11: A flow-diagram of the processing applied to the radio and FIR maps at each pixel position by program `radiofir.f`. The program outputs a model radio synchrotron map (see the lower panels of plates C.6 to C.14 in appendix C) and a histogram of the distribution of FIR/radio ratios (figure 7.12).

that were obtained by simply subtracting the non-thermal model produced by `radiofir.f` from the input radio map. The thermal maps were cropped at $|b| = 4°$ because there were no significant features in the thermal model at latitudes beyond this limit. The colour-wedge at the bottom of each plate shows the brightness scale spanned by the colour images. Contours at levels of 1, 2, 4, 8, 16, 32 and 64 Jy.Beam^{-1} are used to represent the brighter, less extended sources in the maps.

The crosses ($\times$) in the lower panels indicate the positions of known, small-diameter supernova remnants listed in Green's continuously updated catalogue (Green, 1998). In the upper panels the white crosses ($\times$) represent the positions of HII regions listed in the combined Sharpless (Sharpless, 1953) and Blitz et al. (1982) catalogues, the white pluses (+) represent the positions of HII regions listed in the RCW catalogue (Rodgers et al., 1960a), and the white dots represent the positions towards which radio recombination lines were detected by the Green Bank (Lockman, 1989) and Parkes (Caswell and Haynes, 1987) surveys. Computer-readable versions of these catalogues were extracted from a concordance database (Barnes and Myers, 1997). The additional annotations in the lower panels of the plates are described in chapter 8.

The thermal/non-thermal discrimination process appears to have been quite successful. Except for sources that are too faint to be seen in the *SKYMAP* data, the vast majority of known thermal and non-thermal sources have been correctly classified, i.e. appear in the correct panel of the appropriate plate.

The FIR/radio Ratio

Although the radio and FIR emission features for HII regions are spatially coincident, there is a wide dispersion in the ratio between the radio and FIR intensities, both within individual objects and between different objects. This dispersion is evident in figure 7.12, which shows the frequency distribution of the ratios obtained using the method outlined above. This histogram is somewhat noisier than a similar plot obtained by Reich et al. (1987) when comparing their 2695 MHz data of the northern galactic plane with the 60 μm *IRAS* data. It is clear from this histogram that the assumption that the FIR/radio ratio is constant is quite incorrect.

A possible future line of enquiry would be to test whether the FIR/radio ratio depends on the colour of the FIR emission, as might be expected if the IR-excess for HII regions depends on the absorption properties of the embedded dust grains (Mezger et al., 1974;

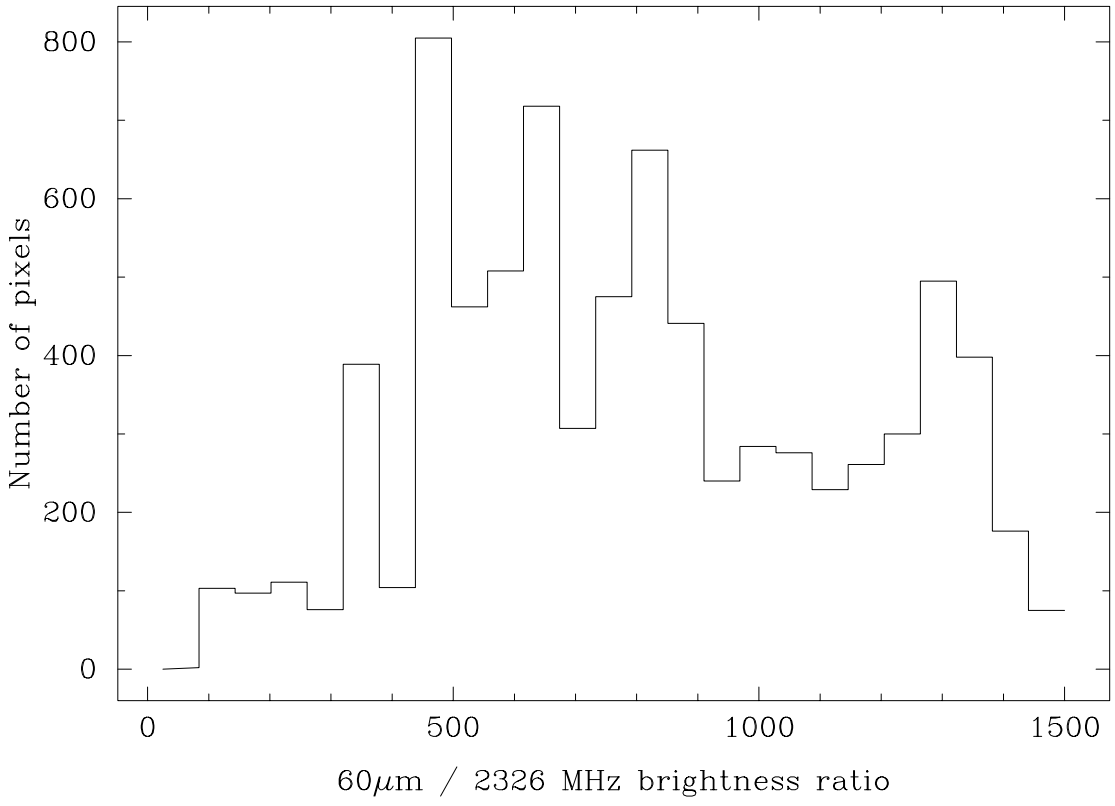

Figure 7.12: A histogram of the frequency distribution of the ratio between the 60 μm FIR brightness and 2326 MHz radio continuum brightness for map pixels coincident with HII regions in the galactic plane.

Emerson and Jennings, 1978).

7.3.3 FIR Cirrus

The diffuse, filamentary FIR cirrus emission extending to high latitudes was one of the first new FIR phenomena discovered by the *IRAS* satellite (Low et al., 1984). A strong correlation between the FIR cirrus brightness and HI column density has been measured (Tereby and Fich, 1986; Boulanger and Pérault, 1988; Désert et al., 1988; Joncas et al., 1992; Boulanger, 1994; Waller and Boulanger, 1994) which indicates that the cirrus emission is thermal emission from dust that is coextensive with the galactic HI gas.

Some authors have reported that the morphologies of the high-latitude emission from the various phases of the ISM are very similar (Wall and Waller, 1998; Waller et al., 1998), and that there may be significant correlations between the FIR cirrus and radio emission. Possible physical processes that would lead to a correlation between the FIR cirrus and radio emission are discussed below, and the results of a search for a correlation between the cirrus emission and the galactic 2326 MHz radio continuum are presented.

Physical Processes

Although the direct thermal emission of the dust grains is not detectable at centimetre wavelengths there are a number of physical processes that may lead to a correlation between centimetre-wavelength radio continuum features and the infrared cirrus emission. The most plausible of these are discussed in turn below.

SNRs and Superbubbles. The cirrus clouds may be preferentially aligned with the shells of high-latitude supernova remnants and superbubbles, in which case there is expected to be a correlation between the FIR cirrus emission and the synchrotron emission of the SNR shells. This mechanism is expected to produce a strong correlation because the small-scale structures in the high-latitude radio emission are predominantly the non-thermal emission from such shells.

Diffuse HII. The optical and radio emission from diffuse galactic HII regions has been reported to correlate spatially with the FIR cirrus:

- Optical H-α emission has been found to correlate weakly, but significantly, with the 100 μm infrared cirrus (Kogut, 1997; McCullough, 1997)
- A correlation between the 53 GHz and 90 GHz *COBE-DMR* maps and the *COBE-DIRBE* FIR maps has been reported (Kogut et al., 1996b).
- Data from ground-based CMBR experiments has been shown to correlate with the FIR cirrus (Leitch et al., 1997).

These correlations indicate that a substantial fraction of the warm ionized medium (WIM) resides in partially-ionized HI clouds associated with the FIR-emitting dust. The low-frequency radio bremsstrahlung emission emitted by the WIM may, therefore, show some correlation with the FIR emission. This galactic foreground free-free emission has obvious implications for CMBR work.

If the WIM is assumed to have a typical HII region electron temperature of 8000 K then the hydrogen Balmer-α intensity and 2326 MHz free-free radio brightness temperature of the medium are related to the emission measure, EM, by:

$$\begin{aligned} I_\alpha &= 0.44 \times \mathrm{EM} \quad [\mathrm{R}] \\ T_\mathrm{B} &= 6 \times 10^{-4} \times \mathrm{EM} \quad [\mathrm{K}] \end{aligned} \tag{7.19}$$

where the emission measure has units of cm^{-6}.pc. The H-α/100 μm ratios determined by the published work on H-α/FIR correlation (Kogut, 1997; McCullough, 1997) lie in the range 0.34–0.85 R.MJy^{-1}.sr. Combining this range of values with the relationships given in equation 7.19 results in an expected $T_{2326}/I_{100\mu\mathrm{m}}$ ratio in the range 0.46–1.15 mK.MJy^{-1}.sr. This amplitude of thermal radio emission is more than an order of magnitude fainter than the RMS fluctuations seen in the predominantly non-thermal high-latitude 2326 MHz emission. As a result of this low thermal signal level a very weak correlation may be expected between the *SKYMAP* and FIR maps.

Dust Grain Destruction. Boulanger et al. (1996) point out that some ISM theories predict that dust grain destruction occurs in the low-density WIM. This would lead to an anti-correlation in the spatial distribution of dust and diffuse HII, and would cause a corresponding anti-correlation in the angular distribution of the FIR and thermal radio emission. This would result in an extremely weak negative correlation between FIR and centimetre-wavelength radio maps.

Spinning Dust Grains. Recently Draine and Lazarian (1998) have suggested that the correlation between the 14–90 GHz microwave emission and the 100 μm FIR emission (Kogut et al., 1996b; De Oliveira-Costa et al., 1997; Leitch et al., 1997) is anomalous because it is difficult to reconcile the observed radio intensities with free-free emission from the interstellar gas associated with the dust. They propose that the source of this excess millimetre-wavelength emission is a population of rotating dust grains that have an electric dipole moment. The spectrum of this proposed rotational emission has a peak near 20 GHz and falls rapidly towards lower frequencies. At 2326 MHz the rotational emission would be undetectable in the *SKYMAP* data, and would not contribute towards a correlation with FIR maps.

Correlation of the *DIRBE* and *SKYMAP* Data

The *DIRBE* FIR maps (Hauser et al., 1997) were chosen for the correlation analysis because their resolution matched the *SKYMAP* data more closely than the *IRAS* maps. The computational effort required to smooth the *SKYMAP* map to match the resolution of the *DIRBE* maps was some orders of magnitude less than that required to smooth and regrid the *IRAS* maps to the *SKYMAP* resolution. The 140 μm and 240 μm *DIRBE* maps

also extended the wavelength coverage beyond the 100 μm limit of *IRAS*. Conventional correlation and regression analyses were carried out between the *SKYMAP* 2326 MHz map and the *DIRBE* 60 μm, 100 μm, 140 μm and 240 μm maps. These wavelengths were chosen because they straddle the peak in the spectrum of the cirrus emission. A two-point correlation analysis was considered for the *DIRBE*/*SKYMAP* comparison, but the computational burden resulting from the size of the maps precluded the use of this analysis option.

All of the maps were regridded onto the *COBE* Quadrilateralized Spherical Cube Projection (Hauser et al., 1997) for the correlation analysis. This projection was chosen because of its equal-area property and its convenient data format. The *SKYMAP* map was smoothed to the nominal *DIRBE* beamshape during the regridding process.

The aim of the correlation analysis was to search for a very faint signal in the *SKYMAP* data that correlated with the FIR cirrus, so all regions of the maps that contained interfering bright sources were flagged for exclusion from the analysis. The *COBE* custom galaxy cut (Banday et al., 1997) was used to exclude the bright emission from the galactic plane, and both the LMC and SMC were masked out of the radio and FIR maps. The *DIRBE* data that was badly contaminated by zodiacal emission was also excluded. The limited *SKYMAP* sky coverage, the custom galaxy cut, the exclusion of the LMC and SMC and the exclusion of bright zodiacal features reduced the number of pixels used in the correlation analysis to 174082 out of a maximum all-sky total of $256^2 \times 6 = 393216$ pixels. These remaining pixels were still sufficiently numerous to allow a very sensitive correlation analysis to be performed.

All of the maps were high-pass filtered using a ring-median filter with a diameter of 10° which removed all emission features with angular scales larger than 10° from the maps. This filter removed brightness gradients due to the diffuse galactic background emission that would cause spurious correlations between the radio and FIR maps, but left the small-scale cirrus emission unattenuated.

Figure 7.13 presents contour diagrams of the bivariate distributions resulting from a pixel-by-pixel comparisons of the four selected *DIRBE* maps with the *SKYMAP* map. Contour diagrams were used in preference to the scatter-plots traditionally used for correlation analyses because of the large number of data points. In all four cases the contours show no obvious sign of correlation between the FIR and radio data, and this low level of correlation is quantified by the Pearson's correlation coefficients listed in table 7.2.

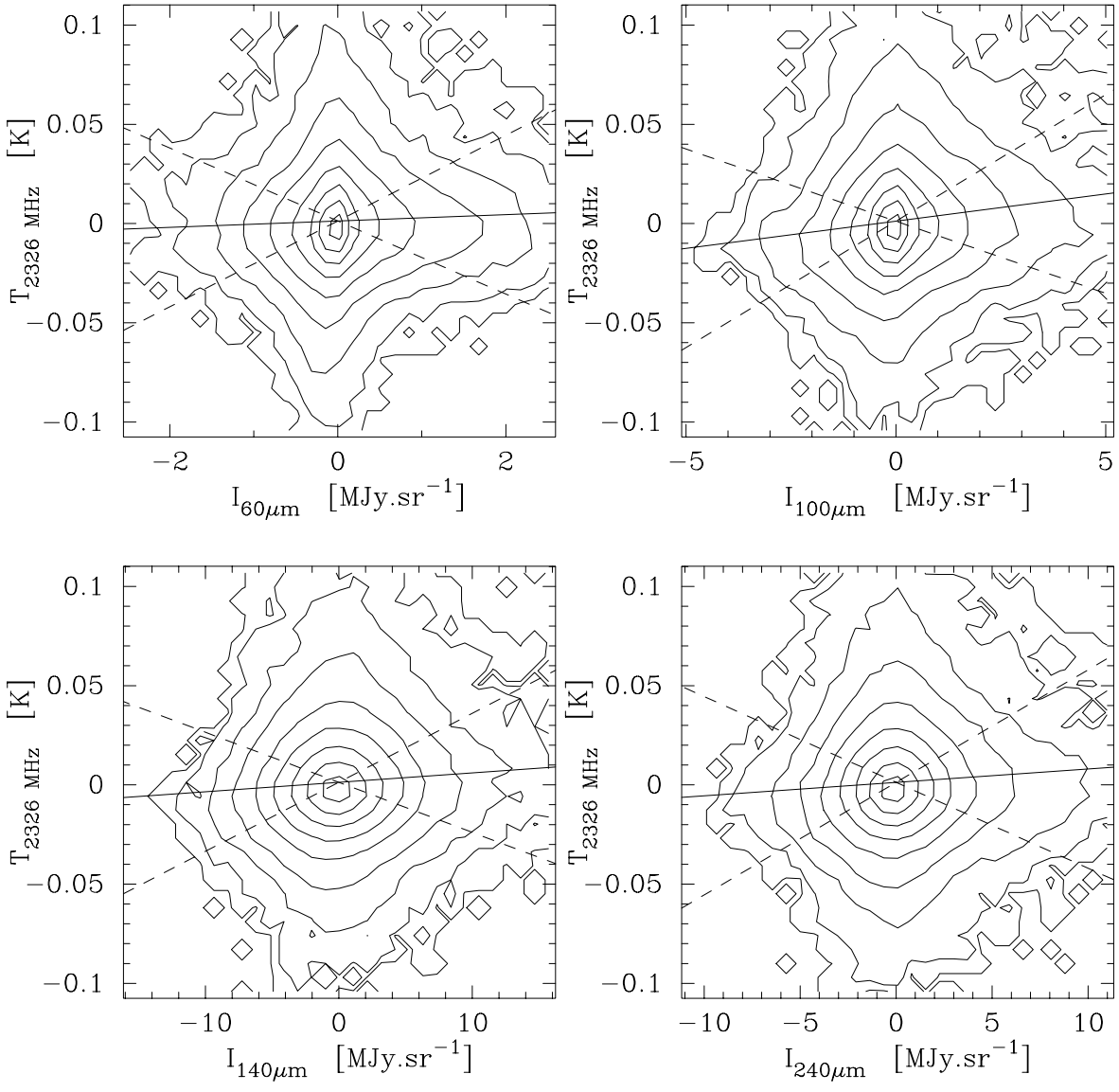

Figure 7.13: Contour plots of the radio vs FIR bivariate distribution for the median-filtered, high-latitude data sets described in the text. The contour levels are set at 0.004%, 0.034%, 0.22%, 1.1%, 4.4%, 13%, 32%, 61% and 88% of the peak distribution value. These contours would appear as equi-spaced circles if the two variables were uncorrelated gaussian noise. The solid line in each graph represents the ordinary least-squares linear regression solution and the dashed lines represent the estimated $\pm 1\sigma$ slopes. The correlation coefficients and slopes resulting from the regression are listed in table 7.2.

λ [μm]	$I_\lambda/I_{100\mu}$ (17.5 K)	T_b/I_λ [mK.MJy^{-1}.sr]	Expected [mK.MJy^{-1}.sr]	Corr. Coeff.
60	0.053	1.60 $\pm$20	8.71–21.7	0.018
100	1.000	2.73 $\pm$10	0.46–1.15	0.065
140	1.958	0.48 $\pm$3	0.24–0.59	0.035
240	1.579	0.67 $\pm$5	0.29–0.73	0.035

Table 7.2: Results of the correlation analysis performed between the *SKYMAP* 2326 MHz map and four *DIRBE* FIR maps. The columns contain the following information: (1) the wavelength of the *DIRBE* map; (2) the predicted FIR brightness relative to 100 μm for 17.5 K dust with a λ^{-2} emissivity law; (3) the slope of the FIR/radio line obtained using ordinary least-squares analysis together with the estimated error (see figure 7.13); (4) the T_b/I_λ ratio expected for free-free emission from HII associated with the cirrus dust; (5) the Pearson's correlation coefficient resulting from the regression analysis.

Although the correlation coefficients listed in table 7.2 are very small they may be shown to be significant by comparing them with the distribution of correlation coefficients obtained using control data sets that are known not to correlate. These controls are required to have similar characteristics to the actual data for this comparison to be valid, and a procedure similar to that used by McCullough (1997) was used. The control correlation coefficients were calculated by correlating the unchanged *SKYMAP* data with versions of the *DIRBE* data that had been rotated about the galactic pole. The rotation angle was incremented by 5.625° before each correlation, resulting in a total of 63 controls for each *DIRBE* wavelength. This method of generating control FIR maps ensured the consistent orientation of any residual diffuse galactic background emission that was not removed by the ring-median filter.

The histograms in figure 7.14 summarize the results of this control analysis for the four *DIRBE* bands. For wavelengths greater than 60 μm it is clear that the positive correlation coefficient obtained is significant, particularly at 100 μm. The significance at 60 μm is marginal, but the correlation coefficient value is larger than any returned by the controls.

The correlation coefficient gives no information about the value of the ratio between the correlating signals. This ratio must be obtained by fitting a straight line to the appropriate bivariate distributions shown in figure 7.13. The formal errors in the slopes of the regression lines must necessarily be very large because of the very low values of the correlation coefficients.

It is assumed that all of the FIR emission has some free-free radio emission associated with it (but not vice-versa), therefore the relationship between the radio and FIR brightness

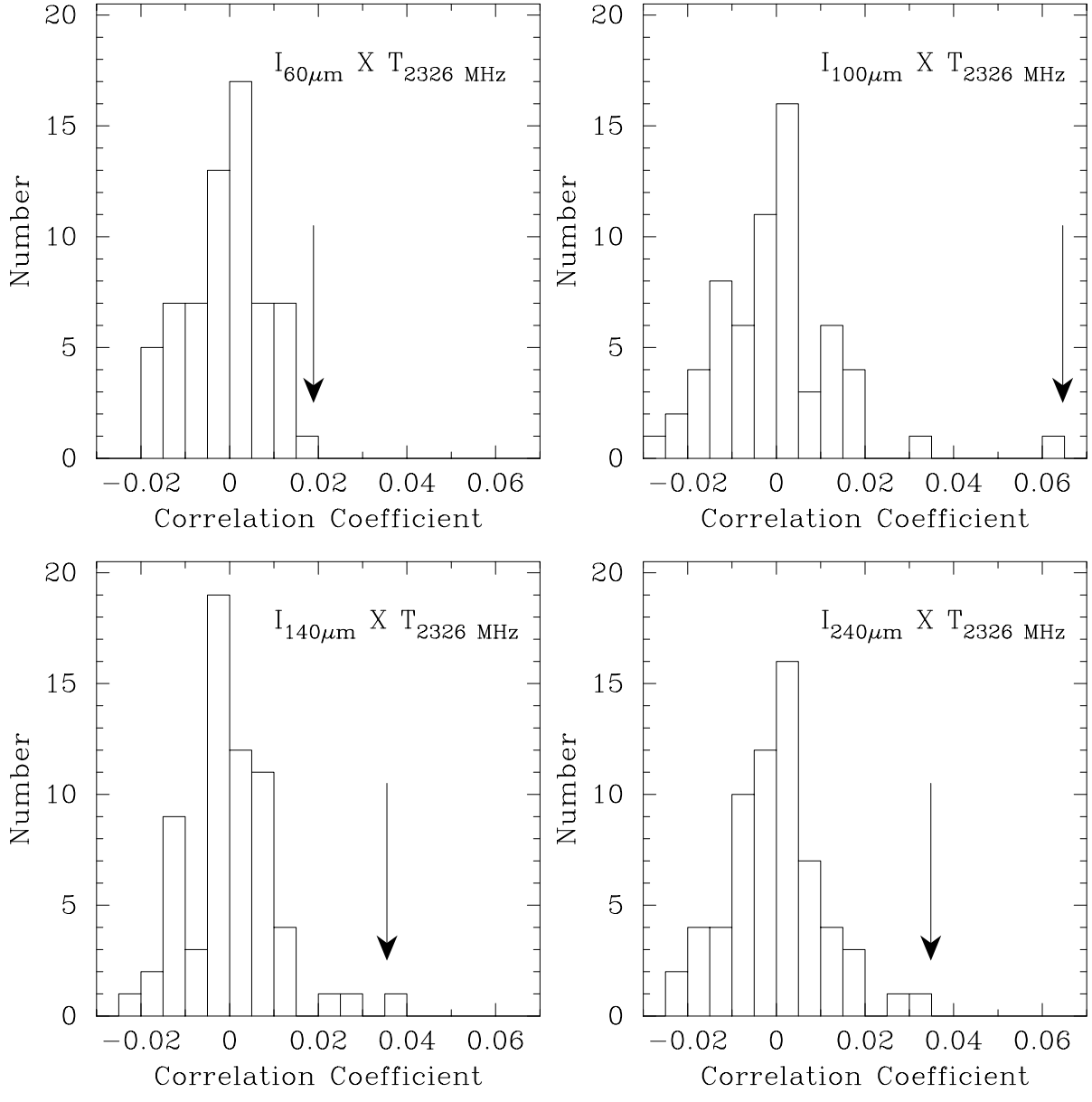

Figure 7.14: Histograms showing the distributions of correlation coefficients obtained by calculating Pearson's correlation coefficient for the *SKYMAP* data paired with the *DIRBE* data and 63 control data sets. The controls were generated by performing Eulerian rotations about the galactic pole on the FIR data. The arrow in each plot indicates the value of the "real" correlation coefficient listed in table 7.2.

may be written as:

$$T_{2326} = a_\lambda I_\lambda + T_{\rm nc} \tag{7.20}$$

for each map pixel, where a_λ is the required ratio and $T_{\rm nc}$ accounts for excess radio emission not correlated with the FIR emission. The vertical extensions near $I_\lambda = 0$ in the contours (figure 7.13) are evidence of excess variance in the radio data that is not correlated with the FIR emission. These non-correlated radio signals are treated as noise which is non-gaussian and not necessarily zero-mean. Ordinary least squares regression is an appropriate technique for estimating a_λ for this situation, and the resulting slopes obtained for the four parallel analyses are listed in table 7.2. Data pairs that are obviously contaminated by radio sources were excluded prior to calculating the errors quoted for these slopes.

The conclusions that can be deduced from these results are:

- There is a small but significant positive correlation between the high-latitude FIR cirrus emission and the 2326 MHz radio data. The positive sense of the correlation rules out dust grain destruction as a physical mechanism causing the correlation, and the small magnitude of the coefficient probably excludes the association of the cirrus with the non-thermal radio emission. No significant correlation would be expected if the radio emission resulted from spinning dust grains.

- The Radio/FIR ratios are consistent with the values expected for thermal free-free radio emission from diffuse HII associated with the cirrus dust, but the large errors in these ratios make this conclusion very speculative. The RMS variance of the thermal radio emission is estimated to be of the order of 1 mK at 2326 MHz.

A more conclusive result could be obtained if extensive high-latitude hydrogen emission line data were available to perform a correlation analysis with the radio data. These data would provide an independent and more direct test as to whether the thermal radio signal from the WIM does exist. An H-α optical emission line survey of the entire southern Milky Way is currently being made (Parker and Phillipps, 1998; Duncan and Haynes, 1998), but unfortunately it is not planned to extend this survey to high latitudes. Another tracer of the WIM that could possibly be used for a correlation analysis with the radio data is the 205 μm fine structure transition of N^+ that was detected by the *COBE–FIRAS* spectrometer (Wright et al., 1991; Bennett et al., 1993). Because of the low angular resolution (FWHM = 7°) of the *FIRAS* instrument and the sparse sky coverage it was decided not to pursue this line of investigation.

Chapter 8

Supernova Remnants and Low-Latitude Structures

The important effects that galactic supernova remnants (SNRs) have on the chemistry, energy balance and morphology of the Milky Way were highlighted in the review of the Milky Way presented in chapter 5. A thorough understanding of the population statistics of these energetic phenomena is required in order to understand fully the dynamics and energetics of the galactic ISM.

This chapter describes the results of a search for new SNR candidates and other emission structures in the low-latitude emission mapped by the *SKYMAP* 2326 MHz survey. The following attributes of the survey are well-suited to the task of identifying these low-latitude structures:

- The high dynamic range and linearity of the temperature scale allows the faint, extended emission from objects such as SNRs to be isolated from the relatively bright background emission.
- The 20-arcmin FWHM resolution of the map is good enough to allow many sources close to the galactic plane to be identified and isolated from nearby confusing sources.
- The wide sky-coverage of the map allows possible high-latitude extensions of the low-latitude features to be detected and traced.

A number of low-latitude, extended objects that were discovered in the *SKYMAP* maps have been described in previous publications (Jonas, 1986; Woermann and Jonas, 1988).

The SNR candidates and other low-latitude emission features reported in this chapter are useful probes for studying the physical conditions in the ISM because of the intimate connection between the ISM and SNRs. The SNR morphologies are partly determined by

the ambient ISM conditions and the SNRs have a major effect on the ISM. In particular, emission features showing structures preferentially aligned in a direction perpendicular to the galactic plane could be candidates for the hypothesized worm and chimney structures described in chapter 5.

8.1 The Search for Galactic SNR Candidates

The detection of a number of very large, high latitude SNRs in the residual 2326 MHz emission after DGB subtraction was discussed in chapter 6. At lower latitudes the source confusion makes identification of faint, extended sources very difficult, even in the DGB-subtracted maps. The separation of the thermal and non-thermal emission into separate maps using the program `radiofir.f` described in chapter 7 reduces this source confusion. The maps produced by this discrimination procedure are presented as colour plates in appendix C. These maps, with both the DGB and thermal sources subtracted, were used to search for new SNR candidates and other interesting non-thermal structures close to the galactic plane.

8.1.1 The Colour Plates

The 2326 MHz data used in the search for new SNR candidates and low-latitude emission features are shown as pseudo-colour maps in plates C.6 to C.14 of appendix C. The lower panels of these plates are images of the non-thermal emission models derived from the *SKYMAP* survey data using the program `radiofir.f`, as described in chapter 7. The annotation used in the non-thermal emission images is described here:

Crosses ($\times$)

Centre positions of 178 SNRs with angular diameters $\theta_D < 1.5°$ listed in Green's on-line catalogue (Green, 1998).

Pluses ($+$)

Centre positions of 13 SNRs with angular diameters $\theta_D < 1.5°$ identified in the Parkes 2.4 GHz survey (Duncan et al., 1997), but not yet listed in Green's catalogue.

Dashed-line Circles

Outlines of SNRs with angular diameters $\theta_D \geq 1.5°$ listed in Green's catalogue (Green,

1998) or identified in the Parkes 2.4 GHz survey (Duncan et al., 1997). There are a total of 18 of these objects, 6 from Green's catalogue and 12 from the Parkes survey.

Solid-line Circles

41 new SNR candidates identified in the *SKYMAP* 2326 MHz data. The measured parameters and brief descriptions of these objects are listed in table 8.1. Although there are 42 sources listed in table 8.1 the shell-like source G25.0+35.0 does not intersect with the plates because of its high latitude.

Circled Pluses ($\oplus$)

Positions of known pulsars listed in an on-line database (Taylor et al., 1993). An arrow associated with a $\oplus$ symbol represents the direction (but not magnitude) of the published proper motion of the pulsar.

The mapping of the radio brightness to colour is defined by the colour wedge at the bottom of each plate. The mapping was chosen to accentuate the extended, low-brightness features and is fixed for plates C.6 to C.14. Contours are drawn at levels of 1, 2, 4, 8, 16, 32 and 64 Jy.Beam^{-1} in order to delineate the stronger, more discrete sources.

8.1.2 SNR Selection Criteria

SNR candidates were identified by visual inspection of the non-thermal map data. The SNR search was made by viewing the maps on a video screen, using the SAOIMAGE package (Hilst, 1991) which allows the interactive manipulation of the contrast in the viewed image. This permitted a more detailed investigation of the map data than would be possible with the printed maps shown in appendix C.

Similar criteria to those used by Duncan et al. (1997) were used for selecting SNR candidates in the images:

- The SNRs are assumed to have no FIR emission associated with them. Program `radiofir.f`, described in chapter 7, ensured that no objects that are spatially correlated with FIR emission are included in the non-thermal map.

- Only emission features that have a shell structure or are coherent, extended patches of emission in an unconfused area were selected as candidate objects.

The central position and angular diameter of each SNR was determined manually from a printed copy of the SNR image using a transparent template with concentric circles plotted on it. Table 8.1 is a list of the 42 SNR candidates that were identified in this way.

The galactic coordinates of each source listed in table 8.1 may be ascertained from the name allocated to it. The table entry for each source includes the estimated angular diameter of the object and a brief remark about its morphology. Undoubtably many of the identifications are contentious, and many other structures are visible in the maps that could be construed to be SNR candidates. Even if some of the SNR candidates listed in table 8.1 are misidentifications the positions and diameters contribute to the statistical information about the distributions of these quantities for extended, non-thermal galactic sources. All of the objects are worthy of more sensitive and/or higher resolution observations.

It was not possible to determine reliable integrated flux densities for any of these objects because of one or both of the following reasons:

- A large degree of source confusion persists in the maps despite the subtraction of the DGB and thermal emission. The overlap of sources along most lines of sight makes it difficult to apportion radio flux appropriately.

- The emission associated with the objects is faint and superimposed on an uneven background. Many of the candidate sources have surface brightnesses which are comparable with the pixel noise and less than the baseline uncertainty.

The next section examines how these new SNRs affect the statistics of Green's current SNR catalogue (Green, 1998). Following this discussion, selected low-latitude objects are described in more detail in section 8.3.

8.2 Statistical Analysis of Galactic SNRs

Many authors have commented on the problems of incompleteness in galactic SNR catalogues. Statistical analyses indicate that current catalogues of SNRs are incomplete (Caswell, 1988; Green, 1991), despite the fact that extensive SNR searches have been carried out at X-ray (Seward, 1990), optical (van den Bergh, 1973; Raymond, 1984) and radio (Milne et al., 1985; Milne et al., 1987; Whiteoak, 1992; Whiteoak and Green, 1996; Dougherty et al., 1996; Duncan et al., 1997) wavelengths. The two dominant selection criteria leading to the incompleteness are flux and surface brightness limits (Ilovaisky and

No		Name (Position)	θ_D [deg]	Morphology
1	§	G256.7−8.0	14.0	part of Gum nebula
2	§	G260.2+1.4	26.0	part of Gum nebula
3	§	G261.2−8.0	11.2	part of Gum nebula
4	§	G267.2−0.6	11.4	part of Gum nebula
5		G274.1+5.8	8.6	faint, patchy shell
6		G286.2+4.5	4.0	faint, patchy emission
7		G303.0−5.8	6.3	faint, patchy emission
8		G308.2+3.9	2.8	patchy shell
9		G313.7−7.2	4.7	faint, patchy emission
10	†	G314.0−11.0	13.0	very large, faint shell
11		G317.8+8.4	4.5	very faint, patchy shell
12	†	G319.8+17.3	6.5	incomplete shell
13		G322.2−8.2	4.0	faint, patchy shell
14	§	G323.5+0.8	13.7	large, incomplete shell
15		G329.3−0.3	9.4	large, indistinct shell
16	‡	G330.7−4.2	4.5	bright arc
17	‡	G334.6+6.6	3.5	shell with extensions
18	§	G337.2−8.7	6.0	large, patchy clump of emission
19	‡	G340.8−4.8	2.9	patchy shell
20		G342.6+8.2	6.0	bright arc
21	§‡	G344.4−5.3	3.8	bright arc
22		G347.7+6.6	3.4	faint, patchy shell
23	†§‡	G356.9+8.5	9.5	nearly-complete shell
24	‡	G356.9−5.0	5.0	bright arc
25	‡	G1.2−4.0	4.8	bright arc
26		G7.3−5.3	7.2	faint, patchy shell
27		G8.2−4.8	3.0	faint, patchy shell
28		G11.9−3.6	4.0	large bright patch of emission
29	†	G25.0+35.0	8.0	bright arc
30		G27.0+0.5	7.0	bright, incomplete shell
31	†	G27.5−21.0	22.0	very large faint shell
32	†	G31.0−11.0	6.0	large, bright arc
33		G39.7+8.1	2.0	faint, patchy emission
34		G40.3−6.9	5.2	complete shell with bright arc
35	§	G43.3−1.0	8.0	very bright incomplete shell
36		G45.1+8.9	10.0	very indistinct shell
37		G45.3−8.8	5.9	incomplete shell
38		G48.0+8.0	2.4	faint, patchy shell
39		G48.2+4.2	4.0	incomplete shell
40		G53.8+5.0	3.8	patchy emission, possible shell
41		G55.8−6.2	6.0	very faint barrel-shaped
42		G56.8+0.0	1.6	incomplete shell, possibly discrete sources

Table 8.1: A table of the 42 newly identified, large diameter galactic SNRs found in the *SKYMAP* 2326 MHz survey data. The entries marked with a dagger (†) were discussed in chapter 6, while those marked (§) are discussed in more detail in section 8.3 of this chapter. Objects previously identified by Jonas (1986) are marked with a double dagger (‡).

Lequeux, 1972b; Green, 1991). Small, distant SNRs are difficult to detect because of their low flux densities, and the low surface brightness of large angular diameter SNRs results in their confusion with strong foreground and background sources. The consequences of an incomplete statistical knowledge of the galactic SNR population are outlined below.

The galactic supernova rate.

Estimates of the galactic SN rate vary from 1 in 18 years (Wu and Leahy, 1988) to 1 in 170 years (Clarke and Caswell, 1976). Bias caused by incompleteness in the statistics of galactic SNRs is the major factor responsible for this wide range of uncertainty (Ilovaisky and Lequeux, 1972a; Wu and Leahy, 1988; van den Bergh, 1990). Most estimates place the galactic SN rate in the range 1 in 30–50 years (van den Bergh, 1990).

The Σ-D relationship.

There is no consensus as to whether there is a general law relating the surface brightness (Σ) of SNRs to their physical diameter (D) (Berkhuijsen, 1983; Green, 1984; Huang and Thaddeus, 1985; Berkhuijsen, 1986; Green, 1991; Huang et al., 1994). The lack of reliable distances to most known SNRs is the major reason for this dissent. Green suggests that the apparent Σ-D relationship is in fact an artifact due to the surface brightness limit of SNR catalogues (Green, 1984).

The N-D relationship.

The cumulative number/diameter relation is, potentially, a useful statistical tool for studies of the dynamics of SNRs. The theory of SNR evolution predicts a power-law dependence of linear diameter on time ($D \propto t^{\alpha}$) for all stages in the evolution. For a complete sample of SNRs in the same stage of evolution the cumulative number density should have a power-law dependence on diameter which has the form $N(< D) \propto D^{1/\alpha}$ (Ilovaisky and Lequeux, 1972b). Cumulative statistics calculated for existing galactic SNR catalogues deviate quite markedly from this power-law (Ilovaisky and Lequeux, 1972b; Berkhuijsen, 1987; Leahy and Wu, 1989; Green, 1991), indicating incompleteness in the sample populations or errors in the theory.

The distribution of SNRs in the galaxy.

The spatial distribution of SNRs in the galaxy provides an historical record of sites of star formation. An incomplete knowledge of the positions and ages of the galactic

SNRs has obvious consequences for the study of the star formation history of the Milky Way (van den Bergh, 1988; Leahy and Wu, 1989). Monte Carlo modelling of the distribution of galactic SNRs indicates that only about 10% of the SNRs in the Milky Way have been detected (Li et al., 1988; Li et al., 1991).

The association between SNRs and pulsars.

There is still much debate in the literature about the statistics of pulsar/SNR associations, and whether the progenitors of shell-type SNR form pulsars at all (Narayan and Schaudt, 1988; Gaensler and Johnston, 1995a; Gaensler and Johnston, 1995b). A more complete galactic SNR catalogue is required to provide more reliable statistics that can be used in the investigation of pulsar/SNR associations.

The statistical distribution of SNR morphologies.

SNRs exhibit a wide range of morphologies (Manchester, 1987; Caswell, 1988) with many of them possessing a bilateral symmetry (Kesteven and Caswell, 1987). There is some debate as to whether this barrel-shaped structure is a result of an intrinsic property of the initial outburst (Kesteven and Caswell, 1987; Kesteven and Caswell, 1988; Różyczka et al., 1993) or is a result of extrinsic factors such as the interaction of the shell with the ISM and ambient magnetic field (Roger et al., 1988; Storey et al., 1992; Gaensler, 1998). Computer modelling does not provide a conclusive distinction between the predicted effects on the SNR morphology caused by these intrinsic and extrinsic factors (Bisnovatyi-Kogan et al., 1990; Mineshige and Shibata, 1990). Incompleteness in the SNR sample populations used to examine the relationship between SNRs and their interstellar environments can result in misleading conclusions.

8.2.1 Spatial Distribution

The simple statistical analysis presented here is not intended to rectify any of the incompleteness problems listed above, but rather to investigate the nature and causes of the incompleteness in galactic SNR catalogues.

The cross-hatched columns and open squares in figures 8.1 and 8.2 characterize the distributions of the positions and angular diameters of the SNRs listed in the on-line catalogue maintained by Green (1998). The extensions to the histogram columns and the filled squares in the scatter-plots show the effect of augmenting the 182 objects in

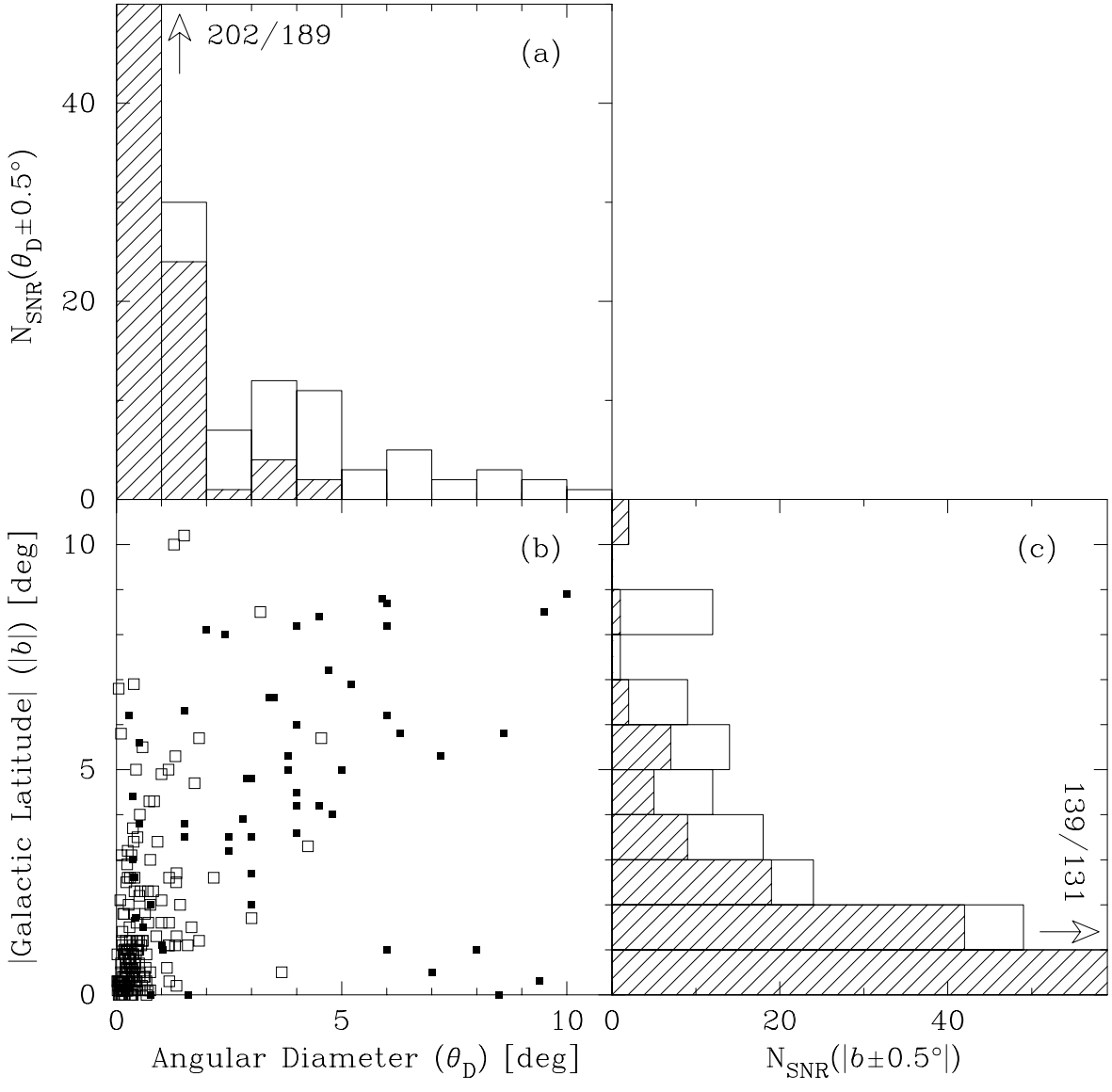

Figure 8.1: Histograms and a scatter-plot characterizing the galactic latitude and angular diameter distributions of objects listed in Green's catalogue of galactic SNRs (Green, 1998) and new SNRs identified in the Parkes 2.4 GHz survey (Duncan et al., 1997) and the *SKYMAP* 2326 MHz survey. The 220 SNRs from Green's catalogue are represented by open squares in the scatter-plot (b) and cross-hatched columns in the histograms (a & c). The SNRs identified in the Parkes (25 sources) and *SKYMAP* (42 sources) surveys are represented by the filled squares in the scatter-plot and the clear extensions to the columns in the histograms. Note that the first columns of both histograms extend well beyond the limits of the associated axes. The heights of these columns are given by the pairs of numbers adjacent to the arrows. The parameters for the 4 galactic loops have not been included in these plots.

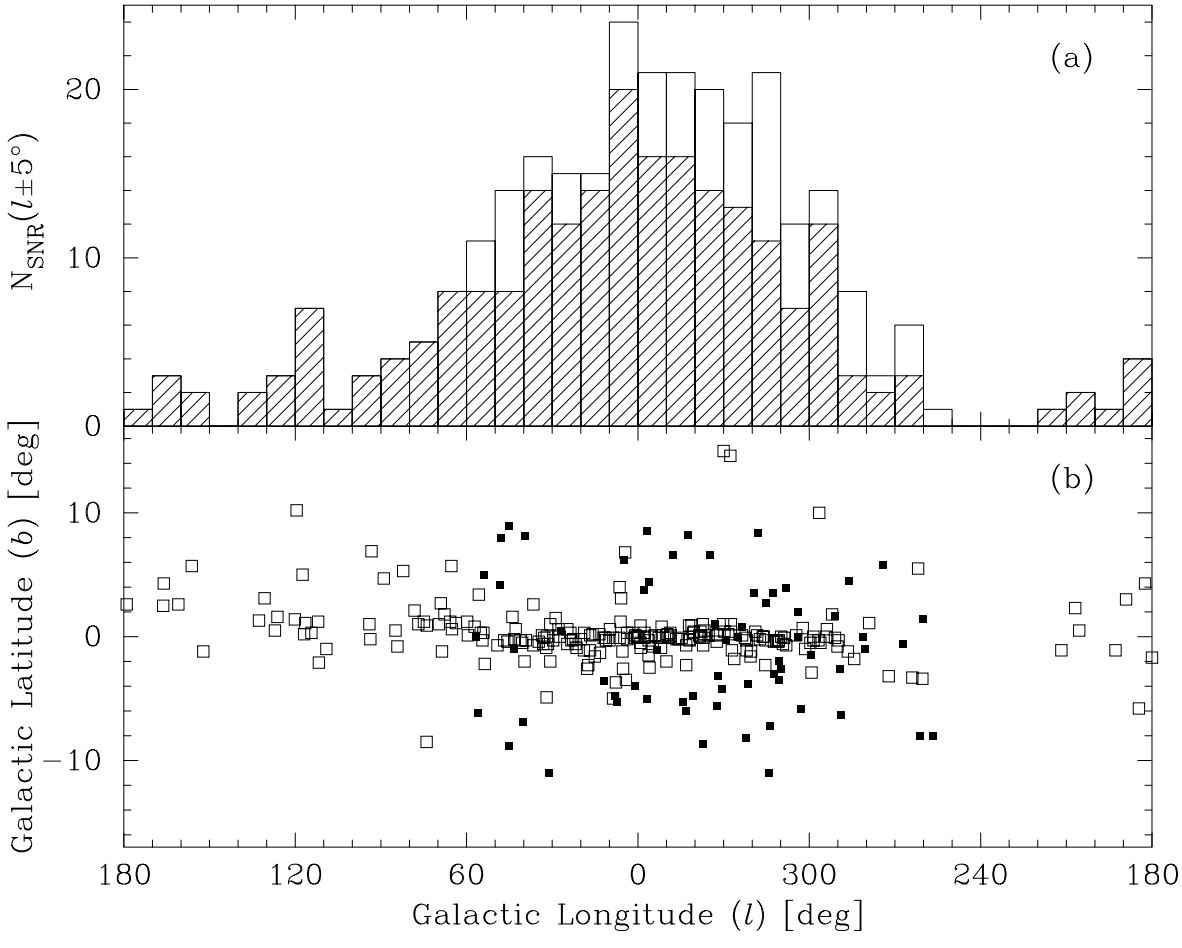

Figure 8.2: A histogram and scatter-plot characterizing the galactic longitude distribution of SNRs listed in Green's catalogue of galactic SNRs (Green, 1998) and new SNRs identified in the Parkes 2.4 GHz survey (Duncan et al., 1997) and the *SKYMAP* 2326 MHz survey. The 220 SNRs from Green's catalogue are represented by open squares in the scatter-plot (b) and cross-hatched columns in the histograms (a). The SNRs identified in the Parkes (25 sources) and *SKYMAP* (42 sources) surveys are represented by the filled squares in the scatter-plot and the clear extensions to the columns in the histogram. The longitude extent of the *SKYMAP* survey is $70° \leq \ell \leq 200°$, and the Parkes survey is entirely contained within this longitude range. The parameters for the 4 galactic loops have not been included in these plots.

Green's catalogue with the 25 SNRs identified in the Parkes 2.4 GHz survey of the galactic plane (Duncan et al., 1997) and the 42 SNR candidates listed in table 8.1. The new objects discovered in the Parkes and *SKYMAP* continuum surveys clearly broaden the latitude and angular diameter distributions of the original catalogue quite significantly, and increase the number of large angular diameter SNRs towards the inner galactic quadrants. These new SNRs reduce the selection effect precipitated by the limited sky coverage of previous SNR searches at radio wavelengths.

The longitude distribution of SNRs in the first and fourth quadrants is seen to closely mimic the equatorial profile of the diffuse galactic background model in figure 6.2 of chapter 6. This correspondence implies that the DGB is closely related to the SNR activity. The cosmic rays responsible for the DGB emission are either electrons that have diffused away from their parent SNR shells, or are trapped in large, old shells that are no longer distinguishable as independent objects.

A conspicuous feature of figure 8.1(b) is the under-density of objects in the lower-right half of the angular diameter/|latitude| scatter-plot, implying an apparent paucity of large-diameter SNRs that straddle the galactic plane. This anomaly is interpreted as evidence of a surface brightness limit resulting from source confusion at low latitudes. Large, faint shell structures centred near the galactic equator are difficult to isolate from the confusion of sources at low latitudes ($b < 10°$), particularly in the first and fourth galactic quadrants. The emission from these missing SNRs would be very confused and the smooth component of the aggregate emission probably contributes to the low latitude region of the diffuse galactic background model that was subtracted from the data. The incompleteness of the SNR sample represented in figure 8.1(b) therefore provides evidence that a substantial fraction of the galactic ridge emission is due to the superposition of SNR shells.

8.2.2 Angular Diameter Distribution

Figure 8.3 shows the cumulative-number/angular-diameter (N-θ_D) distributions of the SNRs listed in Green's catalogue both with and without augmentation by the new SNRs from the Parkes and *SKYMAP* surveys. If the cumulative-number/linear-diameter (N-D) relationship for galactic SNRs is a power-law of the form $N(< D) \propto D^{1/\alpha}$ then the N-θ_D relationship would also be a power-law with the same index, i.e. $N(< \theta_D) \propto \theta_D^{1/\alpha}$. Most SNRs are expected to either be in the adiabatic expansion phase or the subsequent isothermal expansion phases, which correspond to power-law indices of $\frac{5}{2}$ and 4, respectively, for

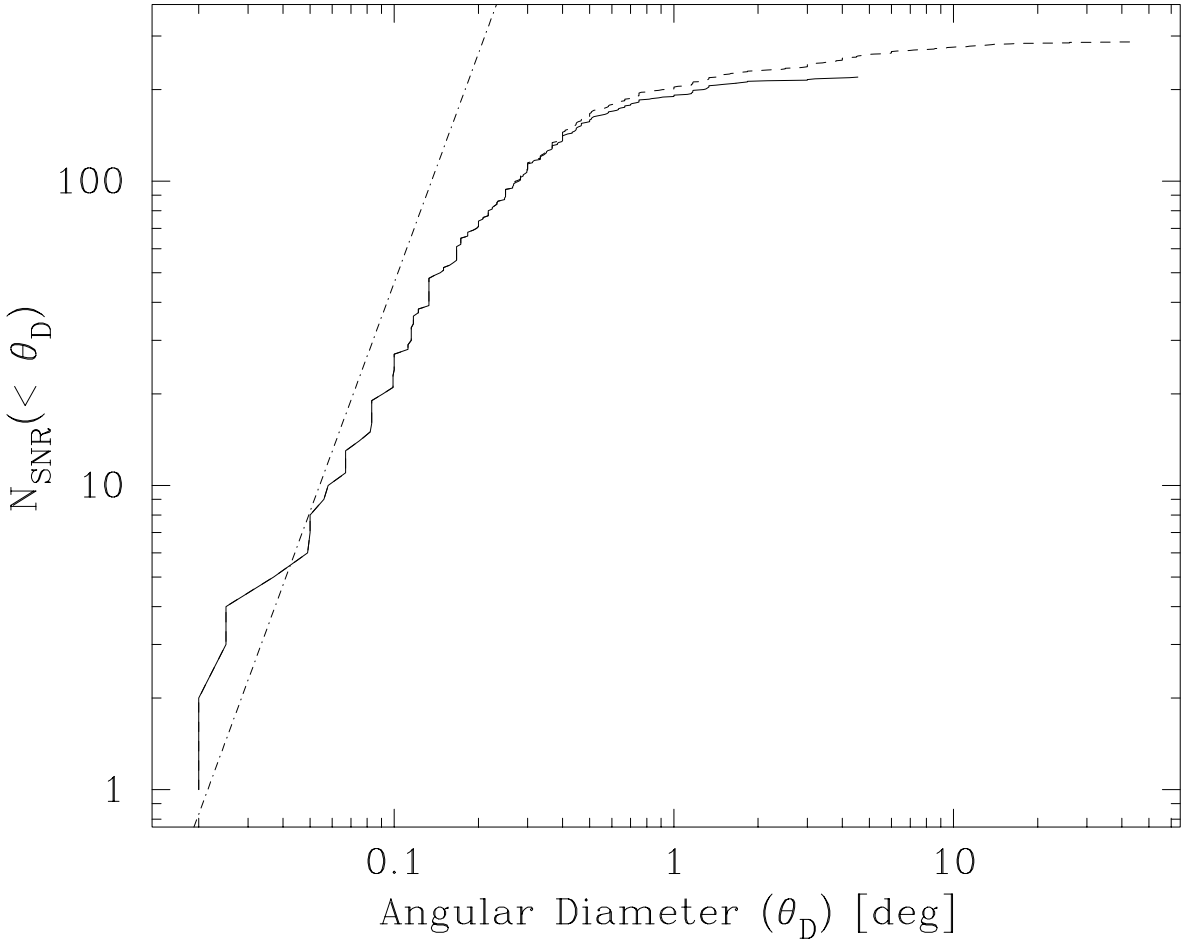

Figure 8.3: The cumulative-number/angular-diameter distribution derived from Green's catalogue of galactic SNRs (Green, 1998) (solid line) and the distribution obtained when the catalogue is supplemented with the new SNRs identified in the Parkes (Duncan et al., 1997) and *SKYMAP* surveys (dashed line). The straight line (dot-dash) shows the slope expected for this cumulative distribution if all galactic SNRs have an adiabatic expansion law ($D \propto t^{2/5}$) (Ilovaisky and Lequeux, 1972b) and survive indefinitely. The parameters for the 4 galactic loops have not been included in this plot.

the cumulative statistic. The power-law index increases with the age of the remnant population because of the deceleration of the shell (see the discussion of the N-D relationship earlier in this chapter). As can be seen from figure 8.3, the cumulative distribution curves derived from SNR observations are less steep than even the lowest expected power-law index, and the slope decreases with increasing angular diameter. This negative curvature indicates an under-density of SNRs with large angular diameters, which may be understood to result from two processes:

- SNRs do not expand or maintain their identity indefinitely. Once they expand beyond a linear-diameter of ≈ 100 pc the energy density in their shells matches the general ISM energy density, and they become indistinguishable from the diffuse galactic background. These "invisible" large linear-diameter SNRs must account for a large fraction of the missing large angular-diameter SNRs and therefore contribute to the DGB.

- The low surface brightness of the large angular-diameter SNRs makes them susceptible to surface brightness limiting effects, i.e. they are not identified because of source confusion.

The conclusion that can be drawn from this investigation of the N-θ_D relationship is that a significant proportion of the diffuse galactic background radiation is due to the confused emission of large SNRs. This supports the results obtained by Monte Carlo modelling of the distribution of galactic SNRs (Li et al., 1988; Li et al., 1991).

8.2.3 Morphology of the SNR Candidates

Having investigated the morphologies of a small sample of 17 galactic SNRs Gaensler (1998) has suggested that there is a tendency for bilateral, or barrel-shaped, SNRs to have their symmetry axes aligned parallel to the galactic plane. This result contradicts an earlier analyses that found no statistically significant preferred direction of alignment for bilateral SNRs (Manchester, 1987). Gaensler interprets his result to imply that the galactic magnetic field plays an important role in the evolution of the SNRs. Although some of the new SNR candidates listed in table 8.1 have a apparent bilateral morphology there is no evidence of a preferred position angle for the axis of symmetry for these objects. There may, however, be evidence that many of the non-symmetric objects have bright arcs

or shell segments that are aligned parallel to the galactic plane. Examples of such objects are G1.2−4.0, G356.9−5.0, G342.6+8.2 and G319.8+17.3.

It has been reported previously that there is a general trend for SNRs to exhibit a latitude-dependent brightness gradient, with the brightest side closest to the galactic plane (Caswell, 1977; Caswell, 1988). Such a correlation suggests that the horizontal stratification in the density of the ISM and the z-height gradient of the galactic magnetic field are important factors in the evolution of SNRs. A number of the SNRs listed in table 8.1 are incomplete shells with the open (or very faint) segment of the shell directed away from the galactic equator. Examples include G45.1+8.0, G356.5+9.0 and G319.8+17.3, but there are also counter-examples such as G342.6+8.2.

8.2.4 Morphology of the Low-latitude Emission

These is a conspicuous lack of linear emission features aligned in a direction perpendicular to the plane that might be tracers of the galactic worms and chimneys proposed in chapter 5. All filamentary emission features in the colour plates exhibit curvature that suggests that they are segments of coherent shell structures. The conclusion drawn from this paucity of candidate objects is that if worms and chimneys do exist then they do not produce significant synchrotron signatures in the galactic radio emission. This conclusion parallels that of Waller et al. (1998) who found that the fine-scale structure of the galactic FIR emission does not show evidence for the worm and chimney structures seen in the HI data (Heiles, 1984). Although the lack of evidence for worms and chimneys in the synchrotron and FIR emission does not deny their existence, there is cause for suspicion that the linear features seen in HI maps are artifacts of the spatial high-pass filtering applied to the data in order to accentuate small-scale structures.

Recent numerical models suggest that magnetic confinement may prevent the blowout of superbubbles (Tomisaka, 1998). This magnetic confinement would also prevent the formation of worm- or chimney-like structures perpendicular to the galactic plane. If worms and chimneys are not common objects in the galactic disk then there must be some other conduit for hot gas to reach the halo. High-latitude shell sources that appear to open out towards higher latitudes may be evidence for large diameter SNRs or superbubbles breaking out of the galactic disk and depositing their hot interior gas directly into the halo. These objects may represent SNRs and superbubbles at z-heights that are comparable to the scale-height of the galactic magnetic field that can break out of the galactic disk.

8.3 Individual Objects

A number of interesting objects and regions that are evident in plates C.6 to C.14 are discussed individually below. These objects include some of the new SNR candidates listed in table 8.1 as well as well-known objects that have been discussed by others in the literature.

8.3.1 G205.5+0.5 (Monoceros Nebula) & Rosette Nebula

These two objects have been extensively observed at radio and optical wavelengths (Milne and Hill, 1969; Caswell, 1970; van den Bergh, 1973; Milne and Dickel, 1974; Dickel and De Noyer, 1975; Davies et al., 1978; Graham et al., 1982; Odegard, 1986). This region has a mix of well-defined thermal and non-thermal sources, and as such it is a good benchmark region for testing the efficacy of the thermal/non-thermal separation procedure implemented by `radiofir.f`. The top panel in plate C.14 illustrate the success of the discrimination procedure in identifying the known HII regions in the region. An extended, apparently non-thermal source is evident at ($\ell \approx 203°$,$b \approx +2°$) which is probably an unresolved SNR associated with the H-α nebula S273. This radio source is not listed in table 8.1 because its morphology is not resolved in the map.

8.3.2 G216.5+1.0

This small, faint patch of emission with an angular diameter of about 1.5° is not listed in table 8.1 because its morphology is not resolved in the non-thermal map shown in plate C.14. Reynolds (1987) has detected a faint optical H-α feature towards this object and comments that there is no ionizing star associated with this emission. It is, therefore, quite likely that this object is a SNR.

8.3.3 S296 (Canis Major OB1)

The ridge-like radio continuum feature near ($\ell \approx 224.5°$,$b \approx -2°$) is associated with the CMa OB1 stellar association (Clariá, 1974b), the CMaR1 reflection nebula (Clariá, 1974a) and the H-α emission nebula S296 (Sharpless, 1953; Reynolds, 1978) which lie at a distance of 1150 pc from the sun. A number of radio continuum maps have been made of the region (Gaylard and Kemball, 1984; Nakano et al., 1984; Pyatunina, 1985; Pyatunina and Taraskin, 1986) which indicate that the radio emission is a mixture of thermal and non-

thermal emission. Hydrogen recombination lines have been observed towards the bright ridge of continuum emission (Gaylard and Kemball, 1984) confirming that there is a thermal component to the emission. Phenomena such as the presence of an HI shell around the region (Herbst and Assousa, 1977), an expanding H-α shell (Reynolds, 1978) and evidence of compressional magnification of the local magnetic field (Vrba et al., 1987) suggest that this region may be a site of SNR-induced star formation. The thermal/non-thermal discrimination process has not identified the bright ridge as thermal emission, implying that the FIR/radio flux ratio is inconsistent with the value expected for normal HII regions, further supporting the SNR hypothesis. Faint emission is seen to extend above the bright ridge towards positive latitudes which could be part of a large, incomplete SNR shell. No pulsars have been recorded in this region. The nearby discrete HII region RCW 5 (S298) at ($\ell = 227.75°$,$b = -0.15°$) has been correctly identified as a thermal emission object by the discrimination process.

8.3.4 The Vela/Gum Region

The Vela SNR (G263.9−3.3) has been mapped over a wide range of radio frequencies (Milne, 1968; Davies and Gardner, 1970; Milne, 1980; Dwarakanath, 1991; Milne, 1995; Woermann, 1998) and is seen as an optical emission nebula (van den Bergh, 1973) and an X-ray source (Seward, 1990; Aschenbach et al., 1995). It is best categorized as a composite SNR because it possesses a plerion component (Vela X) and a weak shell (Vela Y and Vela Z). The *SKYMAP* (plate C.12) and Parkes 2.4 GHz (Duncan et al., 1996) maps of the Vela SNR indicate that there is extended, diffuse emission associated with the SNR that fills a $\approx 6°$ diameter circle centred on $\ell \approx 263.8°$,$b \approx -1.9°$. A partial HI shell seems to correlate with bright optical filaments associated with the Vela SNR, but it is not as extensive as the radio continuum emission. The position of the Vela pulsar (PLS0835−4510) is very close to the peak in the emission of Vela X, which has a relatively flat spectral index of $\beta = 2.4$ (Milne, 1980) and shows linear polarization (Milne, 1995; Duncan et al., 1997). These factors support the supposition that Vela X is a plerion component of the SNR, receiving its energy from the pulsar (Weiler and Panagia, 1980).

High resolution X-ray images of the Vela SNR made using *ROSAT* show fragments of ejecta outside of the shell boundary (Aschenbach et al., 1995). Evidence for radio counterparts to X-ray features "A", "D" and "E" identified in the *ROSAT* map are seen in the *SKYMAP* data.

The nature of the extended emission features associated with the Gum Nebula (see plates C.12 and C.13) has been reported in some detail by Woermann (1998) and Duncan et al. (1996). The T-T plot in figure 7.5(d) (chapter 7) confirms Woermann's conclusion that the Gum nebula is a composite source with both thermal and non-thermal components. The non-thermal classification of a large fraction of the radio emission by the discrimination procedure is the result of a lack of detailed spatial correlation between the FIR and radio emission. This non-correlation further supports Woermann's hypothesis that the Gum Nebula is a relic of a single or multiple SNRs. The four white circles superimposed on the emission of the Gum Nebula (plates C.12 & C.13) are a rather speculative attempt to identify multiple SNR shells in the filamentary emission associated with the nebula. These loops are listed in table 8.1 as SNR candidates. A number of known pulsars are seen to be close to the centres of these circles but no claim is made about their association with the proposed SNRs.

8.3.5 G279.0+1.1

This SNR was discovered in the *SKYMAP* 2326 MHz data when the component map A05D63 was produced (Woermann and Jonas, 1988). Supplementary observations were made at 1644 MHz in order to confirm its non-thermal spectrum. The shell of emission is brighter towards higher latitudes, which may be a result of interaction with a molecular cloud that is adjacent to the SNR. Higher resolution observations at 1.4 GHz and 2.4 GHz have subsequently been made using a polarimetric receiver on the Parkes telescope (Duncan et al., 1995a). The highly regular tangential magnetic field inferred from these polarimeter observations suggests that the shell is an old SNR.

8.3.6 G323.5+0.8

This large, incomplete shell source with a diameter of $\approx 13.7^\circ$ can be seen in plates C.9 and C.10 of appendix C. Duncan et al. (1997) interpret the emission from this area differently, and propose a somewhat larger shell centred on $\ell \approx 325^\circ$, $b \approx 0^\circ$. Their shell is identified in the plates by a large dashed circle. The source confusion in this region makes it difficult to judge between these two interpretations, but it is very likely that the emission is the result of multiple SNRs with various diameters.

8.3.7 The Ara Region – G337.2−8.7

Combi et al. (1995) have mapped the region bounded by the following galactic coordinates ($350° \geq \ell \geq 320°$, $-23° \leq b \leq +2°$) at 1435 MHz and compared the resulting map with the corresponding data from the 408 MHz survey. They used the BGF technique (Sofue and Reich, 1979) to subtract out the smoothly-varying background components of the 408 MHz and 1435 MHz maps, but their resulting residual maps do not exhibit the dynamic range and detail of the corresponding 2326 MHz map shown in plate C.9. The SNR candidate G337.2−8.7 listed in table 8.1 corresponds to the radio source identified as "Ara 335−11" in their maps. They suggest that the interaction of the cosmic rays from this SNR with a nearby molecular cloud is the source mechanism for the intermediate-latitude γ-ray source centred near $\ell = 334°$, $b = -11°$.

8.3.8 G344.4−5.3

This distinct but incomplete shell of radio emission with a diameter of $\approx 3.8°$ (plate C.9) was first reported by Jonas (1986) who noted its association with the filamentary H-α nebula RCW 114 (Rodgers et al., 1960b). Published investigation of deep H-α plates and FIR images of this region confirm that this object is an SNR at a distance of less than 200 pc (Bedford et al., 1984; Meaburn et al., 1991).

8.3.9 G356.9+8.5

This shell source with a diameter of $\approx 9.5°$ has been discussed previously in chapter 6 and can be seen in plate C.8. The shell is much brighter at lower latitudes and becomes quite indistinct in the upper-right quadrant. This may be a large SNR that is on the verge of breaking out of the galactic disk. The pulsar PLS1654−2707 is situated close to the centre of the shell, suggesting a possible association. Taylor et al. (1993) use the measured dispersion measure and a model of the galactic electron density (Taylor and Cordes, 1993) to calculate a distance of 3.97 kpc for this pulsar. This distance implies a rather large linear diameter of 660 pc for the shell and a z-distance of 600 pc. A large SNR-blown shell this height above the galactic plane would certainly be a good blow-out candidate.

8.3.10 The Aquila Supershell

Maciejewski et al. (1996) have published HI maps of the Aquila Supershell (GS 034−06+65) which has a diameter of about 5.6°. They speculate that the expansion energy of this shell

Longitude (ℓ) [deg]	Latitude range [deg]	HII region	Reference
289.5	$-0.2 < b < +1.4$	unnamed	(Duncan et al., 1995b)
345.1	$+2.0 < b < +3.5$	Gum 56	new identification
18.5	$b > +2.9$	S54,W35	(Müller et al., 1987)
31.0	$b < -1.2$	S67	new identification

Table 8.2: A list of thermal chimney candidates identified in the low-latitude thermal 2326 MHz radio continuum emission. These objects were selected because they satisfy the following criteria: (a) they appear as linear, vertical structures in the thermal maps, and (b) they are rooted in HII regions.

of HI gas was provided by 10–100 supernova explosions and that the shell may be a blow-out phenomenon. There are no features in the non-thermal 2326 MHz map shown in plate C.7 that correlate convincingly with the HI emission of the shell, although there are some faint filaments towards the interior of the shell. The conservative conclusion drawn from the lack of correlating features is that the Aquila Supershell is not detected in the 2326 MHz map.

8.3.11 G43.3−1.0

This SNR candidate appears as an $\approx 8^\circ$ diameter shell of non-thermal emission in plates C.6 and C.7. Downes et al. (1981b) previously identified the shell segments between $\ell = 40^\circ$ and $\ell = 43.5^\circ$ as part of a SNR shell with a diameter of 7.8° centred on $\ell = 43.9^\circ$, $b = -0.2^\circ$, but their parameters are somewhat unreliable because they did not have a full coverage of the object. Part of this shell coincides with the emission from the SNR G39.7−2.0 (W50) (van den Bergh, 1980; Downes et al., 1981a; Downes et al., 1986; Elston and Baum, 1987) that is associated with SS 433 (Romney et al., 1987), but this is probably a chance alignment.

8.3.12 Thermal Chimneys

Although there is no evidence for large-scale SNR-blown worms and chimneys in the 2326 MHz non-thermal galactic emission there are small-scale radio continuum spurs reported in the literature that appear to extend vertically out of galactic HII regions. These objects and their appearance in the 2326 MHz maps are discussed below.

A narrow, collimated thermal spur ("Stockert's chimney") that extends along $\ell \approx 18.5^\circ$ in the latitude range $+3^\circ \leq b \leq 8^\circ$ has been identified in 1420 MHz, 2720 MHz and

4750 MHz continuum maps (Müller et al., 1987). Spectral indices determined from the continuum maps and the detection of H-110α recombination lines provide convincing evidence that the emission is thermal. The spur appears to extend out of the large galactic HII region S54 (W35, NGC6604, $\ell = 18.68°$, $b = +1.97°$), and it is speculated that this object is a thermal chimney which allows the outflow of an admixture of partially ionized hydrogen and cosmic rays into the halo (Kundt and Müller, 1987). The lower part of this spur is visible in the thermal emission map in plate C.7, indicating that there is a similar feature in the 60 μm FIR map that correlates with the radio feature. If this is an outflow phenomenon then this radio/FIR correspondence implies that the dust in the HII region is also being transported with the gas. Faint features that may be part of the spur can be seen in the non-thermal map in the latitude range $+5° < b < +8°$, but these may be part of a filament associated with the fracture in the NPS discussed in chapter 6.

Duncan et al. (1995b) have identified a number of faint, filamentary emission features extending out of the galactic plane near concentrations of HII regions. They speculate that these "plumes and spurs" are outflows of hot gas and dust from the HII regions.

One of their plumes appears to emanate vertically from the cluster of discrete HII regions near $\ell = 271°$ and then spread out parallel to the galactic plane at $b \approx +0.5$ between longitudes 270° and 274° (Duncan et al., 1996). Evidence of this plume can be seen in the non-thermal image in plate C.12, implying that there is no corresponding FIR emission that correlates with the radio continuum. This filamentary emission may be part of a non-thermal shell resulting from supernova explosions or stellar winds associated with the nearby HII region. No corresponding feature can be seen in maps of linearly-polarized 2.4 GHz emission (Duncan et al., 1997).

Duncan et al. identified three faint vertical radio continuum structures in the longitude range $295° > \ell > 288°$ in their 2.4 GHz map (Duncan et al., 1995b). There is very faint evidence for these spurs in the non-thermal image of the *SKYMAP* data shown in plate C.11, and the jet that they identify in their map at the base of the right-hand spur ($\ell \approx 289.5°$) can be seen in both the thermal and non-thermal 2326 MHz maps. The low signal-to-noise ratio of these features probably causes the thermal/non-thermal discrimination procedure to become unreliable, so no great confidence should be placed in the classification and these spurs may well be in the same class of objects as Stockert's chimney. Table 8.2 lists all of the thermal chimney candidates identified in the thermal 2326 MHz maps (plates C.6 to C.14 of appendix C).

Chapter 9

Conclusion

This thesis has reported on the observation technique and data reduction procedures used for the Rhodes/HartRAO 2326 MHz *SKYMAP* survey project, and presented an astrophysical interpretation of the radio continuum map produced by the project. The *SKYMAP* survey map covers two-thirds of the whole sky and thus provides a unique view of the radio continuum emission from the Milky Way. This concluding chapter summarises the main results derived in this thesis and comments on the future work required to complete the *SKYMAP* project.

9.1 Observations, Data Reduction and Calibration

The good quality the survey data is evident both from qualitative inspection of the images presented in appendix C and the quantitative results of the calibration and quality assurance procedures described in chapter 4. The successful outcome of the survey is taken as proof that the modifications described in chapters 2 and 3 that were made to Mountfort's original observing and data reduction procedures were efficacious.

Further observations are necessary before the *SKYMAP* project can be considered to be complete. The only area of the southern sky that has not been covered by the *SKYMAP* survey is the very prominent keyhole-shaped region seen in the colour plates of appendix C that surrounds the southern equatorial pole (SEP). This unmapped region only subtends 0.5% of the entire sky, but it needs to be mapped in order to resolve the baseline problems that are evident towards the extreme southern limit of the current *SKYMAP* map. There is also a strong aesthetic motivation for filling this hole in the map.

A new observing and data reduction technique will have to be devised to map this region. The considerable geometrical distortion of the equatorial coordinate system in this

region makes it impractical and inefficient to use the existing *SKYMAP* scanning pattern. A possible scanning pattern to be used for this area is illustrated in figure 9.1. This pattern ensures oversampling of the entire region without excessive inefficiency or unwarranted data redundancy. Interleaved rasters are not necessary because of the short scan times required and the relatively wide right ascension intervals between the scans. Whether the scans are made at constant right ascension or constant hour angle is a consideration that will be resolved by experience. The scan pattern shown in figure 9.1 provides for significant overlap with the existing *SKYMAP* sky coverage. This overlap will facilitate the merging of the SEP map with the main *SKYMAP* data.

Another factor to be considered when mapping this region is the proximity of the SEP to the physical manoeuvrability limits of the telescope. Although the antenna structure has been modified to allow the antenna to point at the SEP, it is essential that the scans towards $\delta = -90^\circ$ are made slowly in order to avoid excessive overshoot and the resultant damage to the antenna. The scanning pattern in figure 9.1 only requires 1 in 16 scans to extend all the way to the SEP, therefore time lost while cautiously approaching the SEP will not impact significantly on the scan timing.

Using this scanning pattern the SEP temperature is sampled every 32 minutes (once per 8° segment). Any temporal variation in the antenna temperature measured towards the SEP must be the result of anomalous drift in the system temperature because the SEP is a fixed point on the celestial sphere, therefore the recorded SEP antenna temperatures may be used to correct the scan data for these drifts.

The uncertainty in the baseline accuracy of the *SKYMAP* survey has been discussed in chapters 4 and 7. Independent observations of the 2326 MHz sky brightness are required to resolve these baseline uncertainties. A prototype horn telescope that was designed and built for this purpose is discussed in section 9.4 later in this chapter. It is hoped that this instrument will also resolve the temperature scale inconsistency between the *SKYMAP* 2326 MHz survey and the 1420 MHz northern sky survey that was discussed in section 7.1.1 of chapter 7. The Berkeley CMBR research group also intend making 2.3 GHz measurements of the whole sky using small antennas (the GEM project) (De Amici et al., 1993; De Amici et al., 1994; Torres et al., 1996). One of their stated purposes of the GEM experiment is the improvement of the *SKYMAP* baseline.

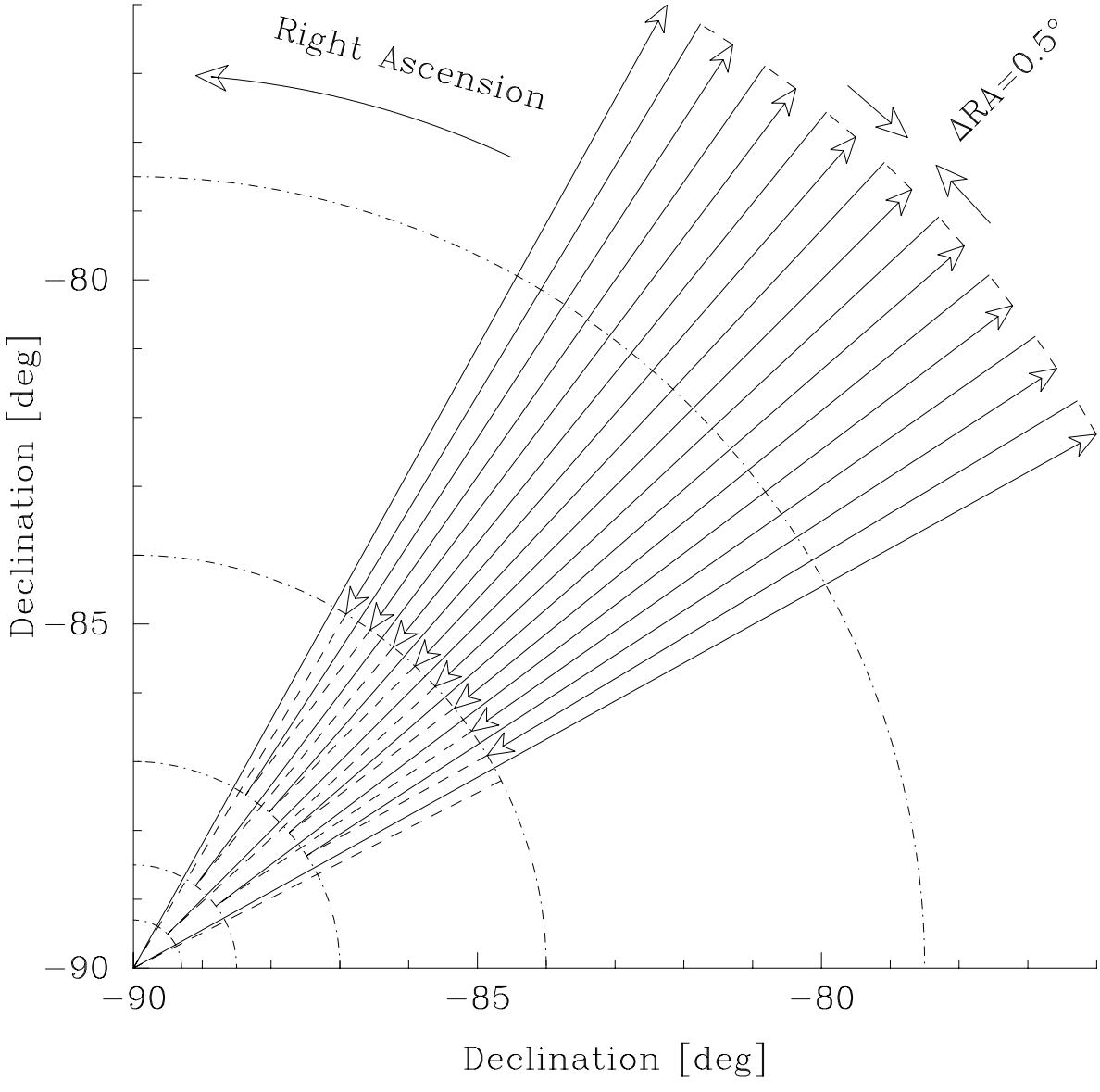

Figure 9.1: A representative 16-scan segment of the scan pattern proposed for mapping the region of sky near the southern equatorial pole (SEP). Note that the 8° angle subtended by this segment has been expanded for clarity. The solid lines with arrow-heads represent actual scans while the dashed lines represent manoeuvres between the end of one scan and the start of the next. The dot-dash arcs are drawn at declinations of −89.3°, −88.5°, −87°, −84° and −78.5°. The northern limit of the scans is $\delta = -74°$. 45 of these 8° segments are needed to cover the entire SEP region. The small-circle scan spacing is less than 0.1° for all declinations south of $\delta = -78.5°$ and less than the Nyquist requirement of 0.14° for declinations south $\delta = -74°$.

9.2 A New Mapping Project

A number of new objects with faint, extended radio emission have been identified in the *SKYMAP* survey map. Most of these objects are SNR candidates that have been discussed in chapter 8. The sensitivity of the current *SKYMAP* data is not sufficient to allow meaningful quantitative analysis of the emission from these objects. Follow-up observations of some of these objects are planned in order to obtain deep 2.3 GHz images with the required sensitivity.

Buchner (1998) has recently devised a "basket weaving" mapping procedure to be used at HartRAO which is well-suited to the task of making such high-sensitivity observations of small target areas. The technique uses orthogonal scans to reduce "scanning effects" in the resulting maps. This scanning procedure requires a more sophisticated antenna control system than the system that was devised by Mountfort and used for the *SKYMAP* observations.

To accommodate this more demanding mapping technique the author devised a new antenna control system at HartRAO which provides all of the required features (Jonas, 1991). This new control system is currently being integrated into the upgraded antenna drive system by the Observatory staff.

9.3 Summary of Scientific Results

The primary objective of the *SKYMAP* survey project is to map the 2326 MHz radio continuum emission from the Milky Way. The scientific rationale of the survey is to investigate the morphology of the galactic emission and determine its spectral characteristics. Various aspects of these two topics were covered in chapters 6, 7 and 8 of this thesis. The main conclusions drawn in these chapters are summarized below.

9.3.1 Morphology

Cursory examination of the 2326 MHz radio emission from the Milky Way (plate C.1 in appendix C) reveals that the galactic emission is dominated by the diffuse ridge of emission that traces the galactic plane. Whether this diffuse emission, designated the DGB in chapter 6, is due to amorphous cosmic ray electrons or is a superposition of emission from a large number of old SNRs is an unanswered question, but the analysis of SNR statistics in chapter 8 implies that some fraction of the DGB is due to the emission from large, faint

SNR shells.

The spatial analysis of the DGB in chapter 6 shows that its distribution in both longitude and latitude is consistent with the emission originating from sources that are coextensive with the spiral arms of the galaxy. The DGB also reveals local and large-scale asymmetries in the galaxy. The high-latitude emission is influenced by objects associated with the Gould Belt system and the low-latitude emission traces the galactic warp that occurs outside the solar circle.

The faint, extended sources superimposed on the DGB were accentuated by subtracting out an empirical DGB model from the survey map. The reduced dynamic range of the residual map greatly facilitated the identification of the superimposed sources. The remaining source confusion in the residual map was reduced by discriminating between thermal and non-thermal radio sources close to the galactic plane. The thermal sources were subtracted out of the residual map, yielding a map of extended, non-thermal galactic radio sources (plates C.6 to C.14 in appendix C). Many of the sources seen in these plate images have shell-like morphologies, suggesting that the sources are galactic SNRs.

The 42 shell-like sources listed in chapter 8 have diameters ranging from $\approx 1.5^\circ$ up to $\approx 26^\circ$ and therefore fill the angular-diameter gap between the majority of previously-identified SNRs and the Galactic Loops. These newly discovered SNR candidates represent some fraction of the galactic SNRs that have eluded detection because of the surface brightness limits of previous SNR searches. Statistical analyses and Monte Carlo models suggest that there must be many more of these objects that are as yet undetected in the galactic radio emission. The aggregate emission from these unidentified objects may be partly responsible for the DGB.

The residual images show emission structures with a wide range of angular scales with most of the emission features showing some form of curvature. There do not seem to be any linear features aligned perpendicular to the galactic plane that could be tracers of the galactic worms and chimneys seen in spatially-filtered HI data (Heiles, 1984). The only indication of large-scale galactic break-out phenomena are the large, incomplete shell-like sources seen at intermediate and high galactic latitudes. The observed morphology of the galactic non-thermal emission suggests that SNR-induced breakout is quite rare. This indicates that the galactic magnetic field and gas pressure are able to constrain SNR-driven bubbles to remain within the galactic disk. This would imply that the Milky Way has a weak halo because of the restricted supply of hot gas from the disk. This deduction is

supported by X-ray measurements (Heiles, 1987; Li and Ikeuchi, 1990).

There may be some evidence for small-scale worm- or chimney-like features extending out of galactic HII regions. These chimney candidates appear to be thermal extensions of the parent HII regions, and are unlikely to be linked to SNR activity.

9.3.2 Spectral Characteristics

In chapter 7 the *SKYMAP* data is compared with other radio survey data at higher and lower frequencies and with FIR maps. The purpose of these comparisons was to investigate the source mechanisms of the various components of the galactic emission and to estimate the galactic signal contamination in CMBR measurements.

Low-frequency Spectrum

The spectral index of the diffuse galactic emission calculated by comparing the 408 MHz and 2326 MHz survey maps lies in the range $2.54 < \beta < 2.90$ where the spread in values is a result of intrinsic spatial variation in the spectral index. There does not appear to be evidence that the spectral index of the DGB depends on galactic latitude in any systematic way, but baseline uncertainties in the *SKYMAP* data prevent the accurate mapping of the spatial distribution of the low-frequency galactic spectral index. Given the limited accuracy of the spectral index map shown in plate C.5 of appendix C it is impossible to support or refute current cosmic ray transport theories.

CMBR Contamination

A composite 2326 MHz all-sky map was compiled by augmenting the *SKYMAP* 2326 MHz data with suitably scaled 1420 MHz northern hemisphere data. This composite map was compared with the *COBE-DMR* 31 GHz and 53 GHz skymaps using cross-correlation and spherical harmonic decomposition analyses in order to determine the high-frequency spectral index of the high-latitude galactic emission. A spectral index of $\beta = 2.95 \pm 0.08$ was determined for the galactic synchrotron emission in the frequency range 2.3 GHz to 31 GHz. Using this spectral index it is estimated that the RMS amplitudes of the higher order ($\ell > 10$) galactic synchrotron multipole components are less than 5.5 μK and 1.1 μK at 31 GHz and 53 GHz respectively.

Cross-correlation analyses between the *SKYMAP* data and FIR maps in the wavelength range 60 μm to 240 μm indicate that the high-latitude galactic radio continuum also has

a thermal emission component. The weak but significant correlation that was measured between small-scale structures in the 2326 MHz radio map and the FIR maps is taken as evidence of free-free radio emission that is associated with the galactic cirrus dust structures. The RMS variance of the galactic 2326 MHz thermal emission is estimated to be about 1 mK. This signal scales to 4.3 μK at 31 GHz and 1.4 μK at 53 GHz assuming a thermal spectral index of $\beta = 2.1$.

Cross-correlation analyses between the 2326 MHz map and the CMBR anisotropy maps derived from the *COBE-DMR* data indicate that there is no significant galactic signal in these maps.

The amplitudes of the galactic synchrotron and free-free contamination components calculated using the 2326 MHz *SKYMAP* data and quoted above are consistent with previously published values (Kogut et al., 1996a; Kogut et al., 1996b). These contaminating galactic signals are weak but need to be considered if reliable estimates of cosmological parameters are to be derived from measurements of the CMBR "doppler peak" (Jungman et al., 1996; Bond et al., 1997; Zaldarriaga et al., 1997). The $20'$ resolution of the *SKYMAP* map will be particularly useful for correcting the CMBR data that will be obtained from the proposed MAP and Planck satellites (Tegmark, 1998).

The presence of non-Planckian distortions in the low-frequency spectrum of the CMBR would have important implications for cosmological theories because these distortions would imply energy release processes in the early universe that are not accounted for in standard Big Bang theories. A number of measurements of the absolute sky temperature have been made at frequencies below 10 GHz, but the uncertainty in the galactic foreground contribution has been a major source of error in the determination of the intrinsic CMBR temperature (Smoot et al., 1985; Sironi and Bonelli, 1986; Smoot et al., 1987; De Amici et al., 1990; Sironi et al., 1990; De Amici et al., 1991; Sironi et al., 1991; Levin et al., 1992; Bensadoun et al., 1993; Witebsky et al., 1993; Bersanelli et al., 1994).

Once the baseline uncertainties have been corrected using measurements made with the horn telescope (section 9.4 below) or the GEM project (De Amici et al., 1993; De Amici et al., 1994; Torres et al., 1996) the *SKYMAP* data will be used to improve the accuracy of low-frequency absolute temperature measurements of the CMBR.

HII Regions

A successful procedure was devised to discriminate between thermal and non-thermal radio sources on the basis of their FIR/radio flux ratios. Besides reducing the source confusion near the galactic equator this procedure provided information about the statistical distribution of the FIR/radio flux ratios for galactic HII regions. A spread of ratio values between 400 and 1400 was obtained using the 2326 MHz *SKYMAP* data and the 60 μm *IRAS* skymap. A future line of enquiry will be to test whether there is any correlation between the FIR/radio ratio and the FIR colour of the HII regions.

9.4 The 2.3 GHz Horn Telescope

The reduction of the uncertainties in the baseline of the *SKYMAP* 2326 MHz survey is an important refinement that needs to be applied to this unique data set in order to improve its scientific value. These baseline uncertainties, which are discussed in chapters 4 and 7 and in section 9.1 above, limit the application of the data to studies of the galactic spectral index and the CMBR. The baseline needs to be more accurately defined over the whole of the mapped region so that the spatial variation of the galactic synchrotron spectral index can be determined to the required accuracy for testing cosmic-ray diffusion theories and so that the predicted synchrotron emission at high frequencies can be extrapolated. The prototype Rhodes/HartRAO 2.3 GHz horn telescope was designed and built in an attempt to implement an experiment that would provide independent sky brightness data that could be used to reduce anomalous gradients in the *SKYMAP* survey map.

The experiment is not designed to determine absolute sky temperatures at 2.3 GHz. This limitation arises because the necessary cryogenic reference loads are not available to the author. Absolute temperature measurements of the SEP have been made at a number of frequencies using helium-referenced radiometers at the South Pole (a list of references was given in the preceding discussion of the low-frequency CMBR spectrum). These measurements will be used to convert the SEP-referenced horn data to an absolute temperature scale. Brief descriptions of the concept of the experiment, the design and implementation of the horn telescope and test results from the experiment are given below.

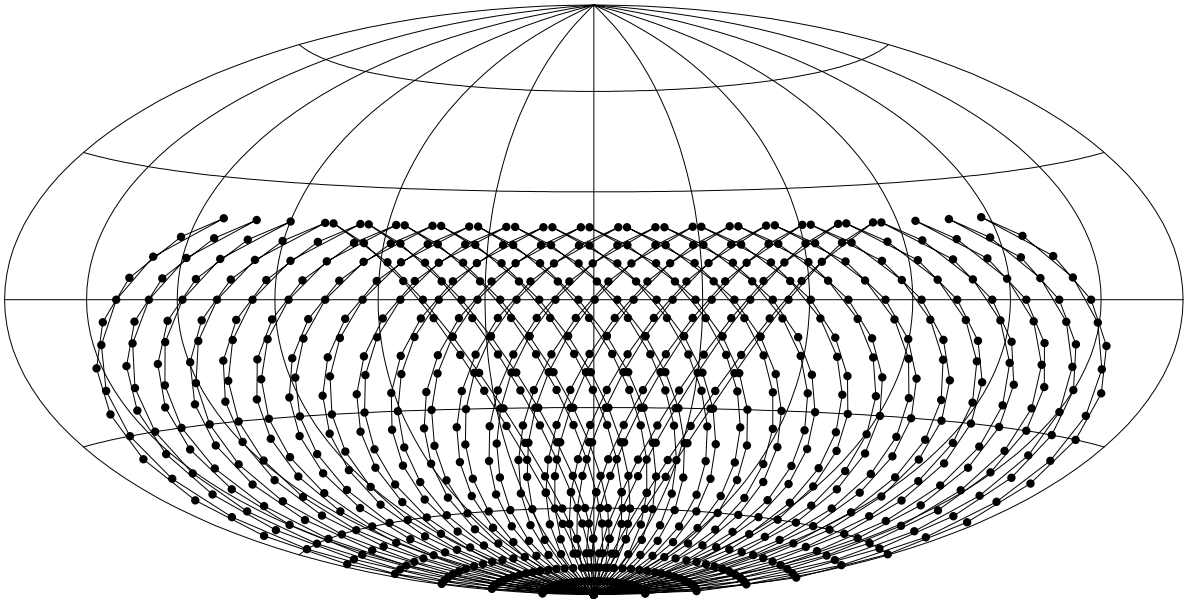

Figure 9.2: The scanning pattern resulting from constant-elevation scans over a continuous 14 hour period. The tracks of the scans are drawn in the equatorial coordinate system using a Hammer-Aitoff equal-area projection. The observing site is assumed to be near Grahamstown, South Africa which is situated at a latitude of $-33°20'$. An interrupted scanning method is used which requires the antenna to slew between sampling positions at regularly-spaced declinations. The black dots represent positions where the antenna is stationary while the antenna temperature is integrated and recorded. An integration period of 55 seconds was used to construct this diagram. An integration period of 10 seconds was used for the trial observations which resulted in a denser sky coverage. The aggregate declination interval is $\Delta\delta = 5°$ when the north and south scans are combined. The most northerly declination that can be accessed from Grahamstown using this scanning pattern is $\delta = +20°$.

9.4.1 The Experiment

An unused pyramidal horn antenna that was in storage at HartRAO provided the inspiration for this experiment. The anomalous gradients resulting from baseline uncertainties are mostly large-scale artifacts in the map, and do not require high-resolution data to effect their rectification. The horn antenna has a beamwidth of 15° which is well-matched to the estimated angular scale of the baseline anomalies. Dr G. Nicolson, Director of HartRAO, has very generously loaned the horn antenna and other microwave devices necessary for the telescope to the author for the duration of the experiment.

The aim of the 2.3 GHz horn telescope experiment is to produce a low-resolution map of the southern sky which has accurate baseline characteristics. This map will then be used to correct baseline errors in the main survey data, and also verify the full-beam temperature scale of the survey data. Two aspects of the observing strategy are intended to control baseline uncertainties in the horn telescope data:

1. Constant elevation scans are used to minimize the variation in the terrestrial foreground emission with scan angle. It is envisaged that the operational telescope will be surrounded by a raised reflective screen that will ensure that the ground radiation is both reduced in magnitude and independent of azimuth angle.

2. Every scan starts and ends at the SEP. The variation in the antenna temperatures recorded at the SEP is used to correct the scan data for system temperature drifts. Using this differential observing and data reduction strategy results in a map with a relative temperature scale referenced to the temperature of the SEP.

The scan pattern resulting from this observing strategy is shown in figure 9.2. The declination grid interval of $\Delta\delta = 5°$ ensures that the 15° beam is oversampled, and the northern measurement limit of $\delta = +20°$ is quite well suited to the sky coverage of the main *SKYMAP* survey.

The telescope is designed to be portable so that various observation sites can be evaluated. The major factors that determine site suitability are the absence of radio interference, low horizons (to reduce ground radiation) and security. Ground-radiation screens will be erected at suitable observation sites and a portable petrol-engine generator is used for electrical power if no mains supply is available. The experiment is completely automatic, being controlled by an ordinary PC-class computer.

9.4.2 The Telescope

The major criterion that was considered in the design of the horn telescope was the stability of the receiver system temperature. For the results of the experiment to be useful the baseline drifts in the receiver output have to be small and have time-scales that are very long compared to the scan duration. The differential technique used to reference the temperature scale to the SEP sky temperature can only correct for these slow baseline variations. Various constraints had to be considered in the implementation of the telescope, chiefly:

- The instrument had to be inexpensive. There were, and are, no funds to purchase RF devices, so spare receiver components had to been loaned from HartRAO.
- All mechanical and electronic construction had to be undertaken by the author using the equipment and materials available.

As a result of these constraints the structural components of the telescope are constructed from wood (except for the road trailer which was built by an engineering firm). The external appearance of the telescope can be seen in figure 9.3. All of the receiver components are contained within the rectangular wooden box, which is lined with polystyrene insulation. A custom-built temperature controller maintains the internal air temperature to within 0.1° C limits.

The receiver configuration is very similar to that of the 13 cm system at HartRAO (see figure 2.1 in chapter 2). Budgeting constrains preclude the use of a cryogenically cooled front-end amplifier, so an ambient GaAsFET amplifier bolted to a heavy aluminium heatsink is used instead. The heatsink increases the thermal capacity of the receiver package, thereby ensuring that the drift in the amplifier noise-temperature has a long time-constant.

The electronic systems that were designed and/or constructed by the author for use in the telescope are described briefly below.

Noise-adding radiometer. The design of this continuum radiometer is based Nicolson's original concept (G. Nicolson, private communication), but uses a solid-state synchronous demodulator in place of the double-balanced mixer employed in the original implementation. The square-law detector is a commonly-used design incorporating

Figure 9.3: The portable 2.3 GHz horn telescope mounted on its road trailer. The scale of the instrument can be ascertained from the height of the author (who is 1.73-m tall). The spotlight directed towards the mouth of the horn antenna is intended to keep the mylar radome clear of condensation. The motorized azimuth drive wheel is visible on the near-side of the azimuth turntable. The entire receiver system is enclosed within the rectangular box, which is lined with thermal insulation.

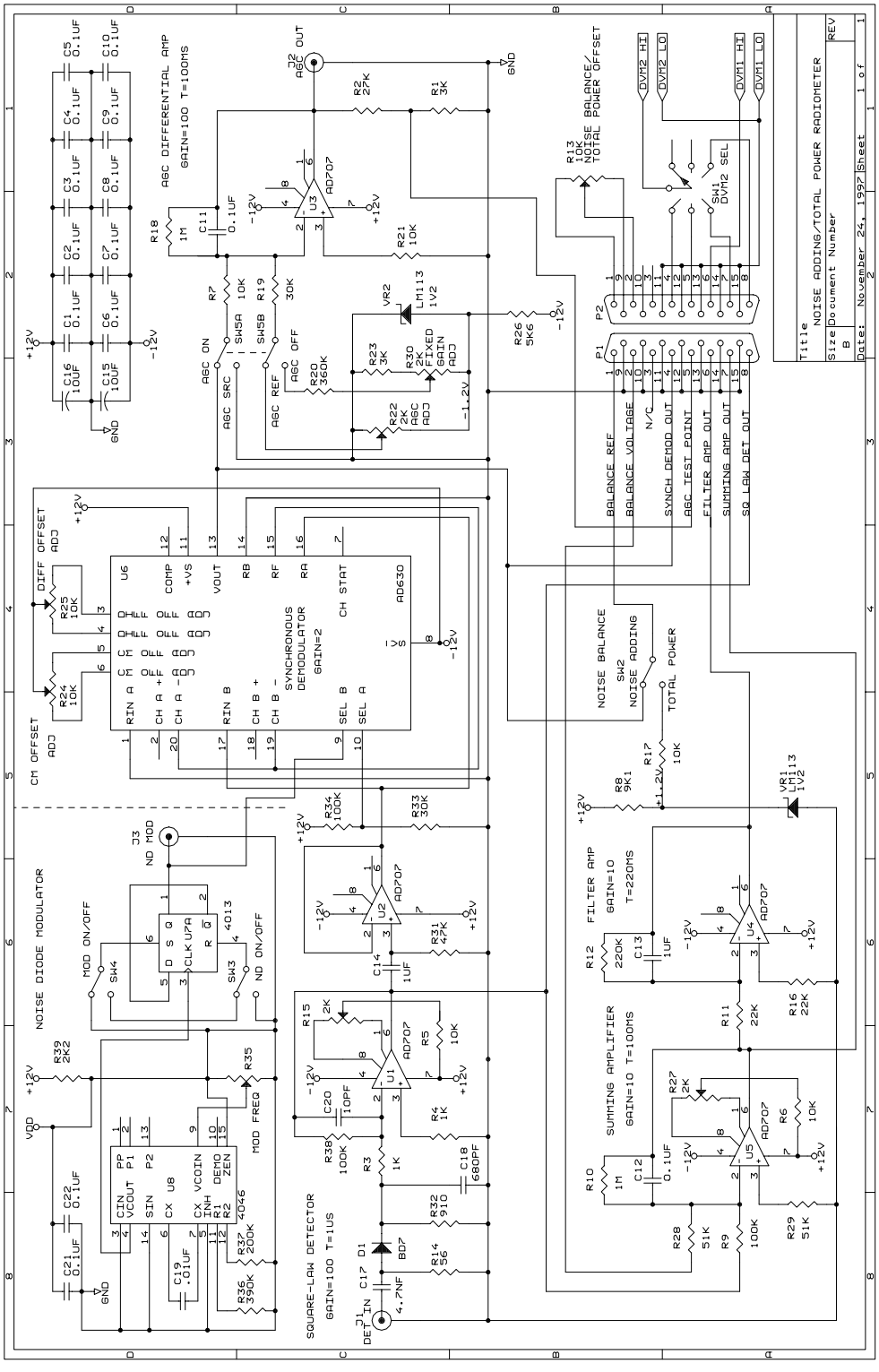

Figure 9.4: A schematic diagram showing the design of the gain-stabilized, noise-adding radiometer used in the 2.3 GHz horn telescope. The implementation of this circuit is shown in figure 9.5(a).

a BD-7 diode (Camara, 1971). The circuit diagram of this radiometer is shown in figure 9.4 and a photograph of the radiometer package is shown in figure 9.5(a).

Digital voltmeter. A single-chip, dual-slope integrating DVM (ICL 7135) and an 8751 microcontroller are employed to sample the radiometer output voltage and transmit the digital signal via an RS-232 connection to the controlling computer.

Azimuth drive. The telescope azimuth turntable (alidade) is rotated by a low-voltage DC-motor driving a reduction gearbox which is connected to a friction-drive wheel. The azimuth angle is measured using a three-pole synchro-transformer device. A simple intelligent electronic servo system allows the controlling computer to drive the telescope to any command azimuth. Drive commands are sent via an RS-232 connection which is shared with the DVM device.

Temperature controller. The air temperature inside the insulated box is controlled to within 0.1° C limits by a simple proportional feedback temperature controller. Four 100 W domestic light-bulbs are used as heater elements. An electric fan mixes and circulates the air within the box.

IF filters. L-C filters are used in the IF chain in order to reject out-of-band noise and interfering signals. These were designed and built using standard methods.

Power supplies. A number of regulated, linear power supplies are needed to provide the DC power requirements of the various telescope components.

A photograph of the layout of the PSU/mixer/IF/radiometer enclosure is shown in figure 9.5(b). Temperature stability and interference immunity were the main technical factors that were considered when constructing the receiver and ancillary electronic systems.

The entire observing procedure is fully-automated. A single PC-class computer controls the telescope azimuth-drive and receiver hardware, and records the radiometer output via the DVM. All of the telescope components communicate with the controlling computer via a single RS-232 connection to one of the computer's serial ports. A simple token-passing ring architecture is used to allow the computer to individually access each microcontroller-based sub-system connected to the serial communication bus.

The controlling program was written using the Turbo-Pascal programming environment. During observations the computer displays a full list of status variables on the

(a)

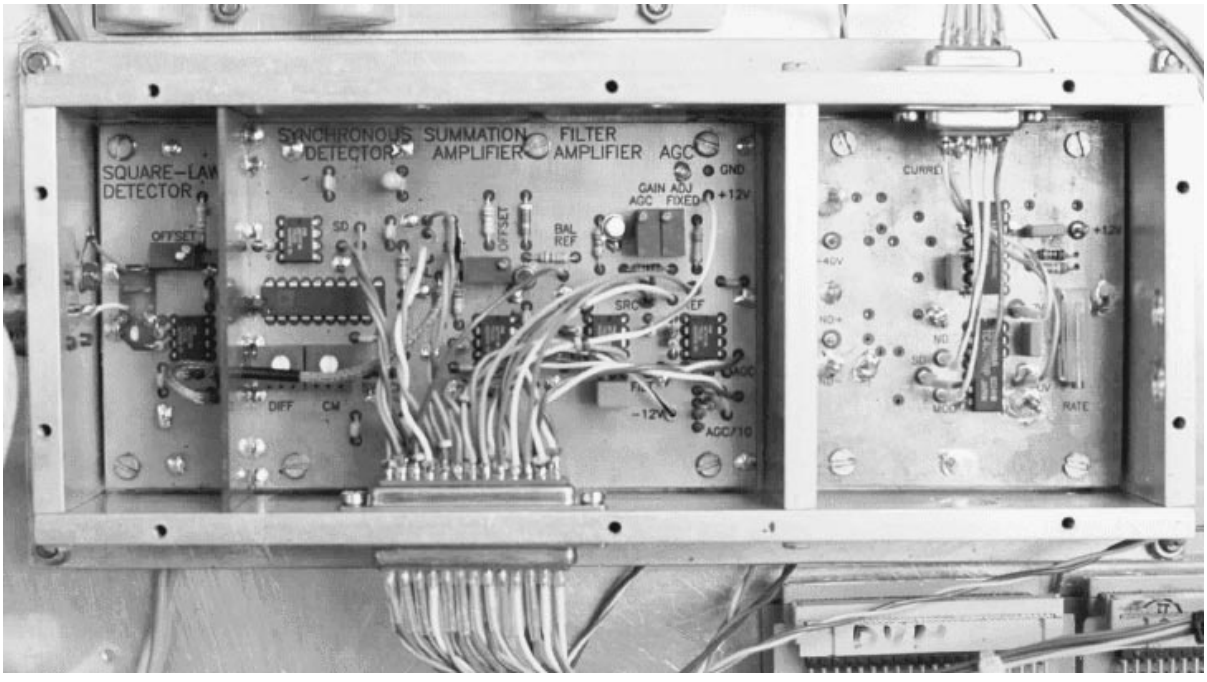

(b)

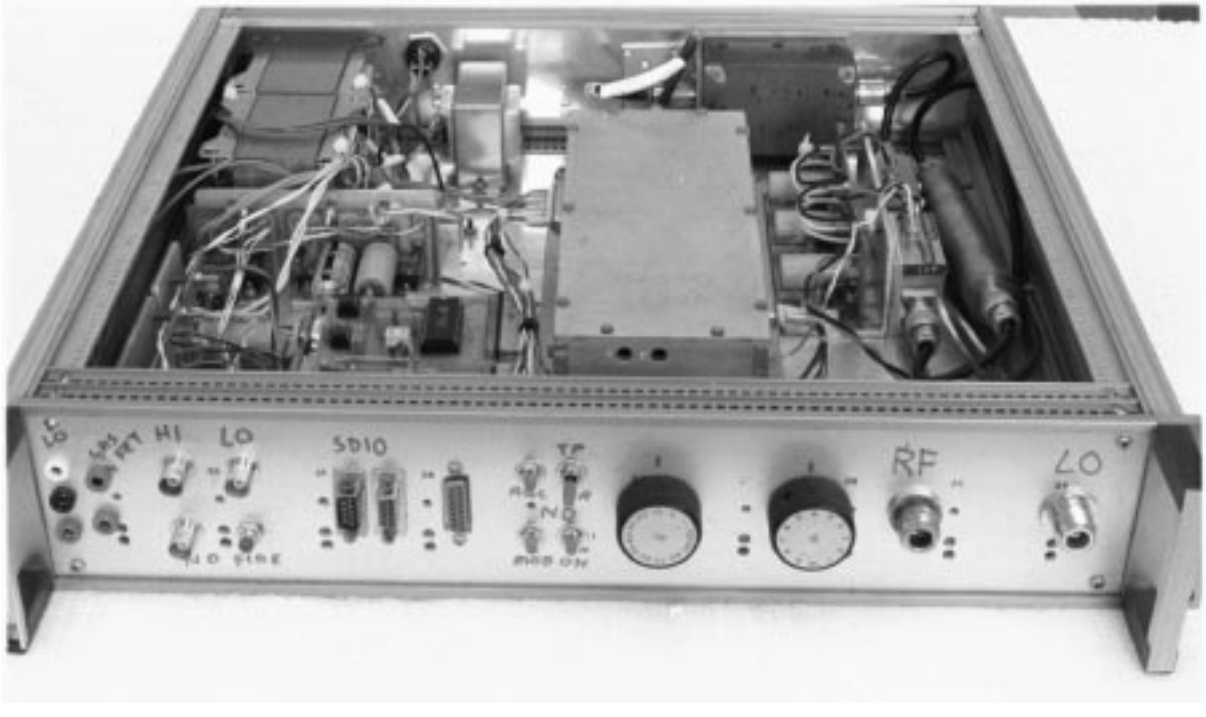

Figure 9.5: (a) The layout of the radiometer circuit shown in figure 9.4. The radiometer enclosure is made from 6 mm aluminium which provides both thermal and RFI shielding. Internal shielding separates the square-law detector (left) and oscillator circuitry (right) from the rest of the synchronous-detector and DC-amplifier components. (b) The layout of the PSU/mixer/IF/radiometer enclosure for the 2.3 GHz horn telescope. All temperature-sensitive components are bolted to heavy gauge aluminium plates in order to ensure long thermal time constants.

monitor screen, such as scan number, current antenna coordinates, date information and radiometer diagnostic voltages. A rough pseudo-colour map of the observed sky brightness distribution is built up on the screen in real-time, with the appropriate pixel being updated after each integration period. The data files produced by the observing program are in a format suitable for importing into standard spreadsheet programs. This allows diagnostic analyses of the data to be made at the observing site. A number of ancillary programs were written to align the antenna using the sun as a fiducial reference and perform various receiver and azimuth-drive diagnostic procedures.

9.4.3 Preliminary Results

All of the individual receiver components were tested for proper operation and stability on the laboratory bench before the entire telescope was tested in the field. The baseline stability of the telescope was tested by pointing the antenna towards the SEP and continuously recording the output throughout a number of nights. These tests indicated that the receiver baseline drift was slow enough to be corrected by the SEP-referencing procedure.

Full-function test observations were made once the correct operation of all of the telescope sub-systems had been verified. Figure 9.6 shows three independent maps of the sky brightness at 2.3 GHz that were derived from the first horn telescope observations made on three nights in July 1994. The results of these initial tests were reported in a poster paper at IAU Symposium No. 168 in the Hague in August 1994 (Jonas, 1996). Although the observing site used for these tests was far from ideal and no ground screens were used, these initial measurements were encouraging and indicated that the instrument was capable of producing data that could be used to correct baseline inaccuracies in the *SKYMAP* data.

Unfortunately no further successful tests have been possible since these early observations because of the sudden proliferation of S-band telecommunication links associated with the launch of cellular telephone systems in South Africa. It is our intent to persevere with the horn experiment despite the burgeoning interference problem. It is hoped that the effects of man-made interference signals can be diminished by suitable site selection and filter design.

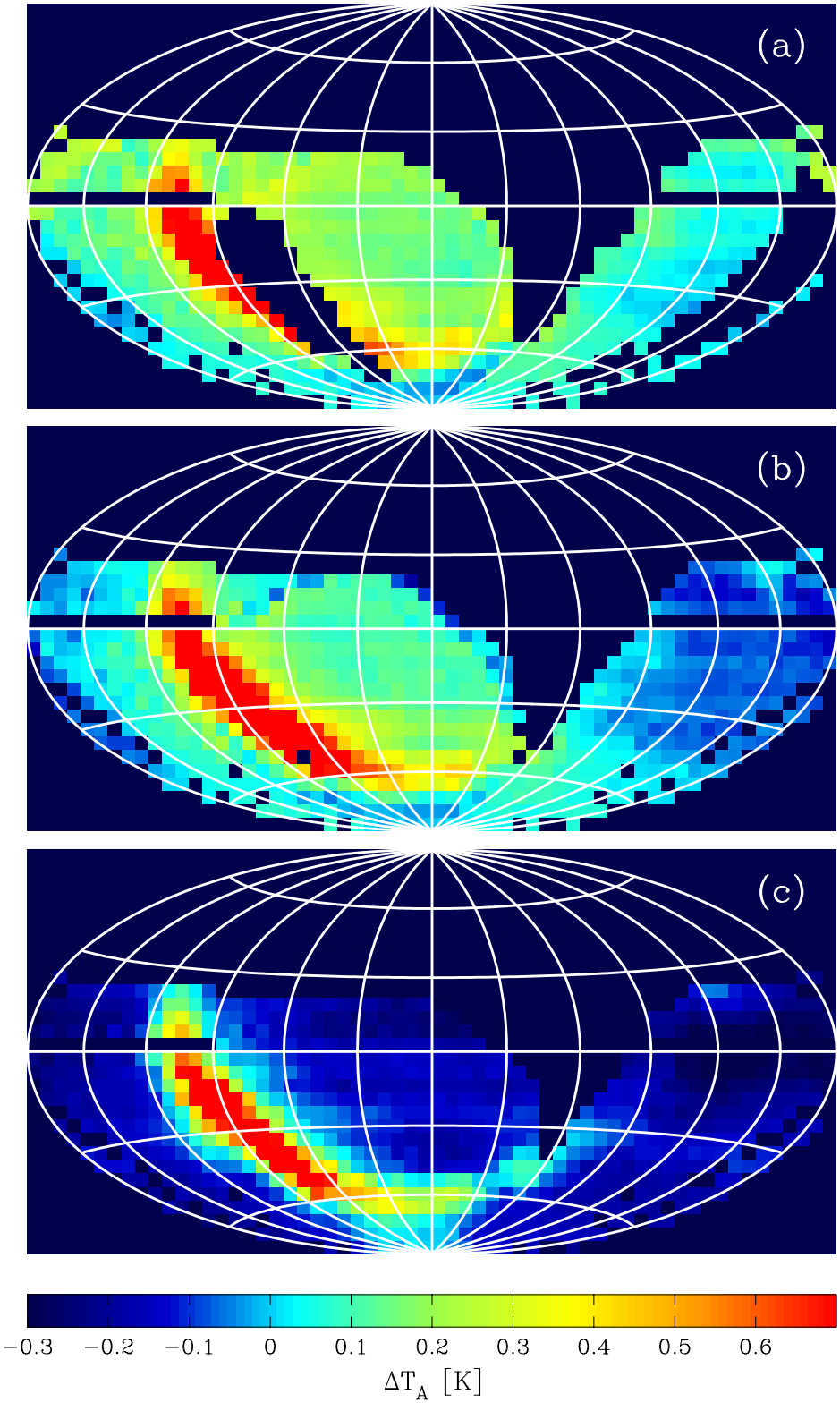

Figure 9.6: Preliminary 2.3 GHz horn telescope maps resulting from test observations made on three nights in July 1994. A Hammer-Aitoff equatorial coordinate projection has been used to display these maps. The maps are not consistent with each other because of the effects of ground radiation. Black pixels indicate missing data, i.e. regions of sky that were not covered by the scans.